Technical Report

TR-14-27

Modelling of critical H-M processes in the engineered barriers of SFR

Lennart Börgesson, Mattias Åkesson, Ola Kristensson,
Daniel Malmberg, Martin Birgersson
Clay Technology AB

Jan Hernelind, 5T-Engineering AB

December 2015

Svensk Kärnbränslehantering AB
Swedish Nuclear Fuel
and Waste Management Co

Box 250, SE-101 24 Stockholm
Phone +46 8 459 84 00

ISSN 1404-0344
SKB TR-14-27
ID 1443509

December 2015

Modelling of critical H-M processes in the engineered barriers of SFR

Lennart Börgesson, Mattias Åkesson, Ola Kristensson,
Daniel Malmberg, Martin Birgersson
Clay Technology AB

Jan Hernelind, 5T-Engineering AB

Summary

One part of the repository for low and intermediate radioactive waste (SFR) is the so called silo repository. At closure, the concrete silo will be surrounded by bentonite based barriers, both in form of backfill between the vertical silo wall and the rock as well as in a top and bottom bed consisting of a mixture between bentonite and sand. The purpose of the bentonite is to act as a seal, reducing water flux in and out from the concrete silo. Different processes in the silo repository have been analyzed and investigated as a part of the safety assessment, and the results from these studies are presented in this report.

Chapter 2:

One of the identified processes, *water uptake and transport during unsaturated conditions*, was here analyzed and investigated by using numerical methods. The main objectives were to: estimate the time from closure until full water saturation of the silo repository, describe the saturation process within the system, and study how variations of the system representation change the saturation process.

Each of the representation variations was considered pairwise; the pair consisted of one model where the host rock was drained and another where the host rock was undrained, respectively. Since the host rock of the "real system" should have properties somewhere in between drained and undrained, the pairwise method provided a time frame within which the "real" system are likely to be saturated.

For the base case, the silo repository was estimated to be fully saturated in the interval between 13 and 53 years. The largest uncertainty came from the host rock representation, both in terms of using undrained/drained and dry representations. The properties of the silo content as well as the top backfill also had significant effect on the overall saturation interval.

Chapter 3:

Self-healing of erosion damages has been analyzed. When the drainage of the rock in the silo is terminated, the water pressure will increase until either: i) it reaches the hydrostatic water pressure, which will lead to piping and subsequent erosion of bentonite , or ii) it penetrates the bentonite based barriers, which will lead to formation of water pockets. Both scenarios will lead to a local loss of bentonite and formation of an open channel or void. How large this void will be and how well it will be sealed by the swelling bentonite has been investigated with analytical modelling of the erosion rate and finite element modelling of the self-healing. The modelling resulted in an incomplete homogenisation caused mainly by numerical problems. The final conclusion is that there will be enough unaffected bentonite left between the rock and the silo in order to fulfil the sealing function.

Chapter 4:

Ion exchange will over time convert the bentonite from its installation state (sodium dominated) to its final state (calcium dominated). Laboratory data shows that for the buffer densities around the SFR silo this leads to a significant reduction in swelling pressure. From the results of the numerical modelling presented in this report it can be concluded that ion exchange will lead to a significant reduction in the stress levels in the clay barrier, as compared to the stress levels at full water saturation before ion exchange. However, the modelling results also shows that no significant changes in the density of the clay will occur and that the downward movement of the top surface of the bentonite barrier will be small (on the order of a few centimetres).

Chapter 5:

The mechanical impact of *cement degradation of the concrete wall* on the bentonite filling in the silo was analysed. As the concrete wall degrades, its volume and strength will decrease, and this can lead to a horizontal displacement of the interface between the concrete and the bentonite, and

also vertical displacements of the bentonite as well as the degraded concrete. An analytical model was developed for the specific problem (with MathCad software), and this was the main tool for performing the actual calculations. A numerical (FLAC) model was developed for verification of the analytical model. A porous-elastic material model was used for representation of the bentonite, which was assumed to be completely Ca-converted. The highest settlement value for which the solution appeared to be relevant was approximately 7 m. This would imply that a significant part of the circumference of the silo would consist of permeable materials only, i.e. sand from the top filling, and aggregates from the degraded concrete.

Chapter 6:

An analysis of *rock block detachment* i.e. how a loose rock block affects the wall filling is presented in Chapter 6. A piece of the rock wall may after long time come loose from the rock and fall out on the bentonite filling. The consequences of such an event have been investigated with both analytical and numerical modelling. The analytical calculations show that the blocks need to be very large and wedge-shaped in order to obtain large movements. For rock blocks that do not go further into the rock than 2 m less than 40 kPa swelling pressure is needed to keep the blocks in place for all possible combinations of form and friction angles.

The finite element calculations confirm the analytical solutions, but also show that large movements can take place also in a theoretical initial equilibrium. To guarantee that the rock blocks are stuck to the wall and that there are no large openings between the blocks and the rock there should be a safety factor of 1.5–2.0 in the bentonite swelling pressure, if the analytical solution is used for the analysis.

Results from FE-calculations of rock blocks that don’t fulfil the swelling pressure requirements, show that there may be a substantial displacement. However, they also show that the consequence is a consolidation of the bentonite and subsequent increase in swelling pressure that ends in a stable situation with a remaining substantial thickness of the bentonite barrier.

Chapter 7:

Effects of *possible gas pressure build-up* in the silo have been assessed. Lab tests of the silo bentonite show that its response due to gas pressurization agrees with other tested bentonite materials. Estimations of the gas pressure required in order to only have diffusive transport suggests that the gas phase will interact mechanically with the bentonite, in case of non-functional evacuation pipes.

Sammanfattning

En del av förvaret för låg- och medelaktivt avfall (SFR) är den så kallade silon. Vid stängning, kommer betongsilon vara omgiven av bentonitbaserade barriärer, både i form av återfyllningen mellan den vertikala siloväggen och berget samt i en övre och nedre bädd bestående av en blandning mellan bentonit och sand. Syftet med bentoniten är att fungera som en tätning och därigenom reducera vattenflödet in och ut från betongsilon. Olika processer i silon förvaret har analyserats och undersökts som en del av säkerhetsanalysen för SFR, och resultaten från dessa studier presenteras i denna rapport.

Kapitel 2:

En av de identifierade processerna, vattenupptagning och transport under omättade förhållanden, har här analyseras och undersökas med hjälp av numeriska metoder. De viktigaste målen var att: uppskatta hur tiden från förslutningen till full vattenmättnad i siloförvaret, att beskriva mättnadsprocessen i systemet och att studera hur variationer i systemets representation ändrar mättnadsprocessen.

Var och en av de systemrepresentationerna benhandlades parvis; paret bestod av en modell där berget var dränerat och en annan där berget var odränerat. Eftersom berget i det "verkliga systemet" borde ha egenskaper någonstans mellan dränerat och odränerat, bör den parvisa metoden visa sen tidsram inom vilken det "riktiga" systemet sannolikt kommer att vara mättat.

För basfallet beräknades siloförvaret att vara helt mättat i intervallet mellan 13 och 53 år. Den största osäkerheten kom från representationen av berget både när det gäller att använda odränerade/dränerade eller torra representationer. Egenskaperna hos siloinnehållet samt toppfyllningen hade också signifikant effekt på det totala mättnadsintervallet.

Kapitel 3:

Självläkning av erosionsskador har analyserats. När dränering av berget i silon avslutas, kommer vattentrycket öka tills antingen i) det når det hydrostatiska vattentrycket, vilket kommer att leda till kanalbildning och efterföljande erosion av bentonit, eller ii) det penetrerar bentonitbarriären, vilket kan leda till bildning av vattenfickor. Båda scenarierna kommer att leda till en lokal förlust av bentonit och bildandet av en öppen kanal eller ett hålrum. Hur stort detta hålrum kommer att bli och hur väl det kommer att förseglas av svällande bentonit har undersökts med analytisk modellering av erosionshastigheten tillsammans med finit elementmodellering av den självläkaningen. Modelleringen resulterade i en ofullständig homogenisering vilken främst orsakades av numeriska problem. Slutsatsen är dock att det kommer att finnas tillräckligt med opåverkad bentonit kvar mellan berget och silon för att uppfylla tätningsfunktionen.

Kapitel 4:

Jonbyte kommer med tiden att förändra bentoniten från dess installerade tillstånd (natriumdominerat) till sin slutliga form (kalciumdominerat). Laboratoriedata visar att för de buffertdensiteter som är aktuella runt SFR-silon så leder detta till en betydande minskning av svälltrycket. Från resultaten av den numeriska modelleringen som presenteras i denna rapport kan man dra slutsatsen att jonbytet kommer att leda till en betydande minskning av spänningarna i lerbarriären, jämfört med spänningsnivåerna vid full vattenmättnad före jonbyte. Emellertid visar modelleringsresultaten också att inga signifikanta förändringar i densiteten av leran kommer att inträffa och att den nedåtgående rörelsen av den övre ytan av bentonitbarriären kommer att vara liten (i storleksordningen några få centimeter).

Kapitel 5:

Den mekaniska inverkan av cementnedbrytning i betongväggen på bentonitfyllningen i silon har analyserats. När betongväggen degraderas, kommer dess volym och styrka minska och detta kan

leda till en horisontell förskjutning av gränsytan mellan betongen och bentoniten, och även vertikala förskjutningar av bentoniten den samt nedbrutna betongen. En analytisk modell har utvecklats för detta specifika problem (med MathCad programvara) och detta var det viktigaste verktyget för att utföra de faktiska beräkningarna. En numerisk (FLAC) modell utvecklades för verifiering av den analytiska modellen. En porös-elastisk materialmodell användes för representation av bentoniten, som förutsattes att vara helt Ca-konverterad. Det högsta värde för sättningen för vilket lösningen föreföll vara relevant var cirka 7 meter. Detta skulle innebära att en betydande del av omkretsen av silon skulle bestå av enbart permeabelt material, dvs sand från toppfyllningen, och ballast från den nedbrutna betongen.

Kapitel 6:

En analys av ett frigjort bergblock, dvs. hur ett löst bergblock påverkar väggfyllningen presenteras i kapitel 6. En bit av bergväggen kan efter lång tid lossna från berget och falla ut mot bentonitfyllningen. Konsekvenserna av en sådan händelse har undersökts både med analytisk och numerisk modellering. De analytiska beräkningarna visar att blocken måste vara mycket stora och kilformade i syfte att erhålla stora rörelser. För bergblock som inte går inte längre in i berget än 2 m behövs det mindre än 40 kPa svälltryck för att hålla blocken på plats för alla möjliga kombinationer av former och friktionsvinklar.

De finita elementberäkningarna bekräftar de analytiska lösningarna, men visar också att stora rörelser kan ske även i en teoretisk initial jämvikt. För att garantera att bergblocken stannar på väggen och att det inte finns några stora öppningar mellan blocken och berg det bör finnas en säkerhetsfaktor på 1,5–2,0 i bentonitens svälltryck, om den analytiska lösningen används för analysen.

Resultat från FE-beräkningar av bergblock som inte uppfyller svälltryckskravet, visar att det kan bli en betydande förskjutning. De visar dock också att följden är en konsolidering av bentoniten och en efterföljande ökning av svälltrycket som resulterar i en stabil situation med en väsentlig andel kvarvarande tjocklek av bentonitbarriären.

Kapitel 7:

Effekter av eventuell uppbyggnad av gastrycket byggs upp i silon har analyserats. Laboratorietester av silobentoniten visar att dess beteende vid uppbyggnad av gastryck överensstämmer med andra testade bentonitmaterial. Uppskattningar av gastrycket som krävs för att bara ha diffusiv transport tyder på att en gasfas kommer att interagera mekaniskt med bentoniten, i fallet med icke-funktionella evakueringsrör.

Contents

1 Introduction

One part of the repository for low and intermediate radioactive waste (SFR) is the so called silo repository. Different processes in the silo repository have been analyzed and investigated as a part of the safety assessment, and the results from these studies are presented in this report.

The silo repository consists of a freestanding concrete silo hosted within a more or less cylindrically shaped rock cavern. A drainage system directing water into a basin below the cavern has been installed at the rock walls. Within the concrete silo radioactive waste is emplaced in compartments which subsequently are backfilled with porous cement mortar. At closure, the concrete silo will be surrounded by bentonite based barriers, both in form of backfill between the vertical silo wall and the rock as well as in a top and bottom bed consisting of a mixture between bentonite and sand. The purpose of the bentonite is to act as a seal, reducing water flux in and out from the concrete silo. The bentonite is of the type GEKO/QI, which originally is a calcium-dominated bentonite, but which for the purposes here has been converted into a sodium-dominated bentonite. The volume above the top bed will be backfilled with friction material at closure of the repository.

An analysis of the *water uptake and the transport during unsaturated conditions* is presented in Chapter 2. The main objectives of this were: i) to estimate the time from closure (2040) until full water saturation of the silo repository; ii) to describe the saturation process within the engineered barrier system, and iii) to study how variations of the system change the saturation process.

Self healing of *erosion damages* is analyzed in Chapter 3. When the drainage of the rock in the silo is terminated, the water pressure will increase until either: i) it reaches the hydrostatic water pressure, which will lead to piping and subsequent erosion of bentonite , or ii) it penetrates the bentonite based barriers, which will lead to formation of water pockets. Both scenarios will lead to a local loss of bentonite and formation of an open channel or void, and the question is how well this void is sealed by the swelling bentonite.

An analysis of the mechanical impact of *ion exchange* is presented in Chapter 4. Ion exchange will over time convert the bentonite from its installation state (sodium dominated) to its final state (calcium dominated). Preliminary data suggests that the swelling pressure developed by the bentonite is significantly reduced as a result of the conversion from Na to Ca. This in turn reduces the pressure which the bentonite exerts on the rock and silo walls, which in turn reduces the friction force acting on the bentonite. The result could be significant movements in the bentonite, causing a gradient in the density profile.

An analysis of the mechanical impact of *cement degradation of the concrete wall* on the bentonite filling is presented in Chapter 5. As the concrete degrades its volume and strength will decrease, and this can lead to a horizontal displacement of the interface between the concrete and the bentonite, and also vertical displacements of the bentonite as well as the degraded concrete. This process was investigated through both analytical and numerical modelling.

An analysis of *rock block detachment i.e. how a loose rock block affects the wall filling* is presented in Chapter 6. A piece of the rock wall may after long time come loose from the rock and fall out on the bentonite filling. The consequences of such an event have been investigated with both analytical and numerical modelling.

In Chapter 7 the case of possible damage of the bentonite barrier caused by high gas pressure build-up due to metal corrosion is investigated.

2 Study of water uptake and transport during unsaturated conditions

The final repository for low and intermediate radioactive waste (SFR) is currently in operation and the operating permit stipulates that the safety assessment of SFR is updated at least every tenth year. As a part of the safety assessment, processes in the Engineered Barrier System (EBS) in the silo repository are investigated. One of the identified processes, *water uptake and transport during unsaturated conditions,* is here analyzed and investigated by using numerical methods. The main objectives are:

- estimating the time from closure (2040) until full water saturation of the silo repository,
- describe the saturation process within the EBS, and
- study how variations of the system change the saturation process.

When identifying relevant issues with a potentially significant effect on the water saturation process in the silo repository, the cases listed in Table 2-1 were obtained.

Table 2-1. Cases considered relevant to investigate.

ID	Description
A	Uncertainty in host rock water pressure
B	Uncertainty in initial conditions (undrained rock cavern)
C	Dry host rock representation (decreased rock permeability)
D	Effect from an impermeable plastic sheet below the concrete pad
E	Uncertainty in top backfill properties (increased porosity)
F	Uncertainty in silo content properties (including waste package porosity)

In addition to the cases listed above the properties of the GEKO/QI material used in the simulations are discussed in the light of preliminary laboratory data obtained for samples taken from the vertical GEKO/QI buffer.

In the next section a short description of the silo repository system is given. Thereafter follow a discussion of the used modelling methodology and a list of models corresponding to the cases in Table 2-1. Next, a brief description of the base case is followed by results and discussions, and finally conclusions are given.

More detailed information about the models, especially so the ones related to the base case, can be found in following appendices:

- Appendix A: Theory.
- Appendix B: EBS representation.
  - B.1 Initial conditions.
  - B.2 Material properties.
- Appendix C: Rock representation.
  - C.1 Initial and boundary conditions.
  - C.2 Material properties.

Convergence investigations regarding mesh dependence and convergence condition parameters have also been carried out as described in:

- Appendix D: Convergence investigation.
  - D.1 Mesh dependence.
  - D.2 Dependence on convergence condition parameters.

2.1 Description of the silo repository system

SFR is located below the Baltic offshore of the nuclear power plant at Forsmark. The construction took place from 1983 until 1986. In 1987 the silo repository was ready for storage and the SFR facility was taken into operation in 1988.

Low and intermediate radioactive waste have been emplaced in the silo compartments which subsequently have been backfilled with porous cement mortar. A drainage system installed at the cavern roof, walls, and bottom has directed ground water into a drainage basin below the cavern.

At the planned closure of the facility, year 2040, the drainage system will be blocked, the now open volume above the concrete silo will be backfilled, and the tunnels leading to the rock cavern will be plugged. This is the starting point for the water saturation process.

2.1.1 Geometry and materials

Figure 2-1 shows two views of the SFR facility where the vertically oriented cylindrically shaped rock cavern, which hosts the silo construction, is clearly seen together with surrounding tunnels and water pressure measurement boreholes.

The silo repository is installed in the excavated rock cavern and consists of a number of components as shown in Figure 2-2 where the current open state is visualized.

At closure, a permanent lid will be placed on top of the concrete silo and on top of that a layer of clay/sand mixture. The remaining empty volume above will then be backfilled with gravel/sand, see Figure 2-3. A more detailed description of the components related to the silo repository is given below.

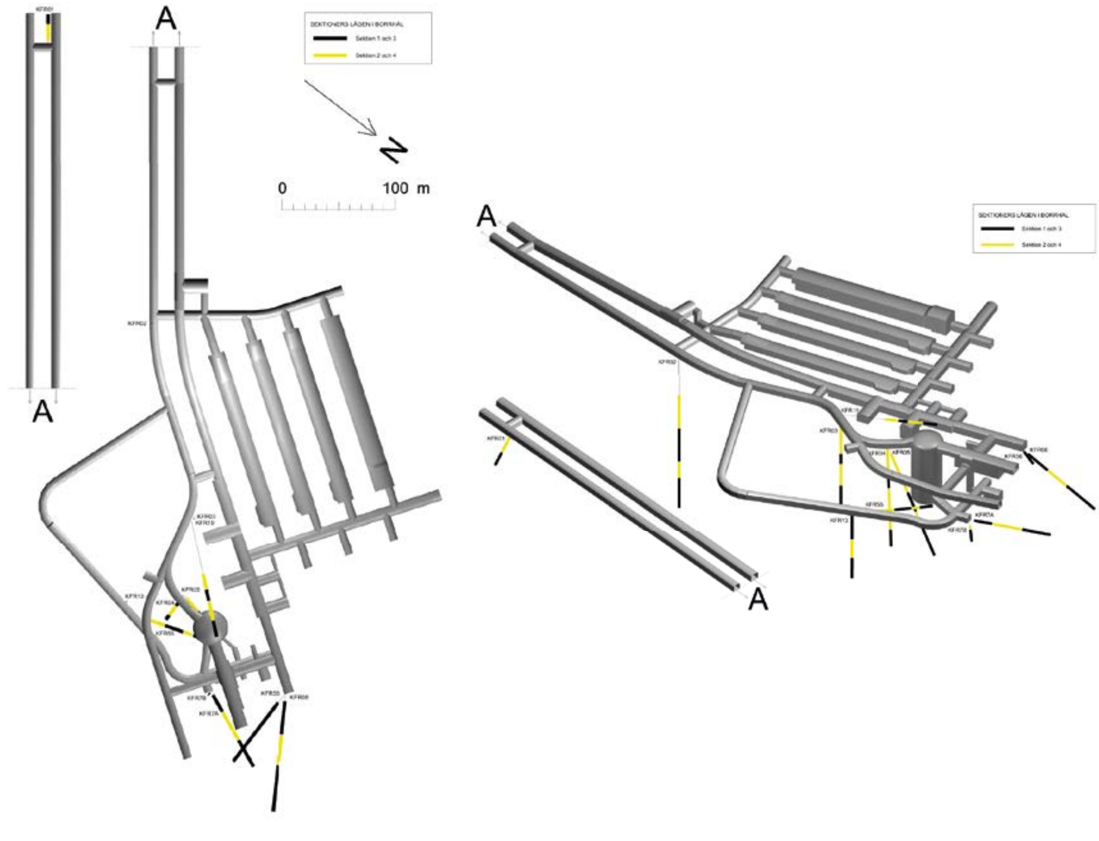

Figure 2-1. *Overview of the excavated volumes in the SFR facility. The cylindrical rock cavern hosting the silo construction is clearly seen. The black and yellow lines indicate borehole sections where the water pressure in the rock is measured.*

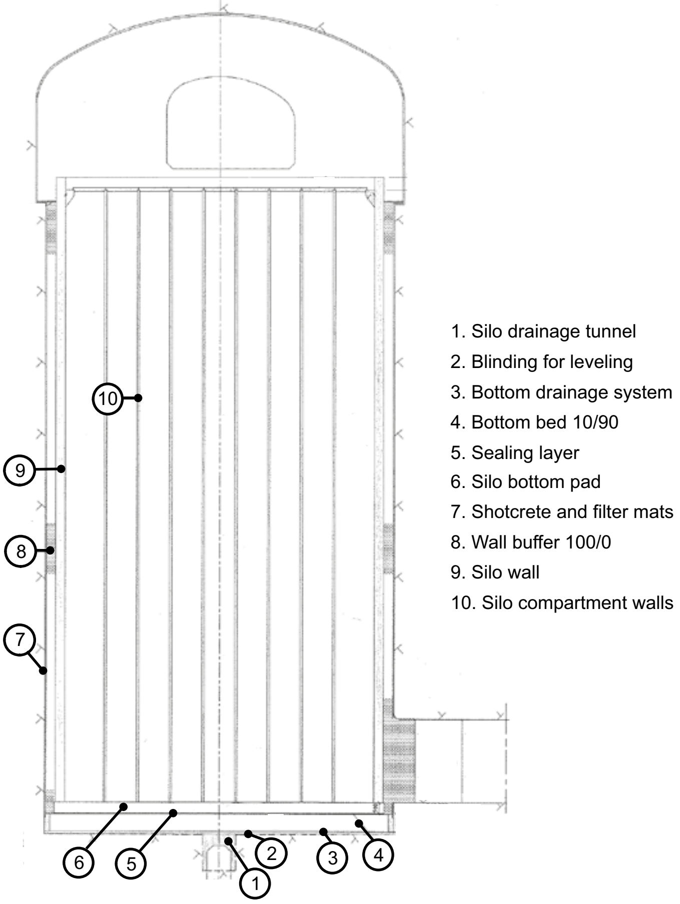

***Figure 2-2.** Overview of the present open state of the silo repository without a backfilled cavern top.*

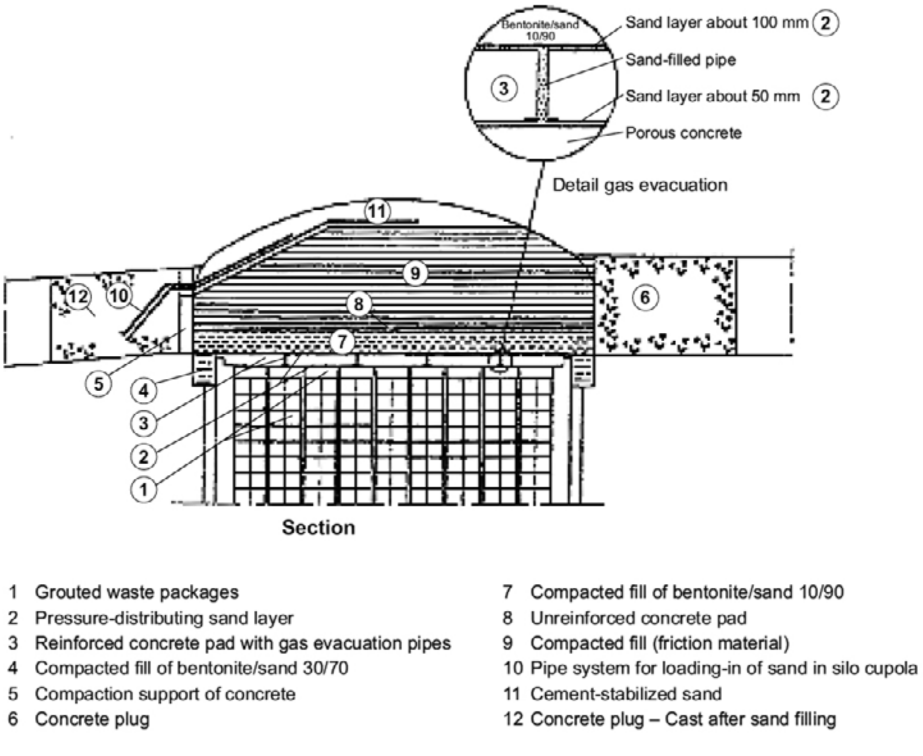

***Figure 2-3.** Overview of the components in the top part of the closed silo repository (SKB 2008, part of Figure 4-3).*

Host rock

No significant water bearing fractures intercept the rock cavern. The rock cavern wall was dry at excavation. A sub-horizontal water bearing zone has been encountered in the lower rock drainage basin (below the actual cavern) and in the gable of the lower construction tunnel. When encountered, the zone gave heavy water inflow. It is, however, ”at safe distance below the bottom of the silo, and in addition it decreased rapidly in thickness to finally disappear below the centre of the silo /Larsson 1996/.” (Carlsson and Christiansson 2007). The sea floor is at 10 m depth above the repository.

Rock cavern

The height of the rock cavern is 69.5 m, not including the 3 m deep drainage basin. The lowest part of the rock cavern (again not including the drainage basin) is situated approximately 131 m below the sea surface which gives a rock overburden of 51.5 m (with the sea floor level at 10 m depth). The nominal diameter above the rim of the concrete silo was planned to be 30.8 m. A scanning profile of the upper part of the cavern shows a diameter of 31.4 m. The nominal diameter below the rim of the concrete silo was planned to be 29.3 m, but a diameter ≥ 29.2 with an overbreak of 250–300 mm has been reported. The cupola of the rock cavern was given elliptical shape.

Connecting tunnels

At the top of the rock cavern, above the concrete silo rim, there are two tunnels, the upper construction tunnel and the loading facility tunnel, and at the bottom there are the lower construction tunnel and the drainage basin/tunnel.

Concrete silo

The cylindrical concrete silo has a height of 53.45 m, including the bottom foundation of 900 mm (or 1,000 mm) thickness, and a diameter of 27.6 m. The thickness of the concrete silo wall is 800 mm. Within the outer cylindrical silo wall there are vertical compartments with, to the largest part, square cross sections with side length 2,550 mm, parted by 200 mm thick concrete compartment walls.

Waste packages

The waste to be stored in the silo is estimated to the largest part be composed of ion-exchange resin mixed in a concrete or bitumen matrix which is placed in different type of containers. There are cubic moulds, with a side length of 1,200 mm, either consisting of concrete or steel, or 200 liters steel drums, with diameter 600 mm and height 900 mm, which are placed four together on a square brick with side length 1,200 mm. Concrete moulds are expected to be most common in the silo. The concrete silo compartments are subsequently backfilled with porous cement mortar, every third layer for the cubic packages and every fifth layer for the steel drum packages.

EBS materials

All components in the EBS are described below in three sequences: #1 EBS from the top of the cavern in Table 2-2, #2 EBS from the side of the cavern in Table 2-3, and #3 EBS from below the cavern in Table 2-4. The sequences start from the rock and goes towards the waste. Relevant dimensions are also given for the EBS materials. For #1 in Table 2-2, the components belonging to the closure system have been taken as described in SKB (2008).

2.2 Modelling methodology

The general modelling methodology has been to use hydraulic, axisymmetric models at a local scale, only incorporating the silo repository and the nearby host rock. By using this local scale method, it becomes numerically feasible to carry out simulations for a large number of variations of models. One issue which has to be considered when applying this strategy, however, is that processes on a larger (global) scale have to be imposed via prescribing relevant boundary conditions (BCs) on the local model.

Table 2-2. Sequence #1 EBS from the top of the cavern.

Component	Dimension
Fiber/shotcrete mixture.	Thickness: ≥ 80 mm at cavern roof, ≥ 50 mm at the wall above the concrete silo rim[b].
compacted friction material, sand or gravel, and cement-stabilized sand[a].	
Unreinforced concrete pad[a].	
10/90 bentonite/sand mixture[a].	1,500 mm thickness[c].
30/70 bentonite/sand ”ring” on top of the vertical buffer just below the concrete silo rim[a].	1,600 mm horizontal thickness and 2,000 mm vertical thickness[d].
By tubing perforated reinforced concrete pad embedded in sand[a].	Concrete pad: thickness = 1,000 mm[c], tubes: diameter = 100 mm[c], sand: 100 mm thickness above, 50 mm thickness below, and in tubing[c].
Grouted waste packages in the concrete silo compartments.	See description in “Waste packages”.

(a) The component belongs to a tentatively described closure system which may be altered.

(b) (Carlsson and Christiansson 2007.)

(c) (SKB 1993.)

(d) (Drawing: 1-1010008.)

Table 2-3. Sequence #2 EBS from the side of the cavern.

Component	Dimension
Shotcrete.	Thickness: ≥ 30 mm.
Filter mats (Fibertex) against the rock.	23 pc. vertical strips, with cc 4 m[a] width 0.3 m[a] (i.e. 7.5% coverage)
Bentonite (100/0).	Planned thickness: 1,200 mm[b]. Obtained thickness: ≥ 800 mm with Obtained overbreak: 250–300 mm. Thus: thickness = 935 ± 135 mm (when adopting 30 mm shotcrete).
Reinforced concrete silo wall.	thickness: 800 mm[b].
Grouted waste packages in the concrete silo compartments.	See description in “Waste packages”.

(a) (Drawing: 1-1009844.)

(b) (SKB 1993.)

Table 2-4. Sequence #3 EBS from below the cavern.

Component	Dimension
Blinding for leveling of the rock floor.	a
Drainage pipes.	D/d = 58/50 mm, cc 2,700 mm, laid out perpendicular to the drainage basin[b].
Concrete pad cast on plastic foil.	Thickness: 200 mm[a].
Bottom bed of 10/90 bentonite/sand mixture.	Thickness: 1,500 mm[c].
Concrete pad (the concrete silo base) cast on a sealing layer.	Thickness: 900 mm[a]–1,000 mm[c].
Grouted waste packages in the concrete silo compartments.	See description in “Waste packages”.

(a) (Drawing: 1-1010008.)

(b) (Drawing: 1-1010004.)

(c) (SKB 1993.)

Since representative water pressure evolutions, to prescribe as BCs on the local model, have not been available, e.g. from models at a considerably larger (global) scale, a strategy where two extreme BCs, bounding the "real" situation, has been applied. In fact, two extreme host rock representations, with different BCs and different geometry have been utilized. The two representations are denoted *undrained* and *drained*, respectively. The undrained representation can be thought of as totally neglecting the effects from the global hydraulic evolution and excavated volumes adjacent to the silo repository and the drained representation as exaggerating the effect from the latter.

The two representations were designed, both considering geometry and BCs, so that the obtained water pressure fields, locally around the silo, overestimates and underestimates measurements to about the same degree for the undrained and drained representation, respectively. Rock permeability was then calibrated by comparing calculated cavern inflows against measured flow from the rock cavern drainage system. When, for a given rock permeability, the correspondence between the two models and measurements was considered good enough, i.e. the modeled inflows overestimated and underestimated measurements to about the same degree, these two models were adopted as to define the base case.

Using the methodology described above, case A. "Uncertainty in host rock water pressure", presented in Table 2-1, can be studied when the responses from the undrained and drained models of the base case are compared. The set of simulations corresponding to the cases A-F in Table 2-1 is shown in Table 2-5 where the performed simulations are indicated.

As can be seen from studying Table 2-5, the evaluation of the effect from the uncertainty in host rock water pressure has only been performed for the base case. This effect is disregarded in the cases that follow where only the drained host rock representation has been used.

The drained base case model is thus chosen as a point of departure when developing the models for the following cases, and their results will be compared with those obtained from the drained base case model. It should be remembered that the reported time until saturation for cases B–F in Table 2-1 is probably overestimated by only using the drained representation. It is left up to the reader to keep this in mind when evaluating the results.

Table 2-5. Complete simulation compilation for the cases addressed in this report. The performed simulations are marked with an X.

ID	Case	Host rock representation	
		Undrained	Drained
A	Base case	X	X
B	Undrained rock cavern		X
C	Dry host rock		X
D	Impermeable plastic sheet		X
E	Altered top backfill		X
F	Altered silo content		X

2.3 Base case description

The models chosen as to define the base case are here described. Information regarding geometry, materials, initial conditions, and BCs are given. References to relevant appendices where more information can be found are given in the text. The models consider water mass balance only, i.e. they are purely hydraulic.

2.3.1 Geometry

The model geometry is here described as belonging to two parts, the rock and the EBS, respectively. A general assumption is that axisymmetry is applicable for representing the system and still being able to capture its main characteristics.

As can be seen when studying the used rock geometries in Figure 2-4 and comparing this with the geometry of the entire SFR shown in Figure 2-1, an approach utilizing models at a significantly smaller scale as compared to the scale of the entire SFR is adopted. Only a small part of the silo host rock is included in the models.

As described in the former section, to account for the influence from processes in the excluded surrounding rock, a method incorporating two different rock representations, undrained and drained, is utilized. The rock representations differ both in terms of geometry and BCs.

The geometries, which can be studied in Figure 2-4, differ in two ways. The "undrained geometry" incorporates a rock embedment material at the vertical outer boundary and the "drained geometry" has a vertical outer boundary with a cutout. The embedment material is used to provide the rock material model with hydrostatic pressure at the vertical outer boundary and the cutout could be thought of as representing neighboring excavated volumes, see Figure 2-1.

The used geometric representation of the EBS can be studied in Figure 2-5. The rock cavern's elliptical cupola is not considered, a flat surface representation is used instead. The thickness of the wall buffer is taken as 0.85 m.

2.3.2 Material properties

More information about the material representations is available in:

- Appendix A: Theory.
- Appendix B: EBS representation.
  - B.2 Material properties.
- Appendix C: Rock representation.
  - C.2 Material properties.

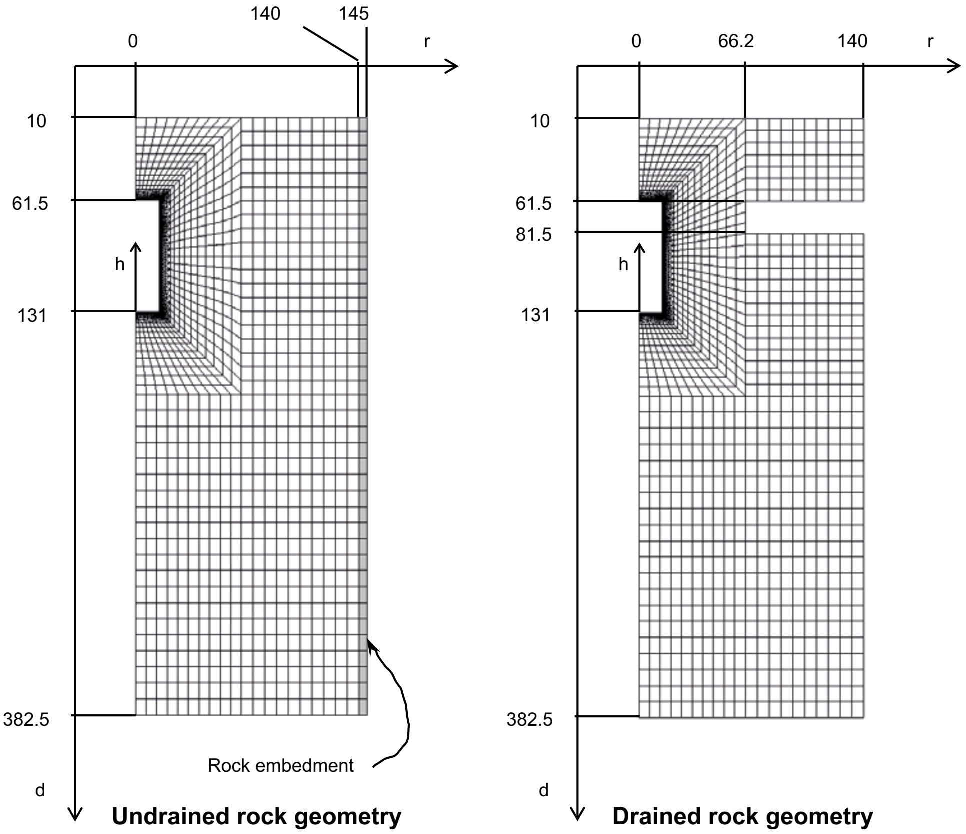

Figure 2-4. Rock geometries where the mesh is shown.

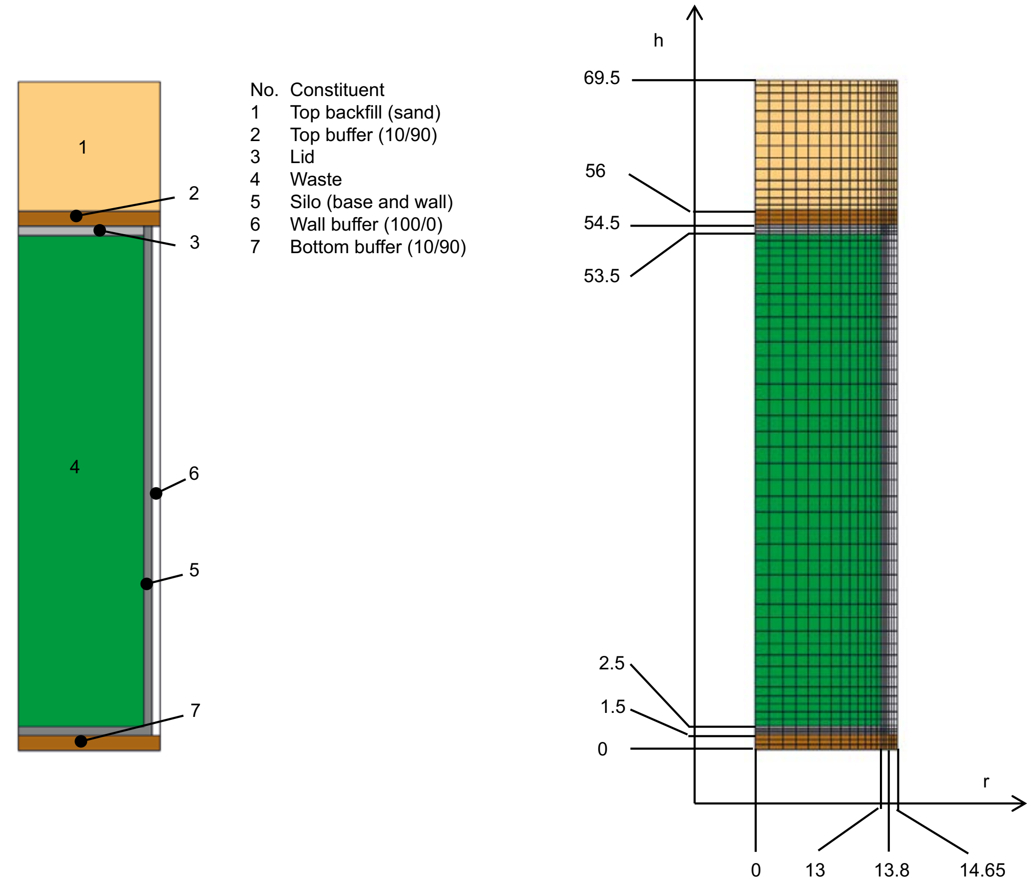

EBS constituents **EBS geometry and mesh**

Figure 2-5. *EBS constituents, geometry, and mesh.*

Retention curve

$$S_l = \left(1 + \left(\frac{s}{p_0}\right)^{1(1-\lambda)}\right)^{-\lambda} \tag{2-1}$$

$$S_l = \left(1 + \frac{s}{p_0}\right)^{-1/2} \tag{2-2}$$

$$s = p_g - p_l \tag{2-3}$$

Table 2-6. Retention curve parameters.

Parameter	Waste [a]	Silo	Lid	100/0	10/90	Sand	Rock	Rock embed.[b]
p_0 (MPa)	0.05	0.05	0.05	0.0685	0.05	0.002	1.74	1.74
λ	–	0.18	0.18	0.165	0.18	0.65	0.6	0.6

(a) The square law expression (2-2) was used.

(b) Only present in undrained models.

Flow through porous medium

$$\boldsymbol{q}_l = -\frac{\boldsymbol{k}k_{rl}}{\mu_l}\left(\nabla p_l - \rho_l \boldsymbol{g}\right) \tag{2-4}$$

$$\boldsymbol{k} = k_{11}\boldsymbol{e}_1 \otimes \boldsymbol{e}_1 + k_{22}\boldsymbol{e}_2 \otimes \boldsymbol{e}_2 + k_{33}\boldsymbol{e}_3 \otimes \boldsymbol{e}_3 \tag{2-5}$$

$$k_{rl} = AS_l^{\ B} \tag{2-6}$$

$$k_{rl} = \sqrt{S_l}\left(1-(1-S_l^{\ 1/\lambda})^{\lambda}\right)^2 \tag{2-7}$$

$$\mu_l = 2\cdot 10^{-12}\exp\left(\frac{1808.5}{273.15+T}\right) \tag{2-8}$$

$$\rho_l = 1002.6\exp\left(4.5\cdot 10^{-4}(p_l - 0.1) - 3.4\cdot 10^{-4}\,T\right) \tag{2-9}$$

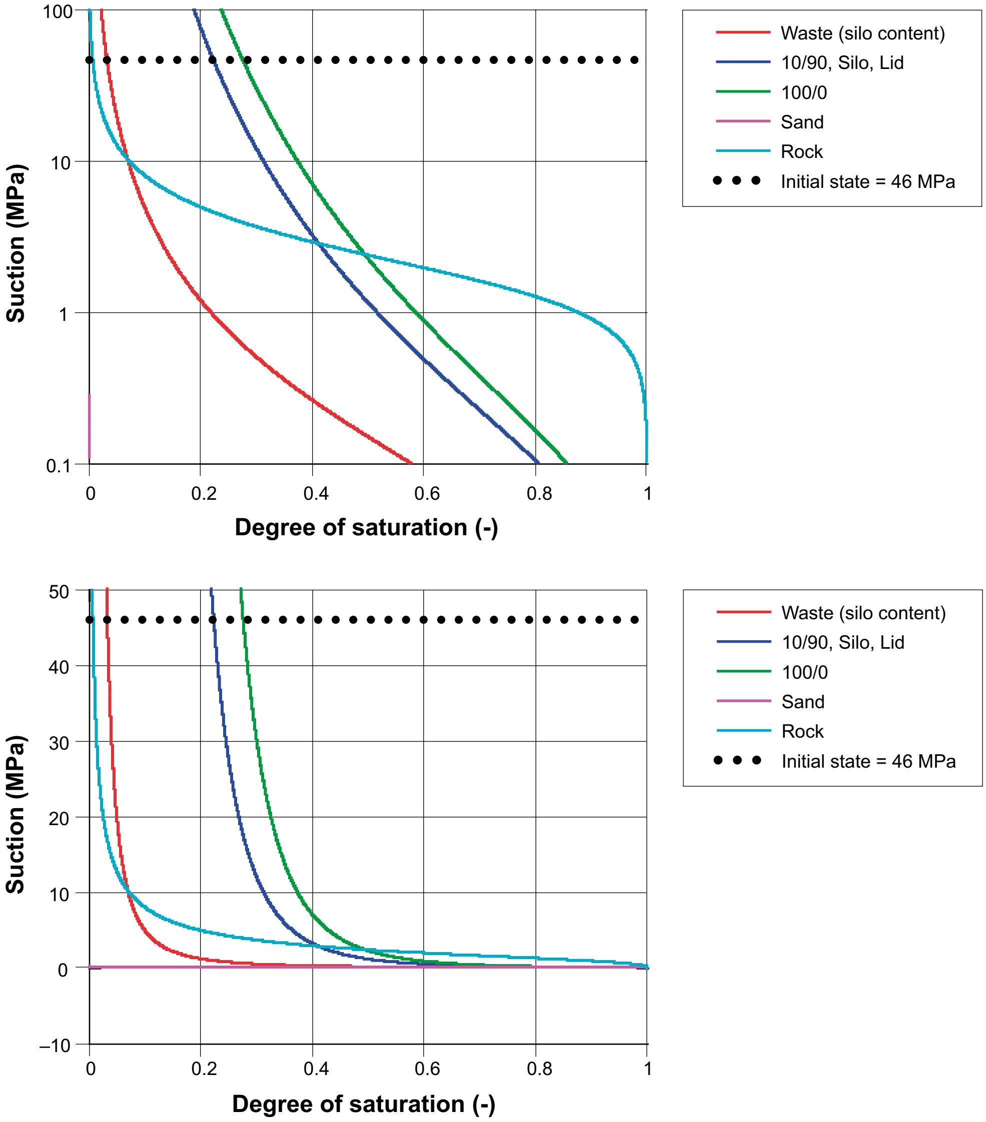

Figure 2-6. *Retention curves used in the base case models.*

Table 2-7. Water transport parameters.

Parameter	Waste	Silo	Lid	100/0	10/90	Sand	Rock a	Rock embed. a b
kxx horiz. (m^2)	$4.5\cdot10^{-16}$	$8.3\cdot10^{-17}$	$2\cdot10^{-16}$	10^{-17}	$3.4\cdot10^{-17}$	10^{-15}	10^{-16}	10^{-10}
kyy vert. (m^2)	$7.4\cdot10^{-16}$	–	–	–	–	–	–	–
kzz horiz. (m^2)	$4.5\cdot10^{-16}$	–	–	–	–	–	–	–
A	1	1	1	1	1	1	–	–
B	3	3	3	3	3	0		

(a) Van Genuchten (2-1) was used.

(b) Only present in undrained models.

2.3.3 Initial conditions

A discussion of the initial conditions can be found in:

- Appendix B: EBS representation.
  - B.1 Initial conditions.
- Appendix C: Rock representation.
  - C.1 Initial and boundary conditions.

The initial condition, i.e. water pressure, of the EBS components is taken as equal to the condition of the 100/0 GEKO/QI buffer at installation with water content 0.17 and a corresponding suction of 46 MPa. The porosity/void ratio and water content/degree of saturation, corresponding to the initial water pressure, are given below in Table 2-8 for all materials.

The initial conditions of the rock are taken as the steady state conditions obtained with an open cavern, i.e. at drained conditions. The temperature and gas pressure are constant, $T = 15°C$ and $p_g = 0.1$, respectively.

Table 2-8. Initial conditions.

Parameter	Waste	Silo	Lid	100/0	10/90	Top backfill	Rock	Rock embed.[b]
ρ_d (kg/m^3)	2,345	2,345	2,345	1,000	2,200	1,723	–	–
ρ_s (kg/m^3)	2,710	2,710	2,710	2,600	2,645	2,650	–	–
n (-)	0.1	0.2	0.2	0.62	0.168	0.35	0.003	0.99
e (-)	0.11	0.25	0.25	1.6	0.202	0.538	0.003	99
S_l (-)	0.033	0.224	0.224	0.276	0.224	$7.9\cdot10^{-9}$	a	a
w (-)	$1.4\cdot10^{-3}$	0.021	0.021	0.17	0.017	$1.6\cdot10^{-9}$		

(a) Steady state conditions with an open cavern.

(b) Only present in undrained models.

2.3.4 Boundary conditions

The boundary conditions are discussed in:

- Appendix C: Rock representation.
  - C.1 Initial and boundary conditions.

The BCs used together with the two different geometries shown in Figure 2-4 are:

Undrained representation

a. $p_l = 0.2$ MPa at $d = 10$ m.

b. $q_l = 0$ elsewhere.

Drained representation

a. $p_l = 0.2$ MPa at $d = 10$ m.

b. $p_l = 0.1$ MPa at the cutout.

c. $q_l = 0$ elsewhere.

2.4 Results and discussion

In this section results obtained from models are shown and discussed. First and most detailed, results of the base case and the related case A. "Uncertainty in host rock water pressure" are investigated and described. After this, results from five different cases:

B. Undrained rock cavern.

C. Dry host rock representation (decreased permeability).

D. Effect from an impermeable plastic sheet below the concrete pad.

E. Uncertainty in top backfill properties (increased porosity).

F. Uncertainty in silo content properties (including waste package porosity), are studied. Finally the adopted representation of the GEKO/QI material is discussed in the light of preliminary laboratory data obtained from analyzing material sampled from the vertical buffer in the silo repository. As stated in chapter 2.2, the models of cases B–F are based upon the drained base case model and it should be remembered that this will introduce overestimation of the duration of the saturation process.

2.4.1 Base case (Uncertainty in host rock water pressure)

Below follows descriptions regarding results related to the base case models. First, two results, water pressures in the host rock and water inflow to an empty cavern, fundamental for the design of the base case models, are discussed. More information about this can be found in *Appendix C: Rock representation*. Then, a description of the evolution in the system during the wetting process in terms of rock water pressure follows. Finally the saturation evolution in the EBS is studied and saturation intervals and saturation limit intervals are given.

Table 2-9. Models used in this case study.

Model description	Model name
Base case, Undrained	undrained_var3B_copy.gid
Base case, Drained	drained_var3B_ext.gid
Base case, Undrained, Empty	BC_undrained_pre.gid
Base case, Drained, Empty	BC_drained_ pre.gid

Steady state solutions of models with an empty cavern are used as the condition at closure (at 2040). When designing the boundary conditions, calculated rock water pressures at the closure-state were compared with measurements made at 1990 and 2011 as well as estimations for 2040 formed by considering the measurements, see *Appendix C: Rock representation* for more details. The data related to the comparison for the adopted base case models is visualized in Figure 2-7. When studying the black lines (modeled pressures at 2040) it can be seen that the undrained model (the graph at top) overestimates the closure state pressures and the drained model (the graph at bottom) underestimates the pressures.

The simulated water pressures after full water saturation are also included in Figure 2-7, indicated by gray lines. As expected, the undrained model obtains a hydrostatic final state, i.e. the results align with the diagonal of the graph. The drained model, on the other hand, attains pressures significantly lower as compared to hydrostatic. The two representations, undrained and drained, may be thought of as providing bounds for the "actual" water pressure evolution and therefore are expected to also produce bounds for the water saturation process regarding the uncertainty in host rock water pressure.

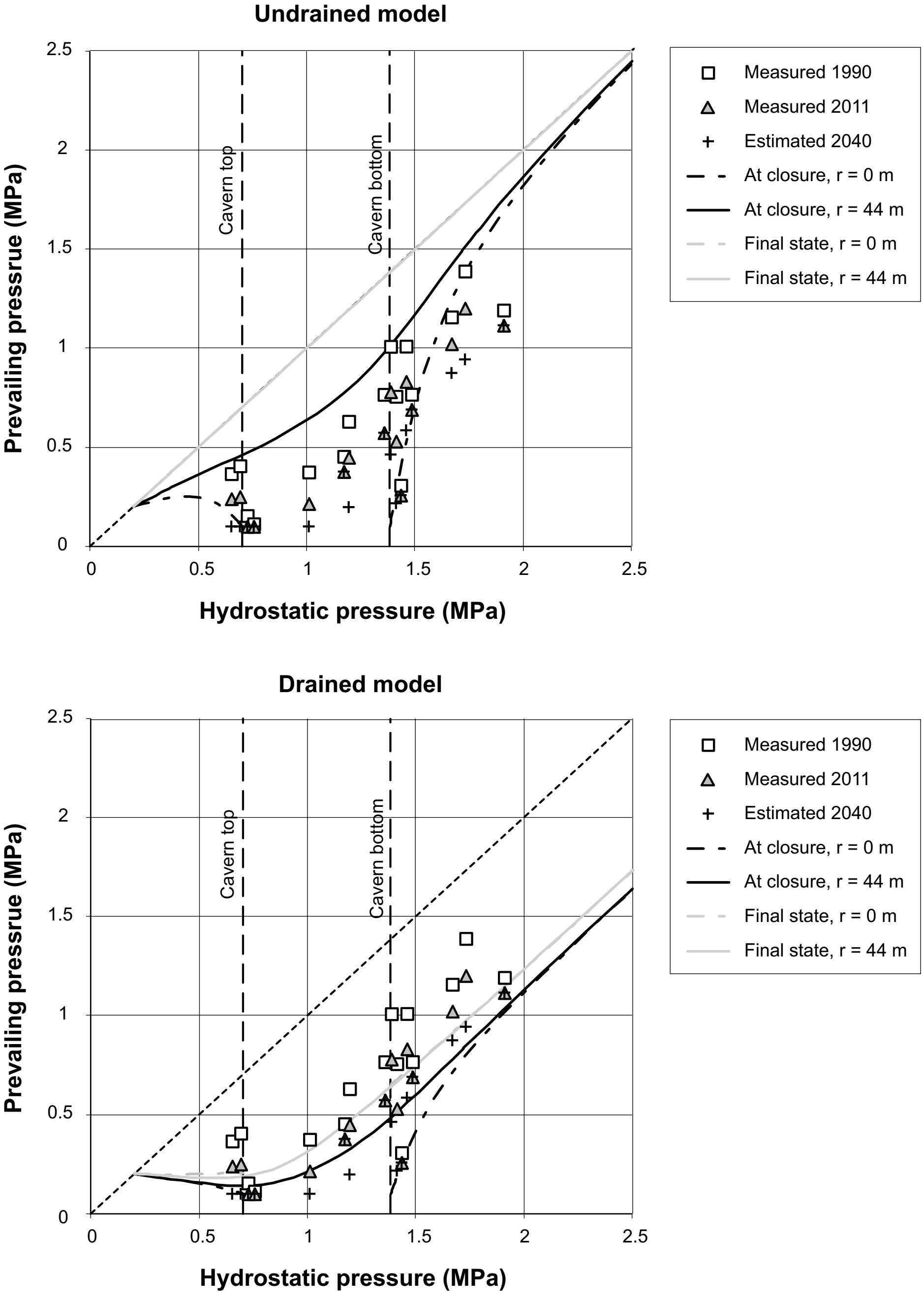

Figure 2-7. *Water pressure state in the cavern host rock. Prevailing pressure in a given position is given as a function of the hydrostatic pressure at that position. Measurements (1990 and 2011) and measurement estimates (2040) are indicated with symbols, model responses at closure (2040) are indicated with black lines, and model responses at final state (steady state at full saturation) are indicated with gray lines.*

If studying the calculated cavern inflows in Figure 2-8, obtained for a rock permeability of 10^{-16} m/s, and comparing them with measurements of total drainage outflow, indicated by symbols, it can be seen that they are quite different in character. The measurements show a slowly decreasing trend, reflecting a large-scale drainage of the entire SFR-site, whereas the flow in the models, defined on a considerably smaller scale, decreases almost instantly down to a constant level due to their local and homogeneous character.

Thus, the models, defined with use of a homogeneous rock representation and on a small scale as compared to the site-scale, cannot mimic this slow evolution when prescribing constant water pressure BCs. But when considering both representations, undrained and drained, together, however, the difference in their responses produces a range somewhat in correspondence to that of large scale evolution effects.

The overall evolution of the system during the wetting process can be studied in Figure 2-9 in terms of pressure development in the two base case models. In Figure 2-9 iso-maps of pressure are shown at different time after closure of the cavern. As can be seen in the legend, pressures are shown for the range 0.1–4 MPa, where 0.1 MPa is the lower limit of saturated conditions (since the gas pressure is prescribed to 0.1 MPa). White areas indicate pressure below 0.1 MPa.

The initial pressure conditions show a clear reduction of pressure around the cavern, due to the assumed drained conditions at the cavern walls. The draw down is seen to be wider for the drained model. One year after closure the rock is desaturated around the cavern due to water uptake of the EBS-materials within the cavern. The rock desaturation is more pronounced for the drained model.

After five years the rock and a part of the silo content have become saturated in the undrained model, whereas the drained model still shows desaturated conditions in the rock close to the upper part of the cavern and the interior of the repository is unsaturated to the largest part. Ten years after closure, only the top-backfill still has unsaturated parts in the undrained model. In the drained model on the other hand, the main part of the cavern interior still is unsaturated and likewise for the rock about the cavern top. In the next pair of iso-maps, at 15 years and 50 years, for the undrained and drained model, respectively, steady state conditions prevail. In the undrained model steady state conditions are hydrostatic and in the drained model the steady state conditions are reduced as compared to hydrostatic due to the drainage from the cut out boundary.

The saturation process within the EBS components in the two base case models can be studied in Figure 2-10 where iso-maps of liquid saturation are shown at different time after closure of the cavern. As can be seen in the legend, saturation is shown for the range 0–0.99, and in the forthcoming 0.99 is taken as defining the upper limit for unsaturated conditions. White areas indicate saturation above 0.99, thus fully saturated conditions.

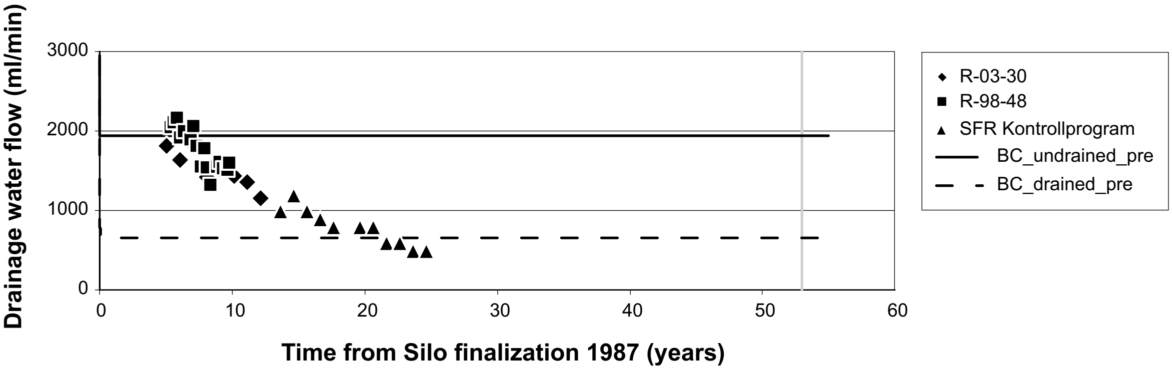

Figure 2-8. Calculated water flows into an empty cavern (lines) and measurements of outflow from the cavern drainage system (symbols).

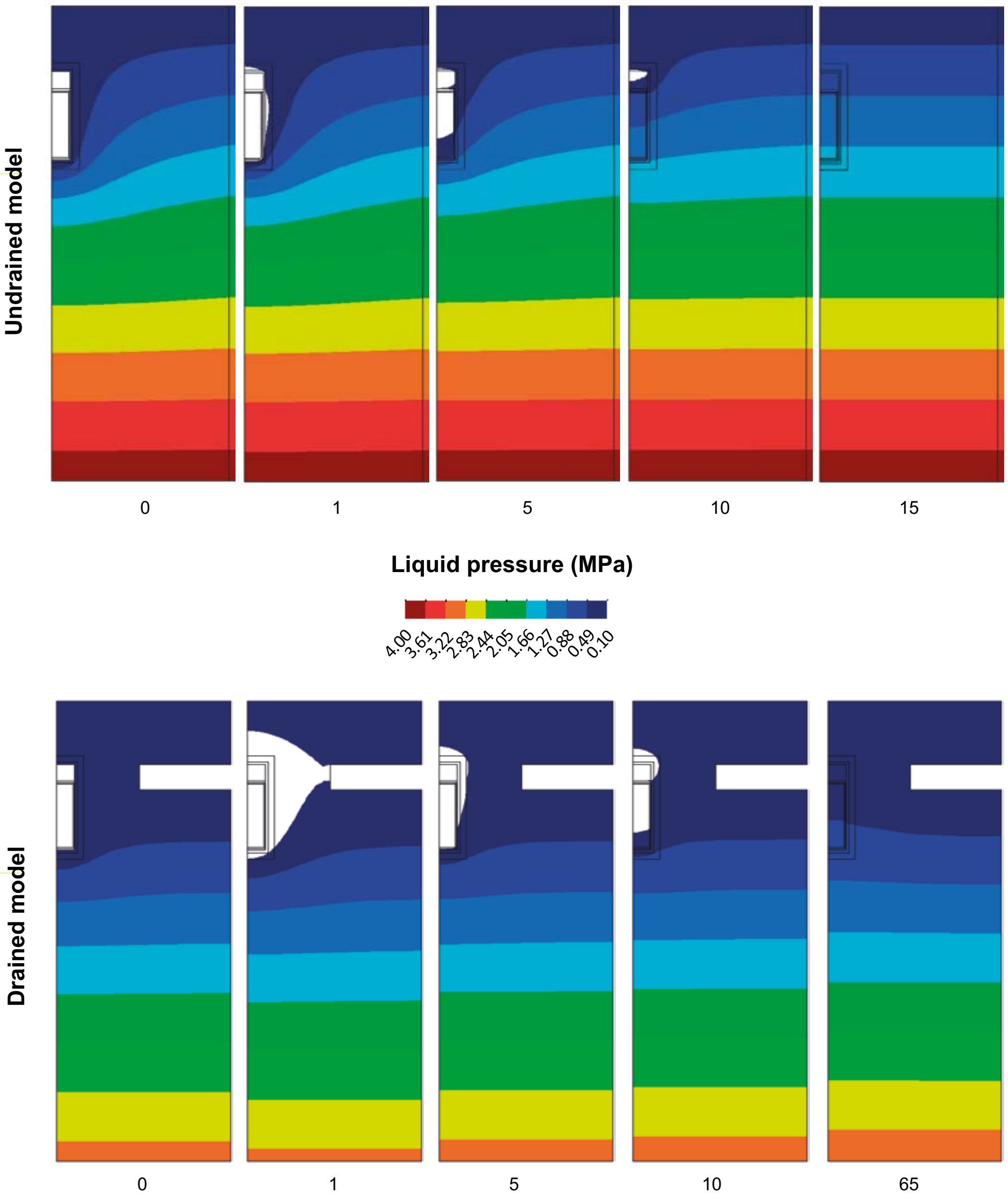

***Figure 2-9.** Water pressure in the host rock for the undrained (top) and drained (bottom) base case model.*

The overall saturation process of the EBS within the cavern is similar for the two models. The saturation process starts at the lower edge of the cavern in the bottom buffer and goes inwards/upwards. Concurrent with the saturation of the interior of the silo, the saturation process also starts in the outer part of the top buffer and progresses inwards/upwards in the top backfill. The saturation finishes at the central/upper part of the top backfill. The slower saturation time scale for the drained model is evident when studying Figure 2-10.

Some small differences in the saturation process character can be observed between the models. The lower pressures and pressure gradients in the drained model give slower radial wetting relative to the vertical wetting in comparison with what the undrained model produces.

This can be seen when comparing the results at 24 years for the drained model with those at 9 years for the undrained model showing similar overall saturation state. The saturation front is more curved upwards in the undrained model due to a larger radial pressure gradient.

In order to specify and get an overview of the saturation evolution in the EBS, times, t_{first} and t_{last}, denoting times when the first and last part of the considered constituent becomes saturated (here taken as when $S_l > 0.99$), respectively, are identified. The time interval defined by $[t_{first}, t_{last}]$ will be called *saturation interval* of the constituent and these are given in Table 2-10 and shown graphically in Figure 2-11. For more information about saturation intervals see chapter A.2 "Definition of saturation intervals and saturation limit intervals". In Table 2-10 the initial available pore volume is also given for all components. It can be seen that the top backfill, waste, and wall buffer dominate the initially available pore volume.

Studying the saturation intervals in Figure 2-11 it can be seen that for the different rock representations they are different. The most prominent overall difference is in the saturation duration for most of the constituents where the drained model produce significantly longer saturation as compared to the undrained model and most so for the top backfill component. The overall general trends of both sets of intervals, however, are similar.

Table 2-10. Saturation intervals for the EBS constituents.

Constituent	Initial available pore volume		Undrained base case $[t_{first}, t_{last}]$ (yr)	Drained base case $[t_{first}, t_{last}]$ (yr)
Top backfill (sand)	3,186 m^3	37%	[2.3, 13.2]	[9.6, 53.1]
Top buffer (10/90)	132 m^3	2%	[1.6, 7.5]	[7.0, 17.7]
Lid	82 m^3	1%	[7.2, 7.5]	[17.5, 17.7]
Waste	2,618 m^3	30%	[2.2, 7.4]	[5.5, 17.7]
Silo (base and wall)	636 m^3	7%	[1.3, 7.2]	[3.6, 17.4]
Wall buffer (100/0)	1,807 m^3	21%	[0.9, 5.9]	[2.3, 16.9]
Bottom buffer (10/90)	132 m^3	2%	[0.5, 2.8]	[1.6, 6.3]
All	8,594 m^3	100%		

In conclusion, it should be noted that the two representations of the surrounding rock mass produce significantly different time intervals for which the EBS constituents saturate. The two representations are used to obtain relevant bounds on the saturation process within the EBS when the uncertainty of the host rock water pressure is considered. The top backfill is the last component in the EBS to become saturated after 13 yr and 53 yr in the undrained and drained model, respectively.

Figure 2-10 and Figure 2-11 also show that the overall characteristics of the EBS saturation process for the two representations are similar. This indicates that the methodology may be considered "stable" or "robust", i.e. the system representations are not over-sensible, and therefore suitable for performing investigations of the system by varying properties from the base case setting.

2.4.2 Undrained rock cavern

As discussed in:

- Appendix B: EBS representation.
  - B.1 Initial conditions.
- Appendix C: Rock representation.
  - C.1 Initial and boundary conditions.

Table 2-11. Models used in this case study.

Model description	Model name
Base case, Drained	drained_var3B_ext.gid
Changed initial conditions, Drained	drained_alt_init_state_2.gid

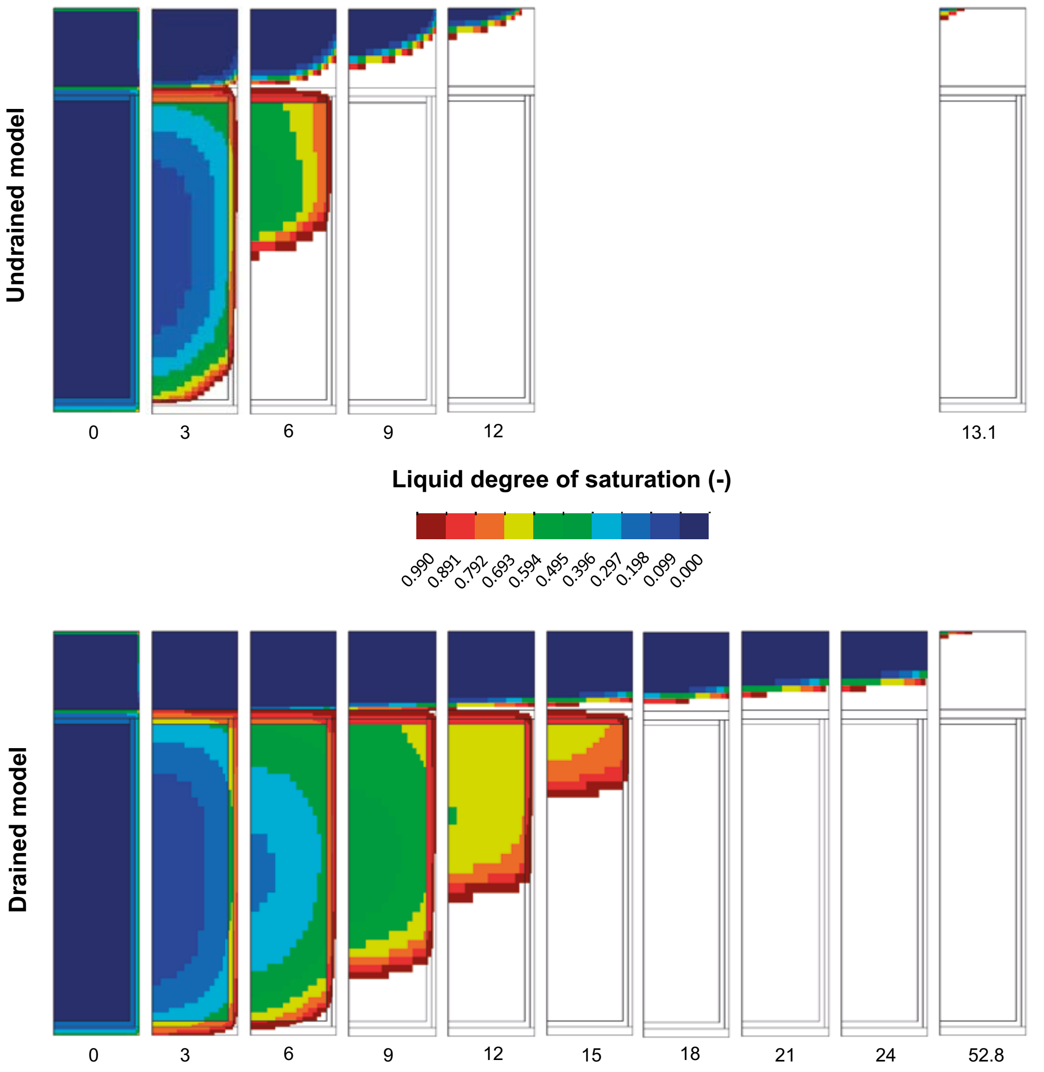

Figure 2-10. *Degree of liquid (water) saturation in the EBS for the undrained (top) and drained (bottom) base case model.*

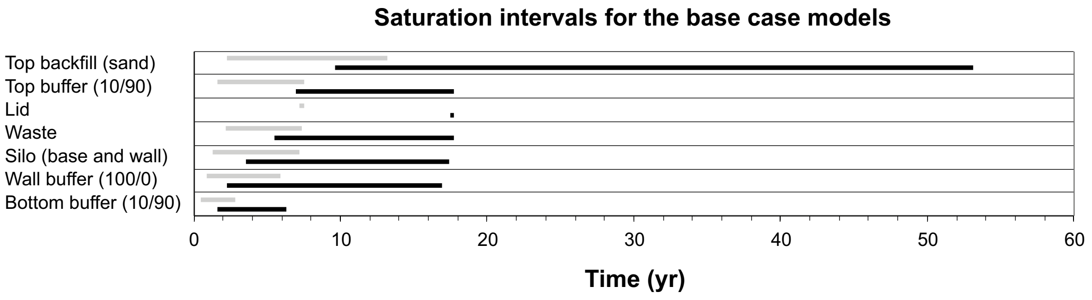

Figure 2-11. *Saturation intervals for the base case models, undrained (gray) and drained (black).*

The assumption made concerning the initial conditions at 2040 for the base case is that the drainage system installed at the cavern wall performs perfectly from the installation 1987 until the closure at 2040. This equals considering the cavern being open without any EBS components present from 1987 to 2040 as schematically shown in the top row of Figure 2-12. At closure 2040 all EBS components are then introduced in the model.

The drainage system might, however, not be working perfectly even though most data suggests that it performs rather well. Here, to investigate the case of a cavern wall drainage performing less than perfectly, the limiting case where no drainage is present at the cavern wall at all is adopted, as indicated in the bottom row of Figure 2-12. When doing so, all EBS components except for the top backfill are introduced in the model at 1987 and only the remaining empty “top volume” is drained. This state remains until 2040 when also the top backfill is introduced in the model and the final saturation takes place.

To facilitate the comparison of the relative saturation process between the models, in Table 2-12 all but the top backfill saturation interval have been given with the installation year 1987 as a reference for the changed initial condition model.

If not regarding the top backfill to begin with, the saturation process can be seen to be rather similar between the models. The largest deviation can be seen for the top buffer where the saturation starts quite a bit earlier but nevertheless ends somewhat later as compared to the base case model. In the model the installed EBS components are all saturated 2005.

Since the EBS components below the top backfill all are saturated at 2040 the saturation of the top backfill will start and end sooner as compared to the base case. The base case saturation interval length becomes 43.5 years whereas the new model has an interval length of 39.3 years.

Table 2-12. Saturation intervals for the changed initial conditions model and drained base case model.

Constituent	Changed initial conditions $[t_{first}, t_{last}]$ (yr)	Drained base case $[t_{first}, t_{last}]$ (yr)
Top backfill (sand)	[1.0, 40.3]	[9.6, 53.1]
Top buffer (10/90)	[4.7, 17.9] [a]	[7.0, 17.7]
Lid	[17.5, 17.8] [a]	[17.5, 17.7]
Waste	[5.4, 17.8] [a]	[5.5, 17.7]
Silo (base and wall)	[3.5, 17.6] [a]	[3.6, 17.4]
Wall buffer (100/0)	[2.3, 17.0] [a]	[2.3, 16.9]
Bottom buffer (10/90)	[1.6, 6.2] [a]	[1.6, 6.3]

(a) The times are given with reference to 1987 instead of 2040, i.e. $t(1987) = 0$.

The saturation intervals are shown graphically in Figure 2-13 where year 2040 has been taken as the reference for all times.

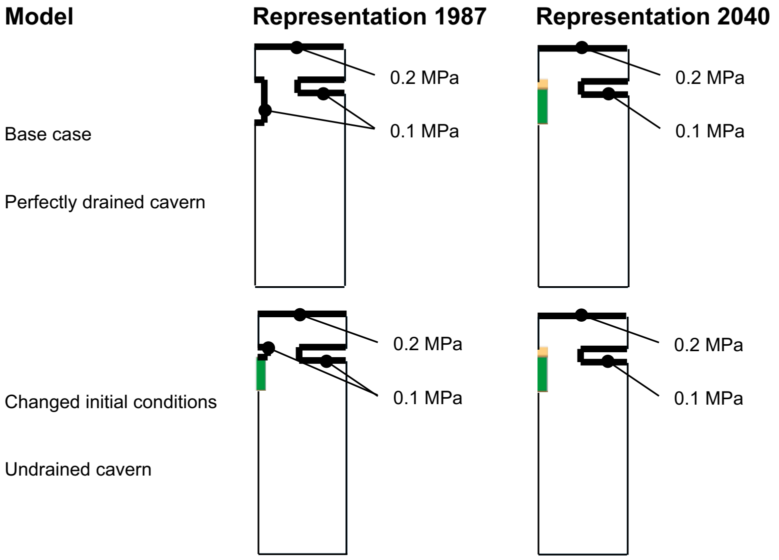

Figure 2-12. Conditions used to represent a perfectly drained cavern (top row) and an undrained cavern (bottom row).

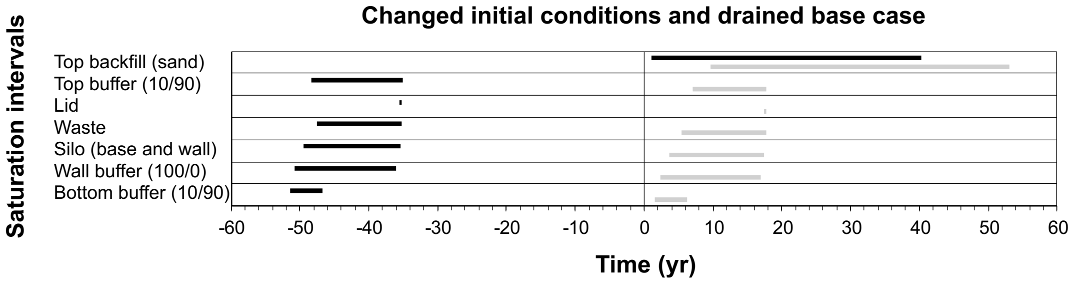

Figure 2-13. *Saturation intervals of the changed initial conditions (black) and base case model (gray). All times are given with respect to the time of closure, i.e. t(2040) = 0. The altered model starts at t(1987) = –53.*

This investigation indicates that if the cavern drainage is not working at all the saturation of the silo repository are significantly decreased, about 13 years with the presently used setup. The saturation of the top backfill starts earlier, ends sooner, and has less duration as compared to the base case model, where a perfectly drained cavern is assumed. For the model setup used here, a simple estimate of the total saturation time of the undrained cavern case can be obtained by translating the start of the drained cavern (here the base case) model's interval of the top backfill to the time of closure (2040).

2.4.3 Dry host rock representation (decreased rock permeability)

To calibrate the rock permeability of the dry rock representation three empty cavern models with permeabilities 10^{-15}, 10^{-16}, and 10^{-17} m^2 were used to find a relation between cavern inflow and permeability. The results are compiled below in Figure 2-14 where computed cavern inflows are plotted against corresponding permeability. As can be seen, a linear relation in log-log space is suitable for describing the relation between cavern inflow and permeability.

Table 2-13. Models used in this case study.

Model description	Model name
Base case, Drained, Empty	BC_drained_ pre.gid
$k_{ii} = 10^{-15}$ m^2 in rock, Drained, Empty	BC15_drained_ pre.gid
$k_{ii} = 10^{-17}$ m^2 in rock, Drained, Empty	BC17_drained_ pre.gid
Base case, Drained	drained_var3B_ext.gid
kii = $7.55 \cdot 10^{-17}$ m^2 in rock, Drained	drained_var3B_1_tight.gid

The recent lowest measurements of total drainage outflow, shown in Figure 2-8, are about 500 ml/min. Therefore, a permeability of $7.55 \cdot 10^{-17}$ corresponding to 500 ml/min according to the identified linear relation in log – log space was used in the dry host rock model.

Saturation intervals are identified for the new model, shown in Table 2-14. To facilitate comparisons, results obtained for the drained base case as well as for the dry host rock representation are shown in Figure 2-15 in terms of saturation intervals and saturation limit intervals

Table 2-14. Saturation intervals for the dry host rock model and drained base case.

Constituent	Dry host rock $[t_{first}, t_{last}]$ (yr)	Drained base case $[t_{first}, t_{last}]$ (yr)
Top backfill (sand)	[13.6, 70.8]	[9.6, 53.1]
Top buffer (10/90)	[9.9, 20.8]	[7.0, 17.7]
Lid	[20.6, 20.8]	[17.5, 17.7]
Waste	[7.0, 20.8]	[5.5, 17.7]
Silo (base and wall)	[4.7, 20.6]	[3.6, 17.4]
Wall buffer (100/0)	[3.2, 20.0]	[2.3, 16.9]
Bottom buffer (10/90)	[2.4, 7.8]	[1.6, 6.3]

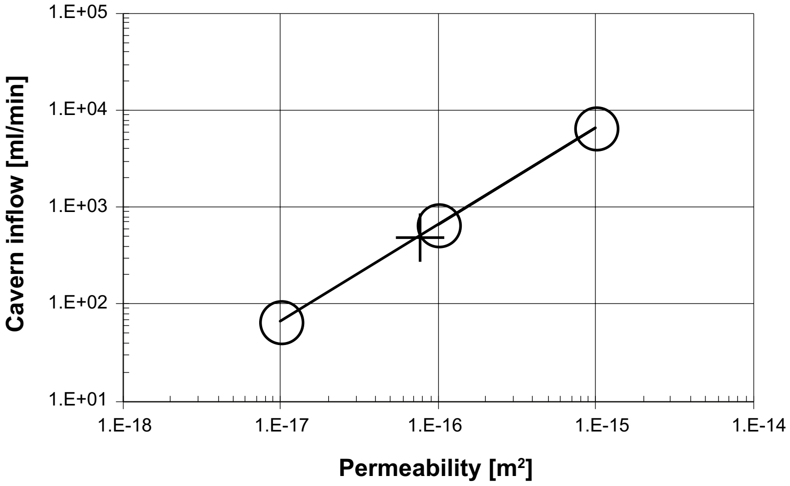

Figure 2-14. Circles indicate simulated inflow to an empty cavern for different rock permeabilies. The cross indicates the (permeability , cavern inflow) combination, given by adopting the linear relation indicated by the line, for a inflow of 500 ml/min.

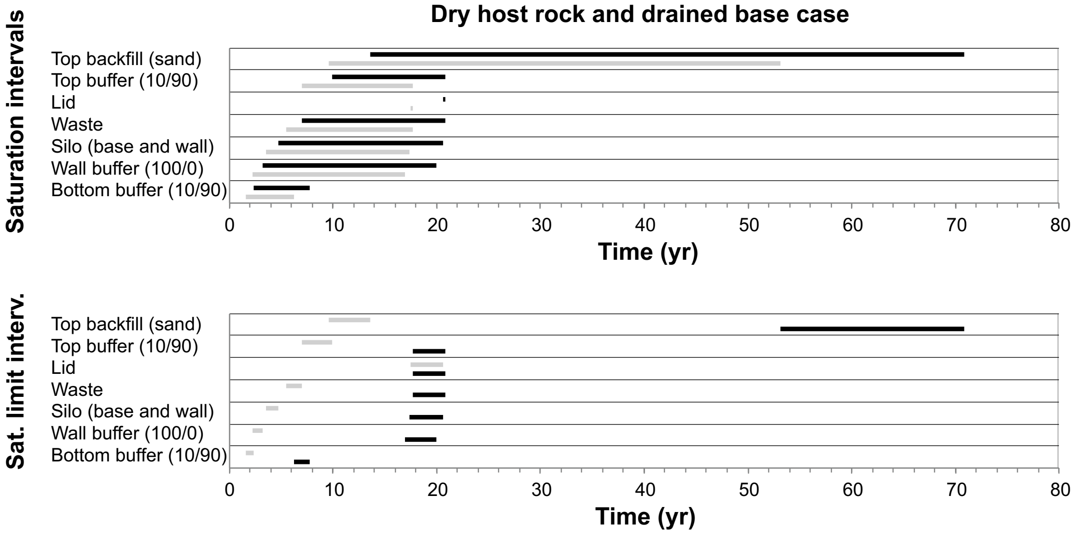

Figure 2-15. Top: Saturation intervals of the dry host rock model (black) and base case model (gray). Bottom: Saturation limit intervals formed between the dry host rock model and the drained base case model where the bars show the difference in time when the saturation process starts (gray bars) and ends (black bars) for the different constituents.

When studying the saturation intervals in Figure 2-15 it is seen that all are shifted later in time and have longer duration when compared to the base case. The top backfill changes its saturation duration most significantly.

When using the dry rock permeability the time to full saturation of the EBS changed from 53 yr to 71 yr. Thus, the system is sensitive to changes in water transport properties in the host rock. The top backfill component has the major duration increase of the saturation intervals.

2.4.4 Effect from an impermeable plastic sheet below the concrete pad

Outflow has been measured from drains at different positions (top, wall, and bottom) in the cavern. In Figure 2-16 the measurements, normalized with respect to total drainage outflow, are shown for the time interval 1991–1997 (symbols). The measured inflow from the bottom is virtually none. The base case model overestimates the inflow through the bottom as compared to measurements. This could come from the impermeability of the plastic sheet upon which the concrete pad was cast.

Table 2-15. Models used in this case study.

Model description	Model name
Base case, Drained	drained_var3B_ext.gid
Impermeable concrete pad, Drained	drained_var3B_ext_imp_copy.gid

In the base case models an assumption of a permeable plastic sheet has been adopted. To study the case where the plastic sheet remains intact, i.e. is impermeable, a model with a hydraulically closed cavern bottom, obtained by removing material below the cavern and prescribing no-flow BCs, was developed.

The pressure profiles obtained for $r = 0$ m and $r = 44$ m are shown in Figure 2-17 for the base case and impermeable pad model at the time of closure and for final, steady state, conditions.

As can be seen from studying the graphs in Figure 2-17, the only significant change in the pressure profiles when representing the impermeable plastic sheet is at closure for $r = 0$ m at positions just below the bottom of the cavern. The water pressure becomes slightly higher (0.4 MPa as compared to 0.1 MPa) for the impermeable pad model.

Saturation intervals are identified for the new model, shown in Table 2-16. To facilitate comparisons, results obtained with/without the permeable concrete pad are shown in Figure 2-18 in terms of saturation intervals as well as saturation limit intervals.

There are not significant overall effects on the saturation process from introducing a representation of an impermeable concrete pad. The intervals are generally somewhat delayed and extended but to a very small extent. Locally, however, in the close vicinity of the cavern floor, in the bottom buffer, significant effects are seen. The final saturation is significantly prolonged for the bottom buffer constituent.

The conclusions are that when an impermeable concrete pad is accounted for, which most probably is more in line with reality at the time being, but not necessary so later on, the saturation process of the EBS is affected locally around the concrete pad, but not significantly in an overall perspective. Thus, if disregarding the impermeable concrete pad as in the base case models, one should be aware of that the results may not be as representative locally around the base of the cavern as elsewhere if the plastic sheet remains intact during the saturation process.

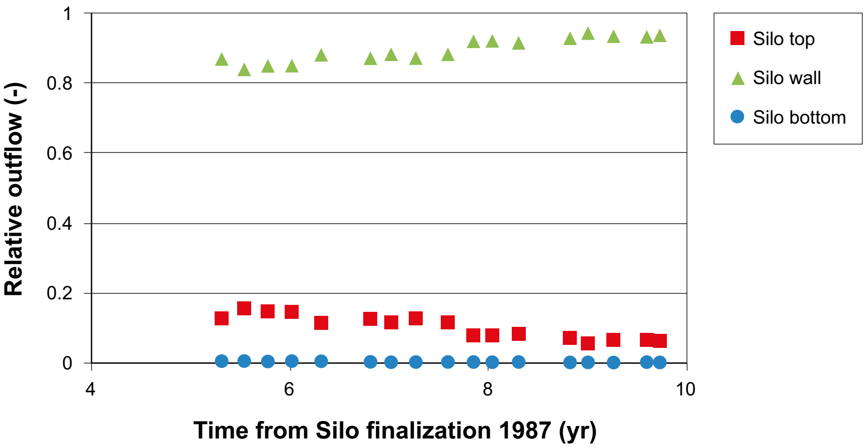

Figure 2-16. Normalized measured drainage outflow.

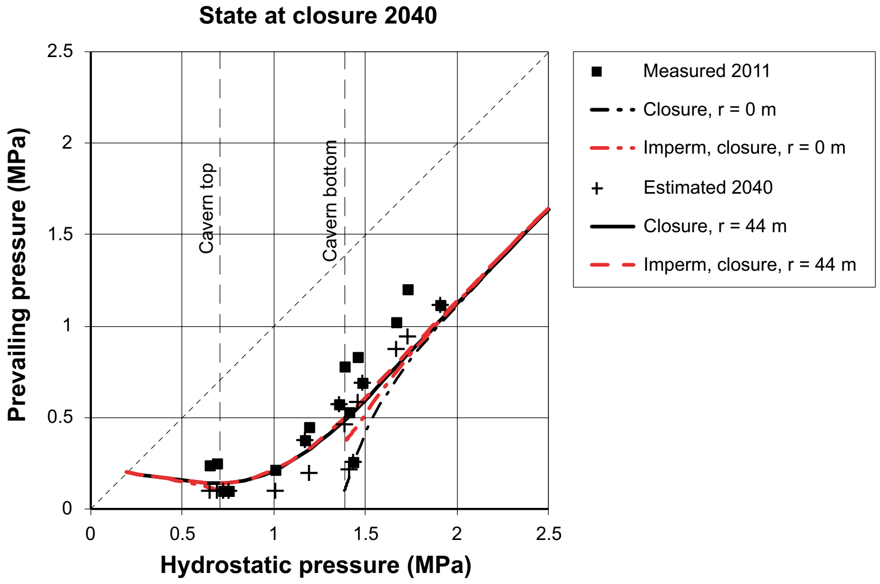

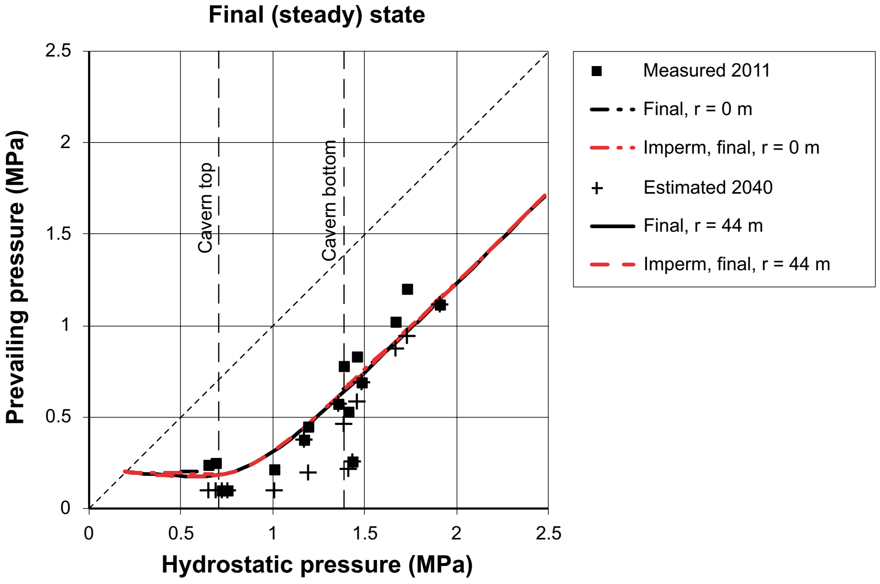

Figure 2-17. *Measured pressures 2011, from measurements estimated pressures at 2040, and calculated pressure profiles, for r = 0 and 44 m, at closure (top) and the final (steady) state (bottom). The red lines indicate results obtained by using the impermeable floor representation.*

Table 2-16. Saturation intervals for the impermeable concrete pad model and drained base case.

Constituent	Impermeable concrete pad [t_{first}, t_{last}] (yr)	Drained base case [t_{first}, t_{last}] (yr)
Top backfill (sand)	[9.6, 53.2]	[9.6, 53.1]
Top buffer (10/90)	[6.9, 18.7]	[7.0, 17.7]
Lid	[18.5, 18.7]	[17.5, 17.7]
Waste	[7.6, 18.7]	[5.5, 17.7]
Silo (base and wall)	[5.0, 18.4]	[3.6, 17.4]
Wall buffer (100/0)	[2.6, 17.9]	[2.3, 16.9]
Bottom buffer (10/90)	[1.8, 10.8]	[1.6, 6.3]

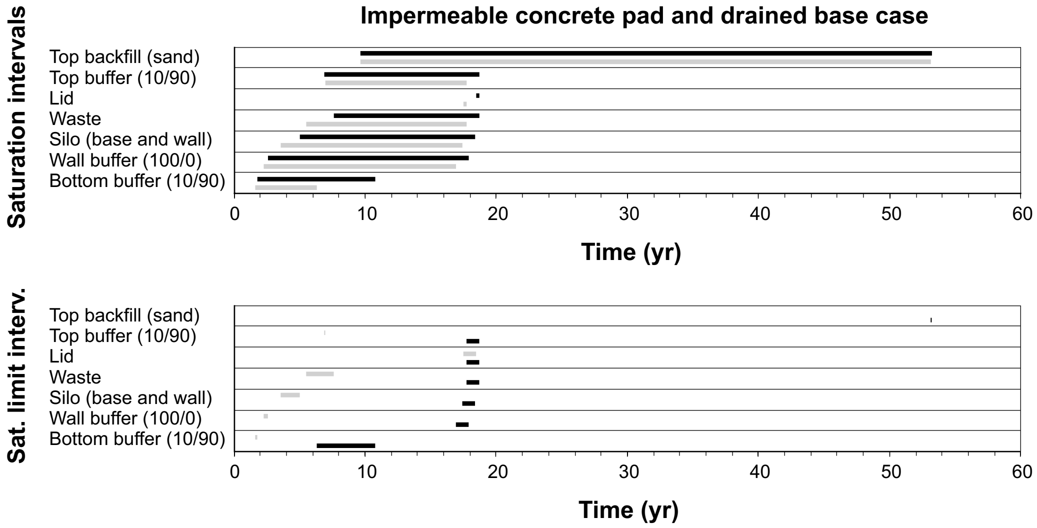

Figure 2-18. *Top: Saturation intervals of the impermeable concrete pad model (black) and the drained base case (gray). Bottom: Saturation limit intervals formed between the drained base case model and the impermeable concrete pad model where the bars show the difference in time when the saturation process starts (gray bars) and ends (black bars) for the different constituents.*

2.4.5 Uncertainty in top backfill properties (increasing porosity)

Since the saturation of the top backfill is influential for the overall saturation duration possible changes in the material description could give significant effects. The "plug filter" material properties given in Åkesson et al. (2010) have been used for describing the top backfill. In Åkesson et al. (2010) however, porosity is given in terms of a range, 0.35–0.39, and here we adopt $n_{top\ backfill} = 0.4$ in this alternative representation. The new model with higher porosity in the top backfill has a total initial available volume that is increased with 5% as compared to the base case.

Table 2-17. Models used in this case study.

Model description	Model name
Base case, Drained	drained_var3B_ext.gid
Alternative top backfill, Drained	drained_var3B_1_top_bf.gid

Saturation intervals are identified for the new model, shown in Table 2-18. To facilitate comparisons, results obtained with/without the permeable concrete pad, saturation intervals as well as saturation limit intervals are shown in Figure 2-19.

Table 2-18. Saturation intervals for the model with more porous top backfill and drained base case.

Constituent	Porous top backfill [t_{first}, t_{last}] (yr)	Drained base case [t_{first}, t_{last}] (yr)
Top backfill (sand)	[10.1, 58.9]	[9.6, 53.1]
Top buffer (10/90)	[7.2, 17.8]	[7.0, 17.7]
Lid	[17.5, 17.8]	[17.5, 17.7]
Waste	[5.5, 17.8]	[5.5, 17.7]
Silo (base and wall)	[3.6, 17.5]	[3.6, 17.4]
Wall buffer (100/0)	[2.3, 17.0]	[2.3, 16.9]
Bottom buffer (10/90)	[1.6, 6.3]	[1.6, 6.3]

As can be seen it is only the top backfill saturation which is significantly affected by the change in its own porosity. For the base case the top backfill saturation interval ends after 53 yr and in the new model the same interval ends after 59 yr.

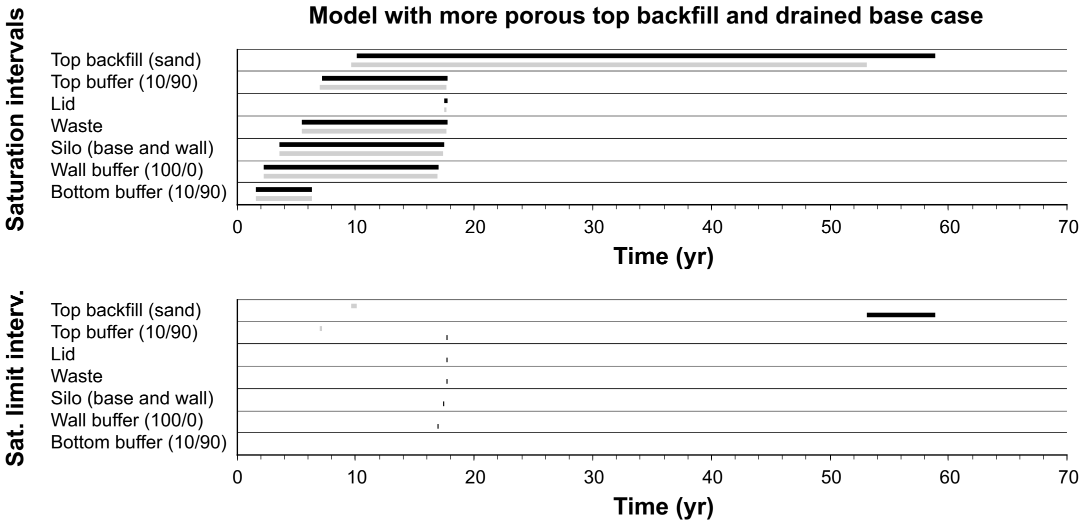

Figure 2-19. *Top: Saturation intervals of the model with more porous top backfill (black) and the drained base case (gray). Bottom: Saturation limit intervals formed between the drained base case model and the model with more porous top backfill where the bars show the difference in time when the saturation process starts (gray bars) and ends (black bars) for the different constituents.*

When changing the porosity of the top backfill from 0.35 to 0.4 only the saturation interval of the same constituent is significantly affected. Since this, however, is the last constituent to be saturated, the overall saturation time is extended by 6 yr.

2.4.6 Uncertainty in silo content properties (including waste package porosity)

The properties of the homogenized representation of the silo content, i.e. the "waste" material are not certain. One property which could have a significant effect on saturation time is the porosity of the material. In the base case it was assumed that the waste packages themselves did not contribute to the porosity of the system and the used porosity was 0.1 of the silo content material. If, however, a porosity of 0.15 is assumed for the waste packages, the silo content material obtains a porosity of 0.2. Thus, the available initial pore volume of the silo content is doubled. This gives an increase of the total initial available pore volume of 30%.

Table 2-19. Models used in this case study.

Model description	Model name
Base case, Drained	drained_var3B_ext.gid
Porous waste packages, Drained	drained_var3B_porous_waste.gid

Including porous waste packages in the model could have an impact on the water retention property of the homogenized material as described in Appendix B, chapter B.2.1. In Figure 2-20 the retention curves involved in the estimate of the waste material are shown. A parameter fit of Van Genuchten's expression gives the values: (λ, p0)Van Genuchten = (0.2, $3.55\cdot10^{-4}$ MPa). Due to difficulties considering convergence, however, the same square law parameter setting (p0 = 0.05 MPa) as used in the base case is here reused. It can be seen in Figure 2-20 that this choice is quite adequate anyway.

Saturation intervals are identified for the new model, shown in Table 2-20. To facilitate comparisons, results obtained with $n_{waste\ packages}$ = 0.0 (the base case setting) and $n_{waste\ packages}$ = 0.15 are shown in terms of saturation intervals as well as saturation limit intervals in Figure 2-21.

When studying Figure 2-21 it can be seen that the saturation intervals of all constituents are affected by the change in the waste representation. The saturation starts and finishes later. The saturation intervals become elongated for the new model.

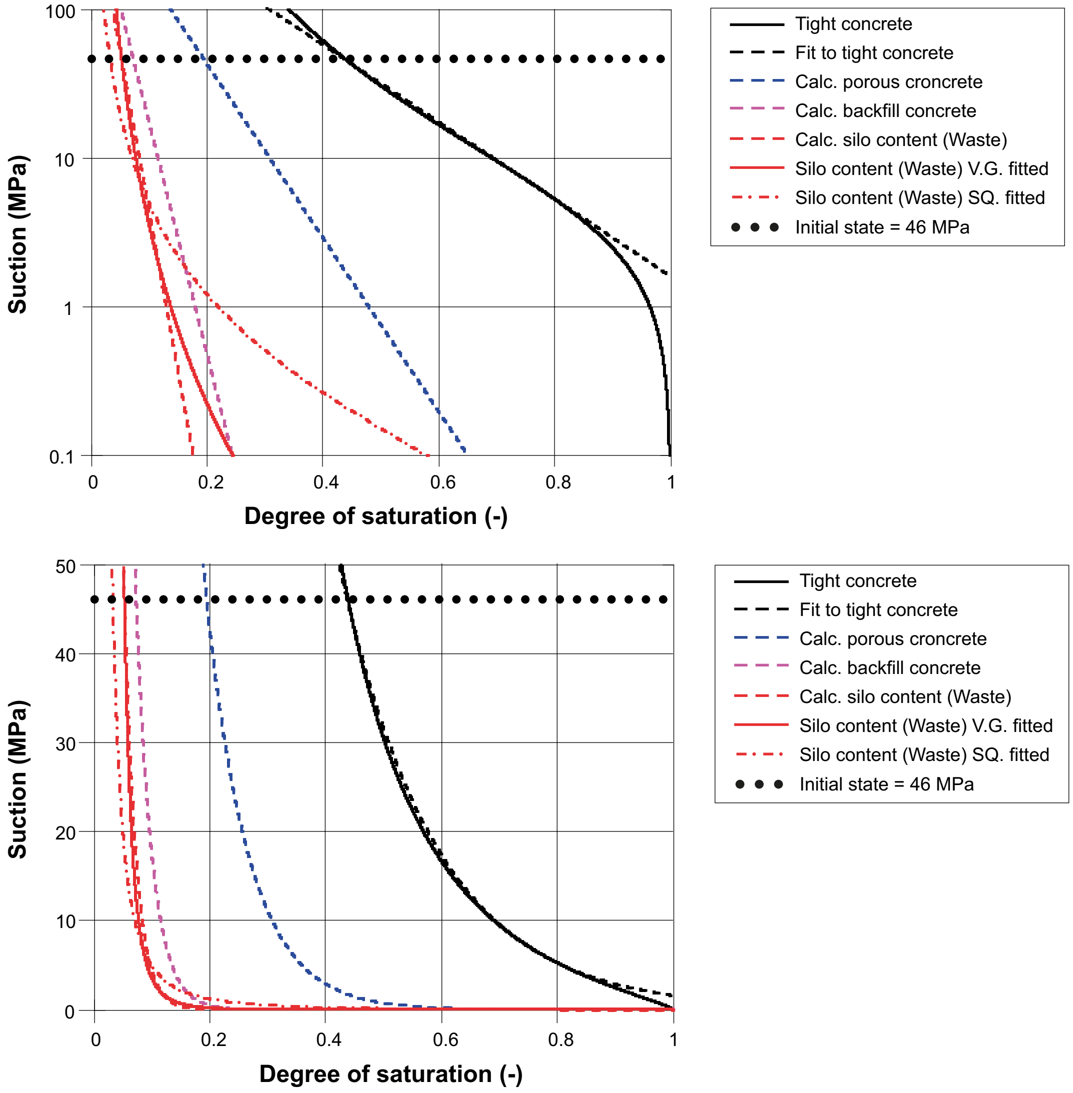

Figure 2-20. *Water retention properties used when estimating the silo contents ("Waste") material given in (top) lin – log and (bottom) lin – lin space, respectively. A porosity of 0.15 was assumed for the waste packages within the silo.*

Table 2-20. Saturation intervals for the model where porous waste packages (n = 0.15) are assumed and the drained base case.

Constituent	Porous waste packages [t_{first}, t_{last}] (yr)	Drained base case [t_{first}, t_{last}] (yr)
Top backfill (sand)	[11.5, 60.5]	[9.6, 53.1]
Top buffer (10/90)	[8.8, 29.3]	[7.0, 17.7]
Lid	[28.9, 29.3]	[17.5, 17.7]
Waste	[7.7, 29.3]	[5.5, 17.7]
Silo (base and wall)	[4.3, 28.8]	[3.6, 17.4]
Wall buffer (100/0)	[2.6, 27.7]	[2.3, 16.9]
Bottom buffer (10/90)	[1.8, 9.2]	[1.6, 6.3]

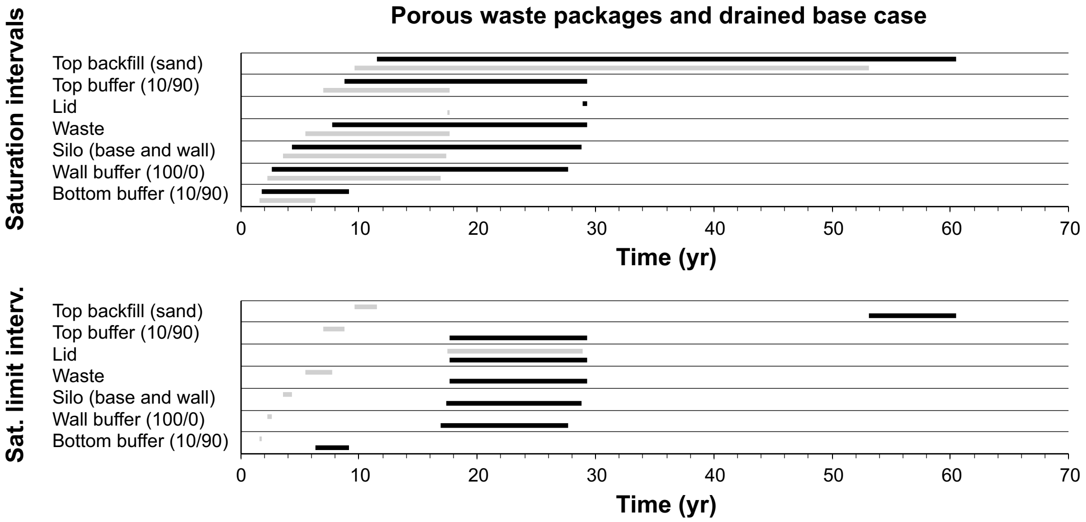

Figure 2-21. *Top: Saturation intervals of the porous waste package model (black) and the drained base case (gray). Bottom: Saturation limit intervals formed between the drained base case and the porous waste package model where the bars show the difference in time when the saturation process starts (gray bars) and ends (black bars) for the different constituents.*

The saturation intervals of all EBS-components are significantly affected, and the overall saturation duration increases from 53 yr to 61 yr. The conclusion is that the silo content properties has a governing role of the saturation process in the system.

2.4.7 Discussion concerning the representation of GEKO/QI

Despite considerable effort made in trying to find relevant existing data from which material properties for the bentonite (GEKO/QI) buffers could be determined the result was poor. Due to the lack of data, permeability of the pure GEKO/QI buffer had to be obtained from extrapolation, and the water retention properties of the pure GEKO/QI buffer was taken as that of Wyoming bentonite (MX-80). The retention of the 10/90 mixture of GEKO/QI and sand was obtained by relating variables belonging to the mixture to corresponding variables of the individual constituents and using retention relations adopted for the constituents.

Close to the deadline of this report, however, preliminary laboratory data from GEKO/QI samples was available. There was not enough time to evaluate parameter values from the data and rerun all the models. Below, the data is, however, compared to the GEKO/QI models used in the simulations and a discussion of the differences is given.

To investigate if the material representations used in the simulations are suitable, direct comparisons are made between laboratory data and models and their parameter values. Moreover, the used GEKO/QI representation is evaluated from its capacity to reproduce the saturation process in water uptake tests, which recently have been carried out for GEKO/QI.

Direct comparisons

The solid density was determined to ρ_s = 2,800 kg/m^3 for the GEKO/QI samples. The setting for the simulations on the other hand was ρ_s = 2,600 kg/m^3. The initial conditions corresponding to the two solid densities are given in Table 2-21, the differences are not expected to affect the results to a great extent.

Table 2-21. Initial conditions based on ρs = 2,600 kg/m^3 or ρs = 2,800 kg/m^3 for the GEKO/QI material.

Parameter	100/0 buffer		10/90 buffer	
GEKO/QI ρ_s (kg/m^3)	2,600	2,800	2,600	2,800
ρ_d (kg/m^3)	1,000	1,000	2,200	2,200
ρ_s (kg/m^3)	2,600	2,800	2,645	2,664
n (-)	0.62	0.64	0.168	0.174
e (-)	1.6	1.8	0.202	0.211
S_l (-)	0.276	0.264	0.224	0.215
w (-)	0.17	0.17	0.017	0.017

The values of determined permeability for GEKO/QI when using Forsmark water are given as a function of dry density in Figure 2-22. As can be seen, the value 10^{-17} m^2 adopted for the simulations might be slightly higher than what the experimental data suggests for 1,000 kg/m^3.

Next the retention curve is addressed by studying the swelling pressure measurements about 1,000 kg/m^3, as given in Figure 2-23, and the retention measurements shown together with the unconfined retention curve used in the modelling in Figure 2-24.

Figure 2-23 shows that for 1,000 kg/m^3 the swelling pressure (pressure obtained under confined conditions at full saturation) should be about 0.1 MPa. This corresponds to a suction of 0.1 MPa at full saturation under unconfined conditions. As can be seen in Figure 2-24 the used unconfined retention curve is close to 0.1 MPa at full saturation.

When comparing the unconfined retention curve with measurements in Figure 2-24 it can be seen to underestimate the laboratory data somewhat. Thereby, in the simulations, the strength of the potential for absorbing water is underestimated and the saturation process prolonged as compared to using a retention curve perfectly matching the data.

Since the initial state of the GEKO/QI material is taken as the initial state of all EBS components in the simulation it is of interest to evaluate a representative initial state from studying the measurements. If interpolating linearly between the measurements as indicated in Figure 2-24, the initial suction, i.e. at a water content of 0.17, becomes 62 MPa which can be compared to 46 MPa used in the simulations. This then, when prescribed as an initial condition instead of 46 MPa in the rest of the EBS components, would in turn render in a “drier” initial state with somewhat larger pore volumes to fill up. Table 2-22 shows the “old” (base case) setup and an estimated “new” setup from using the density 2,800 kg/m^3 and initial suction 62 MPa.

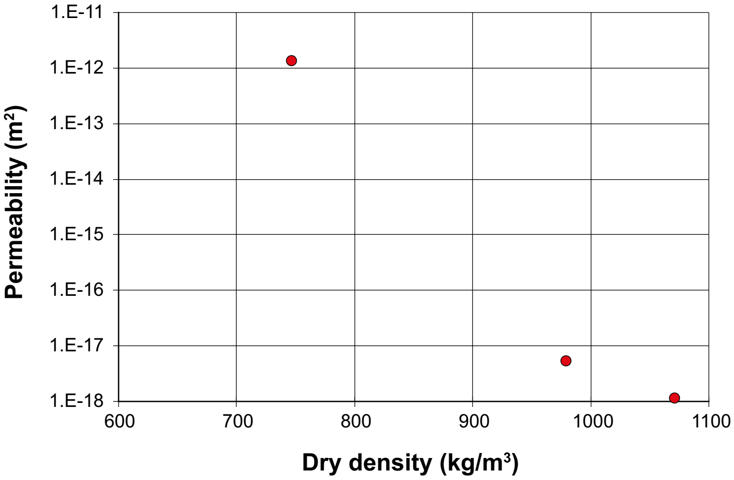

Figure 2-22. Permeability of GEKO/QI samples for Forsmark water given as a function of dry density.

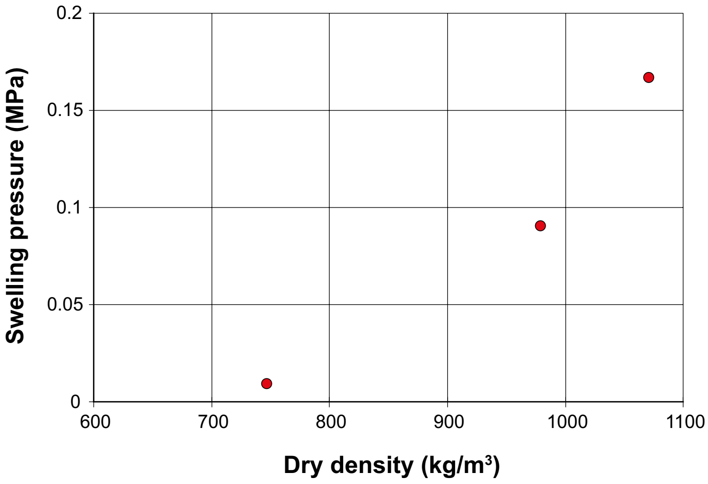

***Figure 2-23.** Swelling pressure of GEKO/QI samples for Forsmark water given as a function of dry density.*

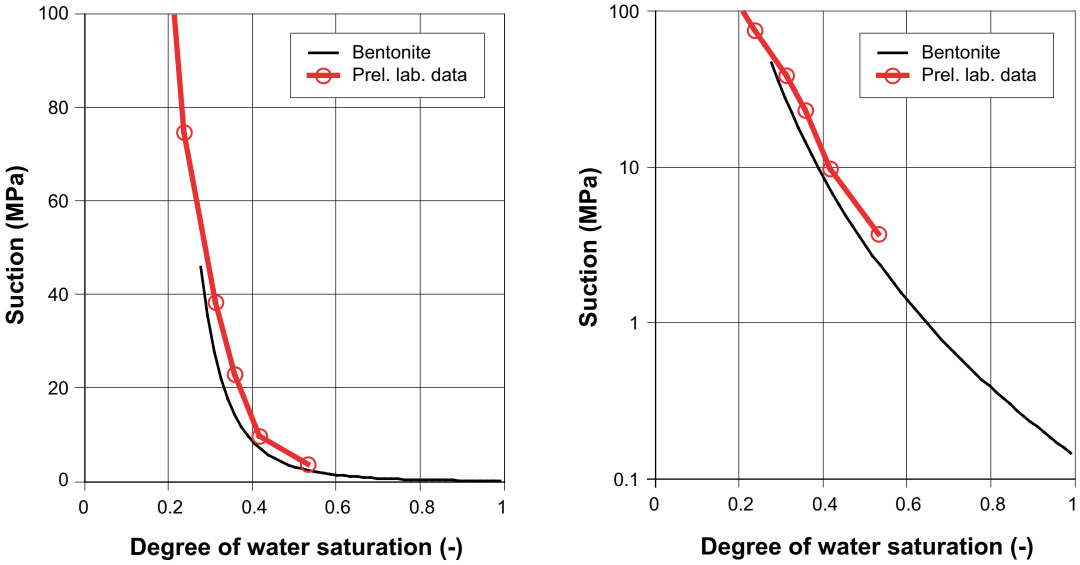

***Figure 2-24.** Free swelling retention curve adopted in the modelling (black line) shown together with measurements (symbols) of water retention for GEKO/QI samples obtained for Forsmark water.*

Table 2-22. Initial conditions used in the base case (old) and in a representation based on experimental data (new). The parameters are obtained from using ρs = 2,600 kg/m³ and an initial suction of 46 MPa or ρs = 2,800 kg/m³ and an initial suction of 62 MPa, for the old and new representation, respectively.

Constituent	V (m³)	n		S_l^0		$V_p–V_w^0$ (m³)	
		old	new	old	new	old	new
Top backfill (sand)	9,102	0.35	0.35	0	0	3,186	3,186
Top buffer (10/90)	1,011	0.168	0.174	0.224	0.215	132	138
Lid	531	0.2	0.2	0.224	0.21	82	84
Waste	27,077	0.1	0.1	0.033	0.028	2,618	2,632
Silo (base and wall)	4,101	0.2	0.2	0.224	0.21	636	648
Wall buffer (100/0)	4,026	0.62	0.64	0.276	0.264	1,807	1,897
Bottom buffer (10/90)	1,011	0.168	0.174	0.224	0.215	132	138
All	46,861					8,594	8,723

Water uptake evaluation

Water uptake experiments, where the saturation process can be approximated as being uniaxial, have recently been carried out for GEKO/QI material samples from the wall buffer in the silo repository. This experimental data may be utilized as to evaluate the performance of the GEKO/QI model setup used in the simulations. When doing so, diffusivity, prescribed in an analytical solution of the one dimensional saturation process (Crank 1975), is calibrated against experimentally obtained water content profiles. The hydraulic representation of the GEKO/QI material in the numerical model can also be recast in terms of a corresponding diffusivity which can be compared to the calibrated analytical diffusivity. For more information concerning the analytical solution of the water uptake process and connection between diffusivity and the hydraulic representation in the numerical model see Åkesson (2013).

Figure 2-25 shows water content profiles for the water uptake experiment (symbols) and analytical solutions (lines) after 5 h, 1 week, 2 weeks, and 4 weeks. The solutions correspond to prescribed diffusivity values of $4 \cdot 10^{-10}$, $6 \cdot 10^{-10}$, and $8 \cdot 10^{-10}$ m^2/s as indicated in the legends.

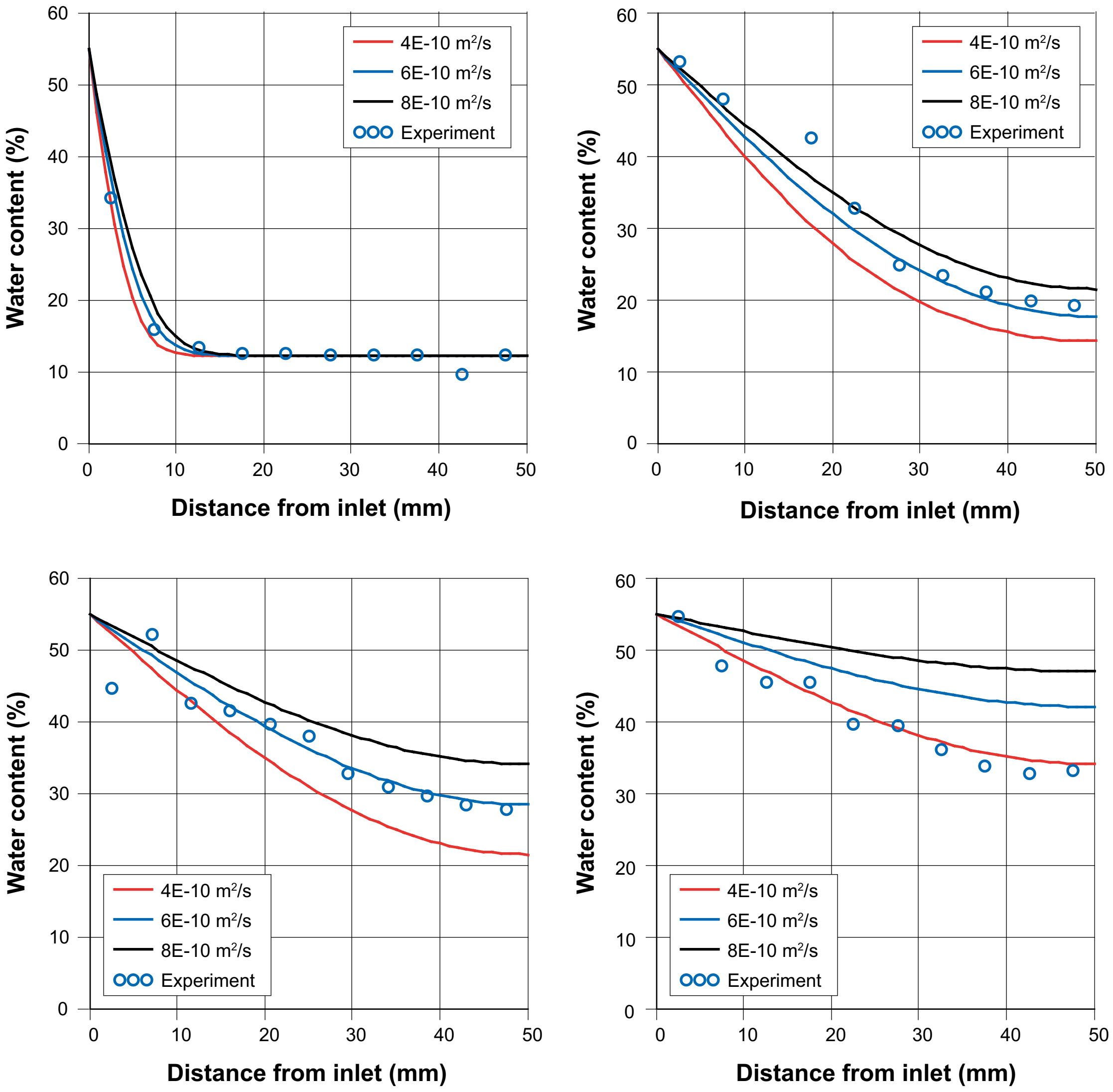

Figure 2-25. *Water uptake water content profiles after 5 h, 1 week, 2 weeks, and 4 weeks. Experimental data is indicated by symbols and analytical solutions, with the diffusivity indicated in the legend, by solid curves.*

The next step is to calculate diffusivity from the hydraulic representation used in the numerical model. The obtained expression of diffusivity, *D*, reads:

$$D(S_l) = \frac{kS_l^{\,B}}{n\mu}\frac{dp_l}{dS_l}(S_l), \tag{2-10}$$

where the last term is obtained from taking the inverse of the derivative of the retention curve

$$\frac{dp_l}{dS_l}(S_l) = \left(\frac{dS_l(p_l)}{dp_l}\right)^{-1}. \tag{2-11}$$

As indicated in (2-10), diffusivity is a function of water saturation. If the base case parameter setup is inserted in (2-10) the result shown to the left in Figure 2-26 is obtained. The fit between the base case setup curve and the results from calibrating the analytical solution is not good. The obtained diffusivity is much too high and also varies too much. The high diffusivity indicates that the base case setup will underestimate the saturation time of the GEKO/QI material.

Below, a discussion how to develop a setup which agrees better with the water uptake experiments and still not violate the findings of the direct comparisons is given.

It is assumed that viscosity should not be changed. Altering the porosity according to what Table 2-22 gives will not give a significant modification of the diffusivity. The data in Figure 2-22 shows that the permeability could be lowered. If taking this to the extreme it could be lowered by one magnitude to 10^{-18} m^2.

Even though fitting the retention curve more precisely against the data shown in Figure 2-24 the derivative of the retention curve will not change much. The derivative of the base case curve is actually in rather good agreement with derivatives estimated from the experimental data, i.e. if shifting the curve generated by the model to the right in the left (linear) diagram it could be positioned as to agree rather well with the experimental data.

Left to be altered is the relative permeability exponent *B*. In the base case model the setting *B* = 3 was based on findings for MX-80 material. For the GEKO/QI material it is therefore considered appropriate to calibrate *B* using the experimental data from the water uptake tests. Together with the setup suggested above an exponent about six seems to generate a diffusivity that agrees rather well with what the analytical study shows.

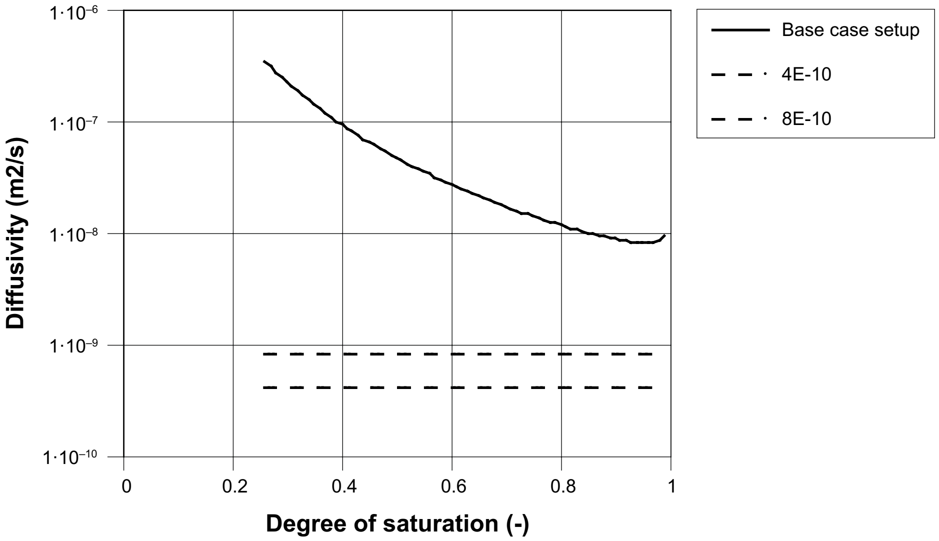

***Figure 2-26.** Diffusivity calculated from the base case setup. The horizontal hatched lines indicate the minimum and maximum values of diffusivity as obtained from evaluating the water uptake data by an analytical model.*

2.5 Summation and conclusions

Overall EBS saturation intervals for the investigated cases are compiled in Figure 2-27, where time = 0 at closure (year 2040). It is only for the base case where undrained host rock conditions have been simulated (indicated by the solid gray line). For all other cases the undrained saturation interval (indicated by hatched gray lines) should be taken with a pinch of salt since they were obtained from a simple estimation by scaling of the drained saturation interval according to what the base case gave. Thus, using this method introduces an uncertainty of the undrained results. The "real" saturation interval should be thought of as to be somewhere between the undrained and drained results.

The largest uncertainty comes from the host rock representation, both in terms of using undrained/drained and dry representations. The properties of the silo content as well as the top backfill also have significant effect on the overall saturation interval.

2.5.1 Base case, Uncertainty in host rock water pressure

Two host rock representations, denoted undrained and drained, were used in the base case. The reason for using two representations was to obtain bounds on the duration of the saturation process within the EBS when addressing the uncertainty of the host rock water pressure, i.e. the boundary conditions of the models. When using a rock permeability of 10^{-16} m^2 the produced inflows to an empty cavern agreed well with measured drainage outflow. This was taken as motivation for adopting this value in the base case setting.

The base case models produce quite different time intervals for which the EBS constituents saturate. The time until full saturation of the EBS is 13 yr and 53 yr for the undrained and drained model, respectively.

The overall characteristics of the EBS saturation process for the two host rock representations are however similar. This indicates that the methodology may be considered "stable" or "robust", i.e. the system representations are not over-sensible, and therefore suitable for performing investigations of the system by varying properties from the base case setting.

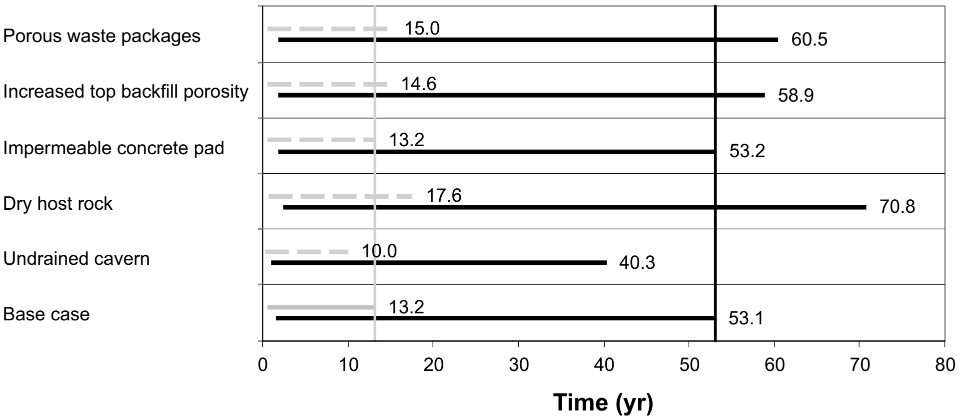

__Figure 2-27.__ Compilation of overall saturation intervals of the EBS in all cases. Results from assuming drained host rock conditions are given by the horizontal black lines. Results from assuming undrained host rock conditions are given by the horizontal gray lines. Solid and hatched lines indicate that the result is based on a calculation or estimation, respectively. Time = 0 at closure (year 2040). To facilitate comparison, the end points of the base case saturation intervals are indicated with the vertical gray and black lines for the undrained and drained model, respectively.

2.5.2 Undrained rock cavern

The performance of the installed cavern wall drainage is uncertain. That is, it is unknown how well the cavern wall drainage isolates the installed EBS components from rock water inflow. Therefore, the state at closure (2040) is uncertain. In the base case it was assumed that the cavern drainage performs perfectly since most data indicate that the drainage performs very well. To study the influence from a less then perfectly performing cavern drainage it is here assumed that it does not work at all, i.e. the rock cavern is undrained.

For this assumption the saturation of the silo repository was significantly decreased, about 13 years with the presently used setup. The saturation of the top backfill started earlier, ended sooner, and had less duration as compared to the base case model. For the present model setup a simple estimate of the total saturation time of the undrained cavern case can be obtained by translating the start of the drained cavern model's interval of the top backfill to the time of closure (2040).

2.5.3 Dry host rock representation

To study the sensitivity to variation in rock permeability an increased value (10^{-15} m^2) and a decreased value (10^{-17} m^2) were prescribed to a drained base case model with an empty rock cavern. The inflow to the empty cavern was found to relate to the rock permeability according to a log-log relation. Using this relation a permeability value of $7.55 \cdot 10^{-17}$ m^2 was obtained for an inflow of 500 ml/min, which equals the presently lowest measured total outflow of the drainage system.

When using this new permeability the time to full saturation of the EBS changed from 53 yr to 71 yr. Thus, the system is sensitive to changes in water transport properties in the host rock. The top backfill component had the major duration increase of the saturation interval.

2.5.4 Effect from an impermeable plastic sheet below the concrete pad

In the base case, an assumption was made that the plastic sheet, upon which the lower most concrete pad was casted, was perfectly permeable. When an impermeable plastic sheet representation was incorporated, the solution showed an increase in the water pressure below the cavern. The duration of the saturation interval for components close to the cavern bottom was increased for the new model, especially so for the bottom buffer. But the overall saturation interval, much governed by the top backfill saturation process, was not significantly changed.

2.5.5 Uncertainty in top backfill properties

When changing the porosity of the top backfill from 0.35 to 0.4, only the saturation interval of this constituent was significantly affected with an increase of 6 years. Since the top backfill, however, is the last constituent to be saturated in the process, the overall saturation time was also extended.

2.5.6 Uncertainty in silo content properties

In the base case setting, the waste packages themselves were assumed to have no porosity. If porosity was to be included, this would contribute to the homogenized representation of the silo content. When assuming a porosity of 0.15 for the waste packages, the porosity of the homogenized silo content increased from 0.1 in the base case to 0.2 in this new case.

The saturation intervals of all EBS-components were significantly affected, and the overall saturation duration was increased from 53 yr to 61 yr. The silo content properties has a governing role of the saturation process in the system.

2.5.7 Representation of GEKO/QI

No large deviations were found when carrying out direct comparisons between preliminary laboratory data and the models used in the simulations. The permeability used in the model was found to be a bit on the high side and the retention curve was somewhat low. Also, a "drier" initial state corresponding to a suction of 62 MPa, as compared to 46 MPa, was obtained when examining experimental data.

When evaluating the base case GEKO/QI setup against water uptake data, it was found to generate a saturation process which was too fast. If attempting to improve the base case model as to agree better with water uptake data, decreasing the permeability and increasing the relative permeability exponent were suggested. It is difficult to estimate how much the new initial state and altered material parameters will change the saturation process without carrying out additional simulations.

3 Self-healing of erosion damages caused in the bentonite in the Silo

3.1 Introduction

When the drainage of the rock in the silo is terminated and the silo closed the water pressure will increase until it either reaches the hydrostatic water pressure at the site which is equal to the depth of the silo (640–1,330 kPa) or penetrates the bentonite based barriers. Since the bentonite barrier in the silo has too low swelling pressure to be able to withstand the water pressure at the actual depth (0.64–1.33 MPa) there will be piping in the bentonite and subsequent erosion of bentonite. An alternative is that piping does not occur due to valve formation in the bentonite, which instead leads to formation of water pockets.

Both scenarios lead to local loss of bentonite and formation of an open channel or void. The question is then how well this void is sealed by the swelling bentonite. The possible erosion of the bentonite will continue until the silo is water filled or the pressure gradient has moved from the rock/bentonite interface to inside the bentonite barrier.

3.2 Eroded mass

The eroded mass at the inflow point depends on the total volume of eroding water that has passed the erosion channel. This has been investigated for other bentonite materials and follows a relation given by Equation (3-1):

$$m_s = \beta \times (m_w)^{\alpha} \tag{3-1}$$

where:

m_s= accumulated mass of eroded bentonite (g),

m_w= accumulated mass of eroding water (g),

β = 0.02–2.0 = parameter defined by the level of erosion at a certain accumulated water flow,

α = 0.65 = parameter defined by the inclination of the straight line relation.

Recent test results (Dueck et al. 2015) show that the silo bentonite (GEQI) stays within the limits set by β = 0.02–2.0, i.e. the same as found for other bentonites. The total amount of eroded material can thus be estimated if the total volume of eroding water is known. The volume of water required to fill up the silo can be estimated by assuming that 5% of the volume is open space available for early water filling. This gives a total of about 2,000 m^3. To get the proportion it corresponds to a water inflow of in average 0.76 l/min in five years. The worst case is if all this water comes in one inflow point, which of course is not realistic so we assume that at most 10% comes in one point which yields 200 m^3. Applying this volume to Equation (3-1) yields the total eroding mass:

m_s=(0.02 to 2.0)·$(2·10^8)^{0.65}$/1,000 = 5 to 500 kg.

The worst case is if the erosion creates an open half sphere around the inflow point. The volume and radius of a half sphere is:

$$V = 2\pi r^3/6, \tag{3-2}$$

$$r=(3V/\pi)^{1/3}. \tag{3-3}$$

Such a sphere yields for the dry density of the bentonite ρ_d = 1,000 kg/m^3 a radius of the half sphere r according to Equation (3-5) and Table 3-1:

$$V = m_s/\rho_d \ (m^3), \tag{3-4}$$

$$r=(3m_s/(\pi \cdot 1{,}000))^{1/3} \ (m). \tag{3-5}$$

Table 3-1. Radius of half sphere at different β-values.

β-value	m_s (kg)	*r* (m)
0.02	5	0.168
0.2	50	0.363
2.0	500	0.782

In the calculations the radius of the half-sphere is set to 0.5 m, the main reason being that all laboratory tests yielded $\beta < 0.2$.

3.3 Finite element calculation

A finite element calculation of the self-healing of a spherical void with the radius 0.5 m has been done. Large problems with convergences due to large deformations occurred and no good solution has been achieved. Several calculations have been performed and the one considered best will be shown.

The material models *Drucker-Prager Plasticity* and *Porous Elastic* has been used (see e.g. Åkesson et al. 2010) with data mainly from MX-80 at the low range of dry density (ρ_d< 1,000 kg/m^3 corresponding to a void ratio e>1.78) as shown in Figure 3-1. However, preliminary recent results from the tests on GEQI indicate that the swelling pressure at high void ratios is lower. If these results are confirmed by some planned new tests the model and subsequent simulation must be revised.

Porous Elastic is defined according to Equation (3-6):

$$\Delta e = \kappa \Delta lnp \tag{3-6}$$

The swelling pressure data in Figure 3-1 yields for $e > 1.5$ the following κ-value of *Porous Elastic*:

$\kappa = 1.37$.

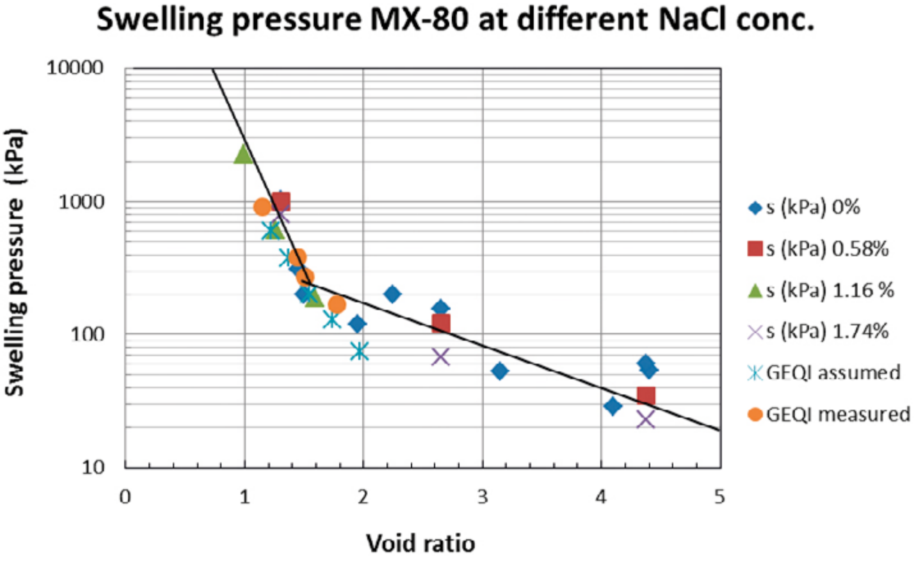

Figure 3-1. *Data from mainly MX-80 used to evaluate the material model. The black line is used for the model.*

Drucker Prager:

The friction angle in the *q*-*p* plane is 37°, which corresponds to a Mohr-Coulomb friction angle of $\phi = 20°$.

The initial conditions assumes that $\rho_d = 1{,}000$ kg/m^3 which yields:

$e_0 = 1.78$ (initial void ratio),

$p_0 = 200$ kPa (initial swelling pressure).

Contact elements have been used The own weight of the bentonite is at water saturation: ρm = 1,640 kg/m^3, which yields the density under water ρ'=640 kg/m3, which will be used for the modelling. Figure 3-2. shows the element mesh and the void ratio distribution after completed homogenisation.

As shown in Figure 3-2 the spherical void is not closed. However, this is judged to be caused by the rather coarse element mesh. The finer mesh the smaller void will be left. A fair judgement is that the void will be closed but also that the density and swelling pressure will be rather low in the centre of the former void (a few kPa). However, although the results cannot be used without reservations the results indicate that the bentonite is fairly unaffected close to the concrete silo with average void ratio of about 1.9 (right hand side in Figure 3-2), which means that the sealing function still works for half a meter of the bentonite filling.

A major reservation is that the material model mainly is based on MX-80 bentonite. When the laboratory results are ready the material model and the calculations may need to be revised as mentioned earlier.

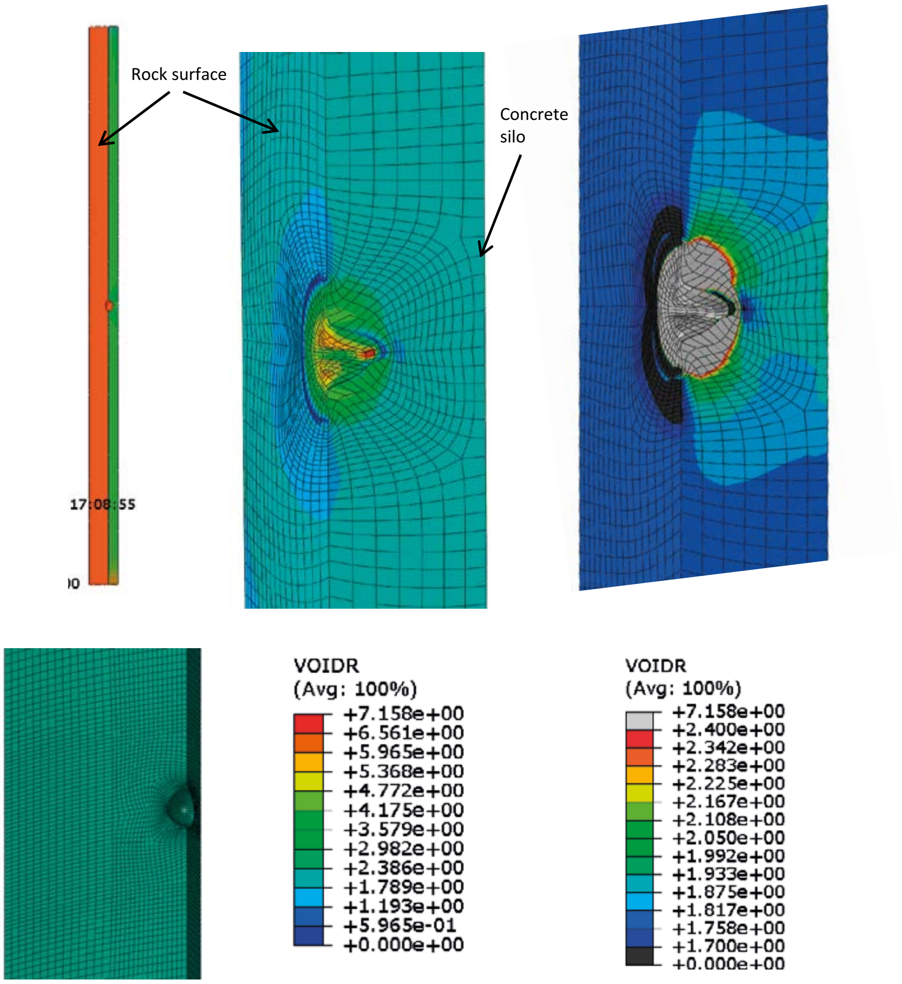

Figure 3-2. *Element mesh (upper left and detail at lower left) and final void ratio distribution after completed homogenisation (different scales). There is a symmetry plane on the right side of the void (green area). The orange or left surface is the rock contact, while the concrete contact is hidden.*

4 Ion exchange

4.1 Introduction

The bentonite emplaced around the silo in SFR is a sodium bentonite. However, over time, ion exchange will convert it into a calcium bentonite. An important question is what impact this will have on the properties of the bentonite barrier.

The dry density, ρ_d, of the bentonite emplaced around the silo in SFR is approximately 1,000 kg/m^3. At such low densities the swelling pressure of calcium bentonite is significantly lower than that of sodium bentonite. This may, for example, make the barrier less resilient to the effects of gravity, which may lead to settling in the vertical direction. Here, we approach the problem both analytically and numerically.

4.2 Schematic evolution and model setup

The bentonite barrier was installed into a cylindrical column (with an inner radius of 13.8 m and thickness of 0.8–1.2 m) around the silo directly after its construction. However, for the first 50 years of operation, the silo is kept open and the rock wall surrounding the silo is drained, preventing water from entering the bentonite. After closure, the drainage will be turned off, allowing for hydration of the clay.

As the bentonite hydrates it will start to swell, at full water saturation a swelling pressure of about 100 kPa can be expected (at this point the bentonite is still a sodium bentonite). With time, ion exchange in the clay between sodium and calcium will convert it into a calcium bentonite. In, for example, Karnland et al. (2006) it has been shown, that in the case of purified MX-80 bentonite, this type of ion exchange could lead to a reduction in swelling pressure of up to a factor of five at the relevant dry density (about 1,000 kg/m^3).

The evolution can thus schematically be divided into four different stages (as is illustrated in Figure 4-1):

1. **The initial settling of the dry bentonite:** The column around the silo is filled with bentonite to a height of about 51.5m above the silo floor. The bentonite settles into a steady state, where the wall-friction forces balances gravity. This steady-state solution can be found straight forwardly both analytically and numerically.
2. **The closing operation:** After 50 years of operation under open conditions the silo will be closed. Exactly how the top of the silo will be backfilled is not yet determined. In the modelling presented here, the following scheme has been assumed:
    a. The column around the silo is "topped-up" with bentonite to a height of 53 m from the silo floor.
    b. Above the bentonite a 10/90 mixture of bentonite and sand is installed to a total height of 54.5 m.
    c. Above the 10/90 mixture, sand is used to fill up the space to the top of the underground opening, which, at the radius of the wall-fill, corresponds to a height of approximately 63.5 m.
3. **Swelling of the bentonite**: As part of the closing operation the drainage will be "turned-off", allowing the bentonite to hydrate and swell. This process will lead to a new steady-state, which is reached after the bentonite has been fully saturated.
4. **Ion exchange:** Over time, ion exchange will convert the sodium bentonite into a calcium bentonite, thereby reducing the swelling pressure, which in turn could cause the bentonite to settle further.

To model the mechanical evolution one must thus take into account 1) the interaction between the bentonite barrier and the confining structures (the rock surface on the outside and the concrete silo wall on the inside), 2) the mechanical properties of dry bentonite (the initial settling), and 3) the swelling pressure of the bentonite (which will depend on the ion content).

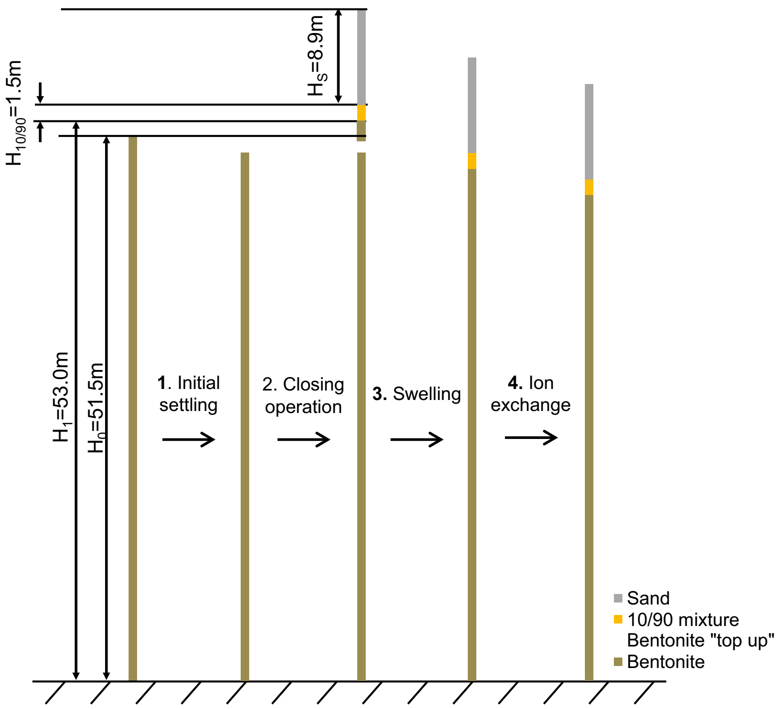

***Figure 4-1.** Schematic overview of the mechanical processes in the clay barrier around the SFR silo. The picture shows a vertical cross-section of the wall will at five different points in time, the main event occurring between the different times are indicated in the figure and further discussed in the text.*

To study the full evolution it is necessary to model all these processes directly, which has been done here using the FEM program Code_Bright. This is well suited at modelling mechanical processes in bentonite clay, and as of version 4 can accurately model the friction between the buffer and the surrounding rock. It does, however, not allow us to directly treat the effect of ion exchange, and as such a simplified approach has been adopted: stage 3 has been simulated using the swelling pressure curve of i) sodium bentonite and ii) calcium bentonite separately. The difference between the two solutions (in terms of final dry-density profiles, height of the bentonite column and swelling pressure) is assumed to quantify the change in these properties due to ion exchange.

However, it is also possible to solve for the final state using a simplified analytical model. This of course does not take into account how the final state is reached, but as is shown below it is still rather accurate at estimating the final state, assuming that this is correctly given by the FEM models. Using analytical models a sensitivity study could also be done, to evaluate the uncertainty in the results due to existing parameter uncertainties.

The analysis of stage 1 is given in section 4.3, while the solution to stage 2 and 3i/ii is given in section 4.4, together with a sensitivity study.

4.3 Initial settling of the dry bentonite barrier

The initial settling of the dry clay is here solved both analytically and numerically. The two solutions are first discussed separately, where after the results are compared with each other and with the data available from the SFR silo.

4.3.1 Analytical solution

The silo pressure can be derived by considering the force balance over a thin slice of the material, as illustrated in Figure 4-2.

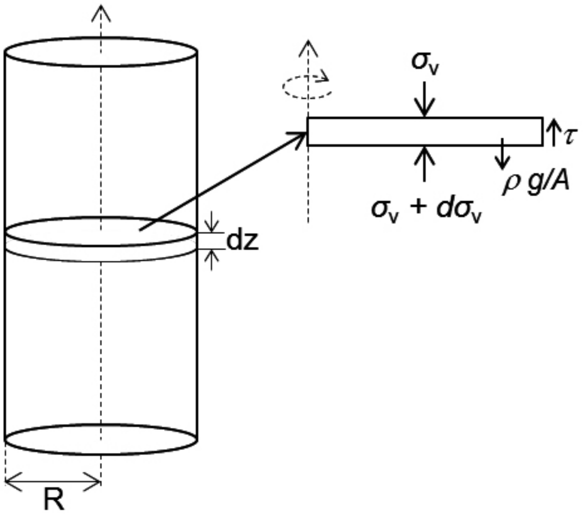

Figure 4-2. Geometry when deriving the silo pressure equation.

There, σ_v identifies the vertical stress and $d\sigma_v$ the incremental change in vertical stress over the thickness of the slice, dz. The wall-friction stress acting on the thin slice is identified by τ, and the weight per unit area of the material in the slice is ρgd$z$. Assuming steady state we can write down the balance of forces acting on the thin slice:

$$(\sigma_v + d\sigma_v)A + \tau U dz = \sigma_v A + \rho g A dz \qquad (4\text{-}1)$$

Here A is the horizontal cross-sectional are of the silo and $U = 2\pi R$. Equation (4-1) can be re-written as:

$$\frac{d\sigma_v}{dz} + \frac{U \cdot K \cdot \tan(\theta)}{A}\sigma_v = \rho g \qquad (4\text{-}2)$$

Here we have used that $\tau = \sigma_h \cdot \tan(\phi)$ and $\sigma_h = K\sigma_v$, where σ_h is the horizontal stress. Equation (4-2) can then be solved analytically as:

$$\sigma_v(z) = \frac{\rho g A}{U \cdot K \cdot \tan(\theta)}\left(1 - e^{-U \cdot K \cdot \tan(\theta) z / A}\right) \qquad (4\text{-}3)$$

Here it has been assumed that the vertical stress at the top of the silo equals zero (i.e. $\sigma_v(0) = 0$), which is appropriate for the initial state of operation in the silo.

Equation (4-3) can thus be directly applied to the clay barrier. The dry density of the bentonite is $\rho_d = 1{,}000$ kg m^{-3} and the water content is w = 0.17 (the initial value). Hence, the bulk density is $\rho = \rho_d \cdot (1+w) = 1{,}170$ kg m^{-3}.

Taking $\theta = 26°$, $A = \pi[R^2 - (R - dr)^2]$, where d$r$ is the width of the buffer column (R = 14.8m, dr = 1 m) and $K = 0.6$ we can solve equation (4-3). The result is plotted in Figure 4-4. A maximum effective vertical stress of 37 kPa is measured at the bottom of the clay column, while the horizontal effective stress has a maximum value of approximately 15 kPa.

Updated analytical analysis

The silo pressure theory applied to the buffer around the silo shown above can be somewhat improved by considering friction also against the inner concrete wall. A schematic of the geometry used when deriving the force balance in this analysis is shown in Figure 4-3. Again assuming steady state, the balance of forces on the slice gives:

$$(\sigma_v + d\sigma_v)A + (\tau_1 U_1 + \tau_2 U_2)dz = \sigma_v A + \rho g A dz \qquad (4\text{-}4)$$

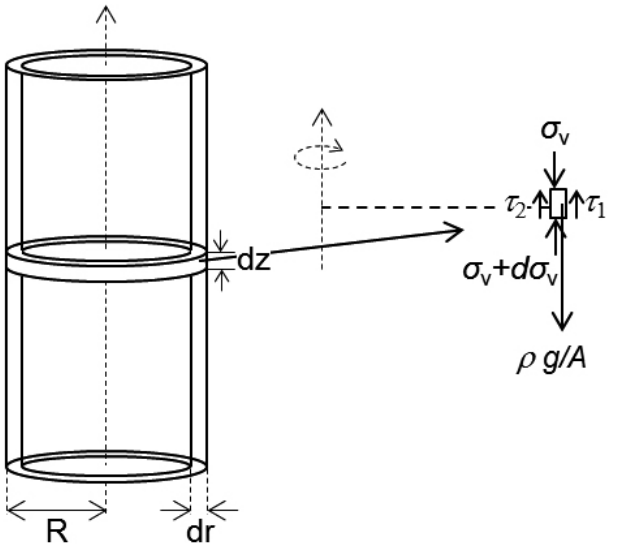

Figure 4-3. *The geometry used when deriving an analytic expression for the settlement of the clay column around the silo considering friction against both the outer rock wall and the inner silo wall.*

Here τ_1, is the friction stress against and U_1 the circumference of the inner wall, while τ_2 and U_2 identify the same properties on the outer rock wall.

Following the same approach as when solving equation 4-1, we can solve equation 4-4 to find:

$$\sigma_v(z) = \frac{\rho g A}{\omega \cdot K}\left(1 - e^{-\omega K z/A}\right) \qquad \omega = U_1 \tan\theta_1 + U_2 \tan\theta_2 \tag{4-5}$$

Assuming that $\theta_1 = \theta_2$ and taking the values of all other quantities as in when solving equation 4-3 in Figure 4-4, the solution of equation 4-5 is also shown in Figure 4-4. As can be seen, the inclusion of friction against the inner wall leads to a somewhat lower vertical pressure on the silo floor.

The next step is to model the settling numerically and compare that solution to that of equation 4-5, which is done in the next section.

4.3.2 Numerical solution using Code_Bright

To study the settling of the bentonite it is of course necessary to include wall friction. In the numerical tool at hand (Code_Bright) this was only recently made available, as part of release version 4 of the code. The wall friction is represented using contact elements and an elasto-visco-plastic parameterization.

Geometry, boundary conditions and material parameters

The geometry with mesh is shown in Figure 4-5. The vertical boundaries are handled using so-called contact elements, which allows for the inclusion of wall friction.

The bentonite is modelled as a linear elastic material during the dry settling phase; the parameters set are thus the bulk modulus, K_B, and Poisson's ratio, v. The friction elements are handled using elasto-viscoplastic theory, as discussed below.

The elastic parameters used to parameterize the bentonite are shown in Table 4-1.

Table 4-1. Linear elastic model for bentonite.

Material	K	v
Bentonite	1.90	0.2

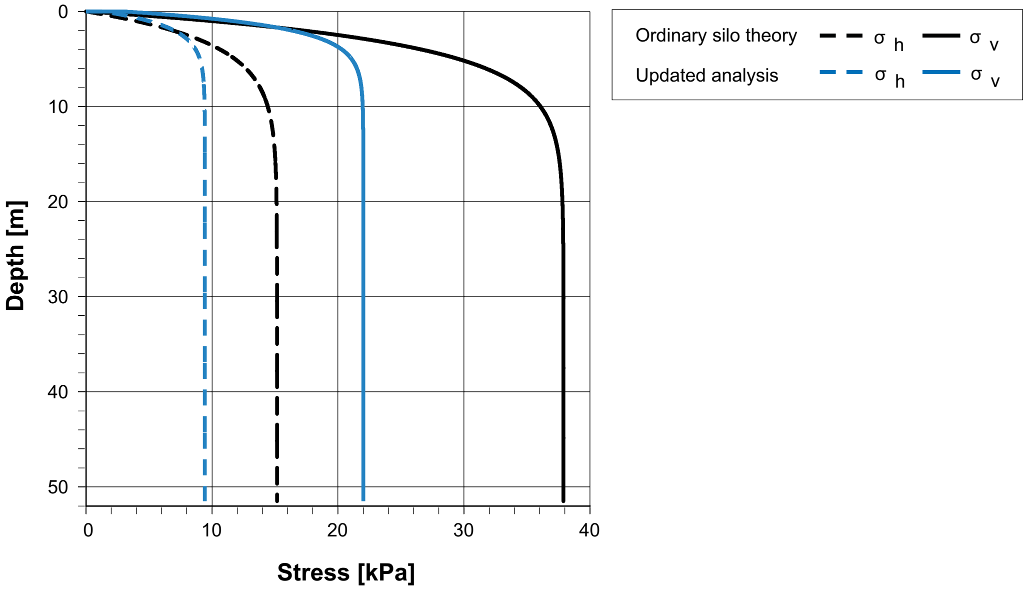

Figure 4-4. *Horizontal (dashed lines) and vertical (solid line) stress in the buffer around the silo as function of depth. Black lines identify the solution when considering friction against the outer wall only, while blue lines identify the solution when considering friction against both walls.*

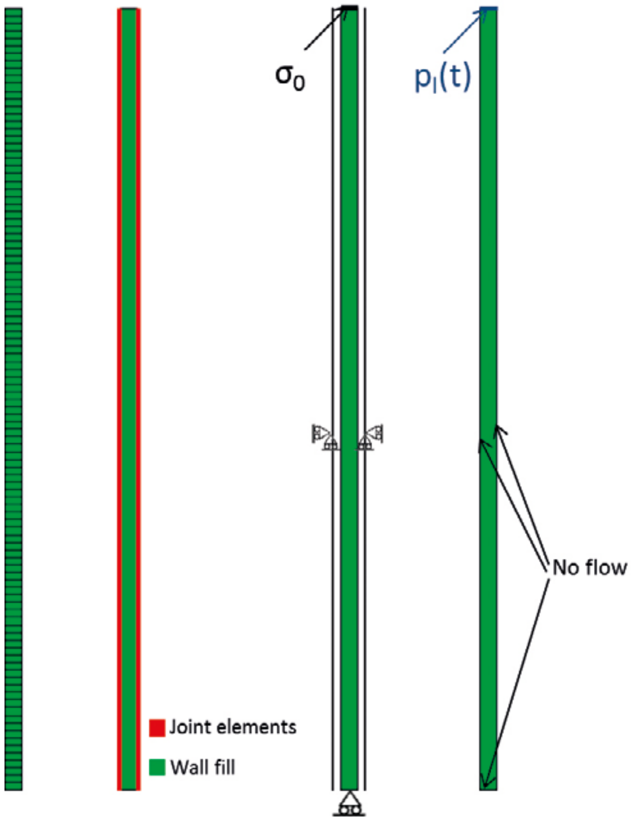

Figure 4-5. *Mesh (left), materials (middle left), mechanical boundary conditions (middle right) and hydraulic boundary conditions (right) used in the Code_Bright simulation of the SFR silo. In the mechanical B. C. used, the wall nodes are locked, while the behaviour of the inner nodes of the contact elements are treated using a friction model.*

The mechanical behaviour of the contact elements in Code_Bright are handled using an elasto-viscoplastic formulation. In the linear elastic regime the change in effective stress, due to displacement is:

$$\begin{bmatrix} d\sigma_n \\ d\tau \end{bmatrix} = \begin{bmatrix} K_n & 0 \\ 0 & K_s \end{bmatrix} \begin{bmatrix} du_n \\ du_\tau \end{bmatrix} \tag{4-6}$$

Here σ_n is the normal stress and τ the tangential stress in the contact surface, while u_n and u_τ is the normal and tangential displacement. The shear stiffness K_s, is assumed constant, while the normal stiffness, K_n, is a function of the aperture, a, of the interface and is defined as $K_n = m/(a-a_{min})$. Here a is the aperture, while a_{min} is the minimum aperture allowed (hence as a approaches a_{min}, K_n goes to infinity). At the start of the model, the initial aperture, a_0, is specified as a material parameter.

The elastic parameters used to describe the contact surface's behaviour are listed in Table 4-2 below.

Table 4-2. Elastic parameters used to describe the friction elements.

Material	K_s [MPa/m]	m [MPa]	a_0 [m]	a_{min} [m]
Friction element	100	90	10^{-4}	10^{-5}

The elastic region is bounded by the yield surface, which is defined as:

$$F = \tau^2 - (c' - \sigma'_n \tan\phi)^2 \tag{4-7}$$

Here, *c'* is the effective cohesion and ϕ the internal friction angle. In Code_Bright all these parameters can undergo softening, and both the effective cohesion and the internal friction angle can be a function of the suction, Ψ. However, in the modelling described here, these options were not utilized, and hence both the cohesion and friction angle were prescribed to be constant throughout the simulations. The viscoplastic strain rate is defined as:

$$\frac{d\varepsilon}{dt} = \Gamma \langle F^N \rangle \frac{\partial G}{\partial \sigma'} \tag{4-8}$$

Here ε is the viscoplastic strain, Γ the viscosity, and $\frac{\partial G}{\partial \sigma'}$ the viscoplastic potential. The latter is given by:

$$\frac{\partial G}{\partial \sigma'} = [0 \quad 2\tau]^T \tag{4-9}$$

In the modelling done to verify the analytical solutions the following choice of parameter were used:

Table 4-3. Parameters describing the viscoplastic behaviour of the friction elements.

Parameter	c_0 [MPa]	ϕ_0 [°]	Γ [s^{-1}]	N [-]
Value	0[1)]	30	10^6	2

[1)] For numerical purposes this parameter cannot have the value 0, and is instead set to 10^{-6} in the calculations.

Initial settling – Results

The results of the numerical verification are shown together with the updated analytical solution derived in the previous section in Figure 4-6. It should be noted that the analytical solution has here been evaluated for K = 1.9MPa, ν = 0.2 and ϕ = 30°, which is appropriate for the dry bentonite.

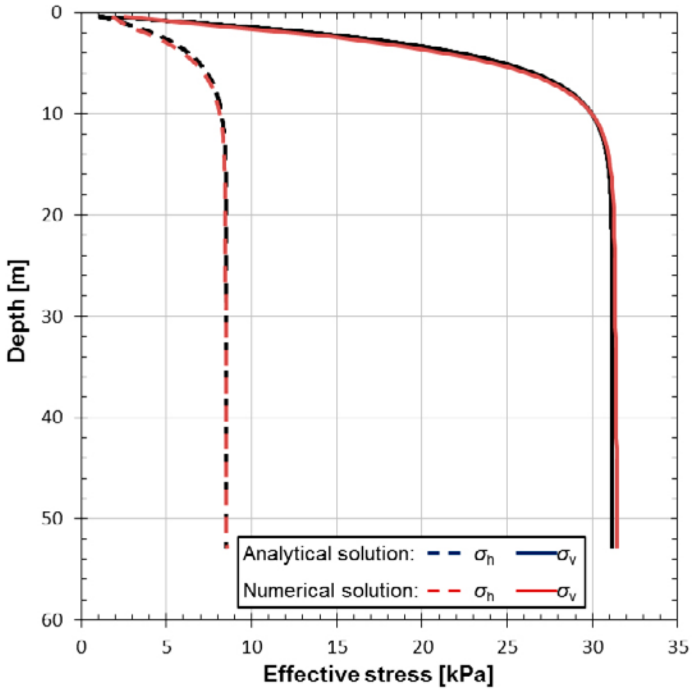

Figure 4-6. *Analytical and numerical solution to the settling of the bentonite barrier, in terms of horizontal and vertical stress, is shown.*

As can be seen the agreement is very good between the Code_Bright model and the analytical solution. This lends support to the wall-friction implementation used in the Code_Bright and allows for a study of the behaviour during the hydration phase and the subsequent fully saturated state.

Comparison with field data

A second test of the models is of course to compare the results with measurements in the field. The silo was instrumented before installation, and total pressure sensors were installed in the bottom, middle and top of the bentonite; an illustration of their placement in the silo is shown in Figure 4-7, and their positions in the silo are described in Table 4-4. The Glötzl sensors used must be externally pressurized when reading off the actual soil pressure; this is called the opening pressure of the sensor. The opening pressure is effectively the smallest pressure that the sensor can measure, if the actual pressure is lower, a value of zero is recorded.

Table 4-4. Sensor placement in the silo (Pusch 2003).

Sensor	Distance from silo bottom (m)	Type
G1, G2, G3	0	Vertical total pressure
G4, G5	2	Horizontal total pressure
G6, G7	25	Horizontal total pressure
G8, G9	45	Horizontal total pressure

In Table 4-5 the measured values during the last 10 years is summarized. As can be seen the total pressures have been largely unchanged in the last decade, with a total vertical pressure in the bottom of the buffer equal to about 100 kPa and a horizontal total pressure of about 60 kPa.

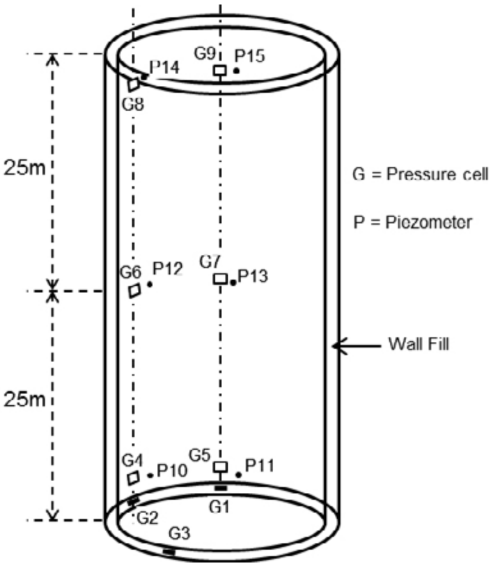

Figure 4-7. Overview of the placement of the pressure sensors in the silo, adopted from Pusch (2003).

As the bentonite in this phase is expected to be unsaturated, these total pressure values should be directly compared to the effective stresses seen in the numerical and analytical calculations shown below. As can be seen, there is a significant difference (factor of three higher) between the measured and predicted pressure values. A few possible explanations are:

- *The measured values are incorrect:* The pressure sensors used are rather coarse, and cannot be expected to give very accurate values in terms of pressure measurements at such low total pressures. Rather, they should be interpreted in terms of that the low pressures measured indicates that the bentonite is *not yet* fully saturated. At that point the total pressure is of course equal to the effective stress + the pore pressure, which at the bottom of the silo then should be about 200 kPa (see section 4.4.5).
- Some water uptake may have occurred in the bentonite: If the sensor readings do in fact represent the actual field conditions this could indicated that some water uptake has taken place in the bentonite. This would have two effects:
  1. An increase in the bulk density of the bentonite, and
  2. A decrease in the wall friction angle at the bentonite/rock interface.

Both of these effects would lead to increase in the total pressure in the buffer.

Nevertheless, it can be concluded that the low pressure values recorded strongly indicates that the bentonite is not fully water saturated at this point in time.

Table 4-5. The measured total pressures in the buffer around the silo from SKB (2014). The position of the sensors is shown in Table 4-4 and Figure 4-7.

Date	G1	G2	G3	G4	G5	G6	G7	G8	G9
Opening pressure	**0.130**	**0.130**	**0.140**	**0.130**	**0.140**	**0.330**	**0.340**	**0.080**	**0.050**
921020	0.070	0.070	0.065	0.055	0.030	0	0	0.045	0.015
000921	0.100	0	0.085	0.070	0.050	0	0	0.050	0.035
010918	0.095	0	0.085	0.065	0.050	0	0	0.050	0.030
021001	0.095	0	0.100	0.070	0.050	0	0	0.030	0.015
040917	0.095	0	0.090	0.065	0.055	0	0	0.050	0.040
060920	0.100	0	0.090	0.070	0.055	0	0	0.050	0.045
070919	0.095	0	0.090	0.070	0.055	0	0	0.050	0.050
080923	0.100	0	0.090	–	0.055	0	0	0.050	0.055
090928	0.105	0	0.095	–	0.055	0	0	0.045	0.050
100927	0.105	0	0.095	–	0	0	0	0.050	0.055

4.4 The saturation phase

The main goal of this study is to understand the effects of ion exchange in the bentonite on the properties of the clay barrier. Ion exchange will take place once the clay has become fully water saturated, at which point the mechanical evolution of the bentonite primarily depend on its swelling pressure and on the strength of the wall friction against the confining walls.

To analyse the effects of ion exchange we must thus analyse the state of bentonite barrier after it has been fully saturated. The saturation process will lead to two major changes in the properties of the bentonite:

1) The bentonite will swell due to water uptake. Since it is situated within a confined volume this will lead to the development of a swelling pressure, which will alter the total pressures in the silo.
2) As the bentonite hydrates and swells the wall-friction angle will decrease. Laboratory results on MX-80 bentonite suggest that it will fall from approximately 30° to 10° at the relevant density.

In total this could lead to significant changes in the clay barrier. An analytical model has been developed to study the state of the clay barrier after full water saturation. This was verified by numerical FEM models analysed using the FEM program Code_Bright. The analytical solution scheme allows us to do a sensitivity study on how the effects of ion exchange varies due to the uncertainties in some key parameters (see section 4.4.7).

4.4.1 Swelling pressure before and after ion exchange

An important aspect of the modelling presented here is of course the behaviour of the bentonite after ion exchange has converted it into a sodium bentonite. The most important change in the properties of the clay due to ion exchange for the problem at hand is the change in swelling pressure.

In Karnland et al. (2006), the swelling pressure of pure sodium and pure calcium bentonite as function of dry density, ρ_d, was compared. The clay buffer in the silo initially has a dry density close to 1,000 kg/m^3, and since no large deviations from this dry density is expected we need only to consider the variation in swelling pressure in the region around $\rho_d = 1{,}000$ kg/m^3. The swelling curve for these two materials was evaluated using distilled water, the results is shown in the left panel of Figure 4-8, where the swelling pressure is plotted as a function of the dry density of the clay. As can be seen, the difference is significant: at the nominal dry density of 1,000 kg/m^3, the swelling pressure of the pure calcium bentonite is only 20% of the pure sodium bentonite.

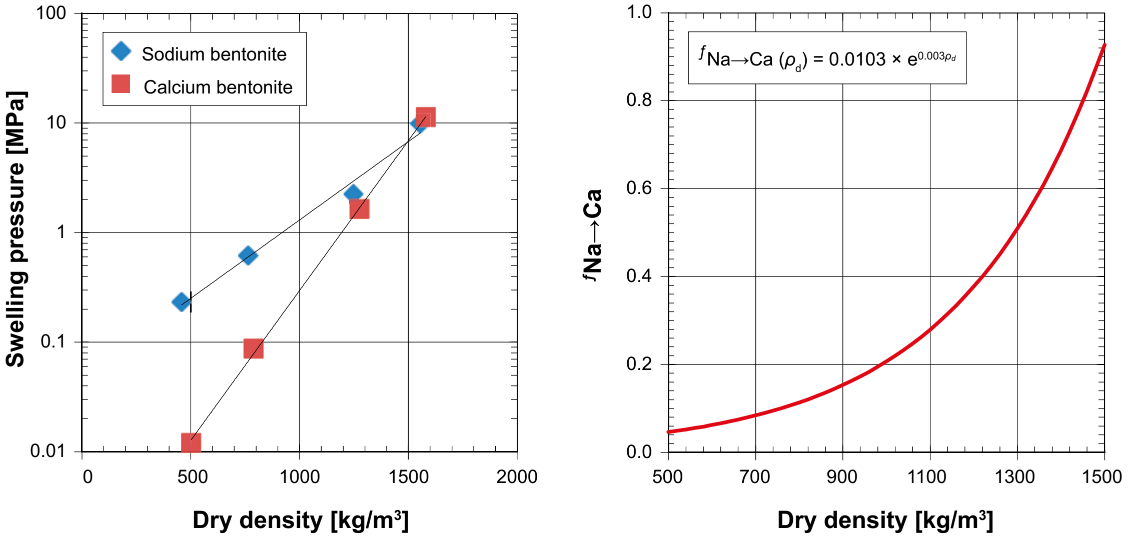

Figure 4-8. *Comparison of the swelling pressure of MX-80 bentonite (left panel) which has been purified into a sodium (blue squares) and calcium (red squares) bentonite respectively. A best fit to the ratio in swelling pressure between the two samples is plotted in the right panel.*

The swelling pressure of the purified samples is much higher than for the bentonite used as buffer material, and thus cannot be directly used when modelling the behaviour of the bentonite buffer around the silo. The swelling pressure as function of dry density has, however, been evaluated for MX-80, here we will use the relation from Åkesson et al. (2010):

$$\log(P_\mathrm{S}) = -3.94 \times 10^{-7} \rho_\mathrm{d}^2 + 4.117 \times 10^{-3} \rho_\mathrm{d} - 1.741 \qquad (4\text{-}10)$$

Using this parameterization for the sodium-dominated clay, the swelling pressure of the calcium-dominated clay can be obtained by multiplying equation 4-10 by the ratio in swelling pressure between the pure calcium and sodium clays (right panel of Figure 4-8):

$$P_\mathrm{S,Ca} = 0.0103 \cdot e^{0.003 \cdot \rho_\mathrm{d}} \cdot 10^{-3.94\times10^{-7}\rho_\mathrm{d}^2 + 4.117\times10^{-3}\rho_\mathrm{d} - 1.741} \qquad (4\text{-}11)$$

4.4.2 Wall-friction angle

The behaviour of the clay barrier is to a large degree determined by its interaction with confining walls. In the models this behaviour is described as wall friction, where the clay begins to slip once the vertical stress is larger than the friction stress. The friction stress, σ_f, is a function of the normal stress which the clay excerpts on the wall, σ_n, as:

$$\sigma_\mathrm{f} = \sigma_\mathrm{n} \cdot tan\varphi \qquad (4\text{-}12)$$

Here we have assumed zero cohesion. The value of the wall-friction angle has not been directly determined using laboratory experiments. However, using preliminary data from an evaluation of the shear strength of the sodium bentonite used around the silo, as function of its dry density, the strength of the wall-friction can be estimated. To do this, we need to know the yield strength of the clay as function of its swelling pressure, which we can obtain using the swelling-pressure relation in equation 4-10. In Figure 4-9 the swelling pressure, p', is plotted against the yield stress, q, in the relevant stress range. As can be seen, the relation between q and p′ is close to one (1) at a dry density of $\rho_\mathrm{d} = 1{,}000$ kg/m^3.

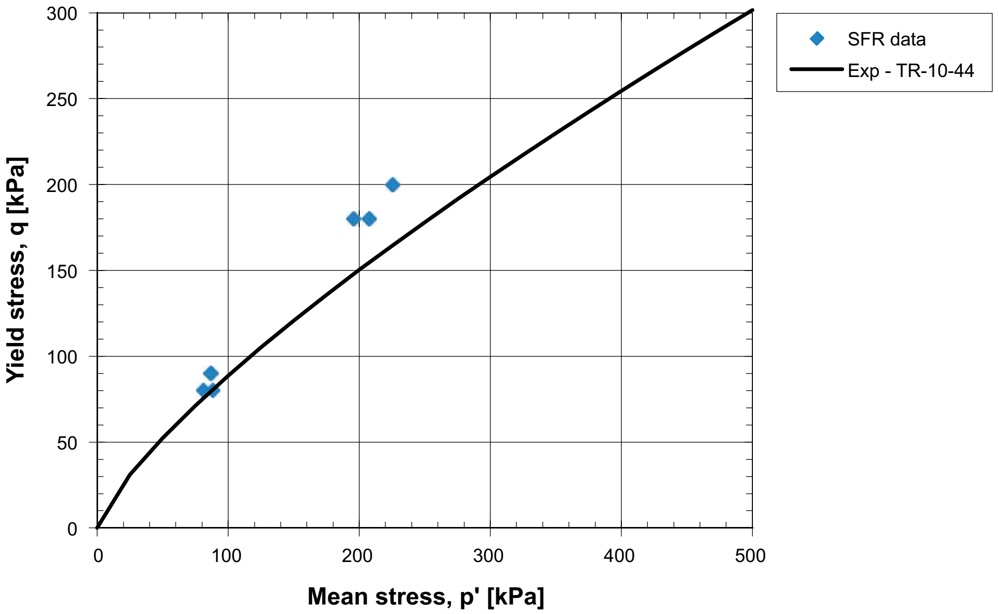

Figure 4-9. *Yield stress at failure, q, (vertical axis) as function of mean stress, p', (horizontal axis). The data points are from preliminary results of laboratory tests on the SFR bentonite, and were obtained in June 2014. The black solid line corresponds to equation 10-11 in Åkesson et al. (2010).*

The failure point in the p'-q plane corresponds to the internal friction angle, θ, as:

$$sin\theta = \frac{3q}{q + 6p'} \qquad (4\text{-}13)$$

As $q/p' \approx 1$ we then have that $\theta \approx 25°$ for the water-saturated sodium clay. The yield stress of the clay is related to the yield stress between the clay and rock/cement wall as (Börgesson et al. 1995):

$$\tau_{clay} = 0.6\tau_{\text{cement/rock-clay}} \qquad (4\text{-}14)$$

Hence, a reasonable value of the wall-friction angle is $\varphi = 15°$ for the sodium-dominated water-saturated clay. As for the calcium dominated clay, no experimental data is available. However, it is reasonable to assume also here $q/p' \geq 1$, hence the friction angle is unlikely to be significantly lower than $\varphi = 15°$.

In the results described below $\varphi = 15°$ has been used as the base-case value for the wall-friction angle, while $\varphi = 10°$ has been used as a worst-case scenario (a lower value of φ leads to more settling in the bentonite barrier).

4.4.3 Analytical analysis – Description

The goal of the analytical model is to describe the final state of the clay barrier after swelling has occurred. No attempt was made to capture the evolution during the swelling, nor the transition phase during ion conversion in the clay.

The main assumptions of the model is that 1) at the final state the clay will at all points have a mean stress equal to the swelling pressure (as function of void ratio), 2) the relation between horizontal and vertical stress is constant, and 3) no upward movement is allowed (i.e. the top-fill in the silo is incompressible in the stress regime analysed.

The clay is assumed to be fully water saturated; hence the buoyancy of the water must be taken into account. The balance of forces on a small segment of clay then gives:

$$\frac{d\sigma_\text{v}}{dz} + \frac{U_\text{i} \cdot \tan(\theta_i) + U_o \cdot \tan(\theta_o)}{A} f \cdot \sigma_\text{v} = (\rho(e) - \rho_\text{l})g \qquad (4\text{-}15)$$

Here U_i and U_o are the inner and outer circumferences of the clay barrier; θ_i and θ_o are the inner and outer wall-friction angles; A is the vertical cross-sectional area of the bentonite column; f the relation between the vertical and horizontal forces, $\rho(e)$ the bulk density of the clay at void ratio, e; and finally ρ_l and g represent the liquid density and acceleration of gravity.

Equation 4-15 is solved in MathCad, with the added criterion that the dry density is not allowed to be lower than the initial dry density (hence no expansion of the clay). The boundary conditions assumed are that at the top of the bentonite column, a vertical effective stress equal to 107 kPa is prescribed, corresponding to the assumed weight of the top filling at full water saturation.

4.4.4 Numerical analysis – Setup

In principle, a numerical model of the evolution in the clay barrier should treat the four main evolutionary states in subsequent order, as described in Figure 4-1. However, this was not feasible using Code_Bright. Thus, a simplified scheme was developed, in which the bentonite was first allowed to settle into its "initial state", where it was treated as a linear elastic material; where after the hydration phase was modelled for two different swelling pressure curves (sodium and calcium) separately.

To study the swelling phase of the bentonite and the effects of ion exchange, two sets of models were done. In both sets of models the bentonite was first allowed to settle into an equilibrium state during dry conditions with close to zero vertical stress on the top of the column. Thereafter the effect of the top fill was introduced as a vertical stress boundary condition, and the bentonite was allowed to hydrate during six years. This time corresponds roughly to the time until saturation as found in the "undrained base case model" of the hydration phase, as described in chapter 2. In the first set of models, the clay was modelled as sodium dominated MX-80 clay, while in the second set it was modelled as calcium converted MX-80 clay. In both sets of models the wall friction angle was set to $\phi = 30°$ during the initial settling phase, and varied between $\phi = 10°$ and $\phi = 15°$ after the clay had been fully saturated.

Geometry and prescribed conditions

The numerical model builds on the one presented in section 4.3.2. Hence, it is a two-dimensional axisymmetric model, representing the column of bentonite clay around the silo. The geometry is shown in Figure 4-10. The mesh employed consisted of quadrilateral elements, with 53 elements in the vertical direction and 6 in the horizontal direction. One of the models presented below (Ca bentonite, $\varphi = 10°$) was modelled using 100 elements in the vertical direction, with no significant differences in the results. Hence, the solutions presented here can be assumed to be grid independent.

The initial porosity of the clay was set to 0.64, corresponding to an initial dry density of 1,000 kg/m^3 (assuming a solid density of 2,780 kg/m^3, corresponding to the value normally used for MX-80 bentonite).

In all materials an initial isotropic effective stress of 5 kPa was prescribed.

The boundary conditions applied are shown in Figure 4-10. With respect to hydraulic processes; no-flow is assumed on all boundaries aside from the top, where the liquid pressure, p_l, is prescribed. During the first 55 years, $p_l = -45.9$ MPa, where after it is increased linearly to $p_l = 0.1$ MPa during the subsequent 6 years, and then kept constant at this value for the remaining 89 years of the model (the total duration of the models was set to 150 years, at which point all models were judged to have reached steady state by evaluating the time-dependence of the state variables. It is worth noting that this time-scale is set by the parameter-choices relating to the viscoplastic-flow behaviour of the wall-friction elements, and hence cannot be used to judge the time until final state in the field.

In terms of mechanical processes, no vertical movement is allowed on the lower horizontal boundary; the vertical boundaries are completely locked (vertical movement is, however, allowed through wall friction). On the top horizontal boundary, the effective vertical stress, σ_v', is prescribed: until t = 55 years it is set to $\sigma_v' = -1$ kPa, where after it is linearly increased to $\sigma_v' = -107$ kPa during the hydration phase and kept at this value during the remainder of the model. The value of $\sigma_v' = -107$ kPa corresponds to the effective stress of the top filling after it has been fully water saturated.

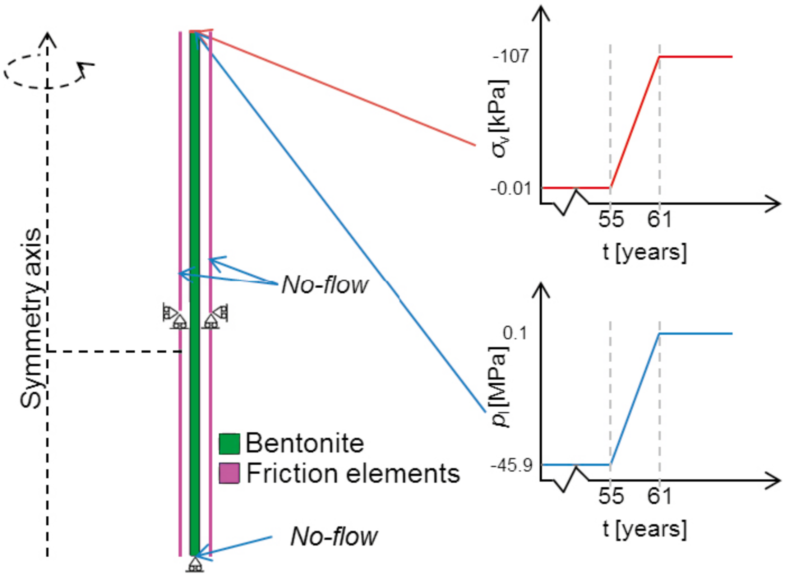

__Figure 4-10.__ The geometry and boundary conditions used in the numerical model of the swelling of the bentonite material. The no-flow boundary conditions concerns to the hydraulic problem.

Material parameters

In terms of mechanical parameterization, the bentonite clay was modelled as a BBM material, and the friction elements were modelled using the contact element parameterization available in Code_Bright v4.1.

In BBM, the elastic bulk modulus (which sets the mechanical response in the bentonite during the initial dry settling phase) is defined as:

$$K = \max\left[K_{\mathrm{min}}, \frac{(1+e)p'}{\kappa_{\mathrm{i}}}\right] \tag{4-16}$$

The elastic parameters used to parameterize the bentonite in the base case models are shown in Table 4-6. The value of Poisson's ratio is set to 0.4, in order to avoid unphysical shear stresses developing in the clay. This could be avoided by including a correctly evaluated yield curve for the bentonite in question, however, this was not numerically feasible. As such, the plastic parameters, were chosen so as to avoid plasticisation in the bentonite.

Table 4-6. BBM model – Elastic parameter values.

Material	κ_{i0} [MPa]	κ_{s0} [MPa]	K_{min} [MPa]	ν [-]	α_{sp} [-]	α_i [-]	p_{ref} [MPa]
Bentonite	0.35/0.23[1)]	0.3	1.9/0.001[2)]	0.4	*	–0.021	0.01/0.001[3)]

[1)] The values 0.35 and 0.23 represent sodium and calcium bentonite respectively.

[2)] The value of 1.9 MPa is used during the dry settling phase, the value 0.001 MPa is used in the subsequent evolution.

[3)] The values 0.01 and 0.001 represent sodium and calcium bentonite respectively.

The friction elements are handled using an elasto-viscoplastic parameterisation, as elaborated on in section 4.3.2. The parameters used are shown inTable 4-7 and Table 4-8 below.

Table 4-7. Parameters describing the elastic behaviour of the wall-friction elements.

Material	K_s [MPa/m]	m [MPa]	a_0 [m]	a_{min} [m]
Friction element	100	90	10^{-4}	10^{-5}

Table 4-8. Parameters describing the viscoplastic behaviour of the friction elements.

Parameter	c_0 [MPa]	ϕ_0 [°]	Γ [s^{-1}]	N [-]
Value	0[1)]	30/10/15[2)]	10^3	2

[1)] For numerical purposes these parameters cannot have the value 0, but are instead set to 10^{-6} in the calculations.

[2)] The value 30° was used until the bentonite was fully water saturated, where after the value 10°/15° was used.

4.4.5 Results – Numerical models

The results from the two sets of base-case models can be illustrated in many ways. The perhaps most important results for the safety analysis of the SFR silo are the depth profiles of horizontal, vertical and total effective stress and porosity. These results are shown in Figure 4-11 and Figure 4-12 for the two sets of base cases, where black lines identify results for sodium bentonite and blue lines identify calcium bentonite.

Starting out with the most realistic case, where the wall-friction strength is represented using a friction angle of $\varphi = 15°$ (Figure 4-11) it can be seen in the left panel that both the horizontal and vertical effective stress (dashed and dotted lines) after swelling is rather different between the sodium and calcium bentonites, with significantly lower effective stress in the Calcium case.

Hence, the mean effective stress (solid lines) is much lower in the Calcium case. This is to be expected as the calcium bentonite has a much lower swelling pressure at the given void ratio.

Even though we have not modelled the actual transition between the two, the results clearly shows that ion exchange in the bentonite will lead to a significant reduction in mean stress in the buffer. This in turn will lead to some differences in the porosity/density profile, as is indicated in the right panel of Figure 4-11; while the sodium bentonites' density/porosity profile is hardly affected by the swelling of the bentonite (before the onset of swelling the bentonite's dry density is very close to 1,000 kg/m^3, and hence a porosity of 0.64, at all depths in the silo), the top part of the clay barrier is compacted when calcium bentonite is considered. Furthermore, while the sodium bentonite undergoes zero settling, the top of the bentonite column moves downward by about three decimetres when using the calcium bentonite swelling pressure curve.

Figure 4-12 shows the same variables at steady-state as in Figure 4-11, only here a value of $\varphi = 10°$ has been used. As discussed in section 4.4.2 above, this can be considered a worst case scenario in terms of the strength of the wall friction, given the laboratory data available for the bentonite in question. A slightly different final state compared to the one with $\varphi = 15°$ is seen, with a more significant change in the density profiles of the bentonite, in particular for the calcium-bentonite case, where the increase in density at large depth in the silo gives rise to a slightly higher swelling pressure there.

As for the sodium-dominated bentonite, the evolution is still rather uneventful with almost no change in the density profile due to the swelling. In the calcium-dominated clay, however, more significant settling is seen, with the top part of the bentonite moving downwards by about 8 decimetres.

4.4.6 Results – Comparison of numerical and analytical results

In Figure 4-13 the results from the numerical models presented in the previous section has been compared to the final state seen in the analytical solution to the problem as described in 4.4.3. Solid lines identify the analytical solution while dashed lines identify the numerical solution. In the left panel the mean stress profiles from the four sets of models are shown, while in the right panel the porosity profiles are displayed.

As can be seen, the analytical models can predict the final state in the numerical models rather well, although some discrepancies are seen at large depth in the silo for the lower value of the wall-friction angle ($\varphi = 10°$) for the calcium dominated clay, and some small deviations at the very top of the bentonite column when considering the sodium dominated clay.

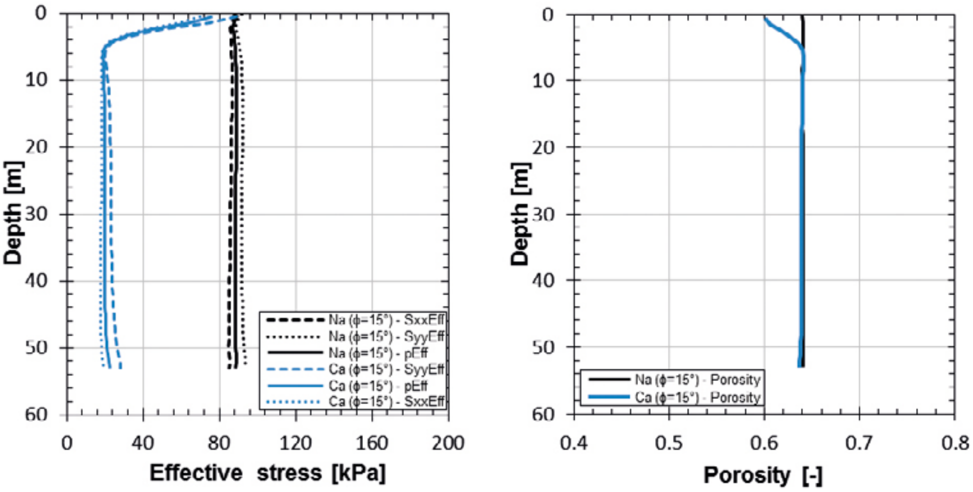

***Figure 4-11.** In left panel the horizontal (long-dashed lines) and vertical (dotted lines) effective stress is shown, together with the mean effective stress (solid lines), while in the right panel the porosity is displayed. All data represent the steady-state situation after swelling of the bentonite. Black lines identify sodium bentonite and blue lines calcium bentonite. Here, a friction angle of φ = 15° has been used to represent the wall friction after the bentonite has reached full saturation.*

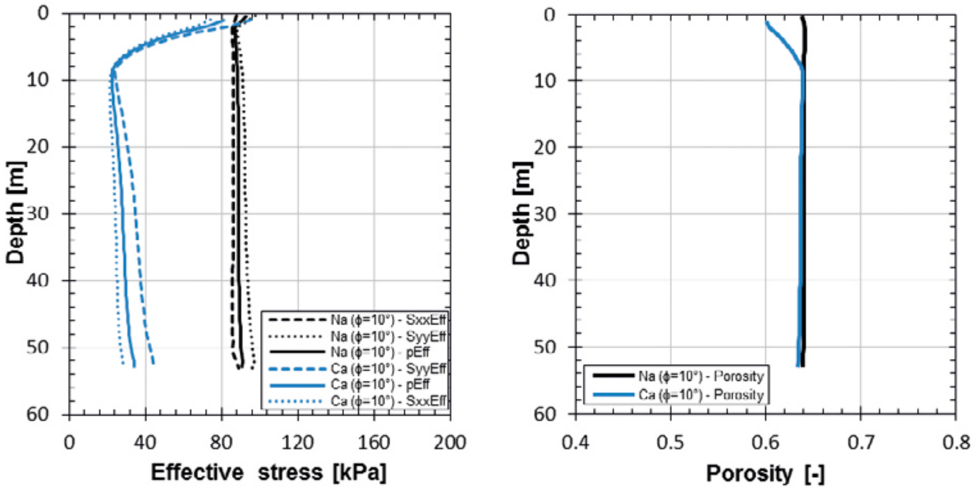

***Figure 4-12.** In left panel the horizontal (long-dashed lines) and vertical (dotted lines) effective stress is shown, together with the mean effective stress (solid lines), while in the right panel the porosity is displayed. All data represent the steady-state situation after swelling of the bentonite. Black lines identify sodium bentonite and blue lines calcium bentonite. Here, a friction angle of φ = 10° has been used to represent the wall friction after the bentonite has reached full saturation.*

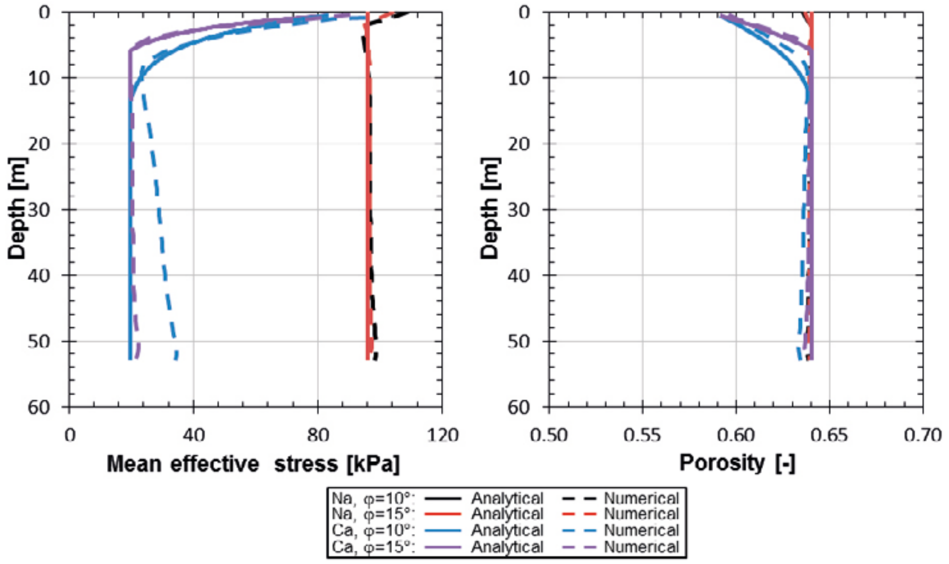

***Figure 4-13.** Comparison of analytical and numerical results when modelling the set of base case models described above.*

In the four cases modelled, the analytical analysis predicts the downward motion of the top part of the clay barrier very well, with discrepancies of only a few per cent. Hence, it can be used to study how much the top part of the clay barrier can be expected to move for different parameter values. This can be highly valuable to know, as any significant settling of the top surface of the clay barrier would lead to the unwanted formation of a gap between the top filling above the silo and the ceiling.

4.4.7 Results – Sensitivity study

The close agreement between the numerical and analytical solutions allows for a more detailed study of the settling of the top surface of the clay barrier.

Wall-friction angle

The strength of the wall friction has not been directly determined using laboratory tests, and thus some uncertainty exists regarding which value of the wall-friction angle, φ, to choose. A conservative estimate, given the measured shear strength of the bentonite (see 4.4.2), however, is that it lies in the interval 10° to 20°. Furthermore, there is some uncertainty regarding the dry density, ρ_d, in the buffer; it has been estimated to lie in the interval 980 kg/m^3 to 1,020 kg/m^3 (Pusch 2003). Using the analytical solution method we can calculated the settling of the top surface of the clay barrier when varying these two parameters; the results of such a study is shown in Figure 4-14. As can be seen the downwards movement is generally small; for realistic values of ρ_d and φ it is on the order of a few decimetres.

Swelling pressure of the calcium dominated clay

Preliminary laboratory data suggests that at a dry density of ρ_d = 1,000 kg/m^3, the swelling pressure of the bentonite emplaced around the SFR silo might be about a factor of two higher than what is given by equation 4-11 (or hence around 40 kPa). Hence, it is appropriate to study what effect this would have on the final result. In Figure 4-15 the downward motion of the top of the clay barrier is again plotted, but here the swelling pressure of the clay has been multiplied by a factor of two. As can be seen, this leads to smaller movements, at the nominal base case with a dry density of 1,000 kg/m^3 and a wall-friction angle of 15°, the settling is now only a few cm.

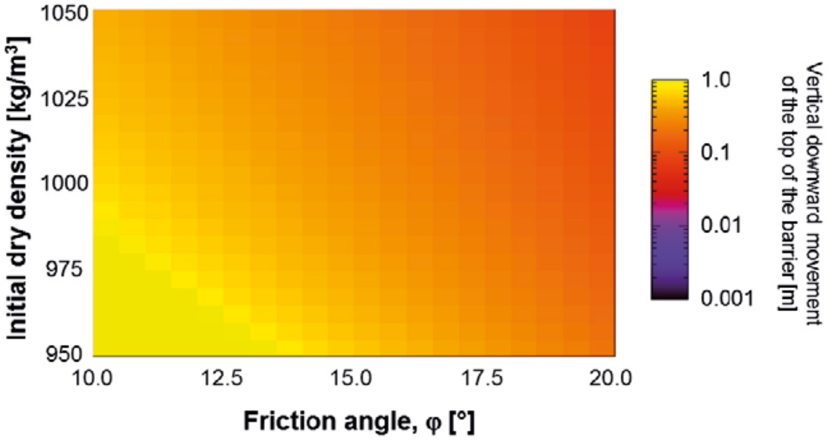

Figure 4-14. *Vertical downward motion of the top surface of the clay barrier as function of wall-friction angle at full saturation (horizontal axis) and initial dry density of the clay barrier (vertical axis). The swelling pressure of the clay is here assumed to equal that of the calcium-dominated clay (e.g. equation 4-11).*

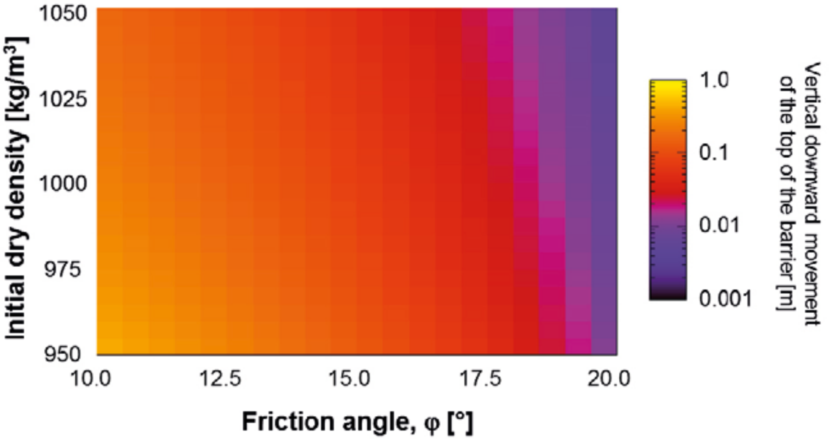

Figure 4-15. *Vertical downward motion of the top surface of the clay barrier as function of wall-friction angle at full saturation (horizontal axis) and initial dry density of the clay barrier (vertical axis). The swelling pressure of the clay is here assumed to equal that of the calcium-dominated clay (equation 4-11) multiplied by a factor of two.*

4.5 Discussion

The analysis of the effects of ion exchange in the clay buffer presented here was numerically rather difficult. Furthermore, direct evaluation of the mechanical properties of the bentonite clay used in the SFR silo was not available at the time when the modelling was done. The implications this has on the results an conclusions drawn in this chapter is discussed in some detail in section 4.5.1 and 4.5.2 below.

4.5.1 Issues with the numerical solution scheme

In order to accurately model the processes in the buffer material around the SFR silo friction against the rock and silo surfaces had to be included. In the numerical modelling tool used here (Code_Bright), the ability to model wall friction had just been implemented when this project was done. Unfortunately this meant that the solution scheme was not well optimized, which in turn led to severe numerical problems (mainly in terms of poor convergence) when solving the models. Given the time constraints of the project this made it impossible to perform a sensitivity analysis using FEM simulations. Instead an analytical solution to the problem was developed and used to perform the sensitivity analyses. While it would have been preferential to use FEM simulations to cover the entire parameter space in the sensitivity analyses, we believe that the analytical solution is accurate enough to draw firm conclusions, as it is very successful in reproducing the final state in the FEM models where these two can be compared.

4.5.2 Properties of the material used in the SFR silo

When the models presented in this report were constructed, very little data on the mechanical properties of the bentonite barrier emplaced around the SFR silo was available. The models presented were thus done with the assumption that the sodium bentonite around the silo is similar to a MX-80 sodium bentonite, whose mechanical behaviour has been studied extensively (e.g. Åkesson et al. 2010). Furthermore it was assumed that the change in mechanical properties due to ion exchange was similar to the difference in mechanical behaviour between purified sodium and calcium MX-80 bentonite.

At the time of writing this report, some preliminary data on the swelling pressure of the bentonite around the SFR silo became available. The measurements concerning the sodium dominated bentonite are shown in Figure 4-16, together with the swelling pressure relation described by equation 4-10 (which was used to describe the swelling pressure of the sodium-bentonite in the models). As can be seen, the swelling-pressure results show excellent agreement with equation 4-10. This gives confidence in using this parameterisation when modelling the sodium-dominated clay.

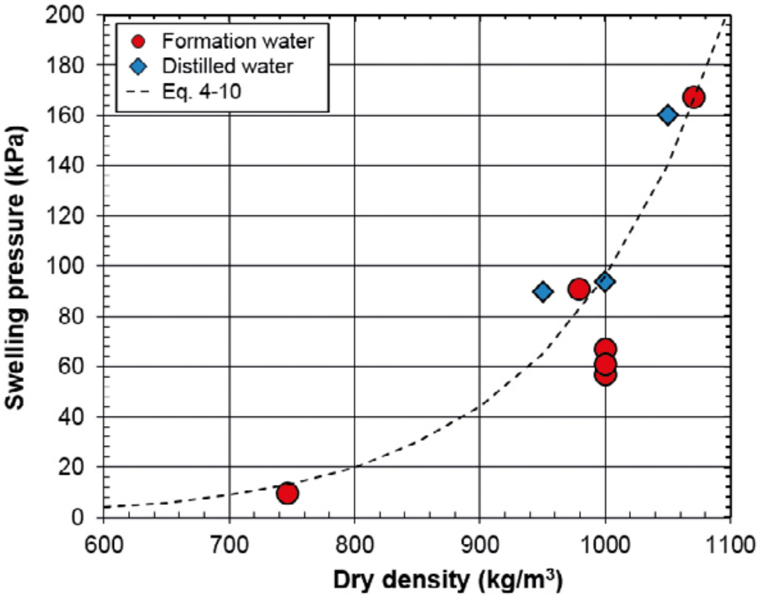

***Figure 4-16.** Swelling pressure as measured experimentally (preliminary data made available to us on June 20, 2014) for the sodium dominated clay (red circles and blue tilted squares), together with the swelling pressure relation described in equation 4-10 (dashed black line).*

As for the calcium-converted clay, the swelling-pressure measurements were on-going at the time of writing. However, preliminary results indicates that the swelling pressure at ρ_d = 1,000 kg/m^3 is close to 40 kPa; about a factor of two higher than what is estimated using equation 4-11. The effect of this uncertainty was evaluated in section 4.4.7; as was seen there it would mean that the effect of ion exchange is smaller than what was seen in the FEM models.

4.6 Conclusions

The behaviour of the clay barrier around the silo has been studied analytically and numerically during the initial dry phase and the water-saturation phase. Furthermore, the change in behaviour of the clay after ion exchange has converted it from a sodium bentonite into a calcium bentonite has been explored.

The investigations show that the mechanical behaviour of the clay barrier is largely dependent on two parameters: the strength of the wall friction and the magnitude of the swelling pressure:

- Wall friction: Evaluations of laboratory data on the shear strength of the bentonite suggests that the wall-friction angle is likely to be about 15°, but somewhat lower values cannot yet be excluded.
- Swelling pressure: Ion exchange will result in a reduction in the swelling pressure of the bentonite at the densities in question. While the exact magnitude of this reduction is uncertain, laboratory data indicates that a factor between two and five is likely.

Using numerical and analytical models of the buffer, and taking the data on wall friction and swelling pressure available, it can be concluded that ion exchange:

- will lead to a significant reduction in the stress levels in the clay barrier (as compared to the stress levels at full water saturation before ion exchange),
- will not cause any large changes in the dry-density profiles of the clay, and
- will only cause small downward movements of the clay barrier's top surface (from a few cm to a couple of decimetres at most).

5 Cement degradation of concrete wall

5.1 Introduction and objective

An analysis of the mechanical impact of *cement degradation of the concrete wall* on the bentonite filling in the silo is presented in this chapter.

The degradation of the cement in the silo wall implies that the aggregates in the concrete will be unconstrained. This, in turn, implies that these aggregates may have a mechanical impact on the bentonite filling. The goal of this task was to make a what-if analysis of this process. Three major sub-processes of this mechanical impact can be identified:

- Vertical displacements of the bentonite and the degraded concrete.
- Horizontal displacement of the interface between the concrete and the bentonite filling.
- Migration of bentonite into the voids between the exposed aggregates.

The first two of these issues can be quite readily addressed through hydro-mechanical modelling, and the objective of such models is therefore to estimate the magnitude of the displacements. Vertical displacement may be of major importance since theses eventually may lead to the intrusion of permeable sand (from the top filling) into the circumferential barrier.

The presentation of this task begins with a description of the key issues regarding the impact of cement degradation in section 5.2. Thereafter follows as a description of the models in section 5.3, and a presentation of the results from these in section 5.4. Finally, the conclusions and the remaining uncertainties are discussed in section 5.5.

5.2 Key issues regarding the mechanical impact cement degradation

The main volume fractions of interest for the cement degradation are illustrated in Figure 5-1. The only volume fraction of solids that will remain after the cement degradation is the one occupied by aggregates in the original concrete ($a = V_a/V_t$). The porosity after the degradation is thus equal to 1-a. Åkesson et al. (2010) regarded 0.67 to be a relevant value for the volume fractions of aggregates in the THM modelling of bentonite-based system components in SR-Site. A value of 0.33 may thus be regarded as relevant for the “initial” porosity of the degraded concrete.

This creation of significant volume fractions of voids can lead to:

i. an irreversible volume reduction, or

ii. the filling of these void with bentonite from the outer filling.

The potential *volume reduction* can be calculated for a specified “final” porosity (n). Such porosity values can be estimated from known porosities for different grain size distributions. For instance, Åkesson et al. (2010) stated values for well sorted material (sand): ~ 0.35; and poorly sorted material (crushed rock): 0.18. The former value is apparently similar to the porosity given by the volume fraction of aggregates, and would thus imply no volume reduction. The latter value, on the other hand, would imply a significant reduction:

$$V^{init} \cdot a = V^{final} \cdot (1-n) \quad \Rightarrow \quad \frac{V^{final}}{V^{init}} = \frac{a}{1-n} = \frac{0.67}{1-0.18} = 0.82 \qquad (5\text{-}1)$$

where V^{init} and V^{final} are the initial and final volumes, respectively. The volume reduction would thus be approximately 18% if these volume fractions and porosity values are assumed.

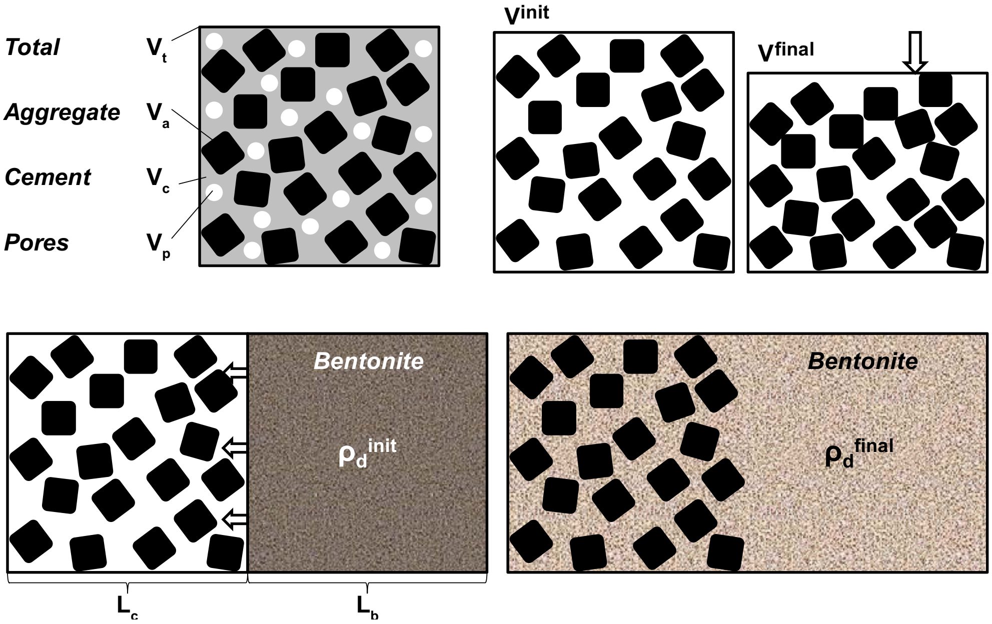

Figure 5-1. Volume fractions of concrete (upper left), and schematic illustrations of volume reduction (upper right) and migration of bentonite into voids (lower row).

The potential *migration of bentonite* into the voids between aggregates would mean that the dry density of the bentonite filling would decrease. This migration is a complex process that may be affected by frictional forces between the aggregates and the bentonite. If complete homogenization is assumed, however, then this would imply a significant density reduction:

$$\rho_d{}^{init} \cdot L_b = \rho_d{}^{final}(L_b + (1-a)\cdot L_c) \;\Rightarrow\; \rho_d{}^{final} = \frac{1}{1+0.33\cdot 1}1{,}000 = 750\ kg/m^3 \qquad (5\text{-}2)$$

where ρ_d^{init} and ρ_d^{final} are the initial and final dry density of the bentonite, respectively, and L_c and L_b are the width of the concrete wall and the bentonite filling, respectively.

The potential *dissolution of bentonite* due to the high pH caused by the concrete was outside the scope of this analysis and therefore not addressed.

The approach chosen for this analysis was to focus on the volume reduction by formulation of an analytical model, in which this reduction was represented with a prescribed horizontal strain of the bentonite filling. This was first verified with a numerical model (implemented with the FLAC code), before it was used for a wide range of cases with different parameter values and conditions. The process was regarded to take place after the bentonite has been completely Ca-converted. The initial stress-state and the stress-strain properties of the bentonite were therefore based on an assumed swelling pressure curve for Ca-dominated bentonite (see section 4.4.1).

5.3 Model of mechanical impact of cement degradation

5.3.1 Introduction

An analytical model was developed in the MathCad software (v 15) for the specific problem of a potential volume reduction of the concrete wall, and this was the main tool for performing the actual calculations. The model was denoted “analytical”, simply because it was implemented in an advanced mathematical spreadsheet, although it also makes use of some numerical techniques. A numerical model (created with the FLAC code) was subsequently developed with the intention to verify the analytical model. These two modelling approaches are described in the following two sections.

The models included the following parts and conditions:

- A plane 1D representation of the bentonite filling (the FLAC geometry was actually 2D). The plane geometry was regarded to be an adequate simplification of the problem, considering the large radius of the silo in relation to the width of the bentonite filling.
- A porous-elastic material model (with two parameters: the κ module and Poisson´s ratio ν) for representation of the bentonite. The exclusion of a yield surface and any plastic strains was a simplification which could be justified, to some extent, by comparing the calculated stress states with an assumed shear strength.
- Settlements caused by the weight of the bentonite.
- Water saturated conditions with a hydrostatic pore pressure distribution (implying that effective stresses had to be considered).
- An external stress boundary for representation of the top-filling.
- Interfaces with specified friction angles toward confining rigid materials representing the concrete wall and the rock wall.
- A displacing boundary towards the concrete wall representing the volume reduction of the concrete.

The models basically consisted of two main steps: i) the initial settlement due to the weight of the bentonite and the load caused by the top filling, and ii) the successive horizontal displacement of the interface towards the concrete wall.

5.3.2 Derivation of analytical model

Coordinate system and other definitions

The coordinate system was defined in the following way (see Figure 5-2a): x was defined as horizontal, y was vertical downwards, and z was also horizontal, perpendicular to section through the bentonite filling. Compressive stresses were defined as negative, and strains corresponding to a decrease in length or volume were also defined as negative.

$$\begin{cases} d\varepsilon_x = \dfrac{1}{E}\left[d\sigma_x - \nu\left(d\sigma_y + d\sigma_z\right)\right] \\ d\varepsilon_y = \dfrac{1}{E}\left[d\sigma_y - \nu\left(d\sigma_z + d\sigma_x\right)\right] \\ d\varepsilon_z = \dfrac{1}{E}\left[d\sigma_z - \nu\left(d\sigma_x + d\sigma_y\right)\right] \end{cases} \tag{5-3}$$

Basic equations

An important part of the model was Hooke’s law, which specifies an equation system with three equations and six variables (the effective stresses: σ_x, σ_y, σ_z; and the strains: ε_x, ε_y, ε_z):

Three of these variables were specified for the current problem: $d\varepsilon_z$ (=0), $d\varepsilon_x$ and $d\sigma_y$, which means that the equation system could be successively solved in the following way:

$$\begin{cases} d\sigma_x = \dfrac{E \cdot d\varepsilon_x + \nu(1+\nu)d\sigma_y}{1-\nu^2} \\ d\varepsilon_y = \dfrac{1}{E}\left[(1-\nu^2)d\sigma_y - \nu(1+\nu)d\sigma_x\right] \\ d\sigma_z = \nu\left(d\sigma_x + d\sigma_y\right) \end{cases} \tag{5-4}$$

The Young's modulus (E) is proportional to the mean effective stress ($p = -(\sigma_x+\sigma_y+\sigma_z)/3$).

$$E = 3(1-2\nu)(1+e_0)\frac{p}{\kappa} \tag{5-5}$$

This property therefore has to be updates unless p is constant during the calculations. Finally, the void ratio (e) can be calculated from the strains (note that $\varepsilon_z = 0$).

$$e = e_0 + (1+e_0)(\varepsilon_x + \varepsilon_y + \varepsilon_x \cdot \varepsilon_y) \tag{5-6}$$

A second major equation was the relation between the gradient in vertical stress, the weight of the bentonite and the friction stress which is proportional to the horizontal stress (see Figure 5-2b).

$$\frac{d\sigma_y}{dy} = -g \cdot (\rho_m - \rho_w) - \frac{2 \cdot \sigma_x \cdot \tan\phi}{B \cdot (1+\varepsilon_x)} \tag{5-7}$$

where g is the gravity, ρ_m and ρ_w is the saturated density of the bentonite and the water density, respectively, B is the width of the bentonite filling, and φ is the friction angle between the bentonite and the confining walls. The friction term in this expression was only included if the vertical strain exceeded the initial stress level.

Structure of algorithm

The bentonite filling was discretized in an array of m elements (from index 0 at the top and to m-1 at the bottom). The problem of settlements during successive horizontal displacement was solved with an algorithm which basically consists of three levels of stepwise calculation (see Figure 5-3). On the lowest level, the Hooke's equations (5-4) were used to calculate the three increments $\Delta\sigma_x$ $\Delta\varepsilon_y$ and $\Delta\sigma_z$ through concurrent integration, from (ε_x, σ_y) to ($\varepsilon_x+\Delta\varepsilon_x$, $\sigma_y+\Delta\sigma_y$), for each element (see Figure 5-2d). On the intermediate level, the stresses and strains for each element were calculated stepwise, starting from the top, in which both vertical stress gradient (5-7) and the Hooke's equations (5-4) were taken into account. On the highest level, the horizontal strains (ε_x) were increased stepwise, from zero to the maximum strain, and stresses and strains for each element were updated for each new strain value.

The used algorithms (implemented in MathCad) are shown in full in Appendix E.

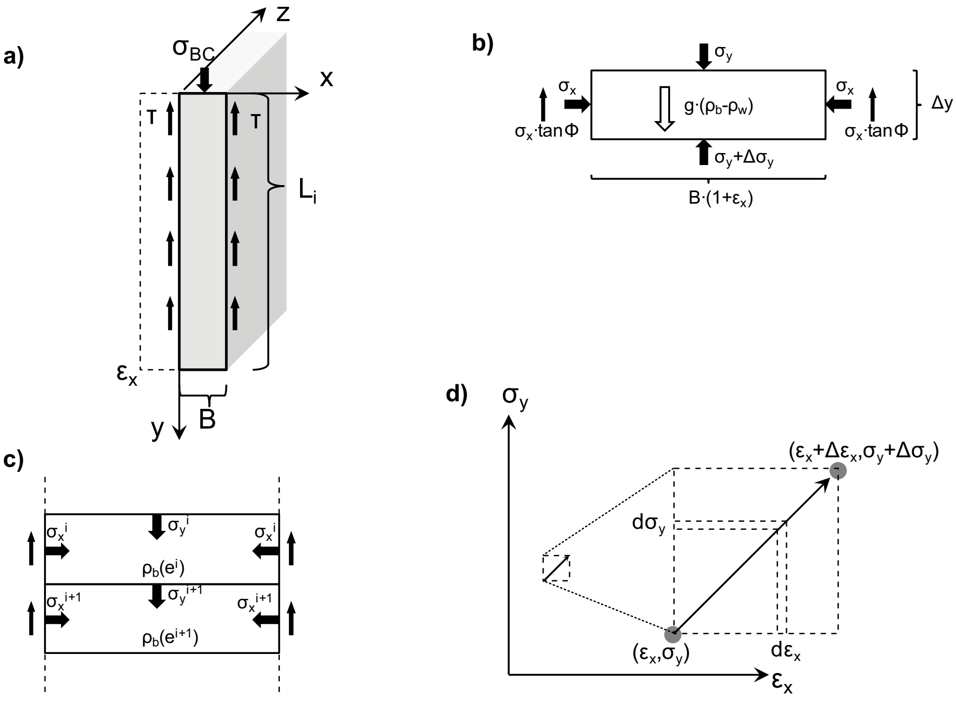

Figure 5-2. Outline of model geometry and coordinate system (a); forces acting on one element (b); definition of stress components and void ratio in elements (c); concurrent integration of horizontal strain and vertical stress (d).

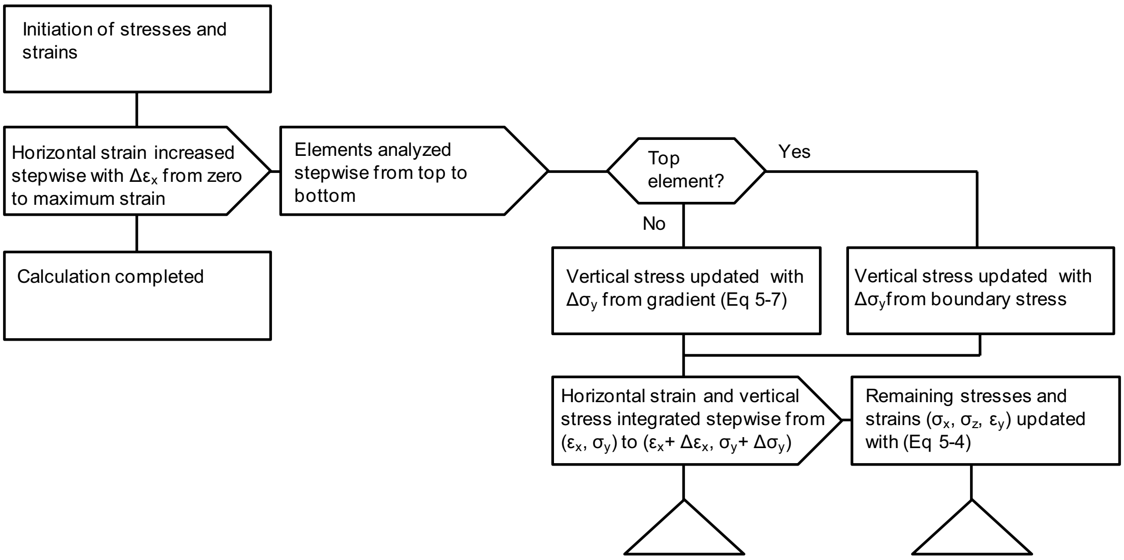

Figure 5-3. Schematic algorithm for analytical model.

5.3.3 FLAC model for verification of analytical model

A numerical model was developed with the FLAC (v 6.0) finite difference code with the intention to verify the analytical model presented in section 5.3.2.

A plane 2D geometry (1.6 m wide and 53 m high) was set up for the problem (Figure 5-4**)**. The corresponding grid (using 5 × 200 zones) was divided in three regions with two represented materials: bentonite and a fictitious confining material. This division enabled the definition of interfaces, with specified friction angles, between these regions.

The models were configured for *ground water* calculation, but specified for **NO FLOW**, which means that the pore pressures were fixed at the nodes. This configuration also implies that dry densities (ρ_{dry}) were specified, and that the total density (ρ_{tot}) was calculated as:

$$\rho_{tot} = \rho_{dry} + n \cdot s \cdot \rho_w \qquad (5\text{-}8)$$

where n is the porosity, s is the degree of saturation (i.e. 1 in this case) and ρ_w is the density of the water. The porosity field was updated "manually" from the current volumetric strain field using a simple look-up table.

Different constitutive models were employed for the two materials. The bentonite was represented with the elastic part of the Modified Cam-Clay model, whereas the confining materials were represented with a linear elastic material, although the grid for these regions essentially were kept fixed throughout the calculations. The two interfaces were defined between the three adjacent regions. The friction angle of these interfaces was both set to 10°.

The pore pressure profile was defined as a hydrostatic distribution with a water table 130 m above the bottom level of the model, which corresponds to a pore pressure of 1,275 kPa at the bottom and 755 kPa at the top of the model (Figure 5-4). The initial total stresses were defined in order to yield an (isotropic) effective stress of –20 kPa, which corresponded to the estimated swelling pressure of the Ca-converted bentonite at a dry density of 1,000 kg/m^3. For simplicity, this initial effective stress was assumed throughout the entire geometry.

The used parameter values are presented in Table 5-1. The bentonite dry density corresponded to the installed dry density, and the porosity and the specific volume were subsequently based on a particle density value of 2,780 kg/m^3. The κ-value corresponded to the -dv/dln(p) module of the estimated swelling pressure curve for of the Ca-converted bentonite at a dry density of 1,000 kg/m^3 (see also section 4.4). The Poisson' ratio was in line with Åkesson et al. (2010), and was chosen in order to enhance the settlement for testing the models. The bulk and the shear modules of the confining material were set high in order to facilitate the intended rigid behaviour.

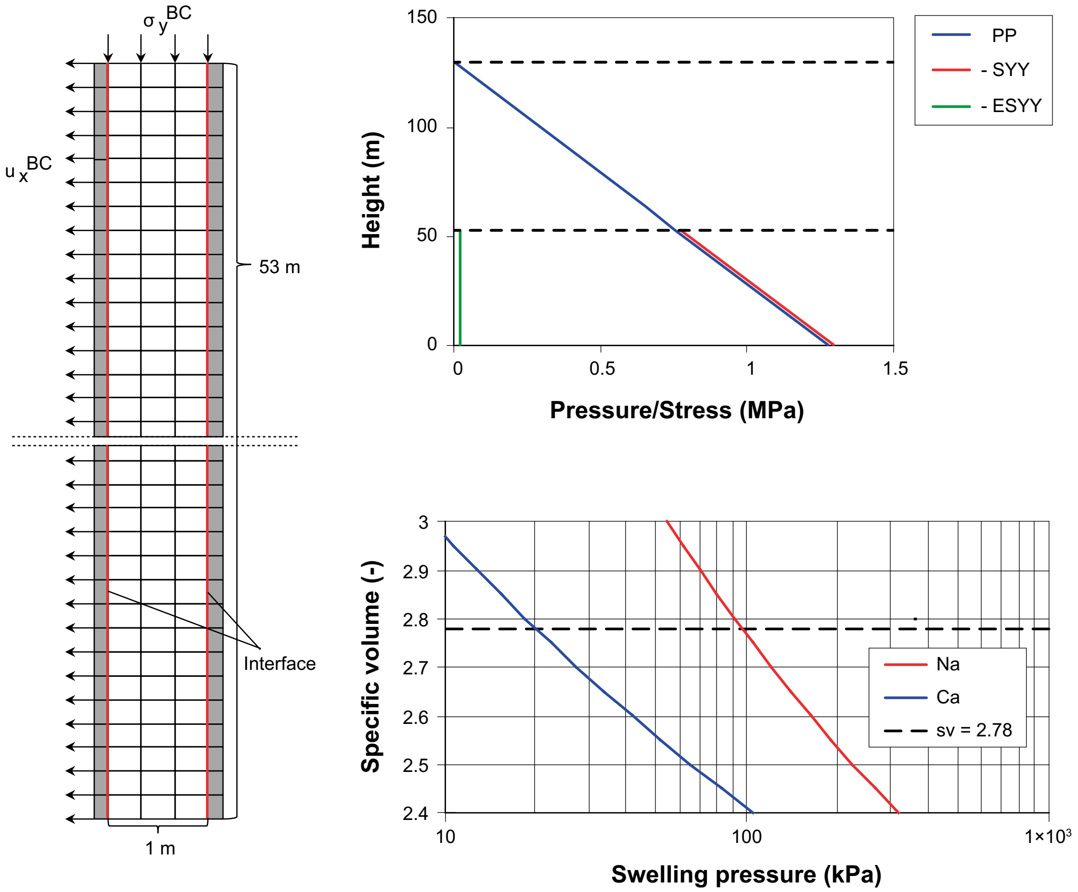

***Figure 5-4.** Model grid and geometry (left). Initial distribution of pore pressure, axial total and effective stress (top right). Swelling pressure curves, Na and Ca dominated, assumed for the bentonite filling (bottom right). For simplicity, compressive stresses are shown as positive.*

The model was executed in two main parts (Table 5-2). The first part simulated the initial settlement of the bentonite, and covered all definitions of the grid, geometry, material properties and the interfaces with their friction angles. It also included the fixing of the grids of the confinement material and at the lower boundary, and the definition of initial stresses, and finally also the stepwise increase of the vertical stress at nodes at the upper boundary, corresponding to an effective stress increasing from –20 to –100 kPa. The model was allowed to go to mechanical equilibrium after each step in the boundary stress. The second part simulated the compression of the concrete, simply by freeing of the grids in the left confining material and subsequent by applying stepwise displacements, from zero to 0.02 m, at the left boundary of this region. The model was allowed to go to mechanical equilibrium after each step.

A copy of the used FLAC model is shown in full in Appendix F.

Table 5-1. Parameter values for different materials.

Parameters	Value
Bentonite initial dry density	1,000 kg/m^3
Bentonite initial porosity/ specific volume	0.64 / 2.78
Bentonite kappa	0.26
Bentonite Poisson’ ratio	0.2
Confining material density	2,000 kg/m^3
Confining material bulk/shear modulus	100/75 MPa

Table 5-2. Procedure for execution of FLAC model.

I	• Grid and geometry defined. • Material properties. • Interfaces and friction angles defined. • Fixed grids in confinement and at lower boundary. • Initial stress distribution. • Stepwise increase of effective vertical stress (–20 → –100 kPa) at upper boundary. → Print results
II	• Stepwise horizontal displacement (0 → 0.01 m) of left boundary. → Print results • Stepwise horizontal displacement (0.01 → 0.02 m) of left boundary. → Print results

The analytical model had to be modified in two ways in order to comply with the formulation of the FLAC model: i) the expression for calculation of the Young's modulus, Equation (5-5), was modified so that it included the current void ratio rather than the initial void ratio; and ii) the expression for calculating the spatial increment in vertical stress, Equation (5-7), was modified so that it used the initial dimensions and densities rather than the current ones, since the FLAC model was executed in a small strain mode. Vertical distributions of vertical and horizontal stresses as well as void ratio are shown for the three different strains in Figure 5-5. The differences between the two models are of such a limited extent that they could be regarded as acceptable. In addition, results from the zero strain case are presented as plots of void ratio vs. mean effective stress, together with the logarithmic relation $v = 2.78 - 0.26 \cdot \ln(p/20 \text{ kPa})$. It can be noted that the agreement between the two models are excellent, but that the model results display a slightly deviating trend with increasing stress levels. This is an effect of the void ratio dependence of the Young's modulus.

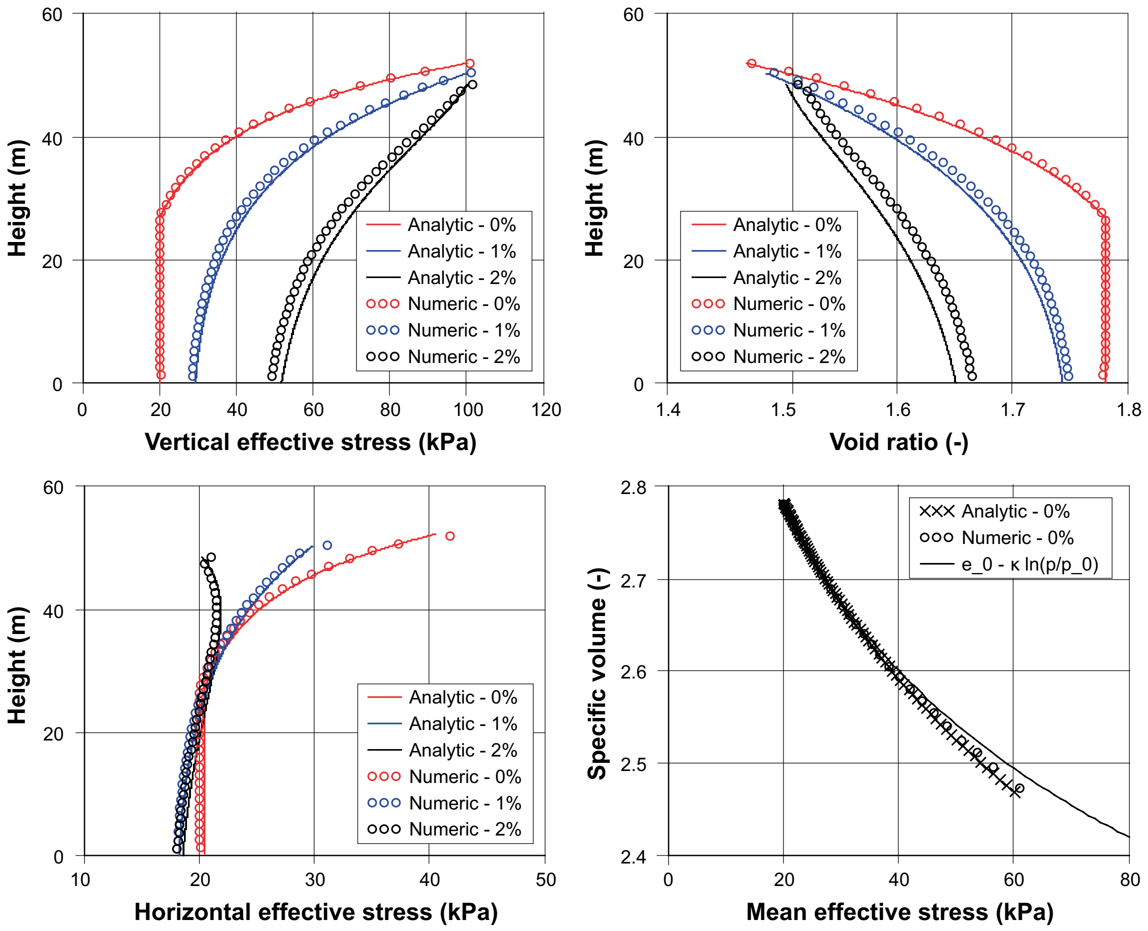

Figure 5-5. Comparison of results from analytical (lines) and numerical models (symbols). For simplicity, compressive stresses are shown as positive.

5.4 Model results

The analytical model was used for calculating stresses and strains for horizontal strains ranging from 0 to 10%. The top range value is slightly higher than half the volume reduction estimated in section 5.2. This was regarded to be a relevant range, since the volume reduction could also lead to vertical strains (in the concrete) and not only horizontal.

The initial height, width and void ratio of the bentonite filling were set to 53 m, 1 m, and 1.78, respectively, and the boundary effective stress, representing the top filling, was set to 100 kPa (compressive). All these values were in line with the models presented in Chapter 4. The used κ value was evaluated from the assumed swelling pressure line and was the same as in section 5.3.3. The filling was discretized in 500 elements, the horizontal strains were divided in 20 steps, and each integration of $\Delta\varepsilon_x$ and $\Delta\sigma_y$ was also divided in 20 steps.

A case with: i) a Poissons' ratio of 0.4; ii) a friction angle of 15°; and iii) an initial isotropic stress state with p_{init} of 20 kPa was defined as a Base case. Results from this are shown in Figure 5-6.

The vertical and horizontal stresses generally display a decreasing trend with increasing depth. The level of the vertical stresses increases with increasing horizontal strains whereas the level of the horizontal stresses decreases. The latter trend is an effect of the horizontal strains. Decreasing horizontal stress results, in turn, with a reduction of the friction forces which can counteract the weight of the bentonite. The calculated stresses are presented as lines in the p-q plane in Figure 5-6 together with an empirical relation for the shear strength of MX-80 (see section 4.4). The von Mises stress (q) is calculated as:

$$q = \sqrt{\frac{(\sigma_x - \sigma_y)^2 + (\sigma_x - \sigma_z)^2 + (\sigma_y - \sigma_z)^2}{2}} \qquad (5\text{-}9)$$

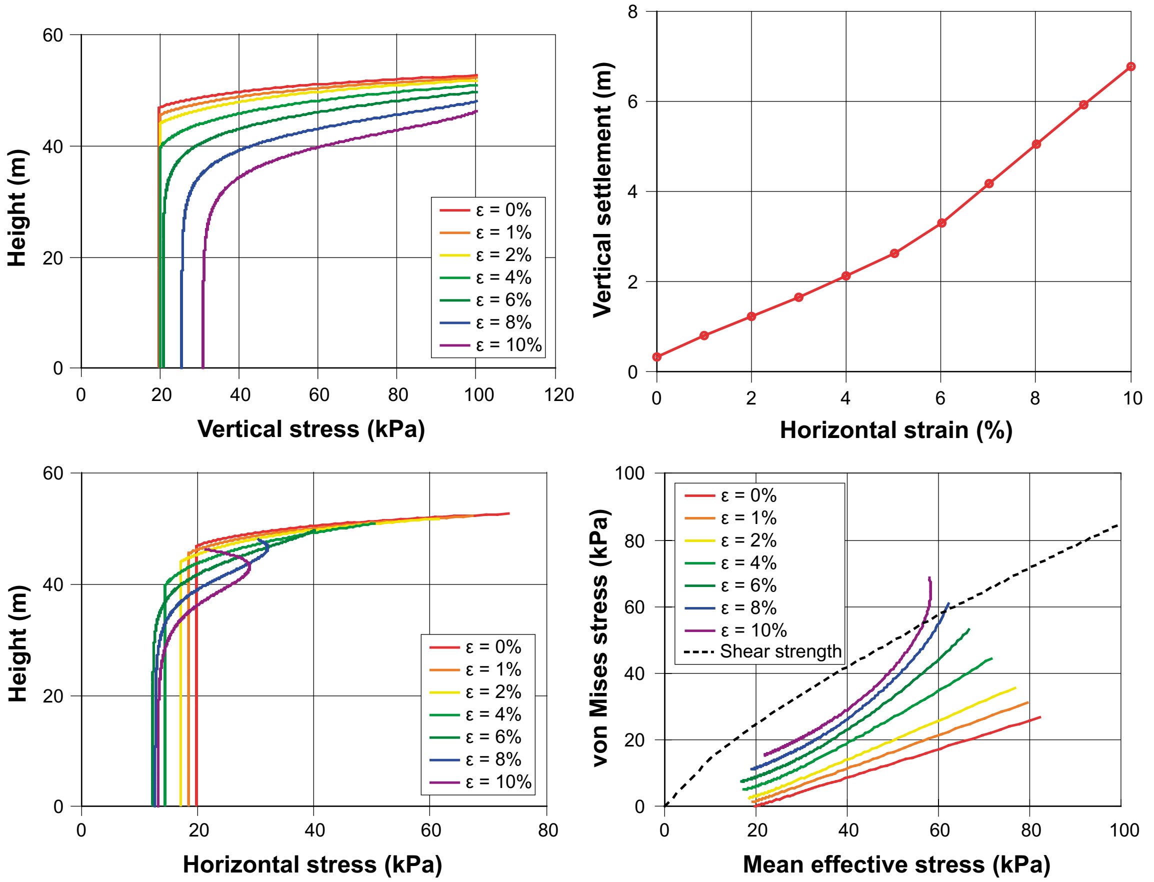

Figure 5-6. *Base case model results: vertical stress vs height (top left), horizontal stress vs height (bottom left), vertical settlement vs horizontal strain (top right) and von Mises stress vs mean effective stress (bottom right). For simplicity, compressive stresses are shown as positive.*

It can be noted that the q-values are below the shear strength curve, except for the highest horizontal strain (10%), and this corresponds to a more pronounced reduction in the horizontal stresses. An interpretation of this is that the model results are not relevant for cases in which the shear strength relation is exceeded. This is important for the interpretation of the calculated vertical settlement, which displays an increasing trend for increasing horizontal strains. These results should however only be regarded as relevant for strains up to ~ 8%, because the q-values exceeds the shear strength beyond that. The maximum settlement for the Base Case is therefore approximately 5 m. Larger strains would lead to plastic deformations which possibly would have an impact similar to an elastic deformation with a lower shear modulus. This could therefore mean that the evolution of settlements would level off at higher horizontal strains.

A parameter variation was performed for eight different combination for the following sets of parameters: i) the Poissons' ratio: 0.2 and 0.4; ii) the friction angle: 10 and 15°; and iii) the initial isotropic stress state: 20 and 40 kPa. Results regarding the relation between vertical settlement and the horizontal strains are compiled for all these cases in Figure 5-7 (top). It can be noted that changing the Poisson's ratio has the strongest influence on the settlement, whereas changing the friction angle has the weakest influence. The relation between the horizontal stress *at the uppermost element* and the horizontal strain are shown in Figure 5-7 (bottom). Only four lines are plotted in this graph since the friction angle has no influence on the horizontal stress at the top. It can be noted that the horizontal stress are tensile for cases with Poissons' ratio of 0.2 and for horizontal strains exceeding 4%. The results are therefore not relevant for these cases.

Results for one of these cases ($\nu = 0.2$, $p_{init} = 20$ kPa, and $\varphi = 15°$) are shown in detail in Figure 5-8.

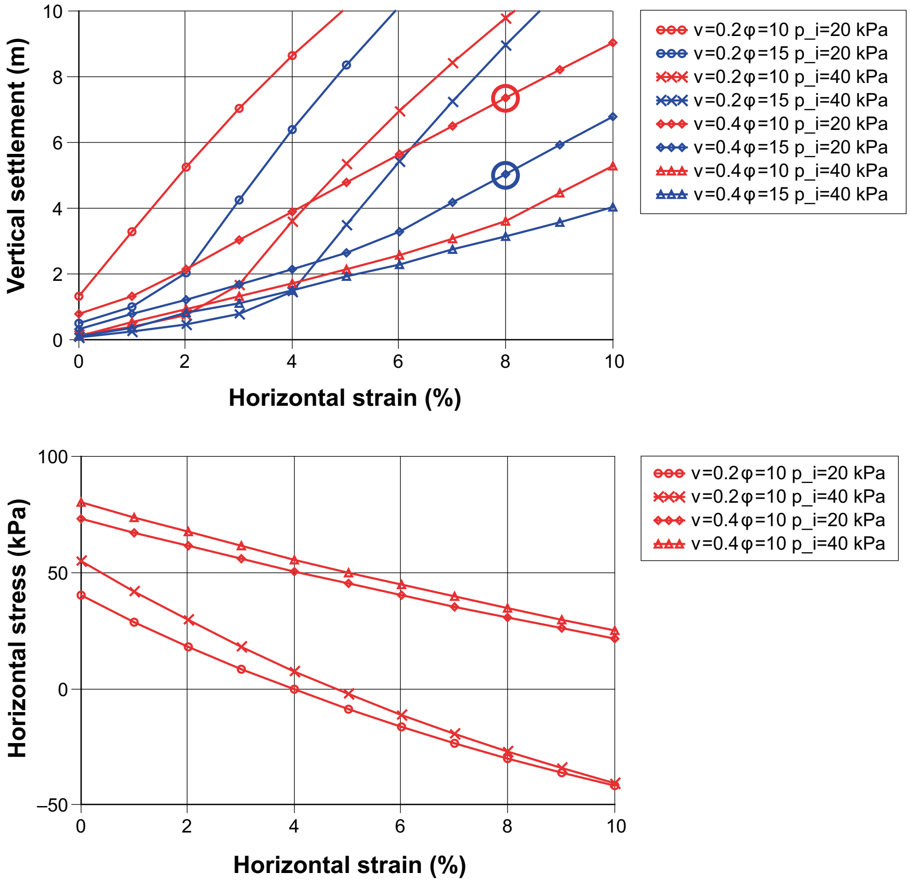

Figure 5-7. *Model results from parameter variation: vertical settlement vs horizontal strain (top) and horizontal stress vs horizontal strain at the uppermost element (bottom). Compressive stresses are shown as positive. The highest relavant settlement for the Base case and the other cases marked with blue and red large circles, respectively.*

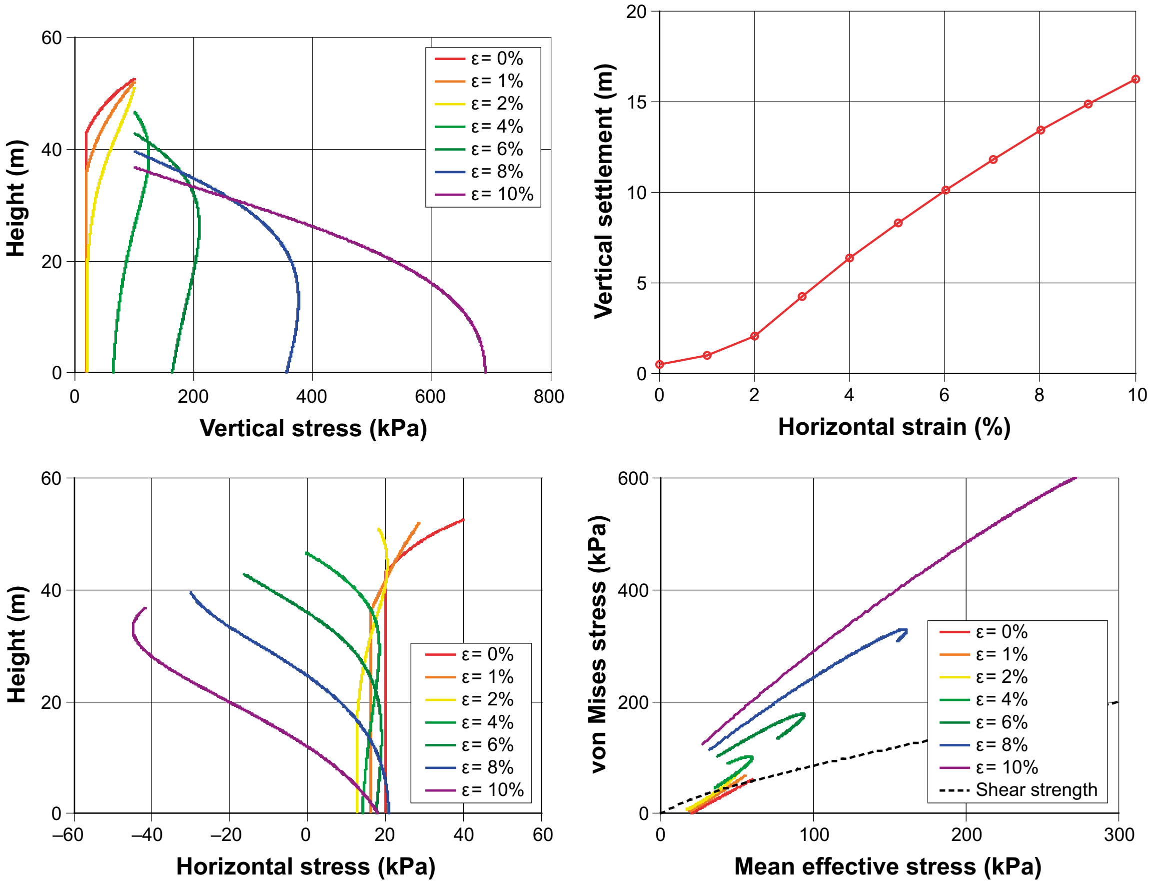

Figure 5-8. Results from modelled with ν = 0.2, p_{init} = 20 kPa, and φ = 15°: vertical stress vs height (top left), horizontal stress vs height (bottom left), vertical settlement vs horizontal strain (top right) and von Mises stress vs mean effective stress (bottom right). For simplicity, compressive stresses are shown as positive. Results for cases with horizontal strains higher than 1% are not regarded as relevant for the problem since the von Mises stresses are higher than the assumed shear strength.

In this case, the vertical stresses display an overall increasing trend with increasing depth for horizontal strains exceeding 4%, which coincide with tensile horizontal stresses. The highest vertical stresses even exceed the initial sum of the boundary stress and the weight of the entire bentonite filling (100 + 332 kPa). It can also be noted that the q-values exceed the shear strength already when the strain exceeds approximately 1%, which means that these results are not relevant. And similar results were found for all modelled cases with ν = 0.2 (higher than approximately 2% for cases with p_{init} = 40 kPa). The highest displacement for which the solution appears to be relevant is therefore for the case with ν = 0.4, p_{init} = 20 kPa, φ = 10° and ε_x = 8%, for which the vertical displacement was approximately 7 m.

5.5 Conclusions and remaining uncertainties

The presented model indicates that the bentonite filling may undergo a significant settlement as a consequence of the *assumed volume reduction* of the degraded concrete. The main reason for this appears to be that the assumed volume reduction of the degraded concrete implies that this material can be compressed by the swelling of the bentonite. This, in turn, means that the horizontal stresses will decrease, which implies that the frictional forces against the confinement material also will decrease. The highest relevant settlement value found for the Base case in this study was approximately 5 m. A higher value (7 m) was found for a case with a friction angle of 10°. This would imply that a significant part of the circumference of the silo only would consist of permeable materials (sand from the top filling, and aggregates from degraded concrete).

The main alternative consequence of cement degradation, i.e. *migration of bentonite* into the voids between the aggregates, may probably also lead to significant settlements of the bentonite. Available swelling pressure data for dry density values down to 750 kg/m^3 is still very limited, especially for Ca-converted GEKO/QI, and settlement calculations for such density levels have therefore not been included in this study.

The potential *dissolution of bentonite* due to the high pH caused by the concrete was outside the scope of this analysis and was therefore not addressed. More complex schemes of deformation, such as localization and intrusion of aggregates beneath the bentonite, are probably too complicated to be addressed through this type of modelling.

The compressive properties of the degraded concrete are regarded to be the most significant *uncertainty* for this analysis, and this was the motive for addressing a quite wide range of investigated horizontal strains. This uncertainty would be reduced if more detailed information about the used concrete, in general, and its properties in a degraded state, in particular, would become available.

More detailed information about for Ca-converted GEKO/QI could potentially call for a modification of the used values for the: initial stress level, the kappa value, and the shear strength. It should be observed that the shear strength relation used in this analysis was derived for MX-80 bentonite, and that this relation very well could be exceeded for Ca-converted GEKO/QI. This would probably mean that even higher settlements could occur than the ones that were found in this analysis.

It should also be noted that the concrete wall, which was not explicitly represented in the presented models, was assumed to be able to support the frictional forces from the bentonite. Even higher settlements could be anticipated if the degraded concrete also was allowed to settle and slip along the material on the inside of the concrete wall. Since the concrete wall has approximately the same width as the bentonite filling, this would mean that the width of the settling materials basically would be doubled, which in turn would imply a more pronounced settlement of both materials.

6 Rock block detachment – Analysis of how a loose rock block affects the wall filling

6.1 General

A piece of the rock wall may after long time come loose from the rock and fall out on the filling of bentonite in the slot between the concrete silo and the rock surface. The consequences of such an event have been investigated with both analytical and numerical modelling.

The geometry of a rock block that may come loose from the wall is not known but will probably be rather unsymmetrical. In order to make an analysis possible the geometry has been simplified to a triangular shape, which for most cases is pessimistic since it entails only two straight contacts surfaces. Figure 6-1 shows the geometry.

Rock block detachment has been studied both with analytical and numerical solutions. Different cases of analytical equilibrium analyses have also been modelled with FEM simulations in order to compare results and understand the consequences of non-equilibrium. The numerical simulations have been done with the finite element program Abaqus. The rock block has been assumed not to be detached until after long time, which means that that the bentonite will be fully water saturated and the swelling pressure developed.

6.2 Analytical analyses of the wall fill

Since only force equilibrium has been regarded in the analytical solution, the thickness of the bentonite filled slot does not affect the calculations. Two cases have been considered; without and with friction between the rock and the bentonite.

1. Friction between the bentonite and the rock block is neglected

Consider a wedge shaped triangular rock block with the height *h* and the depth *b*. The geometry and the influencing forces are shown in Figure 6-2.

The rock block is affected (per meter length) by the gravity force *F*, the friction force *T*, the normal reaction force *N* and the force from the swelling pressure of the bentonite *S* (kN).

$F = mg = \rho_b hbg/2$

where ρ_b = the density of the rock (2.7 kg/dm^3). After full water saturation and establishment of hydro static water pressure the density of the rock block will be 1.7 kg/dm^3 but that case is less critical.

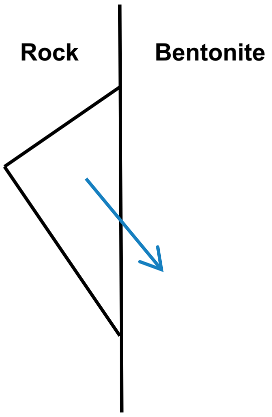

Figure 6-1. Triangular rock block in the wall that is studied.

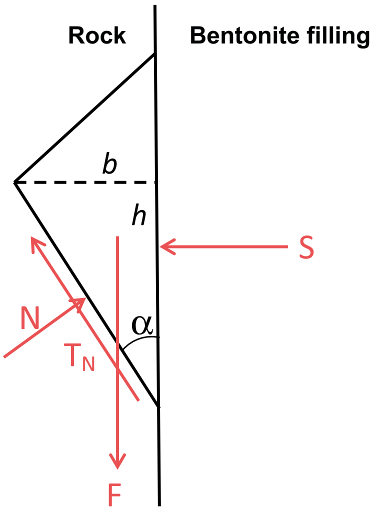

Figure 6-2. Geometry and forces influencing a triangular rock block in contact with a bentonite filling when the friction between the bentonite and the rock block is neglected.

$S = \sigma_s h$

where σ_s = swelling pressure from the bentonite (kPa).

Force equilibrium in T- och N-directions yield:

$$T = mg\cos\alpha - \sigma_s h\sin\alpha \,, \tag{6-1}$$

$$N = mg\sin\alpha + \sigma_s h\cos\alpha \,, \tag{6-2}$$

$$T = N\tan\phi \,, \tag{6-3}$$

where ϕ = friction angle of the fracture between the block and the rock.

Combining the equations yields:

$mg\cos\alpha - \sigma_s h\sin a = (mg\sin\alpha + \sigma_s h\cos a)\tan\phi$.

Required swelling pressure in order to keep the rock block in place is thus:

$$\sigma_s = -\frac{mg}{h}\frac{(\tan\alpha\cdot\tan\varphi-1)}{(\tan\varphi+\tan\alpha)} \,, \tag{6-4}$$

$$\sigma_s = \frac{\rho_b bg}{2}\frac{(1-\tan\alpha\cdot\tan\varphi)}{(\tan\varphi+\tan\alpha)} \,, \tag{6-5}$$

$\rho_b g = 2.7\cdot g = 27$,

$\phi = 35° \rightarrow \tan\phi = 0.7$,

$$\sigma_s = 13.5b\frac{(1-0.7\tan\alpha)}{(0.7+\tan\alpha)} \,. \tag{6-6}$$

No swelling pressure is thus needed if $(1\text{-}0.7\tan\alpha) < 0$, i.e. if $\alpha > 55°$ at $\phi = 35°$ or if $\alpha > (90° - \phi)$ (elementary).

Figure 6-3 shows required swelling pressure for a number of cases.

Figure 6-3 shows that the swelling pressure does not need to exceed 100 kPa at moderate rock block sizes. It is also interesting to note that the height of the rock block is not affecting the results according to Equation (6-5).

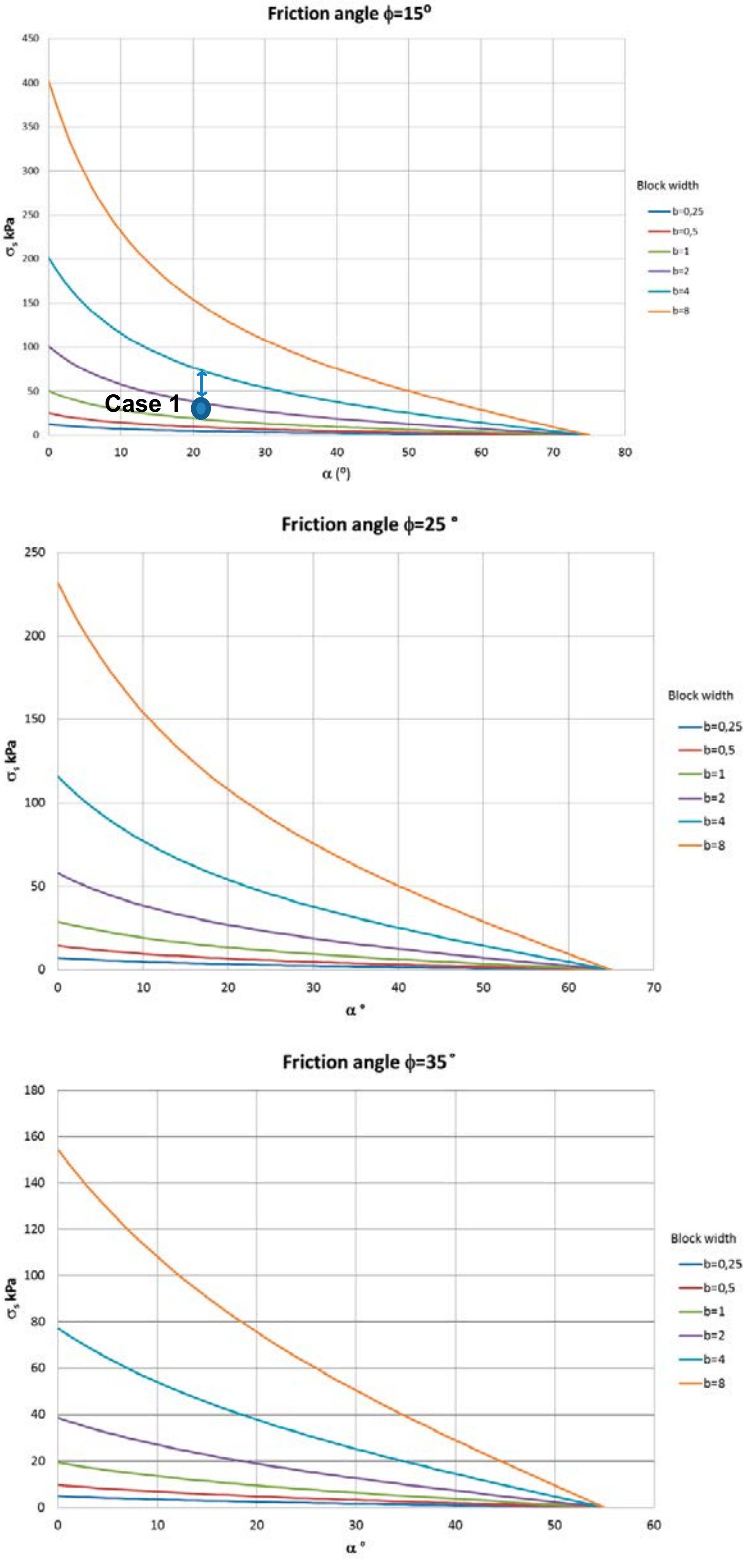

Figure 6-3. *Required swelling pressure of the bentonite filling in order to keep the rock block in place. The swelling pressure is plotted as a function of the rock fracture angle α against the vertical plane at different block widths at different fracture friction angles φ_r. Simplified case with the friction angle $\varphi_b = 0$ between the rock block and the bentonite. Case 1 is numerically modelled. The arrow shows the distance to required swelling pressure.*

2. Friction between the bentonite and the rock block included

If the friction between the rock block and the bentonite is included there will be an additional shear force T_s according to Figure 6-4.

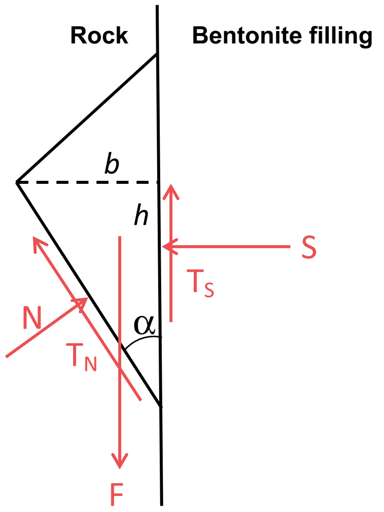

Figure 6-4. Geometry and forces influencing a triangular rock block in contact with a bentonite filling when the friction between the bentonite and the rock block is included.

This case yields the following equilibrium equations:

$$F - T_s - T_N cos\alpha - Nsin\alpha = 0\,, \qquad (6\text{-}7)$$

$$S - Ncos\alpha + T_N sin\alpha = 0\,, \qquad (6\text{-}8)$$

where:

$S = h\sigma_s$,

$F = \rho_b hbg/2$,

$T_N = Ntan\varphi_r$,

$T_s = Stan\varphi_b = h\sigma_s tan\varphi_b$,

φ_r = rock (in the fracture) ,

φ_b = friction angle between the rock block and the bentonite.

Equations (6-7) and (6-8) yield:

$$\frac{\rho_b hbg}{2} - h\sigma_s tan\varphi_b - Ntan\varphi_r cos\alpha - Nsin\alpha = 0\,, \qquad (6\text{-}9)$$

$$h\sigma_s - Ncos\alpha + Ntan\varphi_r sin\alpha = 0\,. \qquad (6\text{-}10)$$

Combining the equations yields:

$$N = \frac{\frac{\rho_b hbg}{2} - h\sigma_s tan\varphi_b}{tan\varphi_r cos\alpha + sin\alpha} = \frac{h\sigma_s}{cos\alpha - tan\varphi_r sin\alpha}\,. \qquad (6\text{-}11)$$

Required swelling pressure in order to keep the rock block in place is thus:

$$\sigma_s = \frac{\rho_b bg}{2} \cdot \frac{(1 - tan\alpha \cdot tan\varphi_r)}{tan\varphi_b(1 - tan\varphi_r \cdot tan\alpha) + (tan\varphi_r + tan\alpha)}\,, \qquad (6\text{-}12)$$

where:

$\rho_b = 2.7$, $g = 10$, $\phi_b = 20°$.

Figure 6-5 shows plots of required swelling pressure σ_s as function of a for $\phi_r = 15$, 25 och 35° for $b = 0.25$, 0.5, 1, 2, 4 and 8 meter.

The derivation of Equation (6-12) shows that the height *h* does not affect the results in this case either.

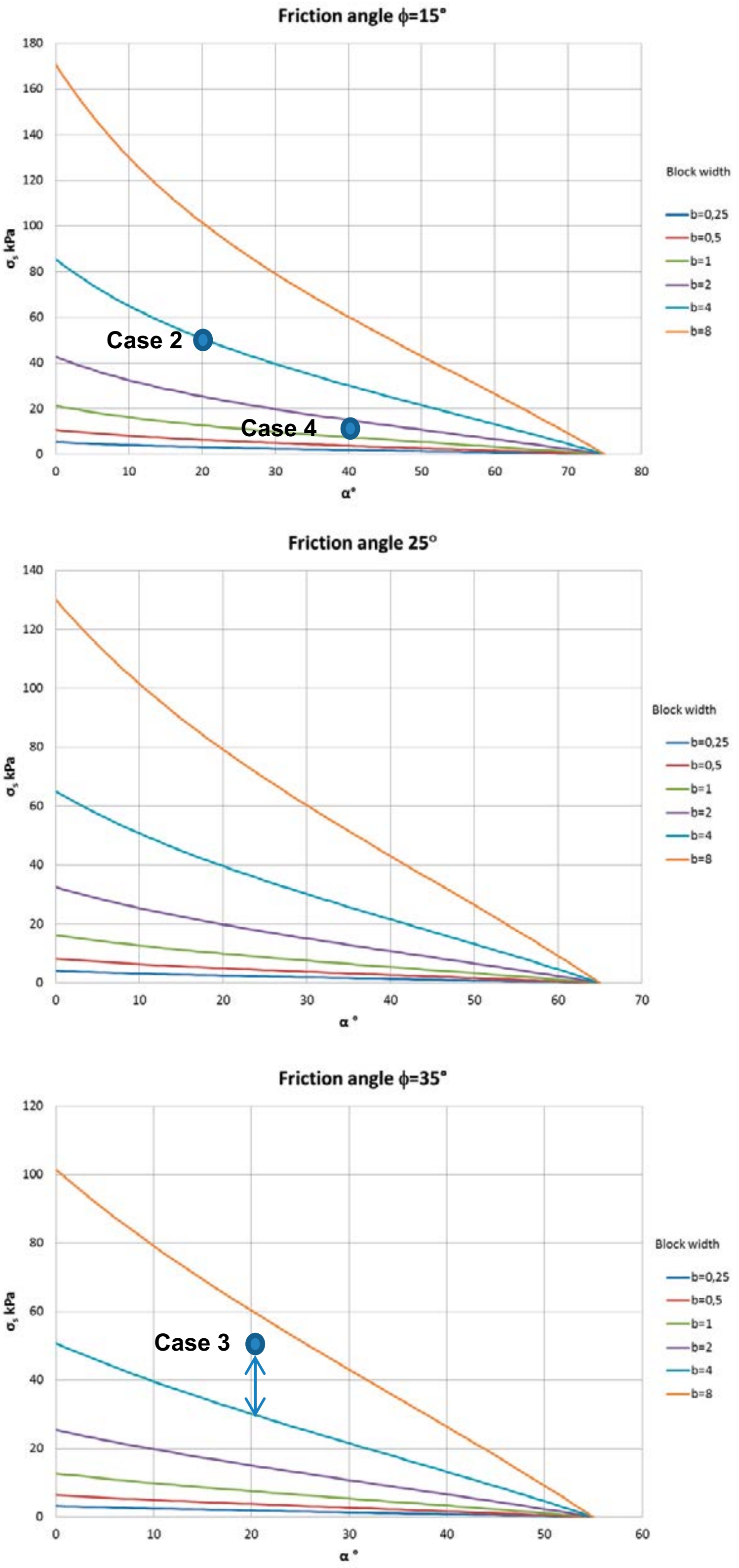

Figure 6-5. *Required swelling pressure of the bentonite filling in order to keep the rock block in place as a function of the rock fracture angle* a *against the vertical plane at different block widths b (m) at different fracture friction angles φ_r. Friction angle φ_b = 20° between the rock block and the bentonite. Cases 2-4 are numerically modelled. The arrow shows the distance to required swelling pressure.*

6.3 Numerical analyses of the wall fill

General

In order to check that the analytical relations are correct and to study what will take place close to the limits derived by the analytical solution a number of cases have been modelled with the finite element program Abaqus. The simulations have been done for different cases where the rock block according to the analytical solution either is kept in place or not kept in place.

Material models

The rock is modelled as an elastic material with very high E-modulus.

The bentonite is modelled in the same way as water saturated bentonite has been modelled in a number of simulations for KBS-3V (*Porous Elastic* with logarithmic compression modulus and *Drucker Prager* plasticity). Since the laboratory tests on the actual backfilling material (GKQI) were not completed the material model of MX-80 has been used. The initial conditions are identical to the initial conditions of the pellet filled slot in the Canister Retrieval Test in Äspö HRL and other simulations with Abaqus for SR-Site. The model is described in e.g. Åkesson et al. (2010).

The initial conditions of the bentonite backfill are the following:

ρ_d = 1,000 kg/m^3 (dry density),

p_0 = 50 kPa (swelling pressure),

u_0 = –50 kPa (pore water pressure).

Boundary and contact conditions

All contact surfaces between the rock wall and the bentonite have contact conditions. The contact conditions imply that a friction angle can be applied between the materials and that they can lose the contact between them. Full friction will be formed in the contact after a small displacement of the contact. The standard value of this displacement is 2 times the element length, which for the present element mesh means about 2 × 0.15 m = 0.3 m. This factor has been used in the first calculations shown below. Since this means that a rather large displacement is required the factor has been decreased in later calculations (see later).

Water is freely available in the rock surface.

The following calculation sequence has been used:

1. At first the rock block is locked to the rest or the rock.
2. Then the pore pressure of the bentonite is equalised for 10^{10} seconds (317 years).
3. Finally the locking of the rock block is released and the bentonite allowed to consolidate until the pore pressure is equalised.

Geometry

Three geometries based on Figure 6-4 have been modelled. Figure 6-6 shows the element mesh of two of the models. In the model the bentonite filled slot has been set to 2 m by mistake, which is more than the actual slot. This may have affected the results if the rock block moves. The larger slot the larger displacements will take place before equilibrium, which thus means that the calculations are somewhat pessimistic.

Geometry *a* corresponds to $\alpha = 20°$, $b = 4$ m and the height $h > b/\tan\alpha = 11$ m.

Geometry *b* corresponds to $\alpha = 20°$, $b = 4$ m and the height $h = b/\tan\alpha = 11$ m.

Both these geometries have been modelled in order to check the conclusion that the height *h* does not affect the result.

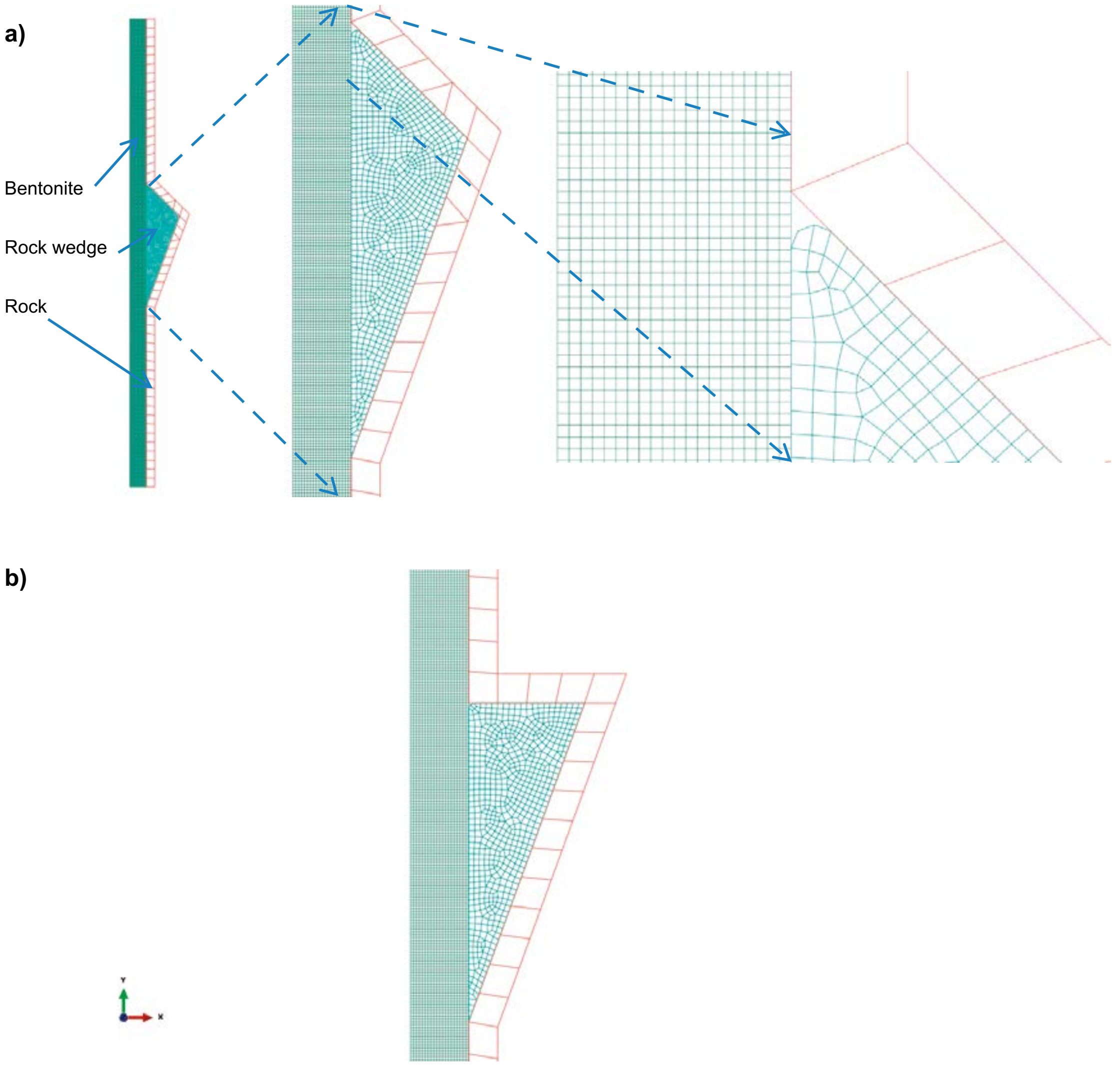

Figure 6-6. *Upper: Element mesh for geometry a. The left picture shows the entire mesh and the other two show details. Lower: Detail of the element mesh for geometry b.*

Calculations

Four main cases have been modelled. Cases 1–3 have the geometries shown in Figure 6-6. Case 4 has another geometry (that will be shown later).

In Cases 1–3 the bentonite has the dry density 1,000 kg/m^3, which yields the initial conditions:

u_0 = –50 kPa (pore water pressure),

p_0 = 50 kPa (average effective stress),

e_0 = 1.78 (void ratio).

Case 1a

$\varphi_r = 15°$, $b = 4$ m, $\alpha = 20°$, $\varphi_b = 0°$.

In this case the contact between the rock block and the bentonite is friction free and corresponds thus to the simplified analytical solution given by Equation (6-6). This case is not in equilibrium according to the analytical solution (see Figure 6-3). According to this solution the swelling pressure needs to be higher than 75 kPa.

The modelling results of this case are shown in Figure 6-7 to Figure 6-10. Figure 6-7 shows the displacement of the rock block as a function of time. During the first 10^{10} seconds the bentonite is allowed to form the swelling pressure against the rock and the fixed rock block. Then the block is released. The figure shows that the rock block moves during about $2 \cdot 10^9$ seconds (60 years) whereupon equilibrium is reached. The total displacement of the block is 25.5cm. The total width of the opened fracture is 20 cm.

Figure 6-8 shows contour plots of the total deformations. The figure also shows that the bentonite has swelled several meters into the opened fracture, but this penetration has been limited by shortcomings of the modelling technique and the element mesh and will probably be larger.

Figure 6-9 shows the distribution of the swelling pressure and the void ratio in the bentonite after equilibrium. The bentonite between the rock block and the silo has consolidated and the void ratio has decreased from 1.78 to about 1.73 and the average stress has increased from 50 kPa to about 65 kPa. Around the upper fracture opening the void ratio has increased and the average stress decreased substantially due to the penetration of bentonite into the fracture. In the lower part of the rock block the fracture has not been opened. Instead the block has slid down along the fracture.

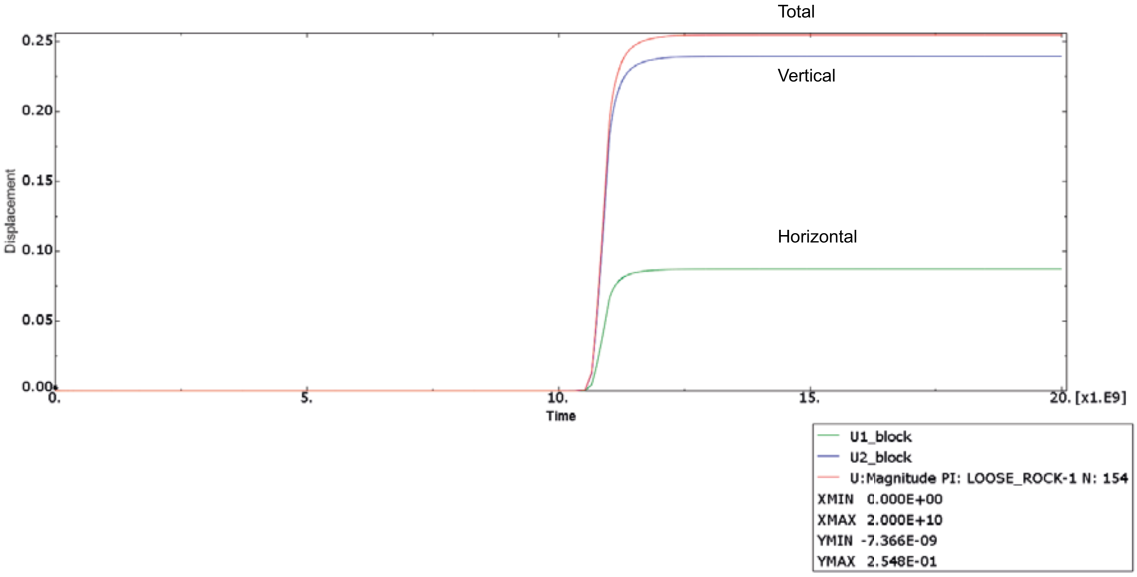

Figure 6-7. Case 1. Displacements of the rock block (m) as function of time (s). The rock block is released after10^{10} seconds.

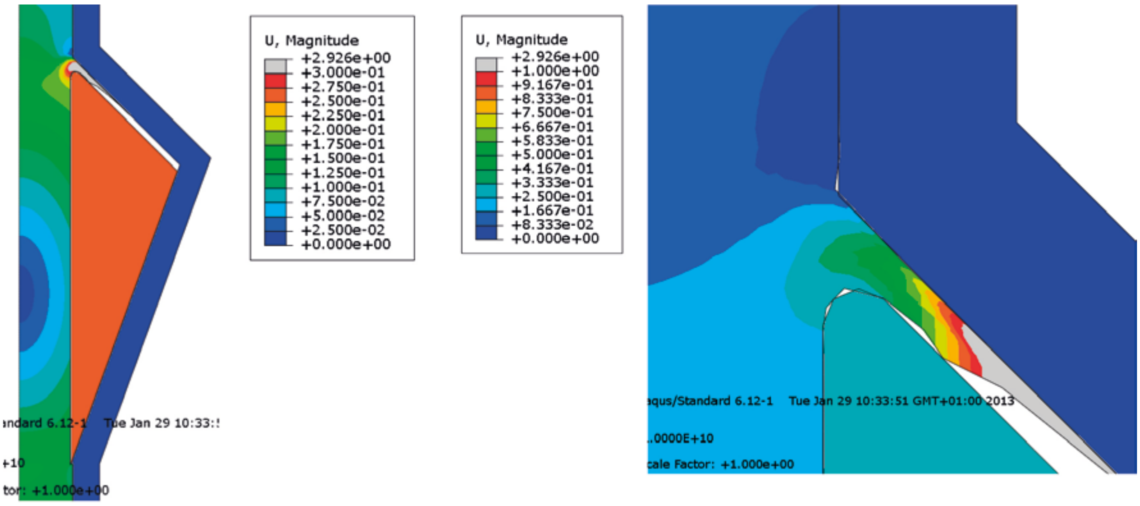

Figure 6-8. Case 1a. Total displacements (m) after equilibrium. The right picture is an enlargement of the area around the upper fracture

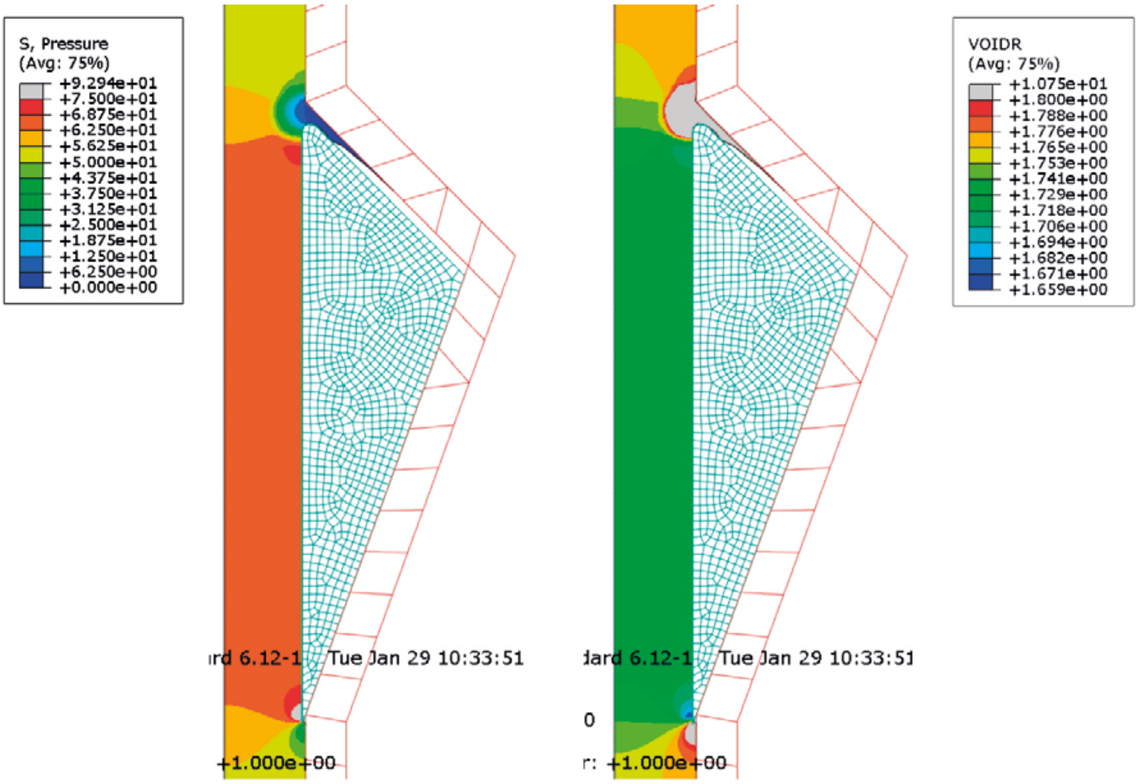

Figure 6-9. *Case 1a. Average stress (kPa) and void ratio in the bentonite after equilibrium.*

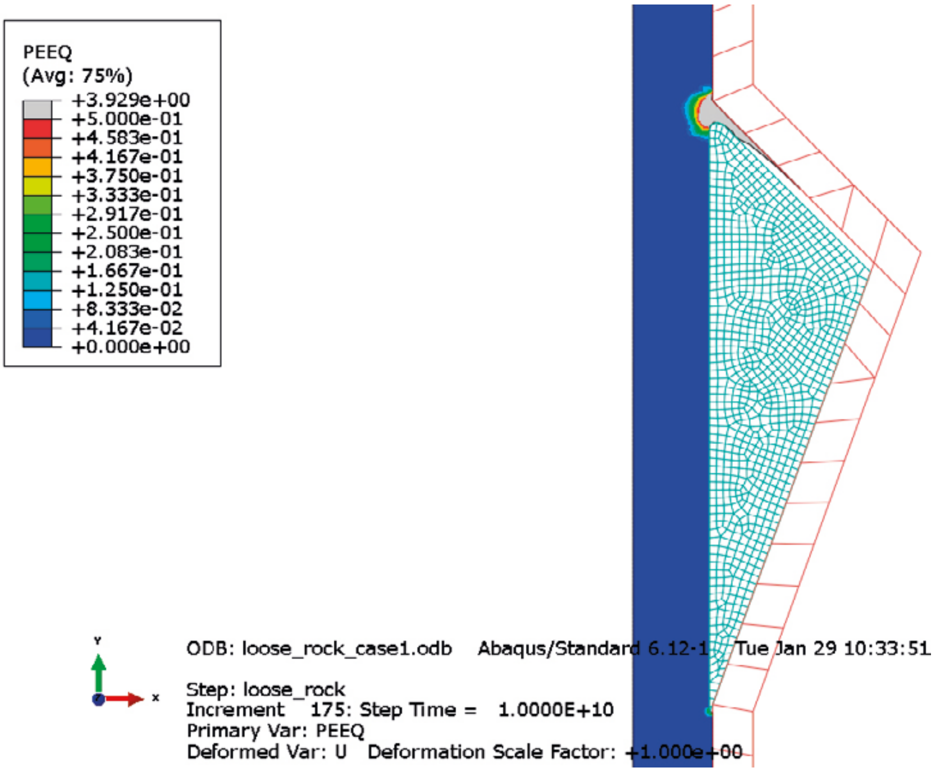

Figure 6-10. *Case 1. Plastic strains in the bentonite after 32 years.*

Figure 6-10 shows the plastic strains. The figure shows that there are no large plastic or shear strains except for around the fracture openings.

The finite element simulation confirms the analytical solution that predicts that the swelling pressure is too low to be able to withstand a rock fall. The simulations also show that the consequences of the rock fall is rather limited but that an opening of about 20 cm is created in the fracture above the rock block.

Case 2a

$\varphi_r = 15°$, $b = 4$ m, $\alpha = 20°$, $\varphi_b = 20°$

The difference between this case and case 1 is that the friction between the rock block and the bentonite has been added with a friction angle of 20 degrees, corresponding to the analytical solution shown in Equation (6-12). This case is on the verge of equilibrium (see Figure 6-5). The required swelling pressure is, according to the analytical solution, 50.7 kPa, i.e. somewhat higher than the actual pressure of 50 kPa.

This case (Figure 6-11 to Figure 6-15) yields the same result as case 1. Figure 6-11 shows the deformations in the rock blocks as a function of time. The figures shows that equilibrium has been reached after approximately 80 years ($2.5 \cdot 10^9$ seconds) after a total displacement of 13 cm. The total width of the open fracture is between 10 and 11 cm.

Figure 6-12 shows contour plots of the total deformations. It also shows that the bentonite has swelled into the upper opened fracture, but not more than approximately 25 cm. However, this penetration has been limited by shortcomings of the modelling technique and will probably be larger in reality. The calculated penetration is considerably smaller than for case 1, but this is mainly due to these shortcomings.

Figure 6-13 shows the distribution of the swelling pressure and the void ratio in the bentonite. The bentonite between the rock block and the silo has consolidated and the void ratio has decreased from 1.78 to approximately 1.71 in the lower part of the silo slot and the average stress has increased from 50 kPa to approximately 75 kPa in the same place. The difference between cases 1 and 2 is here clearly demonstrated, since the friction means that the block drags bentonite down and consolidates the bentonite more in the lower part than in the upper part.

Figure 6-14 shows the plastic strains. The figure shows that also in this case there are no large plastic or shear strains except for around the fracture openings.

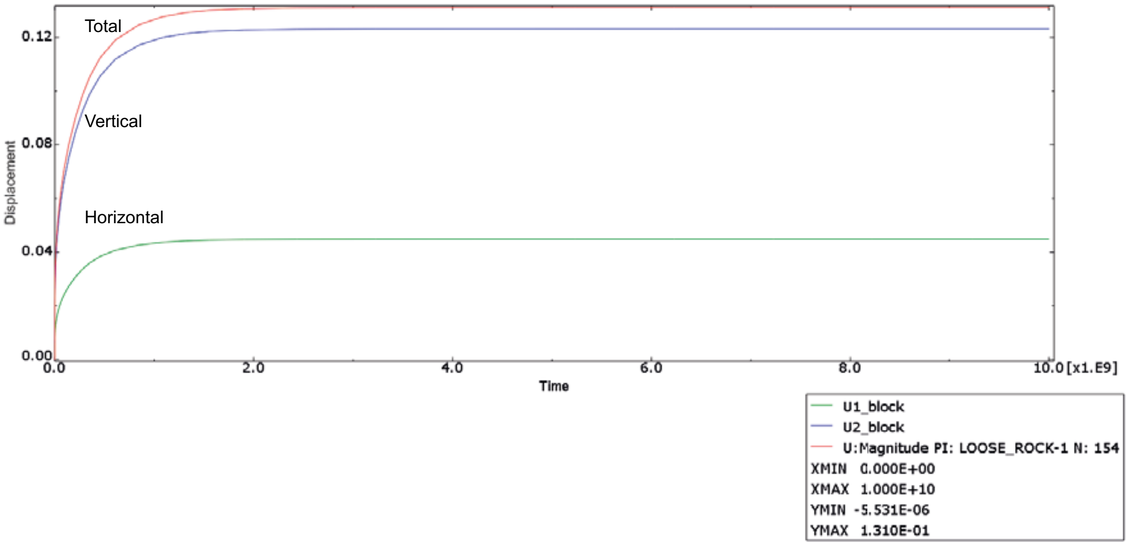

Figure 6-11. *Case 2a. Displacement of the rock block (m) as a function of time (s) after release of the rock block.*

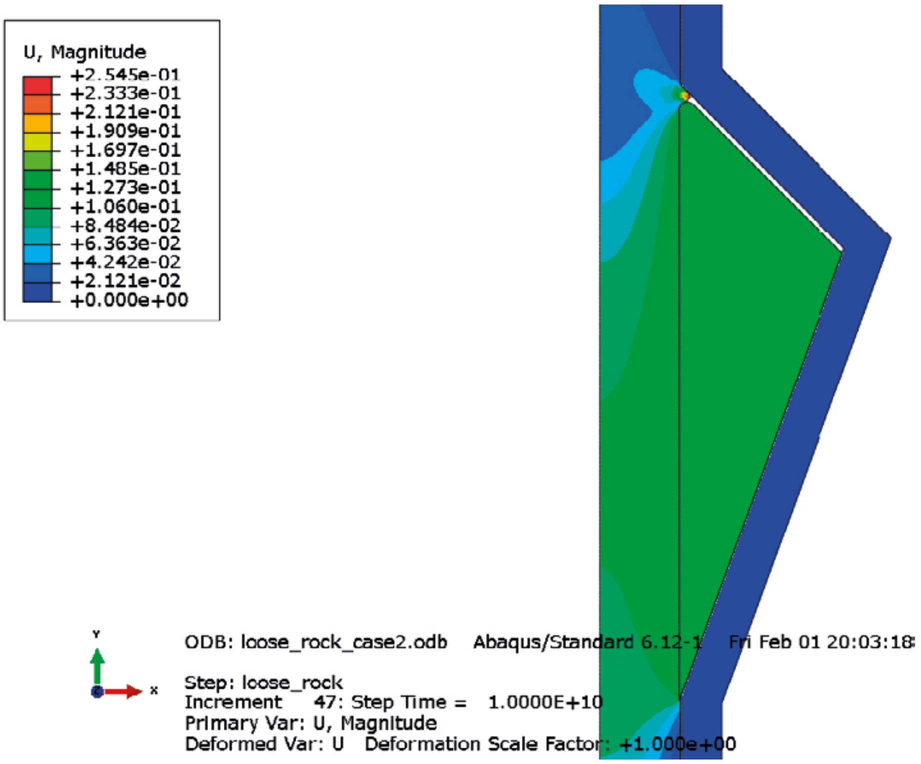

Figure 6-12. *Case 2a. Total displacements (m) after equilibrium.*

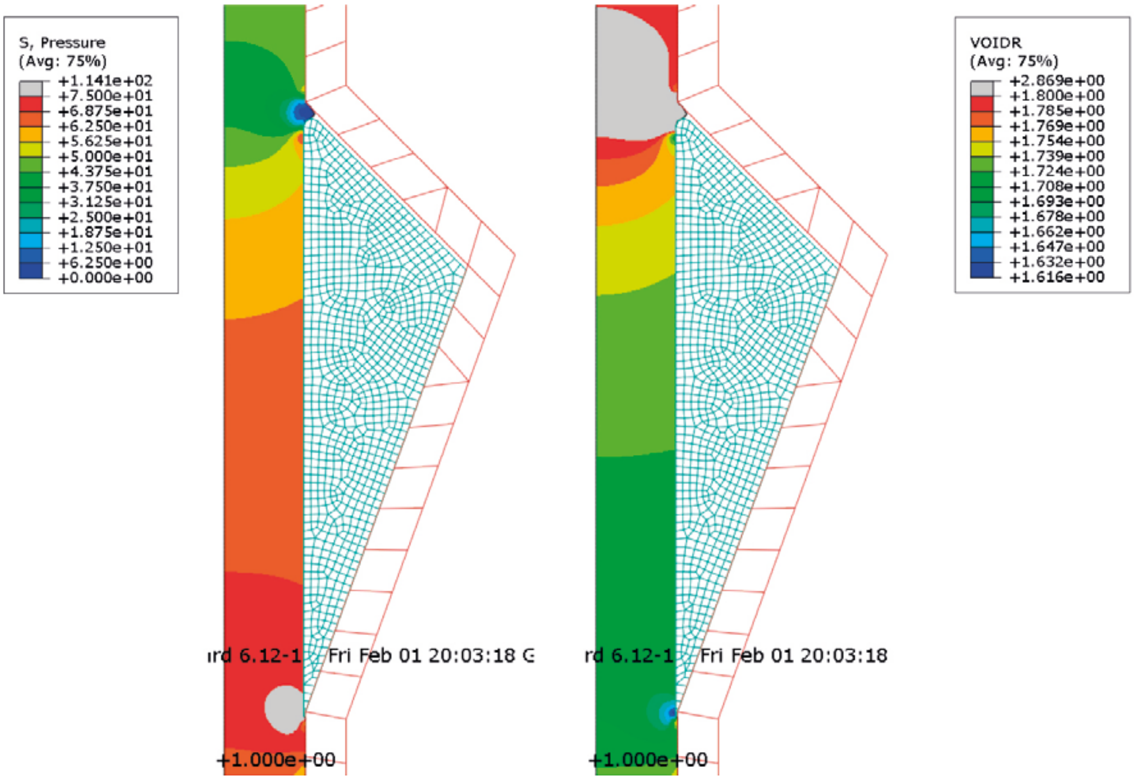

Figure 6-13. *Case 2a. Average stress (kPa) and void ratio in the bentonite after equilibrium.*

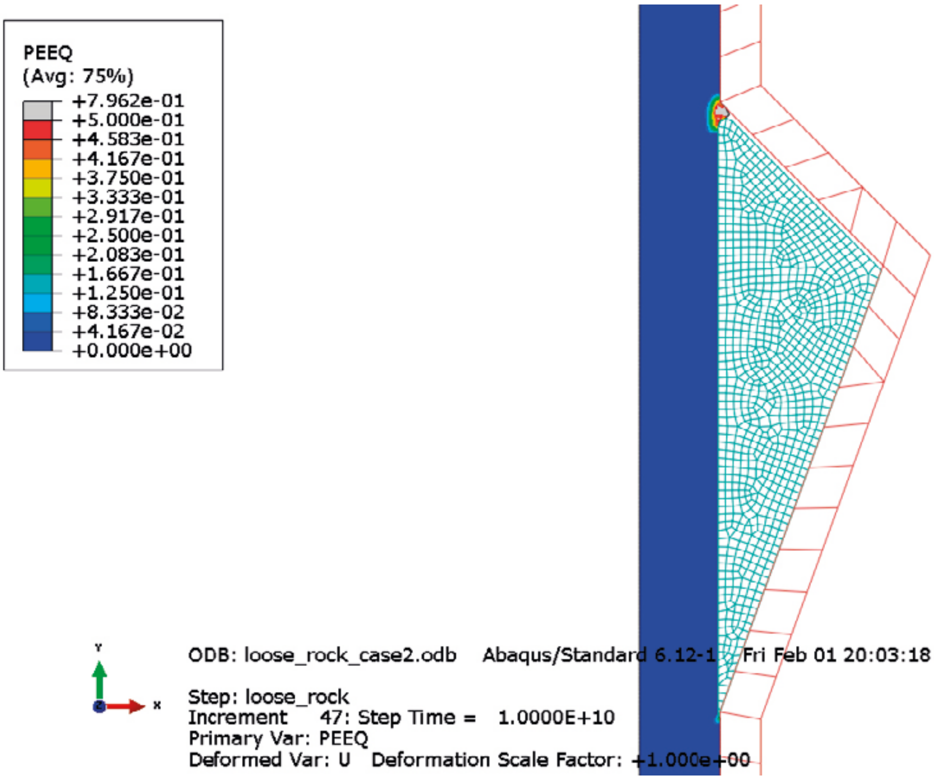

Figure 6-14. *Case 2a. Plastic strains in the bentonite after 32 years.*

The finite element simulation shows that the numerical calculation results in a large movement of the rock block, although smaller than for case 1. Also in this case this is in agreement with the analytical solution, in spite the small margin to a required swelling pressure. Despite this, the consequences of the rock fall is limited, just as for case 1, and an opening of 10–11 cm is created in the fracture above the block.

Case 2b

$\varphi_r = 15°$, $b = 4$ m, $\alpha = 20°$, $\varphi_b = 20°$

The difference between case 2b and case 2a is the height of the rock block, which is smaller (h = 11 m). This is shown in Figure 6-6b. According to the analytical solution this case should yield the same result, which is insufficient resistance to fall out. The necessary swelling pressure is 50.7 kPa, i.e. somewhat higher than the actual swelling pressure.

The same result are shown for this case as for case 2a (Figure 6-15 to Figure 6-18). Figure 6-15 shows the displacements of the rock block as a function of time. The figure shows that the total movement of the block is 11.5 cm, which can be compared to 13 cm for case 2a. The total width of the open fracture is just over 10 cm.

Figure 6-16shows contour plots of the total deformation after equilibrium. It also shows that the bentonite has not swelled into the fracture at all, even though this is just as large as in case 2a. The reason is probably that the rock corner above the fracture is more sharp (90 degrees), which thus results in larger calculation problems. This might also be an explanation why the displacement of the rock block is somewhat smaller.

Figure 6-17 shows the distribution of the swelling pressure and the void ratio in the bentonite after equilibrium. The bentonite between the rock block and the silo has consolidated and the void ratio has decreased from 1.78 to approximately 1.71 in the lower part of the silo slot, and the average stress has increased from 50 kPa to approximately 75 kPa in the same place, i.e. very similar to case 2a. The only difference is that the bentonite has been affected on a lesser distance, obviously due to the rock block having a smaller height.

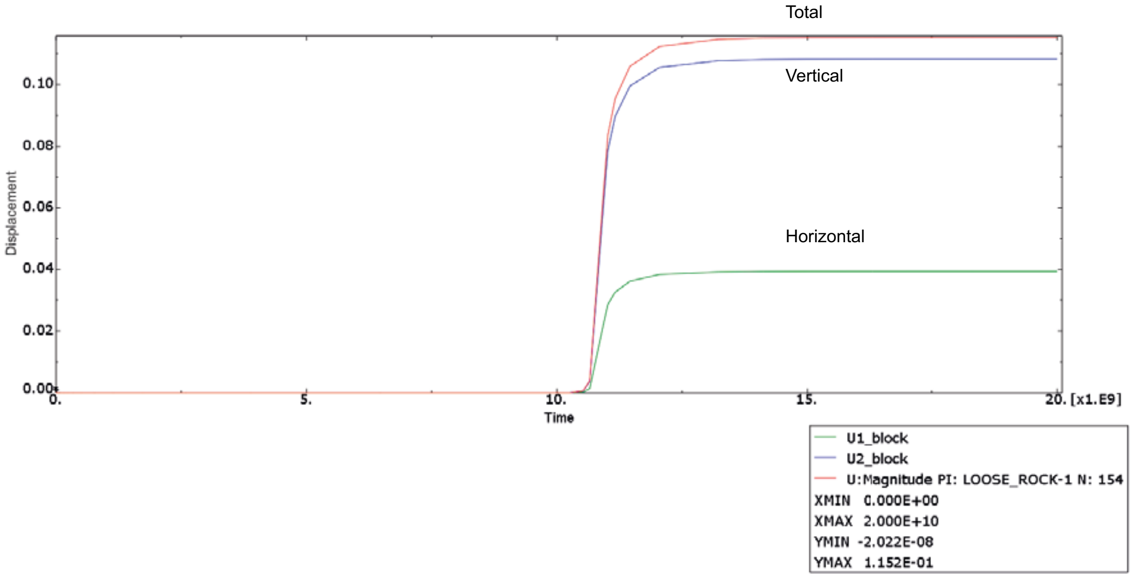

Figure 6-15. *Case 2b. Displacements of the rock block (m) as function of time (s). The rock block is released after*10^{10} *seconds.*

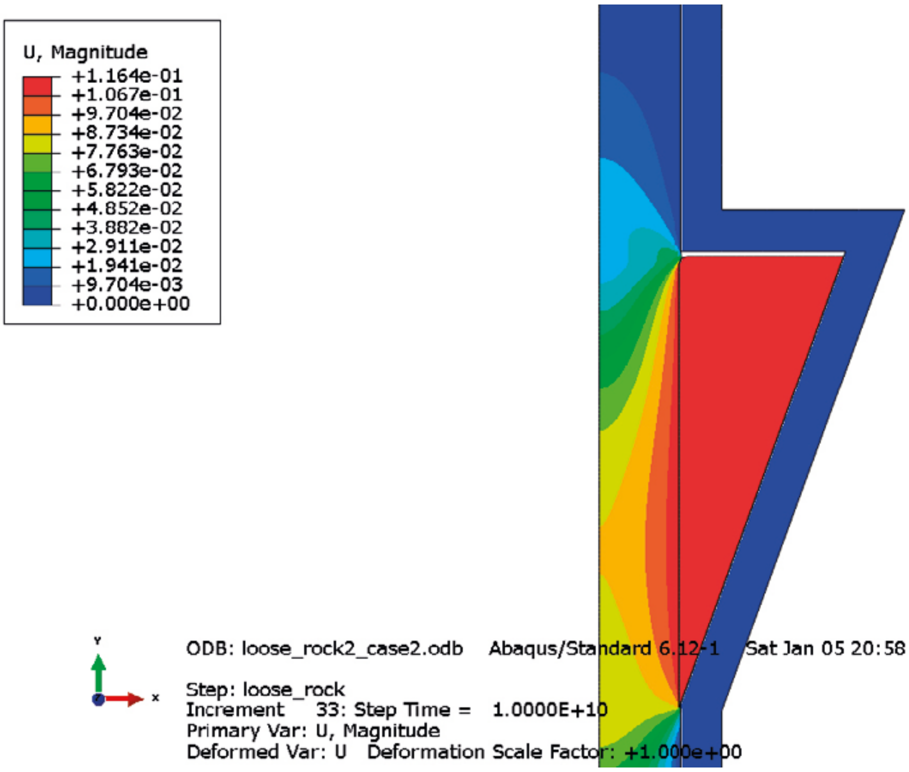

Figure 6-16. *Case 2b. Total displacements (m) after equilibrium.*

Figure 6-18 shows the plastic strains, which are just as small as in case 2a, except for around the upper fracture opening where there are no large strains since the bentonite does not penetrate into the fracture in the calculation of case 2b.

The finite element simulation shows a great similarity in the results between case 2a and case 2b, which confirms the analytical solution conclusion that the height of the rock block has no impact on the result.

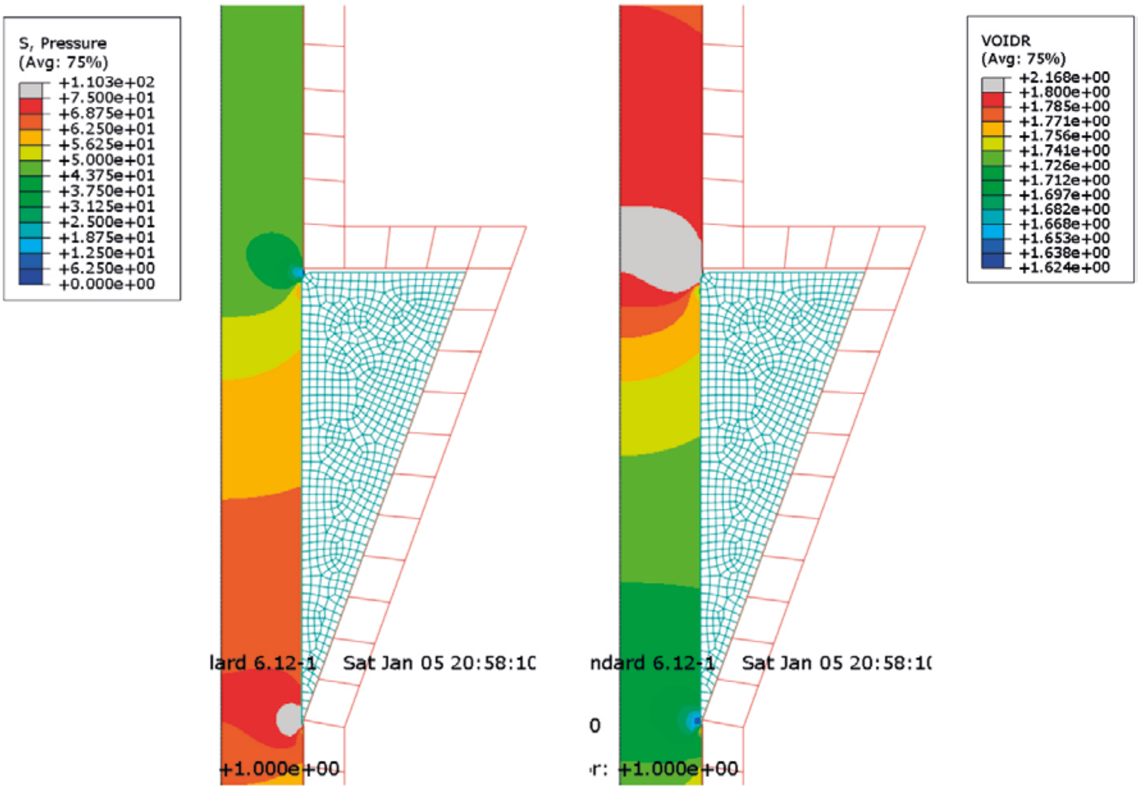

Figure 6-17. *Case 2b. Average stress (kPa) and void ratio in the bentonite after equilibrium.*

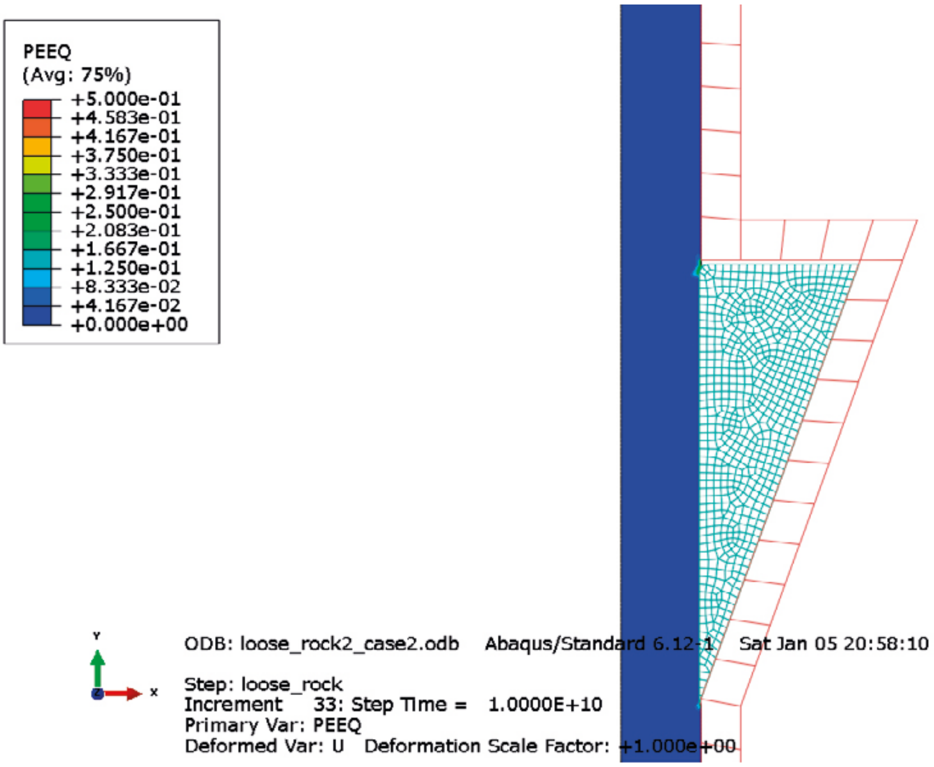

Figure 6-18. *Case 2b. Plastic strains in the bentonite after equilibrium.*

Case 3a

$\varphi_r = 35°$, $b = 4$ m, $\alpha = 20°$, $\varphi_b = 20°$

This case differs from case 2 in that the friction in the rock fractures (between rock block and rock) is 35° instead of 15°. This case is, with a certain margin, in equilibrium from start according to the analytical solution (see Figure 6-5).

Figure 6-19 shows the deformations of the rock block as a function of time. The figure shows that the total movement of the block is very small or less than 1 mm. The total width of the open facture is, according to calculations, just above 0.5 mm.

Figure 6-20 shows the distribution of the swelling pressure and the void ratio in the bentonite after equilibrium. The only change in the bentonite is the swelling into the small opening that was made in the fracture opening of the upper fracture on calculation technical reasons (to facilitate the penetration modelling).

The finite element simulation shows that the swelling pressure is large enough to keep the rock block in place, which is in accordance with the analytical calculation.

Case 4

This case is modelled with the same material model but has a smaller rock block and lower bentonite density and swelling pressure. The dry density ρ_d= 633 kg/m^3 corresponds to the void ratio 3.39 and yields a swelling pressure of only 10 kPa.

Initial conditions:

$u_0 = -10$ kPa,

$p_0 = 10$ kPa,

$e_0 = 3.39$.

Since such low swelling pressure according to Figure 6-5 only can withstand rock fall out of small rock blocks the following parameters have been chosen for this case:

$\varphi_r = 15°$, b = 2 m, $\alpha = 40°$, $\varphi_b = 20°$

The element model is shown in Figure 6-21.

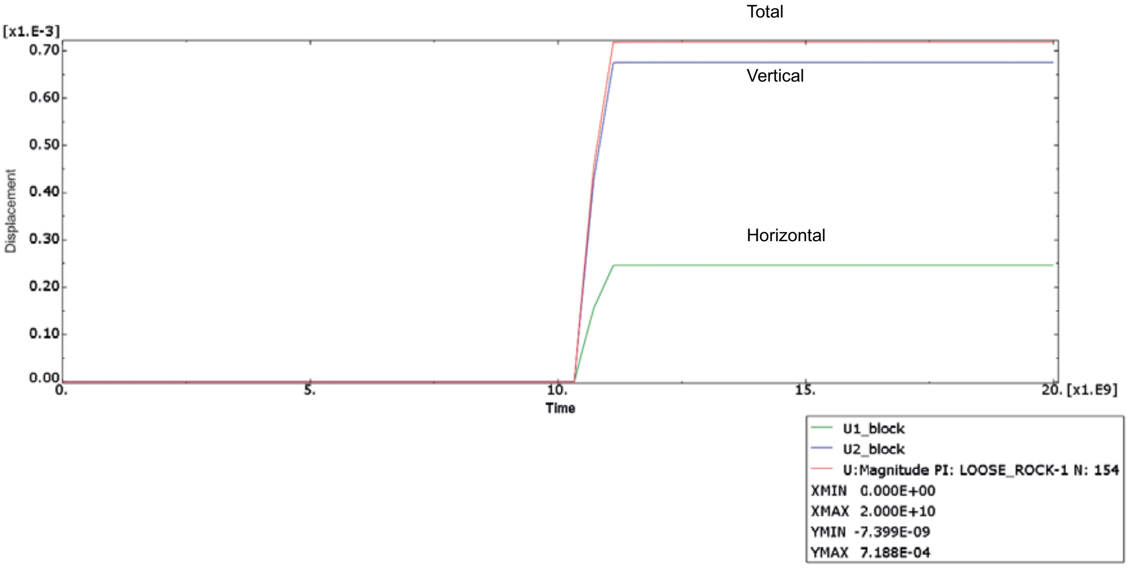

Figure 6-19. *Case 3a. Displacements of the rock block (m) as function of time (s). The rock block is released after10^{10} seconds.*

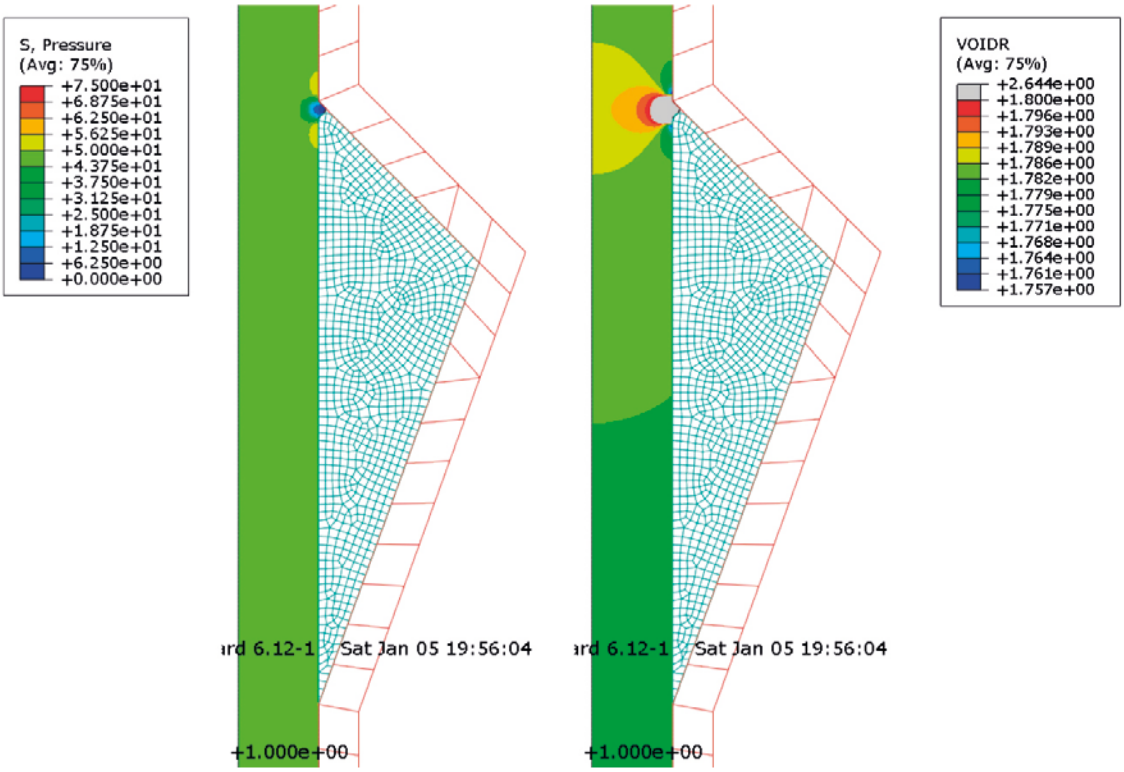

Figure 6-20. *Case 3a. Average stress (kPa) and void ratio in the bentonite after equilibrium.*

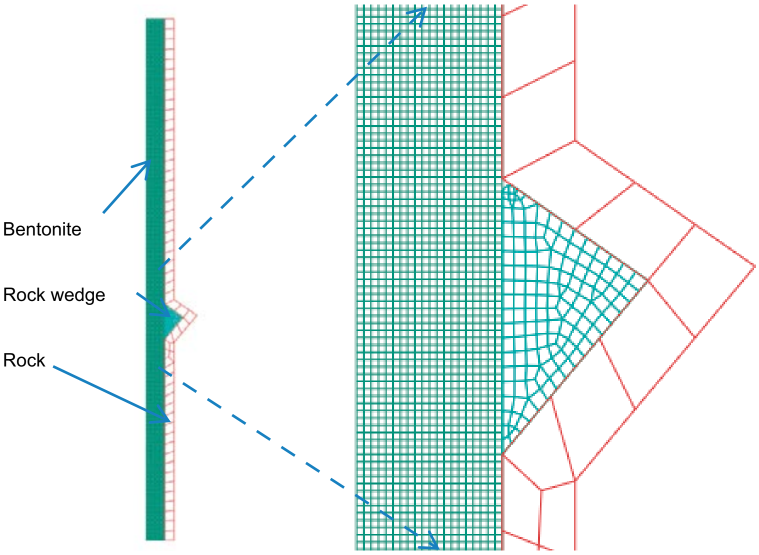

Figure 6-21. *Element mesh for calculation case 4.*

According to Figure 6-5 the required swelling pressure of the bentonite filling for keeping the rock block in place is 15 kPa, i.e. large movements are expected at a swelling pressure of 10 kPa.

The same types of figures are shown for this case.

Figure 6-22 shows the displacement of the rock block as a function of time. The figure shows that equilibrium is reached after a fairly long period of time, and that the total movement of the block is just over 8 cm. The total width of the fracture is also approximately 8 cm.

Figure 6-23 shows a contour plot of the total deformations. It also shows that there is no bentonite penetration into the fracture, which is due to the above mentioned limitation in the calculation technique.

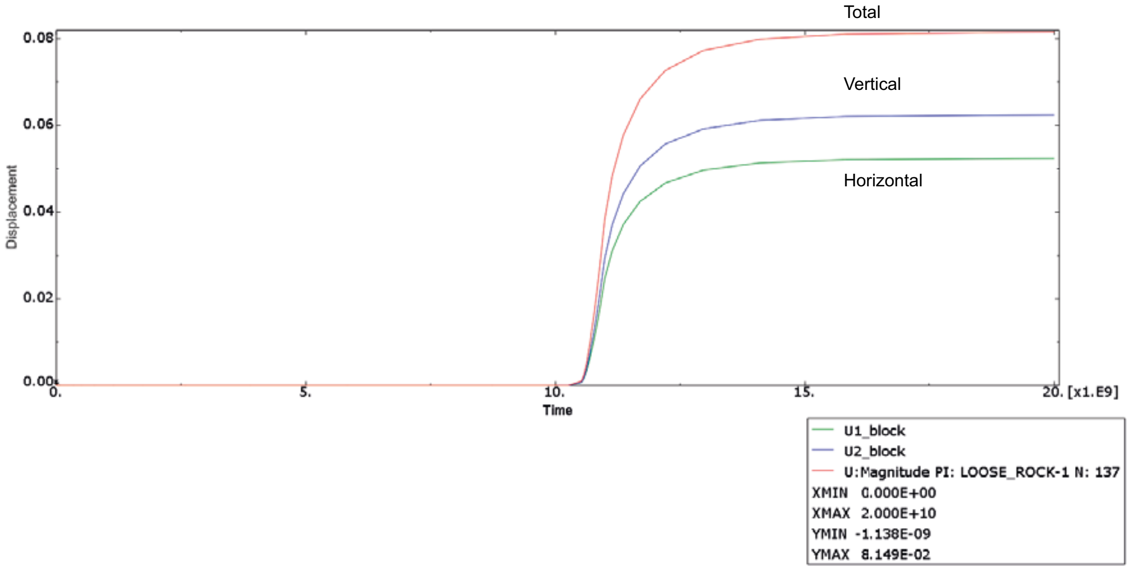

Figure 6-22. *Case 4. Displacements of the rock block (m) as function of time (s). The rock block is released after10^{10} seconds.*

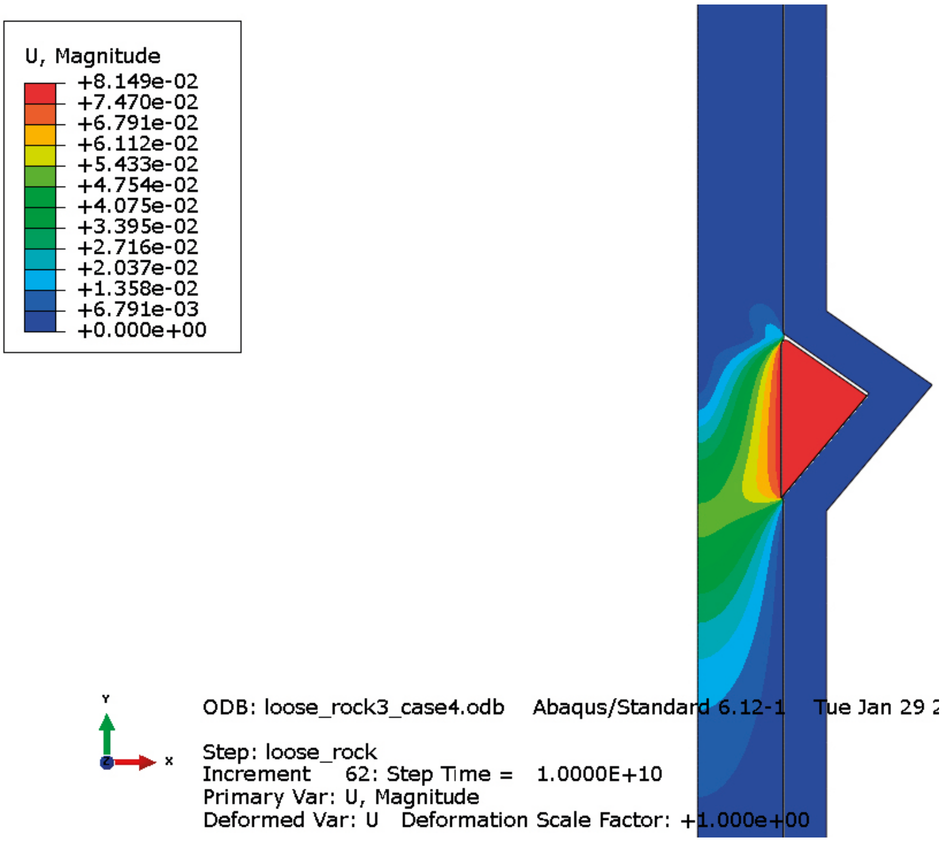

```
ODB: loose_rock3_case4.odb    Abaqus/Standard 6.12-1    Tue Jan 29 2

Step: loose_rock
Increment    62: Step Time =    1.0000E+10
Primary Var: U, Magnitude
Deformed Var: U   Deformation Scale Factor: +1.000e+00
```

Figure 6-23. *Case 4. Total displacements (m) after equilibrium.*

Figure 6-24 shows the distribution of the swelling pressure and the void ratio in the bentonite after equilibrium. The bentonite between the rock block and the silo has consolidated and the void ratio has decreased from 3.39 to approximately 3.30 in the lower part of the silo slot by the block, and the average stress has increased from 10 kPa to approximately 15 kPa in the same place.

Also this model confirms the analytical solution.

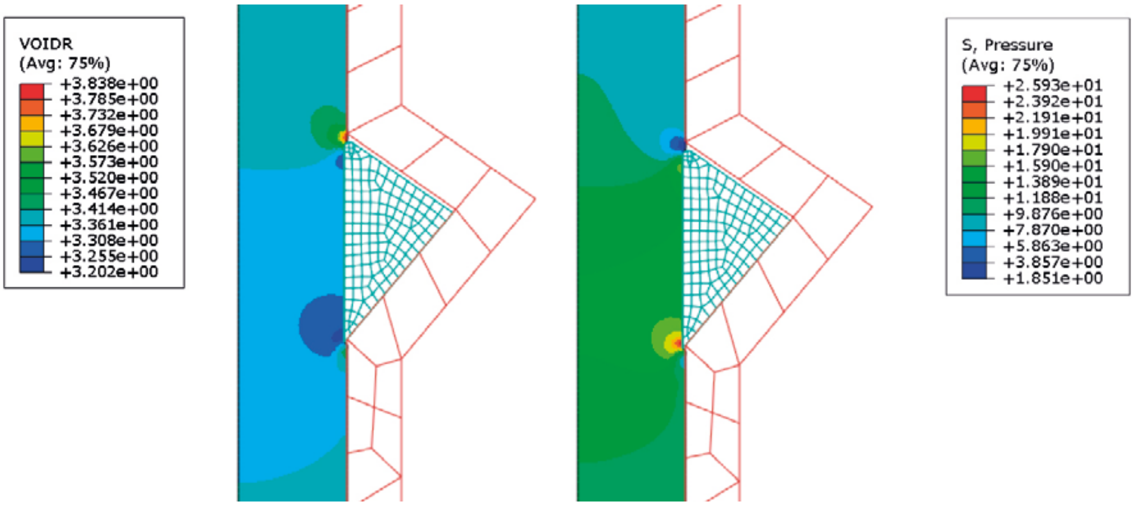

Figure 6-24. *Case 4. Void ratio and average stress (kPa) in the bentonite after equilibrium.*

Some additional numerical calculations have been made for these cases. In order to investigate the sensitivity of the swelling pressure close to a theoretical equilibrium a number of simulations with a swelling pressure varying between 45 kPa and 75 kPa have been made for case 2a where, according to the analytical solution, equilibrium is reached at 50.7 kPa. Table 6-1 shows a compilation of the results from the shown calculations together with additional calculations, and also a comparison between analytical and numerical results.

Table 6-1. Simulations with Abaqus with parameter values and definitions of the parameters

Name	Case	φ_r (°)	b (m)	α (°)	φ_b (°)	h (m)	σ_{sa} kPa
Rock case1	1a	15	4	20	0	14.7	50
Rock2 case1	1b	15	4	20	0	10.99	50
Rock case2	2a	15	4	20	20	14.7	50
Rock2 case2	2b	15	4	20	20	10.99	50
Rock case3	3a	35	4	20	20	14.7	50
Rock2 case3	3b	35	4	20	20	10.99	50
Rock3 case4	4	15	2	40	20	3.69	10
Rock case2a	2a	15	4	20	20	14.7	45
Rock case2b	2a	15	4	20	20	14.7	50
Rock case2c	2a	15	4	20	20	14.7	55
Rock case2d	2a	15	4	20	20	14.7	60
Rock case2e	2a	15	4	20	20	14.7	65
Rock case2f	2a	15	4	20	20	14.7	70
Rock case2g	2a	15	4	20	20	14.7	75

φ_r = friction angle between the rock block and the rock.
b = horisontal width of the rock block.
α = bottom angle of the rock block.
φ_b = friction angle between rock (or rock block) and bentonite.
h = height of the rock block.
σ_{sa} = initial swelling pressure.

Table 6-2. Compilation of simulation results for the shown cases and some additional cases and comparison with analytical solutions.

Fall	Parameter values							Numerical calculation	Analytical calculation	
	φ_r (°)	b (m)	α (°)	φ_b (°)	h (m)	σ_{sa}[1] kPa	σ_{se}[2] kPa	Movement of rock block (mm)	Equilibrium?	σ_{sa}/σ_{se}
1a	15	4	20	0	>11	50	75	255	No	0.67
1b	15	4	20	0	11	50	75	236	No	0.67
2a	15	4	20	20	>11	50	50.7	131	Almost	0.986
2b	15	4	20	20	11	50	50.7	115	Almost	0.986
3a	35	4	20	20	>11	50	30	0.7	Yes	1.67
3b	35	4	20	20	11	50	30	0.7	Yes	1.67
4	15	2	40	20	–	10	15	81	No	0.67

[1] σ_{sa} = actual swelling pressure.

[2] σ_{se} = required swelling pressure according to analytical calculations.

Table 6-2 shows that there are large movements also close to a theoretical equilibrium. In order to study the movement of a rock block close to theoretical equilibrium a number of simulations of case 2a has been made, as shown in the lower part of Table 6-1. Since, as previously mentioned, large displacements have been needed to mobilize full friction between rock block and rock and the bentonite, this has been adjusted so as only a 0.1 mm displacement is necessary for full friction. Some other changes have been made to stiffen the model so that it is more in accordance with the analytical case.

Figure 6-25 shows the displacements of the rock block as a function of time for all calculated cases. Table 6-3 shows a compilation of these cases. Rock case 2b corresponds to Case 2a shown in Table 6-2. The only difference between the cases is the swelling pressure of the bentonite that has been varied between 45 and 75 kPa. The displacement of the block is 90 mm in the new calculation, compared to 131 mm in the old. The difference depends on the changes in the model.

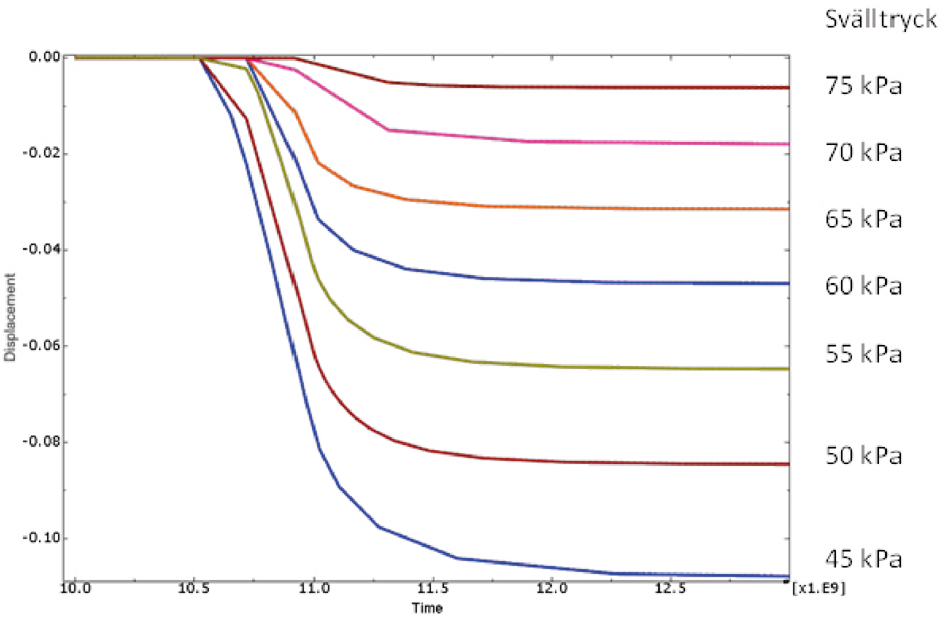

Figure 6-25. *Displacement of the rock block (m) as a function of time (s) for case 2a at different bentonite swelling pressures.*

Table 6-3. Modelling results for case 2a with variations in swelling pressure.

Name	Case	Parameter values							Numerical calculation	Analytical calculation	
		φ_r (°)	b (m)	α (°)	φ_b (°)	h (m)	σ_{sa}[1] kPa	σ_{se}[2] kPa	Movement of rock block (mm)	Equi-librium?	σ_{sa}/σ_{se}
Rock case2a	2a	15	4	20	20	>11	45	50.7	115.3	No	0.888
Rock case2b	2a	15	4	20	20	>11	50	50.7	90.0	No	0.986
Rock case2c	2a	15	4	20	20	>11	55	50.7	68.9	Yes	1.085
Rock case2d	2a	15	4	20	20	>11	60	50.7	50.0	Yes	1.183
Rock case2e	2a	15	4	20	20	>11	65	50.7	33.6	Yes	1.282
Rock case2f	2a	15	4	20	20	>11	70	50.7	19.2	Yes	1.381
Rock case2g	2a	15	4	20	20	>11	75	50.7	6.6	Yes	1.479

[1] σ_{sa} = actual swelling pressure.

[2] σ_{se} = required swelling pressure according to analytical calculations.

Table 6-3 and Figure 6-25 show that, in spite of theoretical equilibrium according to the analytical solution there will be large displacements of the rock block (7 cm) at a swelling pressure of 55 kPa. In order to reach a movement less than 1 cm it is necessary to have a swelling pressure of almost 75 kPa, i.e. a "safety factor" of 1.5.

The reason why equilibrium is not reached when there in theory should be force equilibrium is that the prerequisites for the analytical solution compared to the numerical differ in the following areas:

- In order to reach full friction between rock block and bentonite a movement of 0.1 mm is required.
- The upper part of the rock block is rounded which means that:
  - The counter pressure from the swelling pressure bears on a smaller vertical area than theoretically in the analytical solution.
  - The bentonite swells into the small opening, resulting in a vertical swelling pressure against the block that pushes the block downwards, and a diminished horizontal counter pressure on the upper part of the block depending on a decreased density in that part.

Conclusions

An analytical relationship, Equation (6-12), has been developed to establish the required swelling pressure of the bentonite of the silo to prevent large movements of rock blocks in the wall. The analytical solution, illustrated in Figure 6-5, shows that the blocks need to be very large and wedge-shaped in order to obtain large movements. For rock blocks that do not go further into the rock than 2 m less than 40 kPa swelling pressure is needed to keep the blocks in place for all possible combinations of form and friction angles.

A number of finite element calculations have been made in order to study how the blocks move under different conditions. These confirm the analytical solution, but also show that large movements can take place also in a theoretical initial equilibrium. The explanation probably is that all counter forces in reality and in the numerical calculations are not mobilized until after certain movements, and also that the upper part of the block is rounded in the numerical calculation.

To guarantee that the rock blocks are stuck to the wall and that there are no large openings between the blocks and the rock there should be a safety factor of 1.5–2.0 in the bentonite swelling pressure, if the analytical solution is used for the analysis.

Results from FE-calculations of rock blocks that don't fulfil the swelling pressure requirements, show that there may be a substantial displacement. However, they also show that the consequence is a consolidation of the bentonite and subsequent increase in swelling pressure that ends in a stable situation with a remaining substantial thickness of the bentonite barrier.

6.4 Analytical observation of the ceiling fill

The interaction between possible ceiling fill of bentonite and rock blocks in the rock ceiling has also been analytically studied (see Figure 6-26). This case is simple, since only the gravitation and a counter swelling pressure affect the result. Wedge-shaped blocks with $\beta > 90$ degrees have not been taken into consideration. A triangular rock block in the ceiling with the height h and the width b is considered:

The rock block is affected (per meter length into the plane) of the gravity F and the force from the swelling pressure S (kN):

$\mathrm{F} = mg = \rho_b hbg/2$,

where ρ_b = rock density (2.7 kg/dm^3) ,

$\mathrm{S} = \sigma_s b$,

where σ_s = swelling pressure from the bentonite (kPa) .

Equilibrium in vertical direction yields:

$$\sigma_s b = \rho_b hbg/2 , \tag{6-13}$$

$$\sigma_s = \rho_b hg/2 , \tag{6-14}$$

$$\sigma_s = 13.5h , \tag{6-15}$$

For example, at a swelling pressure of σ_s = 100 kPa h might be up 7.4 m independent of width b and angle α.

If a rectangle instead of a triangle is assumed the weight will be doubled. That case is the most critical one, and means that the height only can be h = 3.7 m.

If a ”safety factor” of 1.5 is added to the swelling pressure, the swelling pressure 40 kPa will keep all block shapes with depth less than 2 m in place.

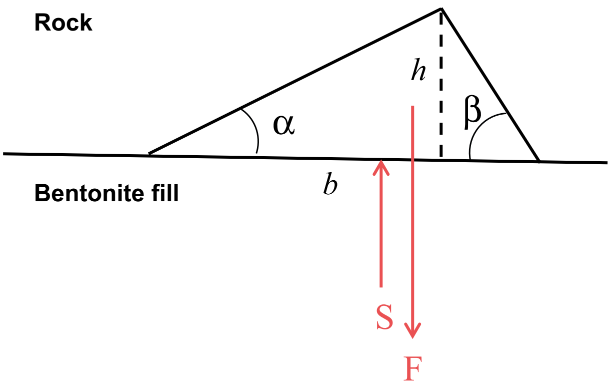

__Figure 6-26.__ Geometry and forces that affect a triangular rock block in the ceiling in contact with a bentonite fill.

7 Possible influence of gas on the silo bentonite barrier

There are several processes which generates gas in SFR. The main source is corrosion of metal components, in particular concrete reinforcements and various containers, but also degradation of organic materials and radiolysis do contribute (Moreno et al. 2001).

Disregarding the evacuation pipes, the SFR silo is planned to be fully embedded in bentonite and bentonite/sand mixtures. As bentonite is known to have rather limited mass transfer capacity in general, and for gas in particular, it is therefore of interest to investigate possible interaction between generated gas in the silo and its bentonite components. In particular, it is of importance to investigate if possible damaging, high gas pressure build-up could be conceived of.

If the evacuation pipes are functional, there is no reason to assume any significant gas pressure build-up within the silo. Here is therefore considered the case of non-functional pipes. This consideration utilizes the general bentonite/gas interaction description given in Birgersson et al. (2008).

7.1 Lab tests

In order to check that the gas migration behavior of the GEKO/QI bentonite complies with the description in Birgersson et al. (2008), a small lab study was conducted. A single sample of nominal density 1,250 kg/m^3 was prepared by compacting room dry bentonite powder in a test cell to a sample of height 5 mm and diameter 35 mm. The sample was subsequently water saturated by deionized water supplied via sintered filters. The axial force was measured by means of a force transducer in the top of the cell. The cell schematics are shown in Figure 7-1.

After water saturation, the bottom inlet was pressurized by a pressure controlling unit (PCU) (from GDS instruments). The tube connecting the test cell with the PCU was filled with air. As the bottom filter at this point still was water saturated, the pressurization situation was as illustrated in Figure 7-2a; water from the PCU pushing on the air, pushing on the residual water in the filter.

Thus, initially after pressurization, the fluid in contact with the clay was water. This water, however, subsequently flowed through the sample, thus being replaced in the filter by the tailing air (Figure 7-2b). By performing the gas pressurization test in this way, it could be assured that the sample was water saturated. Moreover, the pressure response of the bentonite is very different when pressurization is done by water as compared to gas (Birgersson and Karnland 2015). The recorded sample pressure response, deduced from the axial force measurement, can therefore be conveniently utilized for judging when air is the pressurizing fluid.

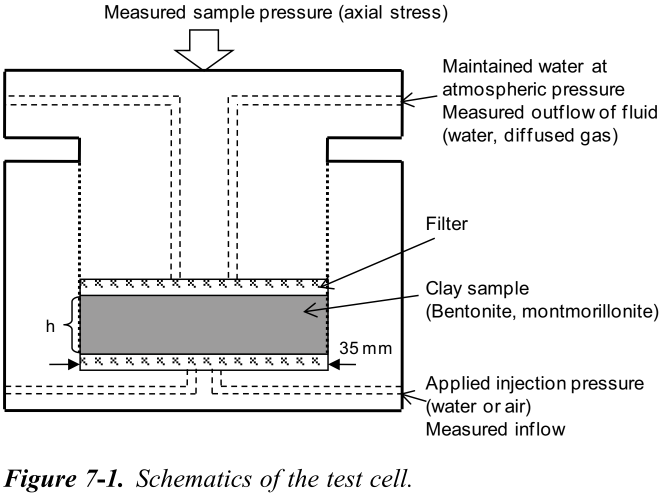

***Figure 7-1.** Schematics of the test cell.*

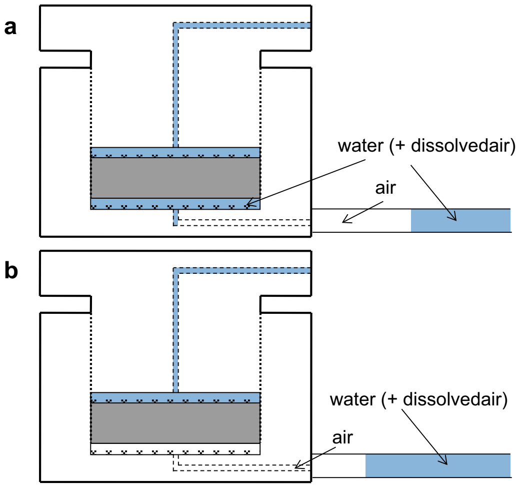

Figure 7-2. *The principle behind the gas pressurization test. Initially (a), the inlet filter is water saturated. As this water is pushed on by air (which, in turn, is pushed on by water from the pressure controlling unit), it flows through the sample. In the final state (b) air has replaced the water in the inlet filter and is now the pressurizing fluid.*

Figure 7-3 shows the sample pressure response as an injection pressure of 500 kPa was applied to the sample in the manner just described. Initially the sample pressure increased from ca 1,030 kPa to ca 1,250 kPa. This is the signature response for pressurizing with water; under these conditions the sample pressure is expected to increase approximately by half the value of the applied water pressure. After approximately 20 hours with basically constant sample pressure, a rather sudden drop was initialized. This signifies that the pressurizing water at this stage is starting to be replaced by air. After a transient period, the sample pressure is seen to even-out at basically the initial pressure (1,080 kPa). This is the expected equilibrium response when gas (and other non-polar fluids) is pressurizing bentonite at a pressure below that of the sample itself. The only interaction between the gas phase and the bentonite sample at this point is a diffusive transport of dissolved gas.

The volumetric flux through the sample was measured during the course of the described water/air pressurization and is also plotted in Figure 7-3. The flux evolution gives an additional strong indication that pressurizing fluids are being exchanged during the course of pressurization; the volumetric flux drops from an initial value of ca $7\cdot10^{-9}$ m/s when water is flowing to ca $1\cdot10^{-9}$ m/s when air is has replaced the water in the inlet filter. The initial value of the flow (water) corresponds to a hydraulic conductivity of $7\cdot10^{-13}$ m/s (the hydraulic gradient is 10,000 m/m), which is in line with other measurements on the GEKO/QI material (Dueck et al. 2015).

From the volumetric air flow, q, a diffusion coefficient for dissolved air in the bentonite can be calculated (Birgersson and Karnland 2015).

$$D_e = q \cdot \frac{K_H \cdot h}{RT} \frac{P_{outlet}}{P_{inlet} - P_{outlet}} \tag{7-1}$$

where K_H is Henry's constant, R is the universal gas constant, T absolute temperature, h the sample height (Figure 7-1) and P denotes (absolute) pressures on the two sides of the sample. Plugging in relevant values in the above equation, and using a value of $K_H = 0.16$ MPa/mM which corresponds to the solubility of pure nitrogen gas in bulk water (Sander 1999), gives $D_e = 6.5\cdot10^{-11}$ m^2/s. This is a reasonable diffusion coefficient for bentonite, confirming that diffusive flux is the only significant active mass transfer mechanism. It may be noted, though, that the present diffusion coefficient for GEKO/QI bentonite is about twice as small as the corresponding value evaluated for MX-80 bentonite at comparable density (Birgersson and Karnland 2015).

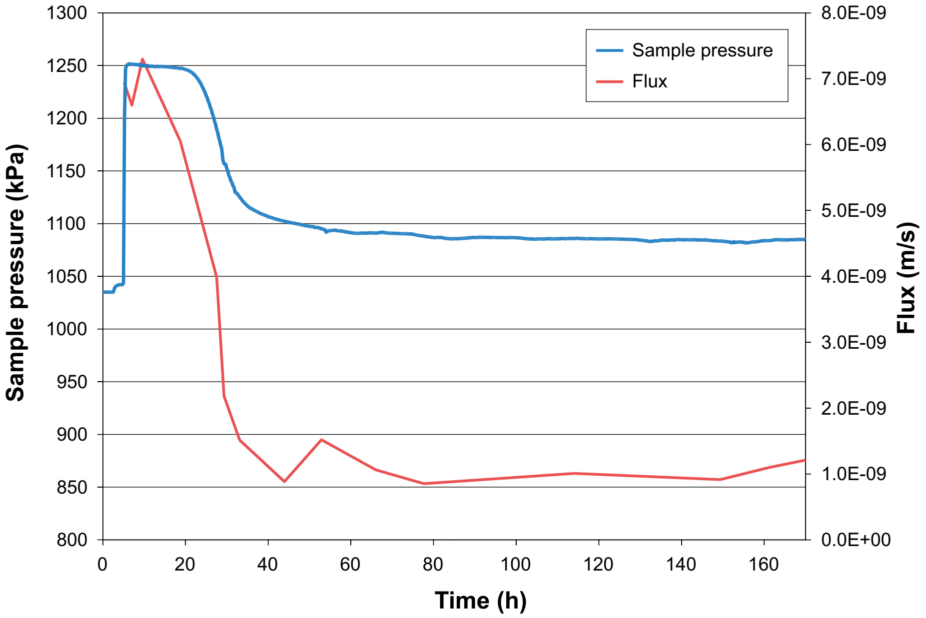

Figure 7-3. *Sample pressure and volumetric flux evolution during the first pressurization stage. Injection pressure is 500 kPa during the entire time span.*

After the above described pressurization phase, several others were initiated, at higher injection pressures (700–900 kPa). However, in none of these pressurization phases a steady-state gas/clay interface was able to be maintained. Instead, gas breakthrough event were induced in the transient state where water was being replaced by the air. In these events, the gas phase very quickly (in a matter of minutes) passed through the sample. These kind of breakthrough events have in earlier tests, made on pure montmorillonites and MX-80 benonite, basically only been induced at pressures at or above the sample pressure (Birgersson and Karnland 2015). The scope of the present test is, however, too small, in order to draw conclusions on whether the mechanical properties of the GEKO/QI bentonite is significantly different than compared to e.g. MX-80; since only one sample was tested there is not much data for a statistical analysis.

After termination of the test, the water content of the sample was determined by weighing before and after oven drying (105°C, > 24 h). The water-to-solid mass ratio was in this way determined to 0.49, which corresponds to a dry density of 1,175 kg/m^3 and porosity 58% (assuming a grain density of 2,800 kg/m^3).

7.2 Estimations

As concluded from a rather large set of tests of gas migration on bentonite and montmorillonite (Birgersson and Karnland 2015), the general picture is that diffusion is the only mass transfer mechanism for gas when the gas pressure is below the pressure of the bentonite. When the gas pressure exceeds the bentonite pressure, on the other hand, mechanical interaction between the two phases are inevitable. This mechanical interaction may manifest itself as gas breakthrough events, or possibly as consolidation of the clay phase (with only diffusive transfer in the bentonite). Although gas breakthrough events were induced below the sample pressure in the single GEKO/QI sample here tested, we will still make the above assumptions regarding gas migration in the silo (after all, a stable state without mechanical interaction between gas and clay, with only diffusive mass transfer was demonstrated at 500 kPa), and now estimate the diffusive mass transfer capacity of the silo bentonite, when it is fully water saturated.

The main contribution to gas generation in the silo is due to metal corrosion (Moreno et al. 2001). Among the metals, aluminum is estimated to corrode so quickly that it can be ruled out that the silo bentonite is completely saturated before the aluminum source has exhausted. Excluding therefore the contribution from aluminum corrosion, the initial gas generation rate due to metal corrosion in the silo is dV/dt = 836 Nm^3/y (Moreno et al. 2001) (volume measured at standard temperature and pressure). This rate may be translated to moles/s using the ideal gas law:

$$\frac{dn}{dt} = \frac{dV}{dt} \cdot \frac{P_{std}}{RT_{std}} = 1.07 \cdot 10^{-3} \text{ moles/s} \ , \tag{7-2}$$

where P_{std} = 100 kPa and T_{std} = 298.15 K is assumed (R = 8.31 J/(mol·K) is the universal gas constant).

The total area of the external surfaces of the silo, through which the escaping gas must pass is:

$$A_{tot} = 2 \cdot \pi (14 \text{ m})^2 + 53 \text{ m} \cdot 2\pi \cdot 14 \text{ m} = 5893.6 \text{ m}^2 \ , \tag{7-3}$$

where a silo radius of 14 m and height of 53 m is assumed. Thus the mean flux due to the initial gas generation rate is

$$j_{av.} = \frac{1}{A_{tot}} \frac{dn}{dt} = 1.82 \cdot 10^{-7} \text{ mol}/(\text{s} \cdot \text{m}^2) \ , \tag{7-4}$$

If this flux should be maintained by diffusion over the bentonite we must have (assuming a 1D-geometry)

$$j_{av.} = -D_e \frac{c_{rock} - c_{concrete}}{L} \ , \tag{7-5}$$

where D_e is the effective diffusion coefficient for hydrogen gas in the bentonite, L is the diffusion length (i.e. the thickness of the silo bentonite), c_{rock} is the concentration of dissolved gas at the rock side of the bentonite, and $c_{concrete}$ is the concentration on the concrete wall side. Assuming $c_{rock} = 0$, and that the concentration on the concrete wall side is set by Henry's law:

$$c_{concrete} = \frac{P_{concrete}}{K_H^{H_2}} \ , \tag{7-6}$$

where $K_H^{H_2}$= 0.13 MPa/mM is Henry's constant for hydrogen gas in bulk water and $P_{concrete}$ is the gas pressure at the concrete wall side, we get (combining equations 7-5 and 7-6)

$$P_{concrete} = \frac{j_{av.} \cdot L \cdot K_H^{H_2}}{D_e} = 2.33 \cdot 10^{-8} \text{ MPa} \cdot \text{m/s} \cdot \frac{L}{D_e} \ , \tag{7-7}$$

This is thus the pressure that must be maintained at the concrete wall side of the bentonite in order to achieve the initial mean gas flux (assuming 1D).

The diffusion coefficient for air at density 1,175 kg/m^3 was determined to $6.5 \cdot 10^{-11}$ m^2/s (section 7.1). Based on the values of diffusivity for nitrogen and hydrogen in bulk water, which have a ratio of about 2.4, it may be argued that the hydrogen diffusivity should be a factor ~ 2.4 higher. Furthermore, as the silo density is considerably lower than the density of the tested sample, the hydrogen diffusivity in the silo is expected to be even larger. Based on measured values of small ions (Cl^- and Na^+) in montmorillonite of various density (Kozaki et al. 2005, 2001), the difference in diffusivity between 1,200 kg/m^3 and 1,000 kg/m^3 in density can be argued to be a factor ~ 1.5. Finally, a transformation of an effective diffusivity between different densities should involve a porosity ratio, in this case equal to 0.64/0.58 = 1.1. Putting all the estimated factors together motivates an increase of the measured air diffusivity value by a factor 2.4·1.5·1.1 ≈ 4 when estimating the hydrogen diffusivity in the silo:

$$D_e \sim 4 \cdot 6.5 \cdot 10^{-11} \text{ m}^2/\text{s} = 2.6 \cdot 10^{-10} \text{ m}^2/\text{s} \ , \tag{7-8}$$

Figure 7-4 displays the resulting pressure (equation 7-7) as a function of the length of the bentonite for this value of diffusivity. Included are also two cases having somewhat larger and somewhat lower values.

The result in Figure 7-4 demonstrates that pressure build-up may be very high – in the order of hundreds of MPa for realistic parameter values (L ~ 1 m). In all cases, the required pressure is many times larger than the pressure of the silo, which is in the other of 1–2 MPa (including the hydraulic head).

The performed analysis thus suggests that the silo, viewed as a pure bentonite barrier, does not have the capacity to transport away the generated gas in a pure diffusive fashion since the sum of the swelling pressure of the bentonite and the hydraulic head is far below these estimates.

The evaluated pressure above (Figure 7-4), which widely exceeds the initial pressure of the silo bentonite, should not be viewed as a realistic value which will be achieved in the silo. Rather, it should be viewed as an indication that other processes than pure diffusion will occur if gas generation of this rate is ongoing while the silo bentonite is water saturated and the excavation pipes are dysfunctional.

Under circumstances where the gas pressure exceeds the bentonite pressure, it has been demonstrated that mechanical interaction between the gas phase and the bentonite will inevitably occur (Birgersson and Karnland 2015). Furthermore, when such interaction occur, the gas has been shown to preferentially follow paths at interfaces between bentonite and other materials. A probable scenario is therefore that the gas will propagate to the bottom of the silo where it will escape through the bentonite/sand mixture. As this mixture contains 90% sand, it will reasonably contain bentonite/sand interfaces at the pore scale to such an extent that gas can escape there in a controlled manner. Should these types of interfaces not be active, however, the action of a mechanically interacting gas phase with water saturated bentonite cannot be fully predicted, with today's process knowledge.

7.3 Conclusions

The GEKO/QI bentonite was shown in a lab test to behave in essence as expected of bentonite materials, i.e. the gas phase does not replace water in a two-phase processes (as is expected in more conventional soils), but rather interacts directly (mechanically) with the full clay phase. Based on the measured air diffusivity, an estimation of the diffusive mass transfer capacity of the silo bentonite show that mechanical interaction between gas and bentonite most probably will occur if the silo bentonite is water saturated, while gas is still generated at large rates, and if the excavation pipes do not function. It is a very difficult task to forecast the details of such mechanical interaction, but a reasonable scenario is that gas will escape through the bentonite/sand mixture in the bottom, since this material contains many continuous interfacial pathways (sand/bentonite).

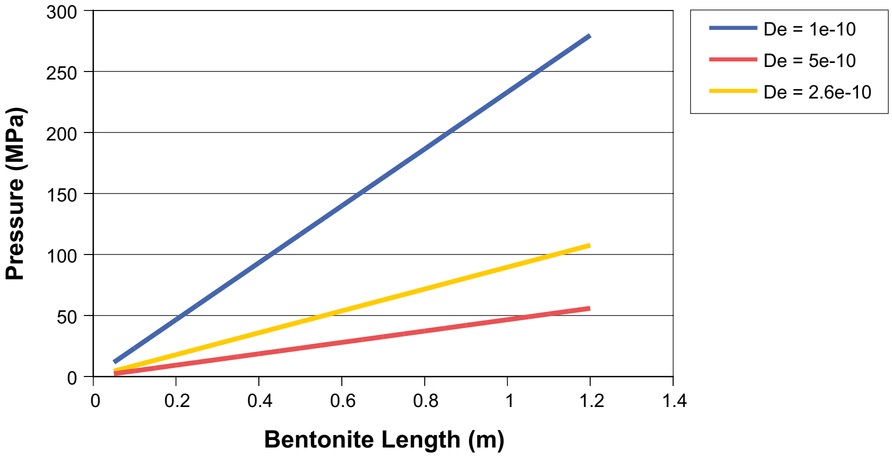

Figure 7-4. *Pressure which should be maintained at the concrete wall side of the silo bentonite in order to maintain an average diffusive flux corresponding to the gas generation rate due to metal corrosion according to the presented model.*

References

SKB's (Svensk Kärnbränslehantering AB) publications can be found at www.skb.se/publications. References to SKB's unpublished documents are listed separately at the end of the reference list. Unpublished documents will be submitted upon request to document@skb.se.

Birgersson M, Karnland O, 2015. Flow and pressure repsonse in compacted bentonite due to external fluid pressure. SKB TR-14-28, Svensk Kärnbränslehantering AB.

Birgersson M, Åkesson M, Hökmark H, 2008. Gas intrusion in saturated bentonite – A thermodynamic approach. Physics and chemistry of the Earth 33, S248–S251.

Börgesson L, Johannesson L-E, Sandén, T, Hernelind J 1995. Modelling of the physical behaviour of water saturated clay barriers. Laboratory tests, material models and finite element application. SKB TR 95-20, Svensk Kärnbränslehantering AB.

Carlsson A, Christiansson R, 2007. Construction experiences from underground works at Forsmark. Compilation report. SKB R-07-10, Svensk Kärnbränslehantering AB.

Crank J, 1975. The mathematics of diffusion. 2nd ed. Oxford: Oxford University Press.

Dueck A, Johannesson L-E, Andersson L, Jensen V, 2015. Investigation of hydraulic and mechanical processes of the barriers embedding the silo in SFR. Laboratory tests. SKB TR-15-05, Svensk Kärnbränslehantering AB.

Hedenblad G, 1996. Materialdata för fukttransportberäkningar. Stockholm: Byggforskningsrådet. (In Swedish.)

Holmén J G, Stigsson M, 2001. Modelling of future hydrogeological conditions at SFR. SKB R-01-02, Svensk Kärnbränslehantering AB.

Karnland O, Olsson S, Nilsson U, 2006. Mineralogy and sealing properties of various bentonites and smectite-rich clay materials. SKB TR-06-30, Svensk Kärnbränslehantering AB.

Kozaki T, Inada K, Sato S, Ohashi H, 2001. Diffusion mechanism of chloride ions in sodium montmorillonite. Journal of Contaminant Hydrology 47, 159–170.

Kozaki T, Fujishima A, Saito N, Sato S, Ohashi H, 2005. Effects of dry density and exchangeable cations on the diffusion process of sodium ions in compacted montmorillonite. Engineering Geology 81, 246–254.

Lundin J, 2012. SFR Kontrollprogram, Bergkontroll. Bergkontrollgruppens årsrapport 2011 (med bilagor). AE-NCS 12-006, Vattenfall. (In Swedish.)

Moreno L, Skagius K, Södergren S, Wiborgh M, 2001. Project SAFE. Gas related processes in SFR. SKB R-01-11, Svensk Kärnbränslehantering AB.

Pusch R, 2003. Design, construction and performance of the clay-based isolation of the SFR silo. SKB R-03-30, Svensk Kärnbränslehantering AB.

Sander R, 1999. Compilation of Henry's law constants for inorganic and organic species of potential importance in environmental chemistry. Version 3. Available at: http://www.henrys-law.org/henry-3.0.pdf

SKB, 1993. Slutförvar för radioaktivt driftavfall – SFR 1. Slutlig säkerhetsrapport. Reviderad utgåva – Maj 1993. Svensk Kärnbränslehantering AB. (In Swedish.)

SKB, 2008. Safety analysis SFR 1. Long-term safety. SKB R-08-130, Svensk Kärnbränslehantering AB.

SKB, 2014. Initial state report for the safety assessment SR-PSU. SKB TR-14-02, Svensk Kärnbränslehantering AB.

UPC, 2013. CODE_BRIGHT, User's guide. Available at: https://www.etcg.upc.edu/recerca/webs/code_bright/code_bright

Åkesson M, Börgesson L, Kristensson O, 2010. SR-Site Data report. THM modelling of buffer, backfill and other system components. SKB TR-10-44, Svensk Kärnbränslehantering AB.

Öhman J, Follin S, 2010. Site investigation SFR, Hydrogeological modeling of SFR. Data review and parametrisation of model version 0.1. SKB P-09-49, Svensk Kärnbränslehantering AB.

Unpublished documents

Åkesson M, 2013. 1.4 Bentonites other than MX-80. Clay Technology. SKBdoc 1415875 ver 1.0, Svensk Kärnbränslehantering AB.

Appendix A

Theory

The theory used in the Code_Bright solver has its roots in a traditional geomechanical porous formulation, see UPC (2013). The formulation is based on considering the material a mixture of the constituents:

- minerals, liquid water, dissolved air, water vapor, and dry air.

The constituents may be considered belonging to the elements:

- minerals (*m*), water (*w*), and air (*a*),

and it is assumed that the constituents can be divided into the immiscible phases:

- solid (*s*), liquid (*l*), and gas (*g*).

The solid phase only consists of the element minerals, so the element index (*m*) will not be written in the following. As a basic assumption in the formulation, all constituents have a common temperature, *T*.

From the structural assumptions of the mixture, primitive entities may be introduced:

- mixture volume element (dv),
- solid volume (dv_s),
- liquid volume (dv_l),
- gas volume ($dv_g = dv - dv_s - dv_l$), and
- pore volume ($dv_p = dv - dv_s$).

Further primitive entities, regarding mass are introduced for the constituents:

- solid mass (dm_s),
- water mass in liquid (dm_l^w),
- air mass dissolved in liquid (dm_l^a),
- water mass in gas (i.e. water vapor mass) (dm_g^w),
- dry air mass in gas (dm_g^a).

With use of the above the definitions below are formulated:

- porosity ($n = dv_p/dv$),
- solid density ($\rho_s = dm_s/dv_s$),
- liquid water mass per liquid phase volume ($\theta_l^w = dm_l^w/dv_l$),
- dissolved air mass per liquid phase volume ($\theta_l^a = dm_l^a/dv_l$),
- water vapor mass per gas phase volume ($\theta_g^w = dm_g^w/dv_g$),
- dry air mass per gas phase volume ($\theta_g^a = dm_g^a/dv_g$),
- liquid degree of saturation ($S_l = dv_l/dv_p$), and
- gas degree of saturation ($S_g = \mathrm{dv_g/dv_p}$).

Using the entities above, the water mass and air mass per mixture volume element can be expressed as:

$$\frac{dm^w}{dv} = \frac{dm_l^{\ w} + dm_g^{\ w}}{dv} = \theta_l^{\ w} S_l n + \theta_g^{\ w} S_g n \quad \text{and} \tag{A-1}$$

$$\frac{dm^a}{dv} = \frac{dm_l^{\ a} + dm_g^{\ a}}{dv} = \theta_l^{\ a} S_l n + \theta_g^{\ a} S_g n\ , \tag{A-2}$$

respectively. If introducing source terms $\{f^w, f^a\}$ and fluxes of water and air in the liquid and gas phase, $\{\boldsymbol{j}_l^w, \boldsymbol{j}_l^a\}$ and $\{\boldsymbol{j}_g^w, \boldsymbol{j}_g^a\}$, the continuity equations:

$$\frac{\partial}{\partial t}\left(\theta_l^{\,w} S_l n + \theta_g^{\,w} S_g n\right) + \nabla \cdot \left(\boldsymbol{j}_l^{\,w} + \boldsymbol{j}_g^{\,w}\right) = f^{\,w} \text{ and} \tag{A-3}$$

$$\frac{\partial}{\partial t}\left(\theta_l^{\,a} S_l n + \theta_g^{\,a} S_g n\right) + \nabla \cdot \left(\boldsymbol{j}_l^{\,a} + \boldsymbol{j}_g^{\,a}\right) = f^{\,a}, \tag{A-4}$$

can be formulated for water and air mass, respectively.

To close the formulation, variables are selected as independent or dependent and material specific constitutive relations are specified where dependent variables are given by expressions of independent variables. In the formulation used within Code_Bright a phenomenological approach towards specifying the constitutive relations is adopted. Below, functions that give values of variables are indicated with ~ above the variable name.

The mass fluxes are additively decomposed in terms of a non-advective (diffusive), $\boldsymbol{i}_\alpha^{\,i}$, and an advective, $\theta_\alpha^{\,i}\,\boldsymbol{q}_\alpha$, contribution, according to:

$$\boldsymbol{j}_\alpha^{\,i} = \boldsymbol{i}_\alpha^{\,i} + \theta_\alpha^{\,i} \boldsymbol{q}_\alpha, \quad \alpha = l, g,\ i = w, a, \tag{A-5}$$

where following relations apply for the non-advective fluxes:

$$\sum_{i=w,a} \boldsymbol{i}_\alpha^{\,i} = 0, \quad \alpha = l, g. \tag{A-6}$$

The advective mass fluxes are taken to be described by Darcy's law:

$$\theta_l^{\,w} \boldsymbol{q}_l^{\,w} = \theta_l^{\,w} \frac{-\boldsymbol{k} k_{rl}}{\mu_l}\left(\nabla p_l - \rho_l \boldsymbol{g}\right) \text{ and} \tag{A-7}$$

$$\theta_g^{\,a} \boldsymbol{q}_g^{\,a} = \theta_g^{\,a} \frac{-\boldsymbol{k} k_{rg}}{\mu_g}\left(\nabla p_g - \rho_g \boldsymbol{g}\right), \tag{A-8}$$

where gradients of liquid and gas pore pressures (which should be considered as defined by chemical potentials) have been introduced. In the following the pore pressures will for brevity be denoted pressure. The relative permeabilities, k_{rl} and k_{rg}, are given by:

$$\tilde{k}_{rl}(S_l) = A_l S_l^{\,\delta_l} \text{ or } \sqrt{S_l}\left(1 - (1 - S_l^{\,1/\lambda})^{\lambda}\right)^2 \text{ and} \tag{A-9}$$

$$\tilde{k}_{rg}(S_g) = A_g S_g^{\,\delta_g}, \tag{A-10}$$

respectively, and $\boldsymbol{g} = -9.81\boldsymbol{e}_z$, $\boldsymbol{e}_z$ denoting a unit vector in the direction opposite to the field of gravity.

The non-advective mass fluxes are taken as described by Fick's law:

$$\boldsymbol{i}_g^{\,w} = -\tau n \rho_g S_g D_m^{\,w} \boldsymbol{I} \nabla\left(\theta_g^{\,w} / \rho_g\right) \text{ and} \tag{A-11}$$

$$\boldsymbol{i}_l^{\,a} = -\tau n \rho_l S_l D_m^{\,a} \boldsymbol{I} \nabla\left(\theta_l^{\,a} / \rho_l\right), \tag{A-12}$$

i.e. concentration driven diffusion, where the diffusion coefficients, $D_m^{\,w}$ and $D_m^{\,a}$, are given by:

$$\tilde{D}_m^{\,w}(p_g, T) = D^w (273.15 + T)^n / p_g \text{ and} \tag{A-13}$$

$$\tilde{D}_m^{\,a}(T) = D^a \exp\left(-Q / (R(273.15 + T))\right), \tag{A-14}$$

respectively.

The liquid degree of saturation is related to the liquid pressure by use of a retention law, here given by an expression of Van Genuchten:

$$\tilde{S}_l(p_l, p_g) = \left(1 + \left(\frac{p_g - p_l}{p_0}\right)^{1/(1-\lambda)}\right)^{-\lambda}, \tag{A-15}$$

and from the definitions, the gas degree of saturation is given by:

$$\tilde{S}_g(p_l, p_g) = 1 - \tilde{S}_l(p_l, p_g). \tag{A-16}$$

Below it is used that $p_g = p_g^a + p_g^w$ and $\rho_l = \theta_l^a + \theta_l^w$. Here:

$$\tilde{\rho}_l(p_l, T) = \rho_{l0} \exp\big(\beta(p_l - 0.1) - \alpha T\big), \tag{A-17}$$

$$\tilde{\theta}_l^a(p_l, p_g, T) = \tilde{\rho}_l(p_l, T)\big(p_g - \tilde{p}_g^{\,w}(T)\big)\frac{M_a}{HM_w}, \text{ and} \tag{A-18}$$

$$\tilde{p}_g^{\,w}(T) = 136075 \exp\big(-5239.7/(273.15+T)\big), \tag{A-19}$$

are used. The relation $\rho_g = \theta_g^a + \theta_g^w$ holds for the gas phase. Here:

$$\tilde{\theta}_g^a(p_g, T) = \frac{\big(p_g - \tilde{p}_g^{\,w}(T)\big)M_a}{R(273.15+T)} \text{ and} \tag{A-20}$$

$$\tilde{\theta}_g^w(p_l, p_g, T) = \frac{\tilde{p}_g^{\,w}(T)M_w}{R(273.15+T)} \exp\left(\frac{-(p_g - p_l)M_w}{R(273.15+T)\tilde{\rho}_l(p_l, T)}\right) \tag{A-21}$$

are used. Left to be specified are viscosities of the liquid and gaseous phase:

$$\tilde{\mu}_l(T) = 2.1 \cdot 10^{-12} \exp\left(\frac{1808.5}{273.15+T}\right) \text{and} \tag{A-22}$$

$$\tilde{\mu}_g(p_g, T) = 1.48 \cdot 10^{-12} \left(\frac{\sqrt{273.15+T}}{1+\dfrac{119.4}{273.15+T}}\right) \frac{1}{1+\dfrac{0.14-1.2\cdot 10^{15}k}{p_g}}, \tag{A-23}$$

respectively.

The closed formulation, in which a constant temperture is prescribed (here $T = 15$°C), may be solved for the adopted indepentents, liquid and gas pore pressure.

In the present report, however, a constant gas pressure ($p_g = 0.1$ MPa) and no diffusive vapor transport has been adopted as well. Thus, liquid pressure becomes the only unknown variable.

A.1 Numerical solution

The Code_Bright manual gives an expression describing the equation system to be solved for each time step $k+1$. (UPC 2013, Equation 11 in Chapter V). If adopting $\varepsilon = \beta = 1$ in this expression, as used in the performed simulations:

$$\boldsymbol{r}(\boldsymbol{X}^{k+1}) = \frac{\boldsymbol{d}(\boldsymbol{X}^{k+1}) - \boldsymbol{d}(\boldsymbol{X}^{k})}{t^{k+1} - t^{k}} + \boldsymbol{A}(\boldsymbol{X}^{k+1})\boldsymbol{X}^{k+1} + \boldsymbol{b}(\boldsymbol{X}^{k+1}) = \boldsymbol{0}, \tag{A-24}$$

is obtained. If a first order Tayler expansion of the residual $\boldsymbol{r}$ is performed from the known state, described by the independent variables $\boldsymbol{X}^{k+1,i-1}$, we obtain:

$$\boldsymbol{r}(\boldsymbol{X}^{k+1,i}) = \boldsymbol{r}(\boldsymbol{X}^{k+1,i-1}) + \left(\frac{\partial \boldsymbol{r}}{\partial \boldsymbol{X}}\right)^{k+1,i-1}(\boldsymbol{X}^{k+1,i} - \boldsymbol{X}^{k+1,i-1}), \tag{A-25}$$

where the index i indicates the number of iterations. If we then require that $\boldsymbol{r}(\boldsymbol{X}^{k+1,i}) = \boldsymbol{0}$, the expression:

$$\left(\frac{\partial \boldsymbol{r}}{\partial \boldsymbol{X}}\right)^{k+1,i-1}(\boldsymbol{X}^{k+1,i} - \boldsymbol{X}^{k+1,i-1}) = -\boldsymbol{r}(\boldsymbol{X}^{k+1,i-1}), \tag{A-26}$$

is obtained, the Newton-Raphson scheme to iterate on. The residual $\boldsymbol{r}$ represents the difference between the true and approximated solution. Thus, by checking the magnitude of the residual (by using some suitable norm) and stop the iteration first when the residual is below some chosen value, we may in an exact way define when the solution has converged and prevent the approximate solution to drift from the true solution. In Code_Bright the norm used is $\|\boldsymbol{r}(\boldsymbol{X}^{k+1,i})\|_\infty \equiv \max|\boldsymbol{r}(\boldsymbol{X}^{k+1,i})|$.

Also, a complementary convergence condition is used in Code_Bright where the differences of the independent variables obtained in two successive iterations are evaluated. The norm used is $\|\boldsymbol{X}^{k+1,i} - \boldsymbol{X}^{k+1,i-1}\|_\infty \equiv \max|\,\boldsymbol{X}^{k+1,i} - \boldsymbol{X}^{k+1,i-1}|$.

In Code_Bright, a logical operator (and, or) together with given tolerances, tol_{var} and tol_{bal}, acting on the "variable-difference" and "balance-residual" criteria, respectively, are used to form a complete convergence condition:

$$\text{convergence} = \begin{cases} \text{true} & \text{if}\left(\left\|\boldsymbol{X}^{k+1,i} - \boldsymbol{X}^{k+1,i-1}\right\|_\infty < tol_{\text{var}} \quad \text{logical operator} \quad \left\|\boldsymbol{r}(\boldsymbol{X}^{k+1,i})\right\|_\infty < tol_{bal} \right) \\ \text{false} & \text{otherwise} \end{cases} \tag{A-27}$$

Thus, the set $\{tol_{var}$, logical operator, $tol_{bal}\}$ defines the convergence condition.

A.2 Definition of saturation intervals and saturation limit intervals

In order to specify and get an overview of the saturation evolution in the EBS, times, t_{first} and t_{last}, denoting times when the first and last part of each of the EBS constituents become saturated (here taken as when $S_l > 0.99$), respectively, are identified. The time interval $[t_{first}, t_{last}]$ define a *saturation interval* of the studied constituent. An example is given in Table A-1 for two models.

Table A-1. Example of saturation intervals for two models.

Constituent	Model 1 $[t_{first}, t_{last}]$ (yr)	Model 2 $[t_{first}, t_{last}]$ (yr)
Top backfill (sand)	[4.0, 14.0]	[9.0, 46.4]

To simplify comparison of the saturation process between two models, here denoted 1 and 2, saturation interval data may be compiled in terms of initial and final *saturation limit intervals*, $[\min(t_{first}^1, t_{first}^2), \max(t_{first}^1, t_{first}^2)]$ and $[\min(t_{last}^1, t_{last}^2), \max(t_{last}^1, t_{last}^2)]$, respectively.

The saturation limit intervals show the range within which the first and last part of the constituent is being saturated considering both models. In Table A-2 the saturation limit intervals are given that correspond to the example saturation intervals in Table A-1.

Table A-2. Example of saturation limit intervals for the data given in Table A-1.

Constituent	Initial limit interval $[\min(t_{first}^N), \max(t_{first}^N)]$ (yr)	Final limit interval $[\min(t_{last}^N), \max(t_{last}^N)]$ (yr)
Top backfill (sand)	[4.0, 9.0]	[14.0, 46.4]

Appendix B

EBS representation

B.1 Initial conditions

From the state at installation of the bottom bed, silo, bentonite buffer, and subsequent waste emplacement/compartment backfilling with porous cement mortar, water redistribution may take place. So, what is the state of the EBS at closure (2040), the initial conditions for the current modelling?

As an assumption, all materials may be considered to be in equilibrium, regarding RH, with the state of the 100/0 GEKO/QI material at installation. This can be motivated from the small magnitudes of changes observed in measurements of total pressure in the bentonite buffer and displacements of the top-surface of the buffer. Thus, the present state of the 100/0 GEKO/QI material seems to be changed insignificantly as compared to its initial state.

Further motivation for the "unchanged state assumption" may be found if considering the governing condition at the open state. The system has been drained at the rock surface since installation and it is assumed that the lids covering the waste compartments are not gas tight, i.e. they allow for moisture transfer. The governing condition of such a system is very likely to be the RH in the surrounding open volumes. When studying measurements of RH obtained for the Prototype Tunnel at Äspö HRL, a mean value of about 70% seems representative. A RH of about 70% is close to the assumed installation state of the 100/0 buffer.

So, the insignificant changes of the 100/0 buffer state, observed up to this moment, and the agreement between the initial state of the 100/0 buffer and an estimated governing condition of the system, suggests that, for the EBS, a homogeneous initial state (at closure 2040), which is close to that of the 100/0 buffer at installation, is representative.

The RH at the initial water ratio ($w_0 = 0.17$) of the 100/0 buffer can be translated into a suction of 46 MPa using Kelvin's relation. Using this together with the adopted retention relations give the initial conditions given in Table B-1.

Table B-1. Initial conditions.

Parameter	Waste	Silo	Lid	100/0 buffer	10/90 buffer	Top backfill
ρ_d (kg/m^3)	2,345	2,345	2,345	1,000	2,200	1,723
ρ_s (kg/m^3)	2,710	2,710	2,710	2,600	2,645	2,650
n (-)	0.1	0.2	0.2	0.62	0.168	0.35
e (-)	0.67	0.25	0.25	1.6	0.202	0.538
S_l (-)	0.033	0.224	0.224	0.276	0.224	$7.9\cdot10^{-9}$
w (-)	$1.4\cdot10^{-3}$	0.021	0.021	0.17	0.017	$1.6\cdot10^{-9}$

It should here also be mentioned that a water content of 37%, as determined for 100/0 samples recently (spring 2014) taken from the top of the vertical clay barrier, indicates that the conditions in the buffer are not unchanged as compared to when it was installed. The 100/0 buffer material was however only sampled at one position close to the top surface of the wall buffer and the determined condition cannot be extrapolated to other positions without doing a highly uncertain assumption. Also, since the main part of the data (small water pressure in rock, still existing flow from the drainage system, low total pressure measurements, and small vertical motion of the buffer top surface) indicate no large changes from the initial conditions, this is the assumption used for the base case setup. An alternative setup is used in the case where the effect from an undrained rock cavern is investigated.

B.2 Material properties

Below, mixture relations, where constituent porosity, n^i, volume ratio, r^i, and degree of saturation, S_l^i, give the mixture porosity, $n^{(mix)}$, and mixture degree of saturation, $S_l^{(mix)}$, are shown.

$$n^{(mix)} = \frac{V_p^{(mix)}}{V^{(mix)}} = \frac{\sum V_p^i}{V^{(mix)}}, \quad n^i = \frac{V_p^i}{V^i}, \quad r^i = \frac{V^i}{V^{(mix)}} \quad \Rightarrow \quad n^{(mix)} = \sum r^i n^i \qquad \text{(B-1)}$$

$$S_l^{(mix)} = \frac{V_w^{(mix)}}{V_p^{(mix)}} = \frac{\sum V_w^i}{\sum V_p^i}, \quad S_l^i = \frac{V_w^i}{V_p^i} \quad \Rightarrow \quad S_l^{(mix)} = \frac{\sum r^i n^i S_l^i}{n^{(mix)}} \qquad \text{(B-2)}$$

An effective permeability, k_{ii}^{xxx}, can be calculated for a composite material in its "serial" and "parallel" orientation according to the expressions below. The length of the composite is l in the serial orientation, where the component lengths are l^k. The area of the composite is A in the parallel orientation, where the component areas are A^k.

$$k_{ii}^{serial} = \frac{l}{\sum \frac{l^k}{k_{ii}^k}} \qquad \text{(B-3)}$$

$$k_{ii}^{parallel} = \frac{\sum A^k k_{ii}^k}{A} \qquad \text{(B-4)}$$

B.2.1 Waste (homogenized silo content)

Waste is here denoting the homogenized representation of the materials contained within the outer most silo wall and silo bottom, i.e. concrete compartment walls, compartment backfill concrete, and waste packages. Compartment walls are represented by silo concrete with a porosity of 0.2. Compartment backfill concrete is represented by concrete with a porosity of 0.4. The waste packages themselves are represented by nonporous material. The used volume ratios of the three materials are, $r^{compartment\_walls} = 0.14$, $r^{compartment\_backfill} = 0.18$, and $r^{waste\_packages} = 0.68$, given by the information that 18,500 m^3 waste (packages) will be stored (SKB 1993) and the geometry of the silo internals. This gives a porosity of 0.1 of the homogenized silo content (waste).

The orthotropic waste permeabilities were taken from Holmén and Stigsson (2001).

Retention was obtained by assuming equilibrium between materials within the silo (all materials have the same suction) and using the mixture relations above together with properties for porous concrete and backfill concrete. The retention properties of backfill concrete were estimated with porous concrete as a starting point and using the mixture relations.

When using $(\lambda, p_0)_{\text{Van Genuchten}} = (0.21, 0.01)$, which was considered a accurate fit, convergence problems occurred. Therefore a somewhat "low" fit according to $(p_0)_{\text{Square law}} = (0.05)$ were instead adopted.

B.2.2 Silo (concrete)

The base case setup for the silo is taken as consisting of porous (fractured) concrete. The representation of the porous concrete was estimated with the properties for tight concrete as given in Åkesson et al. (2010) as a starting point and using the mixture relations given above. A porosity of 0.1 and 0.2 was assumed for tight and porous concrete, respectively.

The permeability was taken from Holmén and Stigsson (2001).

It turned out that the retention curve used for 10/90 GEKO/QI agreed well with the estimated retention, the same parameters are therefore used for porous concrete.

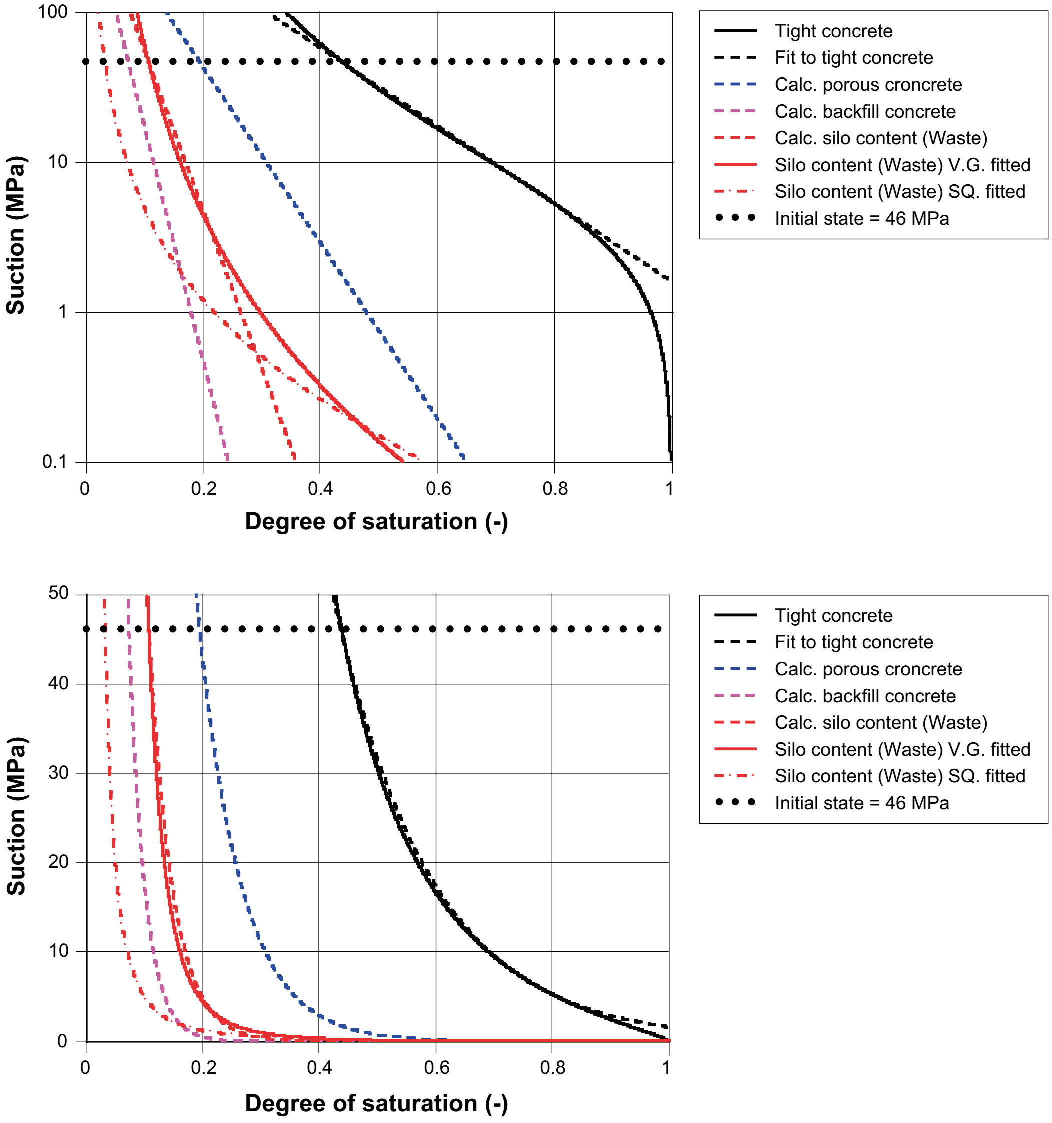

Figure B-1. *Retention curves related to the waste (homogenized silo content).*

As mentioned, the tight concrete properties were obtained from considering data in Åkesson et al. (2010) as the starting point. The Van Genuchten parameters $\{\lambda,p_0\}=\{0.165, 0.0685\}$ were obtained from fitting the expression against an absorption scan line origin from a point close to a desorption curve obtained from evaluating the data of Hedenblad (1996). Adopting the following (superscripts c and a denote cement and aggregate, respectively): $\rho_s^c = 3{,}100$ kg/m^3, $\rho_s^a = 2{,}650$ kg/ m^3, $\rho_d^c = 360$ kg/m^3, and $n = 0.135$, gives: $\rho_d^a = 1{,}985$ kg/m^3, $\rho_d = 2{,}345$ kg/m^3, $\rho_s = 2{,}710$ kg/m^3.

B.2.3 Lid (homogenized concrete and sand system)

Since the lid system, consisting of a 1 m thick perforated concrete pad embedded in sand (1 dm above, 0.5 dm below, and also within perforations), is dominated by the concrete pad, a porosity of 0.2, equal to that of silo (porous) concrete was adopted.

The effective permeability was estimated by considering the concrete lid penetrated and surrounded by sand. The system consists of both serial and parallel couplings and both of the given composite relations were used in order to obtain a representative value.

The retention was taken as that of porous concrete, i.e identical with that used for 10/90 GEKO/QI.

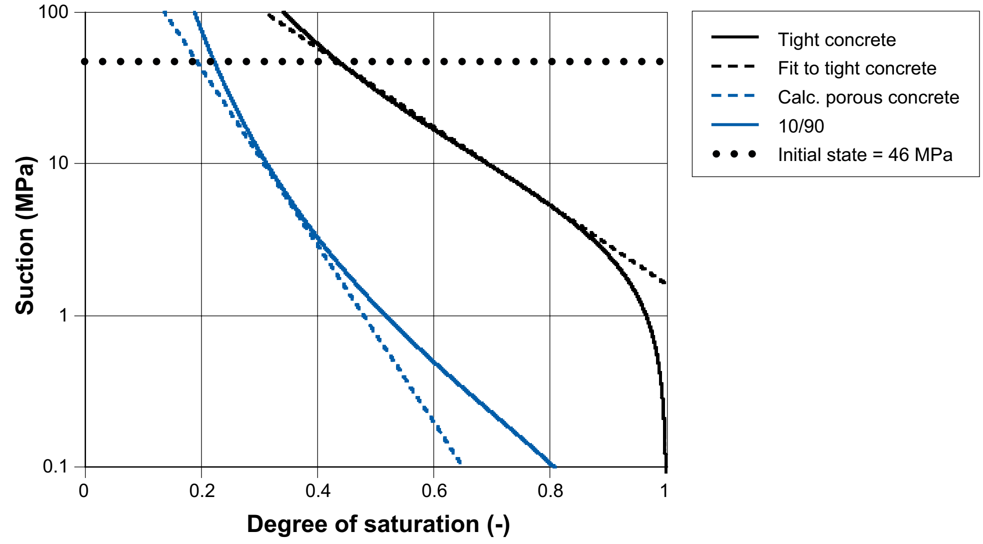

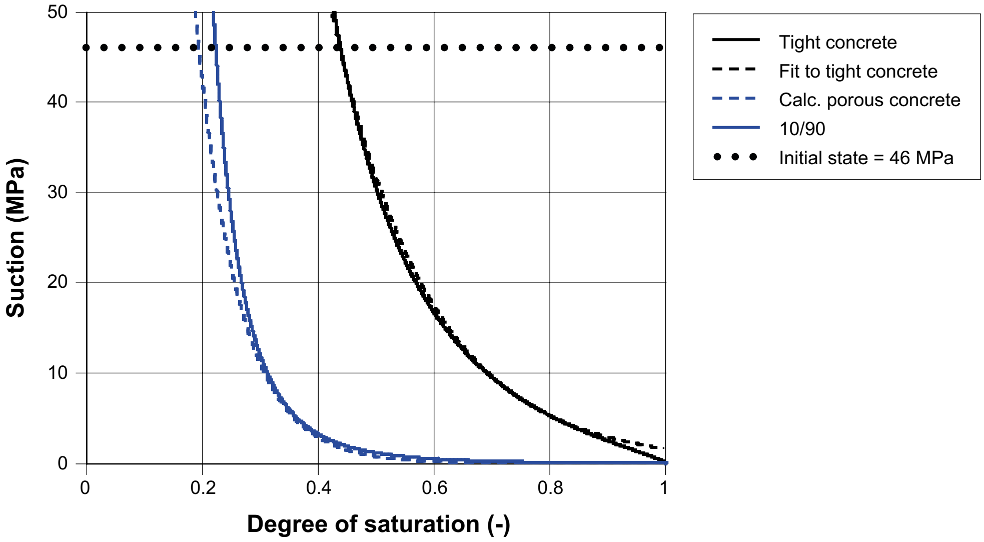

Figure B-2. *Retention curves related to the silo material (concrete).*

B.2.4 100/0 (GEKO/QI)

The permeability, kii, was set according to what is given in Pusch (2003), a conductivity of $9 \cdot 10^{-12}$ m/s corresponds to a saturated density of 1,800 kg/m^3, $6.9 \cdot 10^{-9}$ m/s to 1,300 kg/m^3, and the dry density in the buffer was measured to be about 1,000 kg/m^3. Using a linear relation in ln(kii) – ρd, as shown in Åkesson et al. (2010), a permeability value of 10^{-17} m^2 may be estimated for ρd = 1,000 kg/m^3.

There is a quite limited amount of data concerning the retention properties for this material. Wyoming bentonite data in Karnland et al. (2006) has therefore been used as an approximation. The initial water content, $w_0 = 0.17$, a dry density of 1,000 kg/m^3, and a grain density of $\rho_s = 2{,}600$ kg/m^3 have been used. The used densities correspond to $e = 1.6$.

It has been found that a linear fit in ln(w) – ln(ψ_{free}) corresponds well with experimental retention (or swelling pressure) data. With parameters $\{k, m\}=\{0.0158, -4.5\}$ in:

$$\psi_{free}(w) = kw^m, \tag{B-5}$$

a representative free swelling retention curve for the wall buffer is obtained. If an estimate of the retention under volume preserving conditions is sought one may use the relation:

$$\psi(w,e) = \psi_{free}(w) - \psi_{free}(w_{sat}(e))\frac{w - w_{init}}{w_{sat}(e) - w_{init}}, \tag{B-6}$$

where wsat(e) = e · ρw / ρs. The retention is here given as a function of water ratio and void ratio instead of water saturation. The water saturation is given by:

$$S_l = \frac{V_w}{V_p} = \frac{m_w}{\rho_w}\frac{1}{eV_s} = \frac{w}{e}\frac{\rho_s}{\rho_w}. \tag{B-7}$$

The Van Genuchten model may now be fitted to the evaluated confined retention curve and with $\{\lambda,p_0\}=\{0.165, 0.0685\}$ a representative curve is obtained.

B.2.5 10/90 (mixture of GEKO/QI / and sand)

The permeability was set according to what is given in Pusch (2003), where a conductivity of $3.4\cdot10^{-10}$ m/s is given for a saturated density of 2,200 kg/m^3, which is close to 2,190 kg/m^3, the average of the measured dry density in the bottom bed. The top backfill is estimated to obtain a dry density of at least 2,100 kg/m^3 (SKB 2008), the same properties will therefore be assumed for the top and bottom bed.

For a bentonite (*b*) filling (*f*) mixture with bentonite mass proportion $r = m_s^b/m_s$, $m_s^a/m_s = 1 - r$, $e^b = V_p^b/V_s^b$, $e^f = V_p^f/V_s^f$, $w^b = m_w^b/m_s^b$, $w^f = m_w^f/m_s^f$ (no superscript denotes variables for the mixture).

For the 10/90 mixture: $r = 0.1$, $w_0^b = 0.17$, and $e^b = 1.6$ have been used. $\rho_d = 2{,}200$ kg/m^3, the solid densities $\rho_s^b = 2{,}600$ kg/m^3 and $\rho_s^f = 2{,}650$ kg/m^3, and the individual retention curves $\psi_{free}{}^b$ and $\psi_{free}{}^f$ with $\{k^b, m^b\} = \{0.0158, -4.5\}$, $\{k^f, m^f\} = \{0.0008, -0.3\}$, shown in Figure B-3.

An assumption of equilibrium in RH between the two constituents gives:

$$\psi_{free}{}^b(w^b) = \psi_{free}{}^f(w^f), \tag{B-8}$$

which restricts the constituent water ratio. With the equilibrium assumption follows that the retention for the mixture becomes:

$$\psi_{free} = \psi_{free}{}^b(w^b), \tag{B-9}$$

here chosen to be given with respect to the bentonite. The water ratio of the mixture is given by:

$$w = \frac{m_w}{m_s} = \frac{m_w{}^b + m_w{}^f}{m_s{}^b + m_s{}^f} = \cdots = rw^b + (1-r)w^f. \tag{B-10}$$

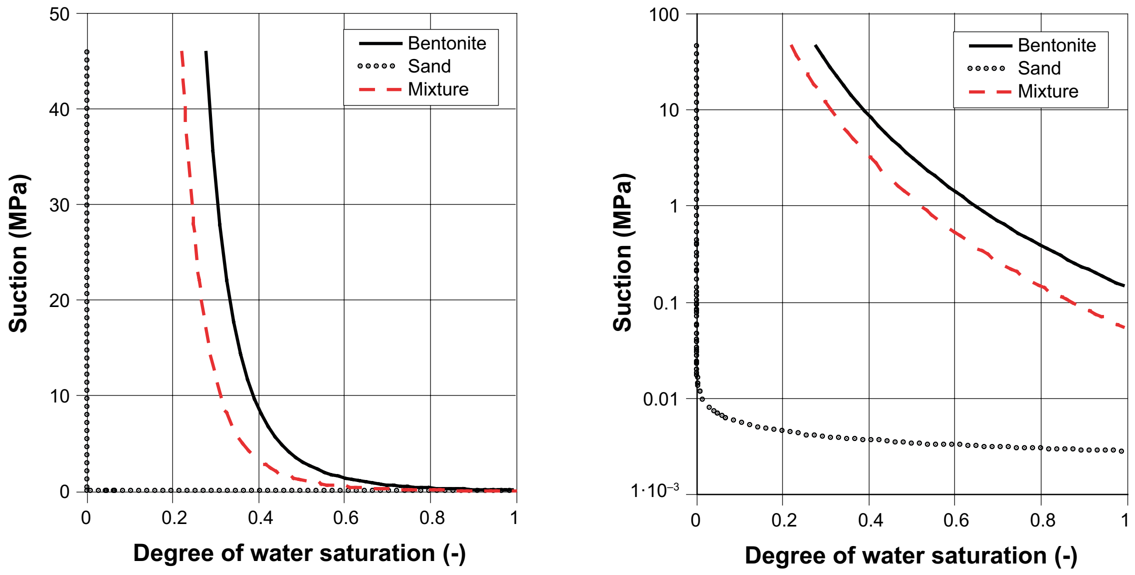

Figure B-3. *Adopted water retention under unconfined (free) conditions for bentonite, sand, and 10/90 bentonite/sand mixture.*

With the relations above, pairs of {ψfree, w} may be calculated which define the mixture retention. The ln w – ln ψfree expression can now be fitted against the obtained {ψfree, w} data, {k, m} = {$5\cdot10^{-7}$, –4.5} are used here, shown in Figure B-3.

If an estimate of the retention under volume preserving conditions is sought one may use the relation:

$$\psi(w,e)=\psi_{free}(w)-\psi_{free}(w_{sat}(e)\;\frac{w-w_{init}}{w_{sat}(e)-w_{init}}\;, \tag{B-11}$$

where wsat(e) = e · ρw / ρs. The void ratio of the mixture e is given by:

$$e=\frac{V_p}{V_s}=\frac{V_p^{\,b}+V_p^{\,f}}{V_s^{\,b}+V_s^{\,f}}=\cdots=\frac{e^b}{1+\dfrac{1-r}{r}\dfrac{\rho_s^{\,b}}{\rho_s^{\,f}}}+\frac{e^f}{1+\dfrac{r}{1-r}\dfrac{\rho_s^{\,f}}{\rho_s^{\,b}}}\;, \tag{B-12}$$

and the relation:

$$\frac{1}{\rho_d}=\frac{V}{m_s}=\frac{V^b+V^f}{m_s^{\,b}+m_s^{\,f}}=\cdots=\frac{r}{\rho_s^{\,b}}(1+e^b)+\frac{1-r}{\rho_s^{\,f}}(1+e^f)\;, \tag{B-13}$$

restricts the constituent void ratios. The solid density of the mixture is given by:

$$\frac{1}{\rho_s}=\frac{V_s}{m_s}=\frac{V_s^{\,b}+V_s^{\,f}}{m_s^{\,b}+m_s^{\,f}}=\cdots=\frac{r}{\rho_s^{\,b}}+\frac{1-r}{\rho_s^{\,f}}\;. \tag{B-14}$$

With the relations given above a mixture retention curve under confined conditions $\psi(w,e)$ may be constructed.

As can be seen the suction is here taken as a function of water ratio and void ratio instead of water saturation. The water saturation is given by:

$$S_l=\frac{V_w}{V_p}=\frac{m_w}{\rho_w}\frac{1}{eV_s}=\frac{w}{e}\frac{\rho_s}{\rho_w}\;, \tag{B-15}$$

which holds for the individual constituents as well as for the mixture if the definitions given above for the mixture parameters/variables are used. The Van Genuchten model may now be fitted to the evaluated confined retention curve. The parameter set $\{\lambda,p_0\}=\{0.18,0.05\}$ has been adopted and the resulting curve can be seen in Figure B-4.

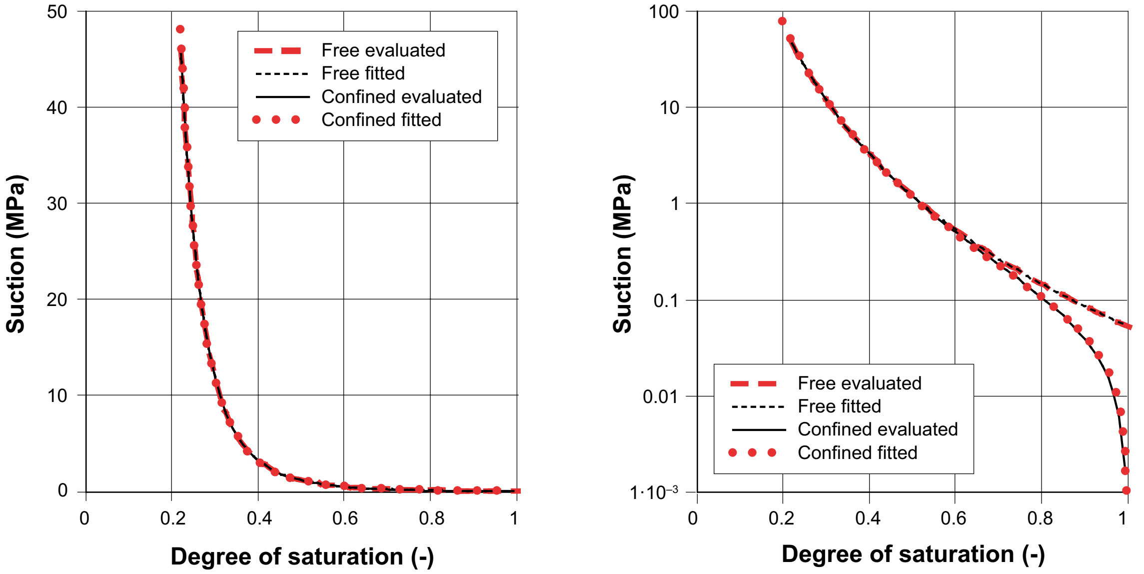

Figure B-4. *Adopted water retention for 10/90 bentonite/sand mixture under unconfined (free) and confined conditions.*

B.2.6 Top backfill (sand)

The retention is based on the representation for sand (Plug filter) in Åkesson et al. (2010). The curve is, however, taken as a bit less extreme for numerical convenience, see below in Figure B-5. The permeability was taken as that of sand (Plug filter) in Åkesson et al. (2010).

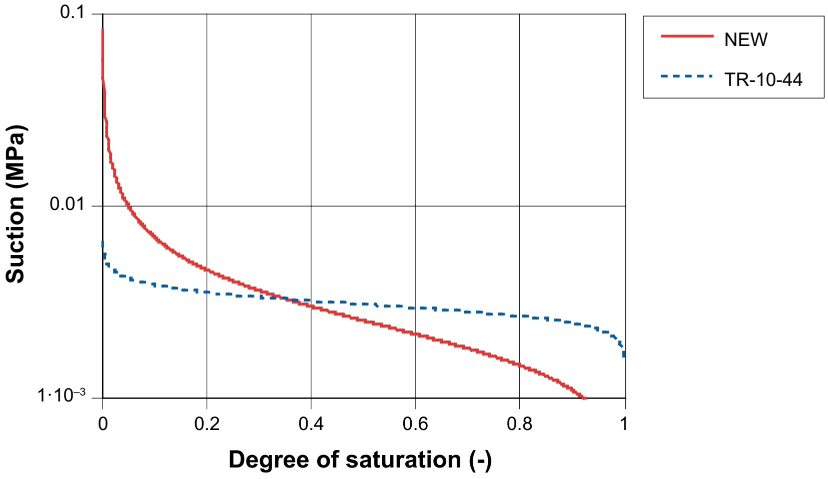

***Figure B-5.** Water retention for sand. The adopted representation in red and the "Plug filter" representation from Åkesson et al. (2010) in hatched blue.*

Appendix C

Rock representation

C.1 Initial and boundary conditions

The horizontal top boundary of the model coincides with the sea floor at 10 m water depth, therefore p_l = 0.2 MPa for d = 10 m. The conditions that are to be prescribed at the other boundaries of the model are discussed below.

Table C-1. Models used in this study.

Model description	Model name
Undrained	undrained.gid
Drained	drained4_new3b.gid
Undrained, Empty	BC_undrained_pre.gid
Drained, Empty	BC_drained_ pre.gid

The evolution of the water pressure in the rock may be described by the following states:

1. Hydrostatic pressure prevails initially before the excavation/construction.
2. Decreasing pressure from hydrostatic, from construction (1983–1986) to closure (2040).
3. Increasing pressure towards steady state conditions, from (2040) to full saturation.
4. Steady state conditions at full water saturation.

In the present work, mainly focusing on the conditions during items 3 and 4 above, the starting point (at 2040) should be a drained rock with pressure lower as compared to hydrostatic. In order to obtain the 2040 conditions, however, the drainage of the rock from construction to closure, during items 1 and 2 has to be simulated as well. So the simulations actually have to cover all items in the list above.

In the base case the processes during 1 and 2 have been simulated by assuming that perfectly drained conditions (p_l = 0.1 MPa) prevail in the installed cavern wall drainage system in the repository, i.e. the cavern can be thought of as empty. This assumption is for instance strengthen by inspection notes from 2011 (Lundin 2012), where it was concluded that the drainage system still is considered to be efficient, on the basis of studying both water pressure in the rock and the flow from the drainage system. It should also here be mentioned, that a high water content of about 37% was determined for samples recently (spring 2014) taken from the top of the vertical 100/0 clay barrier and this indicate a less than perfect working drainage system. The high water content however is only determined locally at one position close to the top surface of the wall buffer and cannot be extrapolated over the entire silo construction without doing a highly uncertain assumption. As mentioned, other data indicate that the drainage system performs rather well. Therefore, no large change from the initial conditions is the assumption used for the base case setup. In an alternative model, the case of an undrained rock cavern is addressed.

The next step in the simulations is to start the phase described by 3 and 4 (at 2040). The EBS is installed with the appropriate initial conditions within the cavern and the saturation process of the EBS can take place.

There is however one issue that complicates the simulations in order to obtain representative results. The initial conditions (at 2040) and the evolution of the rock pressure during the saturation phase are very much dependent on the hydraulic conditions on a global scale that embrace the entire SFR-site.

Here, to avoid the troublesome task of simulating the entire SFR-site, a simplified approach has been adopted. Geometrically, only the silo with a limited part of the host rock is considered, but to account for consequences from hydraulic conditions on a global scale, two limiting cases with different rock geometries and boundary conditions are used. The used rock geometries and BCs are shown in Figure C-1.

The geometries and their respective boundary conditions define two model types:

- *Undrained* models (Geometry without cutout).
    1. $p_l = 0.2$ MPa at the top boundary.
    2. $q_l = 0$ elsewhere.
- *Drained* models (Geometry with cutout).
    1. $p_l = 0.2$ MPa at the top boundary.
    2. $p_l = 0.1$ MPa at the cutout.
    3. $q_l = 0$ elsewhere.

When designing the "two-model approach", water pressures obtained for models with an empty rock cavern were compared with rock water pressure measurements. The rock water pressure has been measured in borehole-sections around the silo construction. The measurements started in 1985, i.e. before the repository was excavated. Water pressure data for boreholes, KFR04, KFR05, KFR19, and KFR55 were used when evaluating the boundary conditions.

Figure C-2 shows the water head change from the initially hydrostatic state, where the rapid initial decrease in water pressure is a consequence of the drainage starting when constructing the SFR repository (1983–1986). After the initial rapid decrease, there still is a more or less general decreasing trend in the pressures measured around the silo repository. This indicates that a global drainage process takes place in the rock mass surrounding the silo.

In Figure C-3 the measured water pressures at the end of 1990, 2011, and estimated water pressures for 2040, are given as a function of the hydrostatic pressure at the depth corresponding to the midpoint of the borehole sections. The estimation for the 2040 water pressures was performed by "hands-on" extrapolation of the trends of Figure C-2 and should therefore at best be regarded as indicative. However, it can be seen that all measured pressures have decreased from hydrostatic pressure at all shown locations, i.e. the data-points are below the diagonal of the graph.

As described earlier, the steady state solution of a model with an open cavern is to be used as the condition at closure (at 2040). Pressures of this closure state may be compared to the measurements. For both models, undrained at top and drained at bottom in Figure C-4, closure pressure profiles at radius = 0 m and 44 m are shown by the black curves. The outer radius of 44 m is approximately equal to the distance from the cavern center line to the mid-point of the most distant borehole-section. For the undrained model the closure state pressures are somewhat overestimated and the drained model gives an underestimation of the pressures.

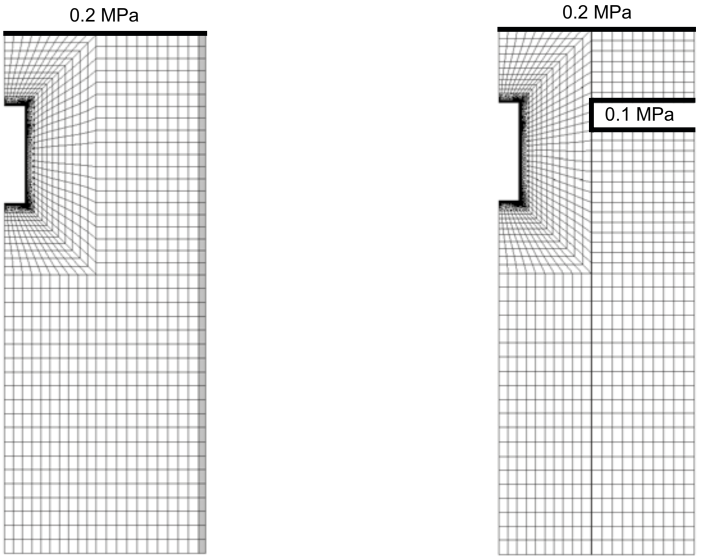

Undrained rock geometryand BCs **Drained rock geometryand BCs**

Figure C-1. *Host rock representations, geometry and boundary conditions.*

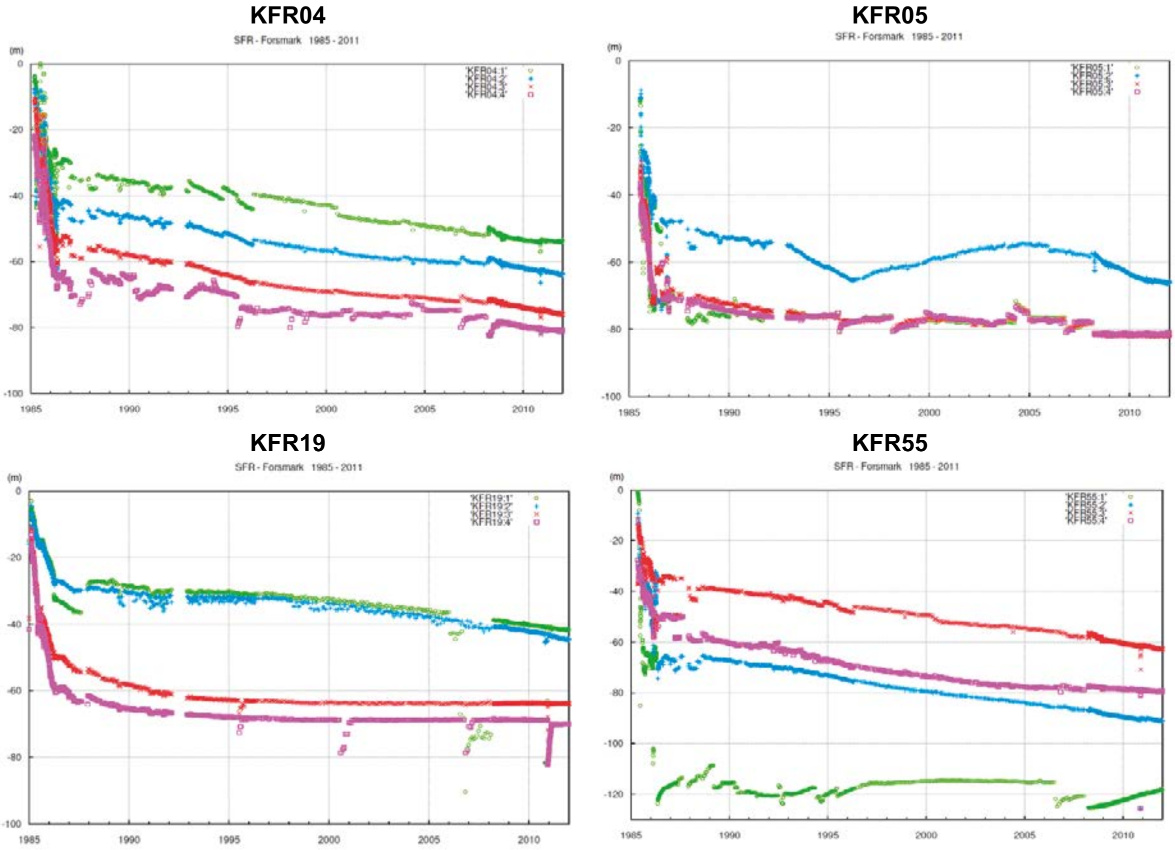

Figure C-2. *Measured water head change from the initially hydrostatic state in the vicinity of the silo repository.*

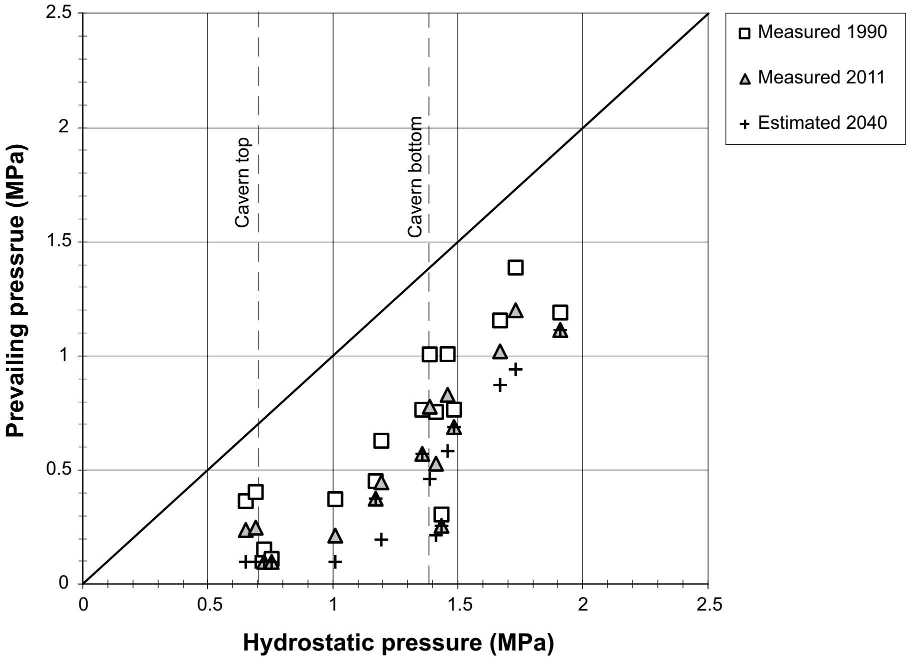

Figure C-3. *Measured water pressure at 1990, 2011, and estimated pressure 2040 as a function of hydrostatic pressure.*

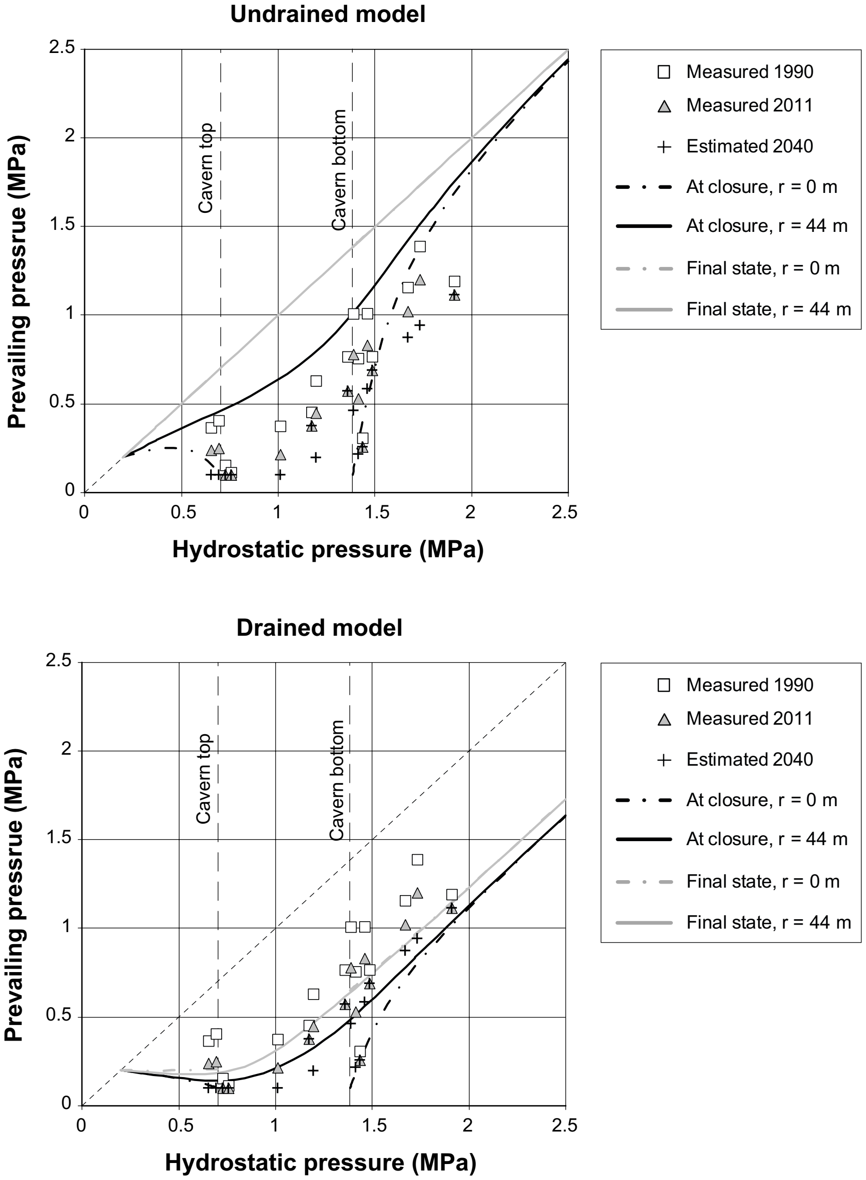

Figure C-4. *Measured pressures 1990 and 2011, from measurements estimated pressures at 2040, and calculated pressure profiles, for r = 0 and 44 m, at closure and the final state (i.e. steady state).*

The water saturation phase was also simulated in the two models. At the closure state, the EBS constituents were installed in the cavern and the models were run to a stage where a final steady state prevailed. The pressure profiles for this final steady state, again shown for $r = 0$ m and $r = 44$ m, are given as the gray lines in Figure C-4. For the undrained model it is, as expected, seen that the final state is hydrostatic, i.e. the results align with the diagonal of the graph. The drained model, however, attains pressures much lower as compared to hydrostatic. As a consequence, with a suitable choice of rock permeability, the undrained and drained model have potential for providing low and high estimates of the saturation time, respectively.

To calibrate the permeability of the rock, the simulated water flow into an empty rock cavern was compared against the measured outflow from the drainage system installed in the silo construction. Again, as when designing the BCs above, this assumes that perfectly drained conditions prevail in the repository drainage system.

It was found that using a permeability of 10^{-16} m^2, the undrained and drained model gave the responses shown in Figure C-5, in which the measured total drainage outflow also is shown. As can be seen, the measurements show a slowly decreasing trend reflecting a large-scale drainage of the entire SFR-site, whereas the flow in the models decreases almost instantly down to a constant level due to their local character. Thus, the models, working on a small scale as compared to the site-scale, cannot mimic this slow evolution using constant BCs. Using the chosen permeability together with the pair of realizations, however, the simulated inflows provide an upper and lower estimate for the real water flow. Thereby, the time of saturation of the system which the models predict will most likely be upper and lower estimates of the real situation.

One could probably design a model with varying BCs which could produce a response in closer agreement with the measurements. But since our actual starting point in this task is at year 2040 (indicated by the gray vertical line in Figure C-5) and we do not have access to data to calibrate the BCs against at that point and onward, the adopted strategy using two limiting cases with well defined BCs is considered robust.

The calibrated rock permeability of 10^{-16} m^2, which gives relevant water inflow into the silo, seems appropriate when compared to what other have used in similar models. Holmén and Stigsson (2001) obtained a value of $5\cdot10^{-16}$ m^2 when performing an analytical calibration against measured water inflow into a drained BMA tunnel and in a following calibration of their so called local realization a value of $6.5\cdot10^{-16}$ m^2 gave good agreement when comparing the model response with tunnel/silo inflow measurements.

Due to scale dependence, depth dependence and character of the rock heterogeneity it can be quite complicated to evaluate a representative rock permeability from field measurement that is relevant to be compared with the calibrated value used in the present model. Anyhow, if for example studying Figure 6-1 and Figure E-1 in Öhman and Follin (2010), and focusing on depths < 400 m, values between 10^{-17} m^2 and 10^{-13} m^2 seem typical.

C.2 Material properties

The retention is taken as the representation for Rock matrix in Åkesson et al. (2010). The permeability of 10^{-16} m^2 was obtained by the calibrating process described in the previous paragraph.

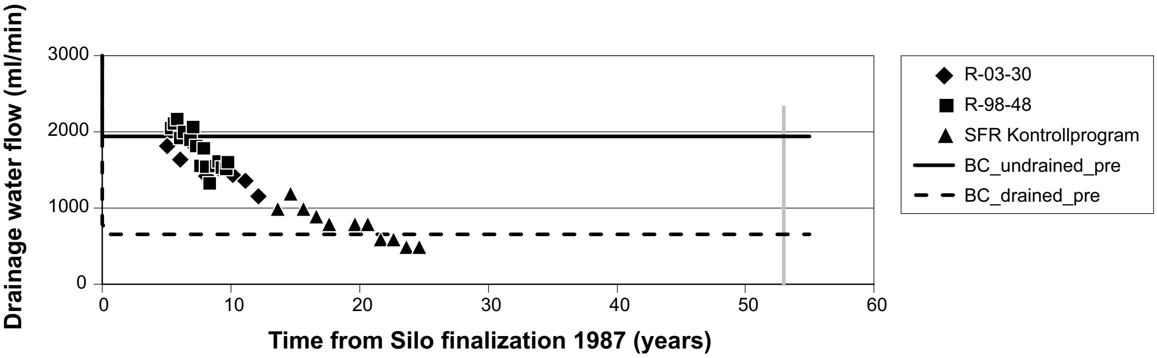

Figure C-5. Measured outflow from the silo repository drainage system (symbols) and calculated water inflow from an empty rock cavern obtained for the undrained (solid) and drained (hatched) base case models. The time when the closure is planned (2040) is indicated by the vertical gray line.

Convergence investigation

Here results of investigations of the mesh dependence and dependence on convergence condition parameters are shown. It should be noted that the model here denoted with “base case” is not exactly the same as defined in the main text of this report. The model, with somewhat different BCs and material parameters, do however resemble the real base case to a high degree, and the results are therefore considered providing us with information relevant also for the real base case.

D.1 Mesh dependence

Drained models with coarse and fine “equidistant” meshes and the drained base case model with a “concentrated” mesh were used for this purpose. When developing the denser mesh the no. of mesh-divisions of lines, belonging to surfaces with ordered mesh, was doubled.

Table D-1. Models used in this study.

Mesh character, ID	Model name
Coarse, equidistant	drained3b.gid
Fine, equidistant	drained3_fine.gid
“Base case”, concentrated	drained4.gid

The same convergence criteria/parameter setup was used in both equidistant models, $\{tol_{var} = 10^{-10}$, or, $tol_{bal} = 10^{-20}\}$, whereas, $\{tol_{var} = 10^{-9}$, or, $tol_{bal} = 10^{-20}\}$ was used in the base case model.

Iso-maps of liquid degree of saturation in the EBS are given for the two equidistant models in Figure D-1. The character of the saturation process in the EBS can be seen to be very similar between the models, but the model with the finer mesh shows somewhat slower saturation as compared to the coarser mesh model.

If studying the obtained saturation interval data, shown in Table D-2, the fine model has somewhat elongated intervals compared to the coarse model. All saturation intervals also end later for the model with finer mesh. No general trend concerning the start of the intervals can be found.

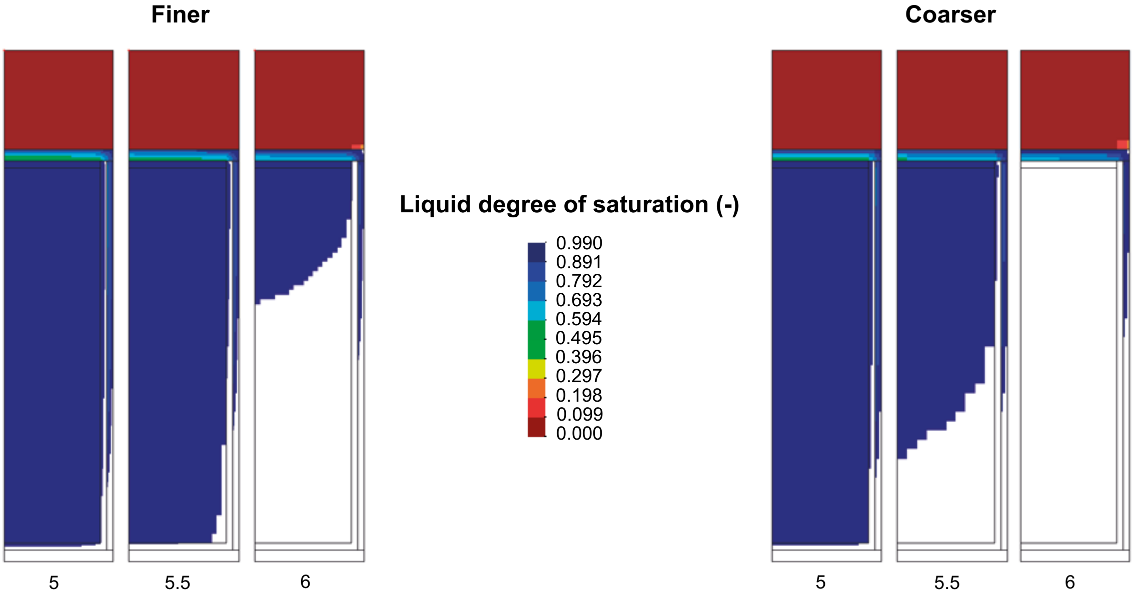

Figure D-1. *Degree of liquid (water) saturation in the EBS for models with finer (left) and coarser (right) mesh.*

The saturation interval limit graph at the top in Figure D-2, shows that there are some differences between the equidistant models, Coarse and Fine, but the magnitudes of the differences are small. The "base case" model has a mesh with concentrations in suitable parts of the geometry and has higher mesh density compared to the coarser model but lower as compared to the finer mesh model. In the bottom graph of Figure D-2, the differences between the "base case" model and the finer meshed model are visualized in terms of saturation limit intervals. Generally, the differences become even smaller using the "base case" model, when compared with the coarse model. Thus, mesh dependency seems not to be an issue using the chosen setup.

Table D-2. Saturation intervals obtained when using a coarse and fine mesh.

Constituent	Coarse $[t_{first}, t_{last}]$ (yr)	Fine $[t_{first}, t_{last}]$ (yr)
Top backfill (sand)	[7.7, 26.3]	[7.1, 26.4]
Top buffer (10/90)	[5.9, 7.0]	[5.9, 7.3]
Lid	[5.9, 5.9]	[6.1, 6.2]
Waste	[5.1, 5.9]	[5.3, 6.2]
Silo (base and wall)	[1.8, 5.8]	[1.6, 6.1]
Wall buffer (100/0)	[2.7, 6.8]	[2.5, 7.1]
Bottom buffer (10/90)	[2.0, 4.1]	[2.0, 4.2]

D.2 Dependence on convergence condition parameters

The drained "Coarse" model used in the mesh dependency investigation was here used again, now identified as the model with the tolerance exponent exp = –10. To investigate the sensitivity to a change in this parameter, setting the convergence condition, the tolerance exponent was changed to exp = –6, which identifies the second model used in this study.

Table D-3. Models used in this study.

ID	Convergence condition parameters	Model name
exp = –10	{tolvar = 10^{-10}, or, tolbal = 10^{-20}}	drained3b.gid
exp = –6	{tolvar = 10^{-6}, or, tolbal = 10^{-20}}	drained3b_conv_copy2.gid

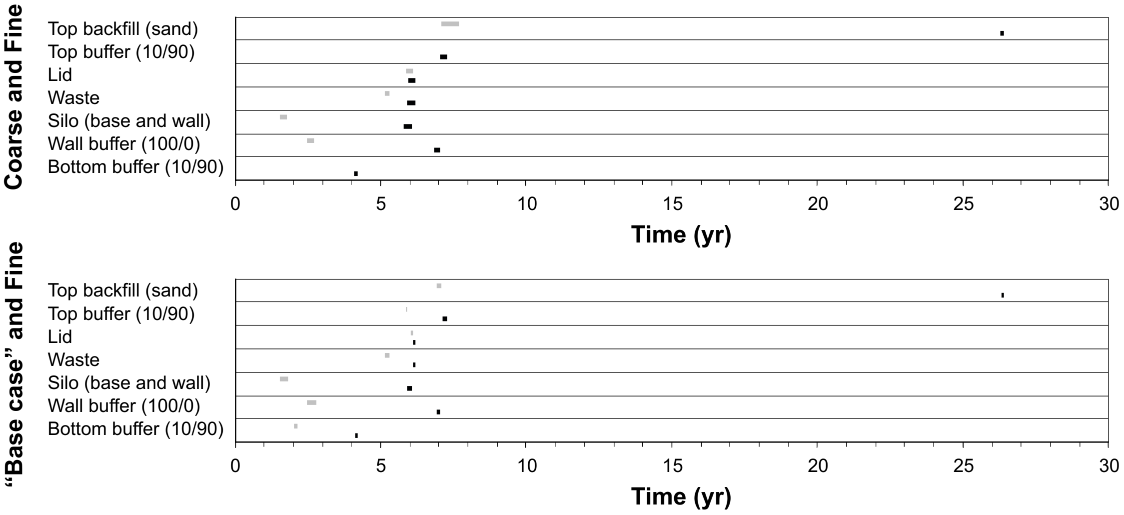

Figure D-2. Saturation limit intervals formed between models with Coarser and Finer mesh (upper) and "Base case" and Finer mesh (lower).

The identified saturation intervals are given in Table D-4. As can be seen, the differences are small. The "Top backfill" is being saturated earlier in exp = –6, otherwise saturation starts later or at the same time as in exp = –10. The end of constituent saturation intervals occur at the same time or later in exp = –6. For the problem studied, no significant dependency on the governing convergence condition parameter is seen for $tol_{var} = \{10^{-6}, 10^{-10}\}$.

Table D-4. Saturation intervals obtained when using different convergence condition parameters.

Constituent	exp = –10 $[t_{first}, t_{last}]$ (yr)	exp = –6 $[t_{first}, t_{last}]$ (yr)
Top backfill (sand)	[7.7, 26.3]	[7.6, 26.3]
Top buffer (10/90)	[5.9, 7.0]	[5.9, 7.1]
Lid	[5.9, 5.9]	[5.9, 6.0]
Waste	[5.1, 5.9]	[5.2, 6.0]
Silo (base and wall)	[1.8, 5.8]	[1.8, 5.8]
Wall buffer (100/0)	[2.7, 6.8]	[2.7, 6.9]
Bottom buffer (10/90)	[2.0, 4.1]	[2.1, 4.1]

Appendix E

Analytical model for cement degradation of concrete wall

Data:

Gravity:	g := 9.81	m/s²	Width of bentonite filling:	B := 1	m
Particle density of bentonite:	ρs := 2780	kg/m3	Height of bentonite filling:	Li := 53	m
Water density:	ρw := 1000	kg/m3	Number of elements:	m := 500	–
Initial void ratio of bentonite:	e0 := 1.78	–	Number of horizontal strain steps:	n := 20	–

Routine for updating of stresses and strains

```
$SI(\Delta\varepsilon, \Delta\sigma, \nu, \kappa, \sigma X, \sigma Y, \sigma Z, \varepsilon X, \varepsilon Y) :=$
    $steps \leftarrow 20$
    $(\sigma x_0 \ \sigma y_0 \ \sigma z_0 \ \varepsilon x_0 \ \varepsilon y_0) \leftarrow (\sigma X \ \sigma Y \ \sigma Z \ \varepsilon X \ \varepsilon Y)$
    $E \leftarrow 3\cdot(1-2\cdot\nu)\cdot(1+e_0)\cdot\left[-(\sigma x_0+\sigma y_0+\sigma z_0)\cdot 3^{-1}\right]\cdot\kappa^{-1}$
    $(d\varepsilon x \ \ d\sigma y) \leftarrow (\Delta\varepsilon\cdot steps^{-1} \ \ \Delta\sigma\cdot steps^{-1})$
    for $i \in 1..steps$
        $d\sigma x \leftarrow [E\cdot d\varepsilon x + \nu\cdot(1+\nu)\cdot d\sigma y]\cdot(1-\nu^2)^{-1}$
        $d\varepsilon y \leftarrow \left[(1-\nu^2)\cdot d\sigma y - \nu\cdot(1+\nu)\cdot d\sigma x\right]\cdot E^{-1}$
        $d\sigma z \leftarrow \nu\cdot(d\sigma x + d\sigma y)$
        $(\varepsilon x_i \ \ \varepsilon y_i) \leftarrow (\varepsilon x_{i-1} \ \ \varepsilon y_{i-1}) + (d\varepsilon x \ \ d\varepsilon y)$
        $(\sigma x_i \ \ \sigma y_i \ \ \sigma z_i) \leftarrow (\sigma x_{i-1} \ \ \sigma y_{i-1} \ \ \sigma z_{i-1}) + (d\sigma x \ \ d\sigma y \ \ d\sigma z)$
        $E \leftarrow 3\cdot(1-2\cdot\nu)\cdot(1+e_0)\cdot\left[-(\sigma x_i+\sigma y_i+\sigma z_i)\cdot 3^{-1}\right]\cdot\kappa^{-1}$
    $(\sigma x_{steps} \ \ \sigma y_{steps} \ \ \sigma z_{steps} \ \ \varepsilon x_{steps} \ \ \varepsilon y_{steps})$
```

Calculation of effective mean stress and von Mises stress

```
$f_P(\sigma X, \sigma Y, \sigma Z) :=$
    $P \leftarrow -(\sigma X + \sigma Y + \sigma Z)\cdot 3^{-1}$
    $Q \leftarrow \sqrt{(\sigma X-\sigma Y)^2 + (\sigma X-\sigma Z)^2 + (\sigma Y-\sigma Z)^2}\cdot\sqrt{2^{-1}}$
    $(P \ \ Q)$
```

Calculation of saturated density:

$$\rho_m(e1) := \frac{\rho_s}{1+e1}\cdot\left(1 + e1\cdot\frac{\rho_w}{\rho_s}\right)$$

Step of vertical stress with depth due to weigh and friction:

$$\Delta\sigma y\ (\sigma xx, \varepsilon X, \varepsilon Y, \phi, e1) := \left[-g\cdot\left(\rho_m(e1)-\rho_w\right) - \frac{2\cdot\tan(\phi)}{B\cdot(1+\varepsilon X)}\cdot\sigma xx\right]\cdot\left[L_i\cdot m^{-1}\cdot(1+\varepsilon Y)\right]$$

Main algorithm for model:

```
$\mathrm{Mod}(\varepsilon X, \nu, \kappa, \sigma_i, \sigma_{BC}, \phi) :=$
    for $i \in 0..m-1$
        $(\sigma x_{0,i}\ \sigma y_{0,i}\ \sigma z_{0,i}\ \varepsilon x_{0,i}\ \varepsilon y_{0,i}) \leftarrow (\sigma_i\ \sigma_i\ \sigma_i\ 0\ 0)$
        $(vr_{0,i}\ l_{0,i}) \leftarrow (e_0\ L_i \cdot m^{-1})$
    $\Delta\varepsilon \leftarrow \varepsilon X \cdot n^{-1}$
    for $j \in 1..n$
        $\Delta\sigma \leftarrow \sigma_{BC} - \sigma y_{j-1,0}$
        $R \leftarrow SI(\Delta\varepsilon, \Delta\sigma, \nu, \kappa, \sigma x_{j-1,0}, \sigma y_{j-1,0}, \sigma z_{j-1,0}, \varepsilon x_{j-1,0}, \varepsilon y_{j-1,0})$
        $(\sigma x_{j,0}\ \sigma y_{j,0}\ \sigma z_{j,0}\ \varepsilon x_{j,0}\ \varepsilon y_{j,0}) \leftarrow R$
        $vr_{j,0} \leftarrow e_0 + (1 + e_0) \cdot (\varepsilon x_{j,0} + \varepsilon y_{j,0} + \varepsilon x_{j,0} \cdot \varepsilon y_{j,0})$
        $l_{j,0} \leftarrow L_i \cdot m^{-1} \cdot (1 + \varepsilon y_{j,0})$
        for $i \in 1..m-1$
            $\Delta\sigma 0 \leftarrow \sigma y_{j,i-1} - \sigma y_{j-1,i}$
            $\Delta\sigma \leftarrow \Delta\sigma 0 + \Delta\sigma y(\sigma x_{j,i-1}, \varepsilon x_{j,i-1}, \varepsilon y_{j,i-1}, \phi, vr_{j,i-1})$ if $\sigma y_{j,i-1} < \sigma_i$
            $\Delta\sigma \leftarrow \Delta\sigma 0$ otherwise
            $R \leftarrow SI(\Delta\varepsilon, \Delta\sigma, \nu, \kappa, \sigma x_{j-1,i}, \sigma y_{j-1,i}, \sigma z_{j-1,i}, \varepsilon x_{j-1,i}, \varepsilon y_{j-1,i})$
            $(\sigma x_{j,i}\ \sigma y_{j,i}\ \sigma z_{j,i}\ \varepsilon x_{j,i}\ \varepsilon y_{j,i}) \leftarrow R$
            $vr_{j,i} \leftarrow e_0 + (1 + e_0) \cdot (\varepsilon x_{j,i} + \varepsilon y_{j,i} + \varepsilon x_{j,i} \cdot \varepsilon y_{j,i})$
            $l_{j,i} \leftarrow L_i \cdot m^{-1} \cdot (1 + \varepsilon y_{j,i})$
    for $j \in 0..n$
        for $i \in 0..m-1$
            $Y_{j,i} \leftarrow \sum_{k=i}^{m-1} l_{j,k}$
            $(p_{j,i}\ q_{j,i}) \leftarrow f_P(\sigma x_{j,i}, \sigma y_{j,i}, \sigma z_{j,i})$
    $(\sigma x\ \ \sigma y\ \ Y\ \ vr\ \ \varepsilon x\ \ \varepsilon y\ \ p\ \ q)^T$
```

Appendix F

FLAC model for cement degradation of concrete wall

```
set log sfr_disp_log.log
set log on
config gw
grid 7 200
;
mod elastic  i=1   j=1,200
mod cam-clay i=3,5 j=1,200
mod elastic  i=7   j=1,200
;
gen  0.7,0     0.7,53     1,53     1,0   i=1,2  j=1,201
gen    1,0       1,53     2,53     2,0   i=3,6  j=1,201
gen    2,0       2,53   2.3,53   2.3,0   i=7,8  j=1,201
;
def make_tab                          ; Make a table of porosity versus
  strain = -0.2                       ; volume strain.
  loop n (1,11)
    xtable(p_tab,n) = strain
    ytable(p_tab,n) = 1.0 - (1.0 - start_n) / (1.0 + strain)
    strain = strain + 0.04
  end_loop
end
;
set p_tab=1 start_n=0.64 ; Set table number & initial poros
make_tab                              ; Create the table
;
prop dens=2000 shear=0.75e8   bulk=1e8               i=1   j=1,200
prop dens=2000 shear=0.75e8   bulk=1e8               i=7   j=1,200
init dens=1000                               i=3,5 j=1,200
prop poros=0.64 por_tab=1                            i=3,5 j=1,200
prop shear=0.75e8 bulk=1e8 mm=10 lambda=0.5 mpc=1e7   i=3,5 j=1,200
prop kappa=0.26 poiss=0.2 mp1=1e5 mv_l=2.78 mv0=2.78    i=3,5 j=1,200
;
int 1 Aside from 2,1 to 2,201 Bside from 3,1 to 3,201
int 1 ks=2e9 kn=2e9 fric=10
int 2 Aside from 6,1 to 6,201 Bside from 7,1 to 7,201
int 2 ks=2e9 kn=2e9 fric=10
```

```
;
set grav=9.81
water density=1000
;
fix x y i=1,2  j=1,201 ;Fixing of inner and outer material
fix x y i=7,8  j=1,201
fix y   i=3,6  j=1      ;Fixing of lower boundaries
;
set small
ini pp = 1.275e6 var 0,-0.520e6 j=1,201
ini sxx=-1.295e6 var 0, 0.520e6 j=1,201
ini syy=-1.295e6 var 0, 0.520e6 j=1,201
ini szz=-1.295e6 var 0, 0.520e6 j=1,201
;
set flow off
set mech on
set st_damp=combined
;
hist ydisp i=3 j=201
hist yvel i=3 j=201
;
def loadsteps
  loop ns (1,nl_steps)
     BC_stress = BC_stress + stress_inc
     command
        apply syy = BC_stress i=3,6 j=201
        solve
     end_command
  end_loop
end
set nl_steps=10  BC_stress=-0.775e6  stress_inc = -8e3
;
set srat=1e-4
;
loadsteps
print y esyy esxx ydis cam_p sv i=4
;
free x y                 i=1,2 j=1,201
fix y                   i=1,2 j=1,201
def strainsteps
```

```
 loop ns (1,ns_steps)
   command
     apply    xvel=-0.00000005 i=1  j=1,201
     step 20000
     apply    xvel=0          i=1   j=1,201
     solve
   end_command
 end_loop
end
set ns_steps=10
;
strainsteps
;
print y esyy esxx ydis cam_p sv i=4
;
strainsteps
print y esyy esxx ydis cam_p sv i=4
set log off
```